ESMRMB

European Society for Magnetic Resonance in Medicine and Biology

ESMRMB 2019 Congress

October 3-5, Rotterdam/NL

Book of Abstracts

Saturday

DOI: 10.1007/s10334-019-00755-1

I19 Teaching Session

08:00–09:00 *Room 1 - Willem Burger Zaal.*

Robustness and Motion Correction

I19.01
Hardware and Sequence Solutions

D. Gallichan
CUBRIC, Cardiff University, School of Engineering, Cardiff, UK

Learning Objectives: To appreciate the range of current state-of-the-art solutions that exist to improve robustness to subject motion in neuro-MRI scans.
Body: In this talk I will summarize the current state-of-the-art solutions that exist to improve robustness to subject motion in neuro-MRI scans. This includes sequence-based techniques that can be used to make the acquisition itself less sensitive to any motion that might occur, as well as sequence (and/or software) solutions to explicitly estimate and correct for motion. Some motion estimation techniques are 'autofocusing' in the sense that they do not acquire additional data to aid the motion estimation—whereas others require a modified pulse sequence to include the acquisition of so-called 'navigator' data which is used for estimating the motion. Furthermore, head-motion can also be measured using external hardware—with a variety of approaches now described in the literature. Hardware approaches include camera/marker arrangements, or fiducial markers without a camera—as well as systems with a camera but without requiring a marker.
References: Selected references:
Atkinson, D. et al. (1999), *Magn Reson Med*, 41, pp. 163–170.
Cordero-Grande, L. et al. (2016), *IEEE Transactions on Computational Imaging*, 2(3), pp. 266–280. https://doi.org/10.1109/tci.2016.2557069.
Frost, R. et al. (2019), *Magnetic Resonance in Medicine*, (January), pp. 1–19. https://doi.org/10.1002/mrm.27705.
Gallichan, D., Marques, J. P. and Gruetter, R. (2016), *Magnetic Resonance in Medicine*, 75(3), pp. 1030–1039. https://doi.org/10.1002/mrm.25670.
Godenschweger, F. et al. (2016), *Physics in medicine and biology*, 61(5), pp. R32–R56. https://doi.org/10.1088/0031-9155/61/5/r32.
Howarth, C., Hutton, C. and Deichmann, R. (2006), *NeuroImage*, 29, pp. 930–937. https://doi.org/10.1016/j.neuroimage.2005.08.004.
Krause, F. et al. (2019), *bioRxiv*. https://doi.org/10.1101/595777
Loktyushin, A. et al. (2013), *Magn Reson Med*, 70, pp. 1608–1618. https://doi.org/10.1002/mrm.24615.
Maclaren, J. et al. (2012), *PloS one*, 7(11), p. e48088. https://doi.org/10.1371/journal.pone.0048088.
Maclaren, J. et al. (2012), *Magn Reson Med*. https://doi.org/10.1002/mrm.24314.
Ooi, M. B. et al. (2013), *Magnetic Resonance in Medicine*, 70(3), pp. 639–647. https://doi.org/10.1002/mrm.24845.
Pipe, J. G. (1999), *Magn Reson Med*, 42(5), pp. 963–9.
Tisdall, M. D. et al. (2016), *NeuroImage*. Elsevier Inc., 127, pp. 11–22. https://doi.org/10.1016/j.neuroimage.2015.11.054.
van Niekerk, A., van der Kouwe, A. and Meintjes, E. (2019), *Magnetic Resonance in Medicine*. John Wiley & Sons, Ltd, 82(3), p. mrm.27790. https://doi.org/10.1002/mrm.27790.
Welch, E. and Manduca, A. (2001), *Magn Reson Med*, 41(May 2001), pp. 32–41. https://doi.org/10.1002/mrm.10012.
Zaitsev, M. et al. (2006), *NeuroImage*, 31(3), pp. 1038–50. https://doi.org/10.1016/j.neuroimage.2006.01.039.

I19.02
Fetal MRI: New Sequences for old problems

D. Prayer
Medical University Vienna, Vienna, Austria

Learning Objectives: to understand which contrasts are necessary to perform Fetal MRI how they can be achieved.
Body: MR sequences, used for FetalMRI should be as short as possible, in order to avoid arifacts that may be generated by fetal movement, and/or intrinsic movement, such as maternal blood flow and breathing. While T2- weighted contrast, either achieved using Fast (Turbo) imaging or by steady state free precession (SSFP) images, is rather robust and consequently has become the mainstay of Fetal MRI, other contrasts may be more difficult to be generated with a short acquisition time. However, especially for imaging of the Fetal brain, T2-weighted and T1-weighted FLAIR sequences (1) have become available, giving more insight into pathological changes of the white matter. Diffusion-weighted imaging and Diffusion tensor imaging can be performed, the latter one allowing tractography of brain structures, such as developing white matter tracts and anisotropic organs as, for instance, the ganglionic eminence. Echoplanar sequences can be used for demonstration of blood breakdown procucts, and, in a dynamic fashion to get information on bloodflow. Blood-oxygene-labeled (BOLD) imaging may be used to demonstrate brain function from gestational week 20 onwards. T1-weighted sequences have always been regarded as the "stepchild" of Fetal imaging, as they have usually to be performed in breathhold. Holding the breath may not be easy for pregnant women. Recently so-called "free breathing" T1 weighted sequences have been devloped, allowing to visualize meconium, glnds(such as the thyroid gland, for instance), fat and methemoglobin. ´Singel voxel Proton spectroscopy may alos be performed. To date it has been used as an adjunct method to morphological imaging, mainly in cases of intrauterine growth restriction. However, it may als have a potential to show white matter damage as a consequence of other pathogenetic agents.
References:
(1) Diogo m et al., Improving subplate visualization in fetal MRI of the brain by using an echo-planar FLAIR sequence, Radiology 2019, in press.

I20 Teaching Session

08:00–09:00 *Room 2 - Van Weelde Zaal*

Segmentation and Classification by Machine Learning

I20.01
Methodology for Segmentation and Classification

M. de Bruijne
Erasmus MC, Rotterdam, The Netherlands

Learning Objectives:- To understand how machine learning can be used to segment medical imaging data.
- To learn about successful applications of machine learning in medical image segmentation
- To understand the requirements and limitations of image segmentation by machine learning.
- To appreciate the potential of machine learning techniques for medical image analysis.

Body: With recent machine learning techniques computers can now solve many image segmentation tasks as good as—or even better than—human experts. I will introduce the basic principles behind machine learning and deep learning for segmentation, discuss successful applications of machine learning in quantitative image analysis, and highlight challenges related to the introduction of machine learning in clinical practice.

References: M. de Bruijne, "Machine learning approaches in medical image analysis: From detection to diagnosis.," Medical Image Analysis 33, pp. 94–97, Oct 2016. https://doi.org/10.1016/j.media.2016.06.032

I20.02
Clinical evaluation of cardiac image segmentation and artificial intelligence

D. O'Regan
Imperial College London, MRC London Institute of Medical Sciences, London, UK

Learning Objectives: 1. To appreciate the motivation for using machine learning in cardiac image analysis.
2. To understand the techniques used for image segmentation and motion tracking.
3. Learn how these can be applied to discover mechanisms of heart disease and predicting outcomes.
4. How to move from technology development to evaluation for clinical use.

Body: Heart and circulatory diseases cause a quarter of all deaths and cardiac imaging offers an effective tool for early diagnosis and risk-stratification. Conventional image interpretation relies on manual analysis but this is time-consuming and often fails to capture important features of cardiovascular physiology. Machine learning (ML) in cardiovascular imaging promises to be a transformative tool and addresses an unmet need for patient-specific management, accurate prediction of future events, and the discovery of tractable molecular mechanisms of disease. In this talk the challenges of applying machine learning to cardiac image analysis will be discussed and how this might be evaluated in clinical practice to benefit patients.

References:
Bello G, Dawes TJ, Duan J, et al. Deep learning cardiac motion analysis for human survival prediction. Nat Mach Intell. 2019; 1:95–104.
Duan J, Bello G, Schlemper J, et al. Automatic 3D bi-ventricular segmentation of cardiac images by a shape-refined multi-task deep learning approach. IEEE Trans Med Imaging. 2019.
Tarroni G, Oktay O, Bai W, et al. Learning-Based Quality Control for Cardiac MR Images. IEEE Trans Med Imaging. 2018.

I21 Teaching Session

08:00–09:00 *Room 3 - Ruys & van Rijckevorsel Zaal*

Clinical Brain Imaging Without Gadolinium

I21.01
Structure and Function of the Blood–Brain Barrier in Health and Disease

E. de Vries
Amsterdam UMC, Amsterdam, The Netherlands

Learning Objectives: Within this seminar, the structure and function of the blood–brain barrier and the so-called neurovascular unit will be discussed. Altered signaling within the neurovascular unit (NVU) and a dysfunction of the blood–brain barrier (BBB) significantly contributes to the pathogenesis of several neuro-inflammatory and neurodegenerative inflammatory diseases, including multiple sclerosis (MS) and Alzheimer's disease (AD) with vascular deposits of amyloid.

Body: In general, the blood–brain barrier (BBB) is responsible for maintaining brain homeostasis by controlling the environment of the central nervous system (CNS), the entry of nutrients, and by protecting it against xenobioticsWithin this seminar, the structure and function of the blood–brain barrier and the so-called neurovascular unit will be discussed. Altered signaling within the neurovascular unit (NVU) and a dysfunction of the blood–brain barrier (BBB) significantly contributes to the pathogenesis of several neuro-inflammatory and neurodegenerative inflammatory diseases, including multiple sclerosis (MS) and Alzheimer's disease (AD) with vascular deposits of amyloid.

In general, the blood–brain barrier (BBB) is responsible for maintaining brain homeostasis by controlling the environment of the central nervous system (CNS), the entry of nutrients, and by protecting it against xenobiotics.

References:

Mult Scler. 2018 Jul; 24(8):1023–1024. https://doi.org/10.1177/1352458518754367. Epub 2018 Mar 5. Studying the blood–brain barrier will provide new insights into neurodegeneration—Yes.
Kamphuis WW[1], De Vries HE[2]

I21.02
Blood–Brain Barrier Breakdown Detection Without the Use of Gd based Contrast Agents

L. Knutsson
Lund University, Medical Radiation Physics, Lund, Sweden

Learning Objectives: Describe how ASL and CEST potentially can replace GBCA administration to detect blood–brain barrier breakdown.

Body: The most common approach to measure blood brain barrier (BBB) breakdown by MRI is to exploit the T1 shortening effect of gadolinium-based contrast agents (GBCAs) due to leakage of the contrast agent into the extra vascular space. However, recent concerns that GBCA can accumulate in brain and bone structures is stimulating the pursuit of new strategies to measure BBB parameters.

Arterial spin labeling (ASL) and Chemical exchange saturation transfer (CEST) are two methods that show similarities in their technical aspect but show different MRI contrast (1). ASL is a method that mainly is used to measure perfusion non-invasively (2) while CEST is a method that can detect low concentrations of molecules due to the existence of groups with exchangeable protons (3). Both ASL (4, 5, 6) and exogenous CEST contrast agents (7, 8) have potential to measure BBB permeability. For ASL, this involves time dependent measurements post-labeling and for CEST time-dependent measurements following infusion of a CEST agent. Examples of these principles will be shown.

References:

1. Knutsson L, Xu J, Ahlgren A, van Zijl PCM. CEST, ASL, and magnetization transfer contrast: How similar pulse sequences detect different phenomena. Magn Reson Med. 2018 Oct; 80(4):1320–134.
2. Detre JA, Leigh JS, Williams DS, Koretsky AP. Perfusion imaging. Magn Reson Med. 1992; 23(1):37–45.
3. van Zijl PC, Yadav NN. Chemical exchange saturation transfer (CEST): what is in a name and what isn't? Magn Reson Med. 2011 Apr; 65(4):927–48.
4. Bibic A, Knutsson L, Schmidt A, Henningsson E, Månsson S, Abul-Kasim K, Åkeson J, Gunther M, Ståhlberg F, Wirestam R. Measurement of vascular water transport in human subjects using time-resolved pulsed arterial spin labelling. NMR Biomed. 2015 Aug; 28(8):1059–68.
5. Hales PW, Clark CA. Combined arterial spin labeling and diffusion-weighted imaging for noninvasive estimation of capillary volume fraction and permeability-surface product in the human brain. J Cereb Blood Flow Metab. 2013 Jan; 33(1):67–75.
6. Lin Z, Li Y, Su P, Mao D, Wei Z, Pillai JJ, Moghekar A, van Osch M, Ge Y, Lu H. Non-contrast MR imaging of blood–brain barrier permeability to water. Magn Reson Med. 2018 Oct; 80(4):1507–1520.
7. Xu X, Chan KW, Knutsson L, Artemov D, Xu J, Liu G, Kato Y, Lal B, Laterra J, McMahon MT, van Zijl PC. Dynamic glucose enhanced (DGE) MRI for combined imaging of blood–brain barrier break down and increased blood volume in brain cancer. Magn Reson Med. 2015 Dec; 74(6):1556–63.
8. Xu X, Yadav NN, Knutsson L, Hua J, Kalyani R, Hall E, Laterra J, Blakeley J, Strowd R, Pomper M, Barker P, Chan K, Liu G, McMahon MT, Stevens RD, van Zijl PC. Dynamic Glucose-Enhanced (DGE) MRI: Translation to Human Scanning and First Results in Glioma Patients. Tomography. 2015 Dec; 1(2):105–114.

I22 Plenary Session

09:15–10:30 *Room 1 - Willem Burger Zaal*

Efficient MR Imaging

I22.01
Hardware for Efficient MRI

D. Brunner
University and ETH Zurich, Institute for Biomedical Engineering, Zurich, Switzerland

Learning Objectives: Relation of hardware and methods efficiency.
Body: The efficiency of MRI depends first on the usability of the device, the practicability of the methods and the validity and significance of the resulting data. There are always benefits justifying extra efforts and critical limitations prohibiting application.
Hence, the hardware must optimally support the envisioned methods and application as well set the ground for new developments. This inherently generates an intimate entanglement between application, methods development on one side and hardware design on the other. The hardware sets the realms in which methods and applications can operate while the latter set the requirement to the hardware.
Take the historical development of parallel imaging acceleration. RF arrays initially meant to increase SNR detection efficiency [1], yielded spatial encoding which enables acceleration of the readout [2–4]. In turn, whole body gradients can perform advanced applications such as single-shot readouts, diffusion encoding etc. Otherwise, local gradients would be required to circumvent nerve stimulation, heavy dephasing problems and prohibitive scan times accepting their impact on usability.
Recently, additional sensors deployed in the scanner restate the rules of the interplay between hardware and methods. Accuracy requirements are shifted giving room for increase in performance.
A very prominent example is motion correction by external tracking devices paired with methods of pro- and retrospective compensation [5].
Similarly, sensors monitoring the system performance and operation in conjunction with advanced feedback and signal processing schemes shift the requirements set to signal encoding. Magnetometers recording field drifts and read-out trajectories [6, 7] allow (non-Cartesian) readouts giving large degrees of freedom in sequence design and open new prospects on reproducibility and quantitation. Gradient coils offering a higher raw performance can be managed albeit inflicting higher eddy currents and tougher accuracy requirements at the same time.
The impact of machine learning and AI approaches on the design of MRI scanners is up for discussion. There is the clear prospect that these algorithms can render high image quality from fewer and less accurate data speaking in favor of reduced requirements. However, the training needs large training data sets of highest quality and automated assessments might benefit from a high level of reproducibility or even quantitative approaches. This indicates that at least some MRI scanners of the future must deliver a higher quality and performance than nowadays.
References:
1. Roemer, P.B., et al., MRM, 1990.
2. Griswold, M.A., et al., MRM, 2002.
3. Pruessmann, K.P., et al., MRM, 1999
4. Sodickson, et al., MRM, 1997.
5. Zaitsev, M., et al., NeuroImage, 2017.
6. Barmet, C., et al., MRM, 2009.
7. Barmet, C., MRM, 2008.

I22.02
Approaches for efficient MRI data acquisition

M. Doneva
Philips Research, Hamburg, Germany

Learning Objectives: Understand the principles of efficient MRI acquisition methods and gain insights about the trends in this area.
Body: This talk will give an overview of the methods for fast MR acquisition.
One approach to fast MRI is using efficient sampling trajectories like EPI and spiral. Recently there has been a renewed interest in optimizing sampling trajectories, that have high efficiency and achieve improved k-space sampling pattern [1].
Another approach to improve the scan efficiency from the exam card perspective is to acquire a single scan that provides multiple contrasts. This includes multi-contrast imaging [2], synthetic MRI [3], and continuous transient state acquisition as employed in MR fingerprinting [4].
Parallel imaging [5, 6] is a well-established method for reducing scan time in 2D and 3D scans. In simultaneous multi-slice imaging (SMS), an RF pulse is applied to simultaneously excite multiple slices, allowing also through-slice acceleration for multi-slice sequences [7].
In the last 10–15 years, another group of techniques was developed, using prior knowledge about the data structure in the reconstruction, such as compressed sensing [8], low rank [9], dictionary learning [10], and manifold techniques [11], providing additional acceleration to parallel imaging alone.
Recently, neural networks have also begun to be explored for image reconstruction [12, 13]. These techniques can further leverage compressed sensing and low rank approaches, providing more data adapted and potentially more stable reconstruction allowing even higher acceleration factors.
References:
[1] Lazarus et al. SPARKLING: variable-density k-space filling curves for accelerated T2*-weighted MRI, *MRM*(81) 3643–61, 2019.
[2] Skare et al. A 1-min full brain MR exam using a multicontrast EPI sequence, *MRM(*79), 3045–54, 2018.
[3] Warntjes et al. Novel method for rapid, simultaneous T1, T2*, and proton density quantification, MRM(57), 528–37, 2007.
[4] Ma et al. Magnetic Resonance Fingerprinting, *Nature,* 187–93, 2013.
[5] Pruessmann et al. SENSE: sensitivity encoding for fast MRI, *MRM* 952-62, 1999.
[6] Griswold et al. Generalized autocalibrating partially parallel acquisitions (GRAPPA), *MRM*(4)7, 1202–10, 2002.
[7] Barth et al. Simultaneous multislice imaging techniques, MRM(75), 63–81, 2016.
[8] Lustig et al. Sparse MRI: The application of compressed sensing for rapid MR imaging, *MRM,* 1182–95, 2007.
[9] Lingala et al. Accelerated Dynamic MRI Exploiting Sparsity and Low-Rank Structure: k-t SLR, *IEEE TMI(*30), 1042–54, 2011.
[10] Doneva et. al Compressed sensing reconstruction for magnetic resonance parameter mapping, MRM(64), 1114–20, 2010.
[11] Poddar et al. Dynamic MRI using SToRM, IEEE TMI(35), 1106–15, 2016.
[12] Hammernik et al. Learning a variational network for reconstruction of accelerated MRI data, *MRM,* 3055–71, 2017.
[13] Zhu et al. Image reconstruction by domain-transform manifold learning, *Nature,* 2018

I22.03
Clinical Impact of Compressed Sensing

S. Trattnig
Medical University of Vienna, High Field MR Center, Department of Biomedical Imaging and Image Guided Therapy, Vienna, Austria

Learning Objectives: To understand how CS can improve imaging workflow.
To learn how the application of CS allows high spatial and high temporal resolution imaging.
To know which patients benefit from CS.
Body: MR imaging is an established yet time-consuming imaging technique. Thus due to high demand, economic pressure and the request to improve image resolution without prolonging image acquisition, efforts have been made to shorten image acquisition times. Acceleration of MR sequences beyond current parallel imaging techniques is possible with the Compressed Sensing (CS) technique that has recently become available for 1.5 and 3 Tesla scanner.
A recently introduced free-breathing radial acquisition scheme for liver imaging was paired with a reconstruction method that combines compressed sensing and parallel imaging, called GRASP (Golden-angle RAdial Sparse Parallel). Dynamic k-space data acquired continuously in free-breathing and reconstructed retrospectively with flexible temporal resolution by grouping different numbers of consecutive spokes in each single-dynamic frame. This allows automatic recognition of liver phases and reconstruction of key images and clinical relevant series. In patients unable to perform breathhold acceptable image quality and diagnostic information can be achieved. Cardiac Perfusion-MRI (MPI) is a promising method to evaluate noninvasively ischemic heart diseases, but high temporal resolution for perfusion MR limits volume coverage, spatial resolution and high SNR. Moreover long breath holds are necessary. This is a challenge for patients with arrythmias and/or restricted lung function and pediatric patients. GRASP with reconstruction of respiratory and cardial motion eliminates blurring and allows visualization of dynamics of normal and abnormal (extrasystole) heart beats. Significant clinical benefits of CS acceleration. have also been shown with single breath hold CS cine cardiac MR which provides similar quality compared to segmented multi-breath hold cine MR which simplifies the imaging protocol. Additional applications which benefit from the acceleration by CS are MR mammography in which high spatial and temporal resolution are required simultaneously with acceleration factors up to 18 with clinically better detection of breast lesions and better differential diagnosis of benign/malign lesions, metall artifact reduction methods such as SEMAC, MR cholangiography and sodium imaging. For complete MR examinations a 45% reduction of total scan time by CS could be demonst Recent development of deep learing have demonstrated improvements in image quality in higher acceleration rates.
In summary, in addition to acceleration of MR examinations CS has the potential to improve diagnostic information.

References

Lustig M, Donoho D, Pauly JM. Sparse MRI: The application of compressed sensing for rapid MR imaging. Magnetic resonance in Medicine 2007; 58: 1182–1195.

S17 Scientific Session

10:50–12:20 *Room 1 - Willem Burger Zaal*

Image Analysis & Post Processing

S17.02

Diffusion-weighted imaging informed gradient-echo myelin water imaging

K.-S. Chan, J. P. Marques
Donders Institute for Brain, Cognition and Behaviour, Nijmegen, The Netherlands

Purpose/Introduction: Multi-echo GRE myelin water imaging (MWI) measure white matter myelination by fitting the multi-echo signal to a 3-pool model[1]. Yet this fitting of three pools with different amplitudes, decay rates and frequency shifts (standard model, Model0) is ill-conditioned. Recent DWI development on WM microstructure modelling allows the intra-axonal (IW) and extracellular water (EW) ratio estimation[2, 3]. Integrating DWI with GRE-MWI thus has the potential to improve myelin water fraction (MWF) measurement.

Subjects and Methods: In this study we evaluated first, the possibility of fixing the IW/EW ratio in GRE-MWI fitting (Model1), by using a multi-shell DWI additional information (ICVF)[2, 3].

In a second model (Model2), the compartmental frequency offsets were modelled by the hollow cylinder model (HCM)[4] given the DWI fibre orientations. The myelin isotropic and anisotropic susceptibility and relative myelin water density are considered being known ($\chi_i = \chi_a = -0.1$ ppm[4], $\rho = 0.43$[5]).

Numerical simulation: The standard deviation (SD) of MWF estimation of the various models proposed were compared by Cramér-Rao bound (CRB) analysis in a range of GRE acquisition protocols (#TE = 10:64 and ΔTE = 1:5 ms).

Simulated 3-pool WM signal with added Gaussian noise was fitted with Models 0&2 2000 times to derive the bias and precision of MWF estimations when the HCM model assumptions were invalid.

In vivo Imaging: Five healthy subjects were scanned at 3T. The imaging protocol comprised:

1) 3D mGRE, TR/TE1/ΔTE/TE12 = 46/2.15/3.05/35.65 ms, res = 1.8 mm, $\alpha = 20°$ and TA = 3.5 min. Repeated 7 times.

2) 2D-MB EPI-DWI, MB = 3, res = 1.6 mm, TR/TE = 3350/71.20 ms, 2-shell (b = 0/1250/2500 s/mm^2, 17/120/120 measurements), TA = 15 min.

DWI was processed with a spherical mean technique[3] and a ball-and-stick model[6] to compute the ICVF and fibre orientation maps before registration to GRE space. Models 0–2 were used to compute MWF maps based on either 1 or 7 averages[1].

Results: Models 1&2, when compared to Model0 in CRB analysis (Fig. 1), estimated MWF with an SD smaller than its true value (12%). Further reduction in SD can be achieved with Model2 when the fibre direction and B0 is perpendicular (Fig. 1). Figure 2 shows that Model2 outperformed Model0 even when the fixed HCM model parameters were invalid. MWF maps from in vivo imaging of Models 0&1 are similar. Model2 significantly reduced the noise in MWF compared to the other models.

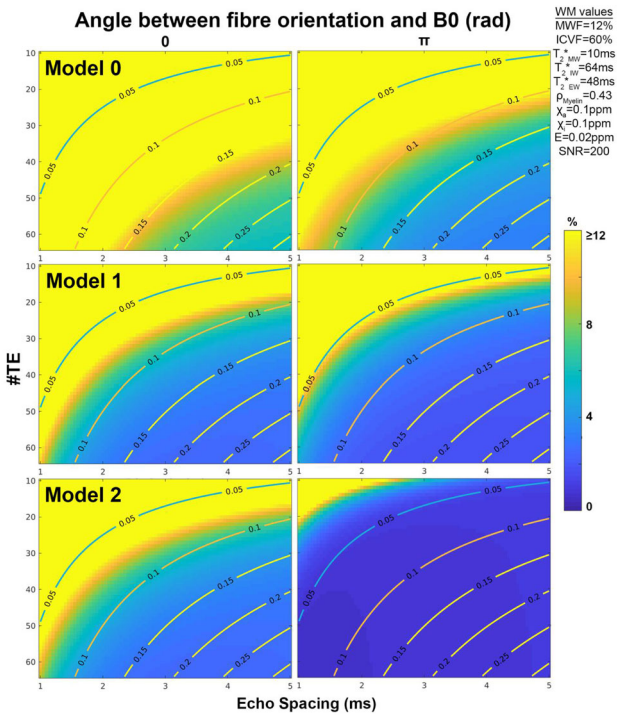

Figure 1: Lower bounds of MWF standard deviation predicted by CRB on different GRE protocols. The DWI informed models (Models 1&2) show that more options achieved lower SD than that of Model0. Contour outlines the protocols' longest TE (in seconds).

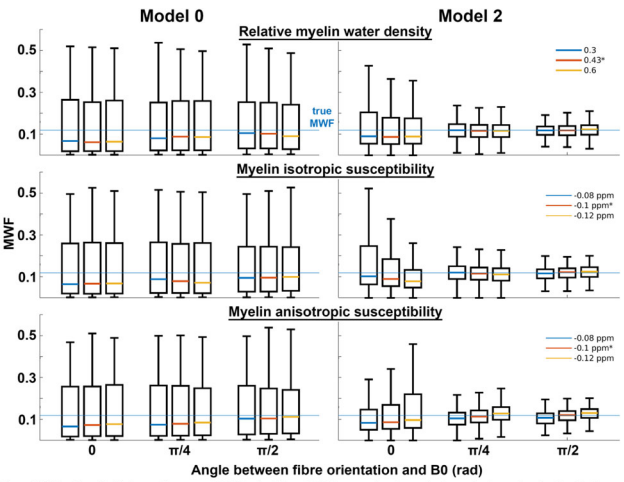

Figure 2: Plots of median±interquartile range of MWF using different HCM parameters. Legends shows the true values in simulated signal. The MWF median of Model2 are close to ground truth even when the fixed parameters of the HCM are wrong.

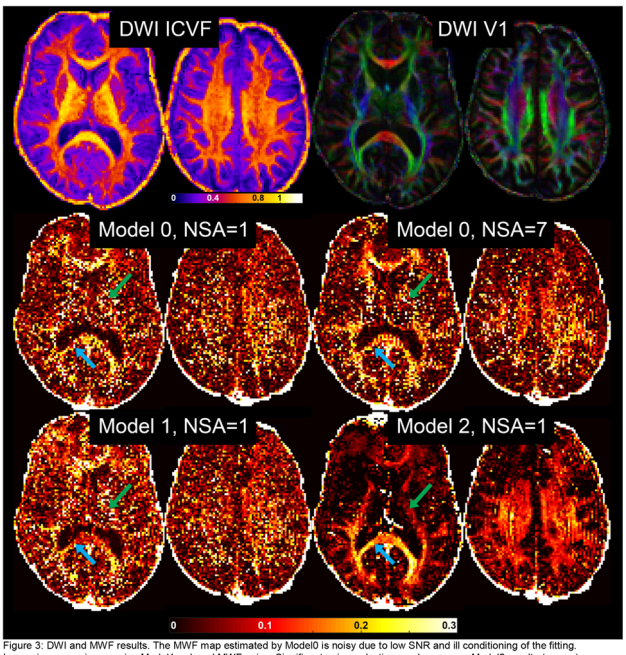

Figure 3: DWI and MWF results. The MWF map estimated by Model0 is noisy due to low SNR and ill conditioning of the fitting. Increasing averaging or using Model1 reduced MWF noise. Significant noise reduction can be seen on Model2 results (arrows).

Discussion/Conclusion: We demonstrated that integrating DWI into GRE-MWI improves MWF estimation significantly. The proposed model will be adapted to other acquisition strategies[7] to explore other myelination markers.

References:

1. Nam et al. *Neuroimage* **116,** 214–221(2015).
2. Zhang et al. *Neuroimage* **61,** 1000–1016(2012).
3. Kaden et al. *Neuroimage* **139,** 346–359(2016).
4. Wharton & Bowtell. *Neuroimage* **83,** 1011–1023(2013).
5. Jung et al. *Neuroimage* **182,** 379–388(2018).
6. Behrens et al. *Neuroimage* **34,** 144–155(2007).
7. Chan & Marques. In Proc. ISMRM **27**, 0421(2019).

S17.03

T_1 saturation effects in myelin water fraction measures: does myelin water have its distinct T_1?

A.-M. Oros-Peusquens, D. Thomas, M. Zimmermann, N. J. Shah
Research Centre Juelich, INM-4, Juelich, Germany

Purpose/Introduction: Myelin is ubiquitous in determining MR contrast in the living brain, especially at high fields [1, 2], but the properties of myelin water—e.g. longitudinal relaxation, exchange with other water pools—are insufficiently studied.

Multiple-echo gradient echo-based myelin water fraction (mGRE-MWF) determination is a potential alternative to spin-echo methods [3], especially at 3T and higher fields [4, 5]. We improve the quality of MWF maps by noise reduction using Principal Component Analysis (PCA) and investigate the interesting question of whether T1 saturation effects are different in myelin and tissue water.

Subjects and Methods: Results using a 2D mGRE acquisition were obtained from twelve healthy volunteers (6 females and 6 males, 30 ± 7yo) scanned on a 3T TIM-Trio Siemens scanner. The parameters of the experimental 2D mGRE protocol included: resolution $1 \times 1 \times 2.5$ mm^3, 'fast pulse' $\alpha = 90^o$, 32 echoes (TE_1 = 3.24 ms, ΔTE = 1.54 ms), TR = 2200 ms (TA = 11:53, 24 slices, 2avgs), 800 ms (TA = 8:39, 14 slices, 4avgs) or 216 ms (TA = 11:42 min, 4 slices, 20avgs), 2 repetitions averaged off-line. Data were denoised using Principal Component Analysis (5 components kept out of 32) and analysed using NNLS with Tikhonov regularisation. T2* intervals were defined based on the relaxometric spectra and were assigned to myelin water, blood (mainly), tissue water and CSF-like components.

Results: SNR of the original data in the first echo was 74 (TR = 2200), 69 (TR = 800 ms) and 92 (TR = 216 ms). Figure 1 shows the effect of noise reduction using PCA on a TR = 2200 ms data set.

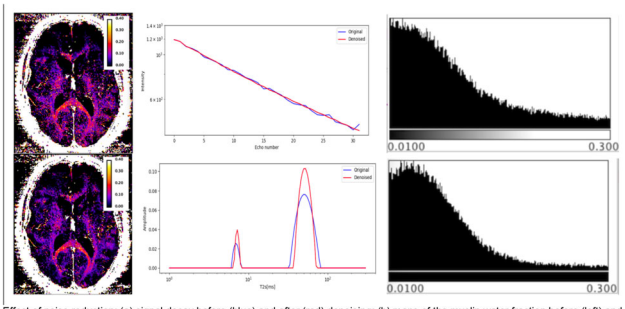

Effect of noise reduction: (a) signal decay before (blue) and after (red) denoising; (b) maps of the myelin water fraction before (left) and after (right) denoising; (c) histograms of the myelin water fraction (top – original, bottom – denoised).

Maps of the different water fractions and T2* values are shown in Fig 2 based on the denoised data.

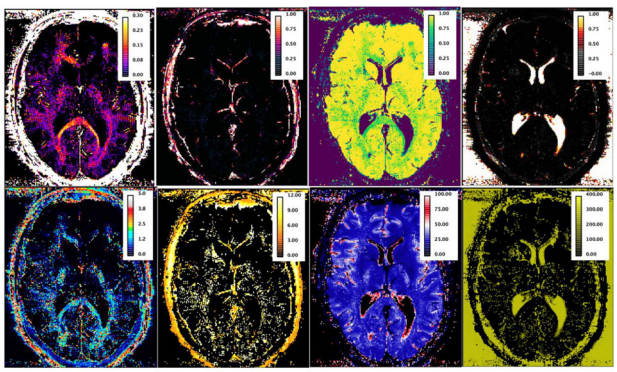

Water fractions in different T2* intervals. The components identified in the whole brain were: myelin water (T2* of ~5ms), blood (T2*~20ms), tissue (T2*~50ms), long-T2* and CSF (T2*>80ms).

Fig. 3 shows myelin water fraction maps using denoised data sets at three different TRs: (a) TR=2200ms, (b) TR=800ms, (c) TR=216ms, and (d) changes in the spectrum of a selected ROI with changing TR.

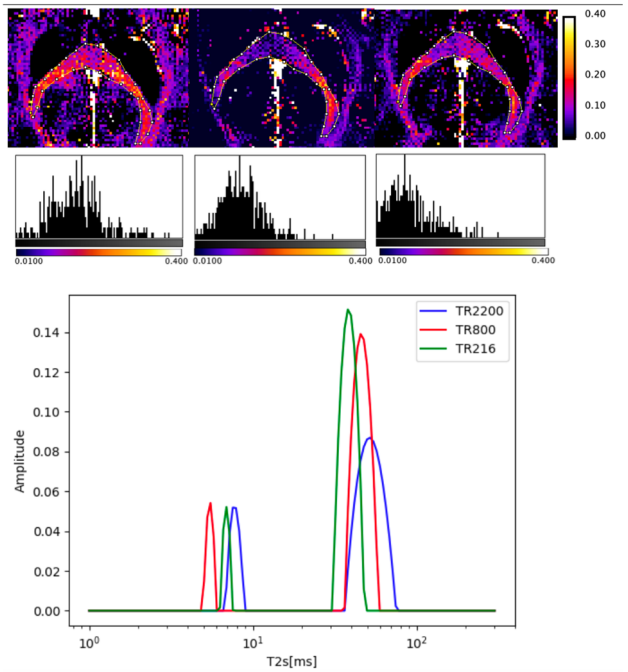

Changes in MWF with TR in a selected ROI including the corpus callosum and forceps major. MWF distributions are shown as image and in histogram form. Most interestingly, changes in the T2* values of the myelin and tissue components are observed.

Discussion/Conclusion: PCA-based denoising increases the visual quality of the MWF maps and reduces the SD of the MWF by nearly 2. The high quality of these data allows us to investigate TR –related changes: the water fractions are affected and also the position of the individual peaks (Fig. 3). Assuming that the effective flip angle is the same for all water pools, changes in MWF with TR are not consistent with myelin and tissue water being two pools with same T1 (fast exchange). The decrease in T2* values of both pools, seen in the spectra, is also not consistent with two pools with different T1 and no exchange. Exchange of one or both pools with an increasingly saturated long-T_1 pool (e.g. axonal water) could qualitatively describe the data.

In conclusion, T_1 effects in myelin water fraction hinting to a complicated exchange picture, similar to that described in [6], are reported in vivo for the first time.

References:

[1] A. MacKay et al., MagnResonMed 31(1994); [2] Oros-Peusquens et al. Procs ISMRM 2013; [3] E. Alonso-Ortiz et al. MagnResonMed 79 (2018); [4] Barta et al. JMagnReson 259 (2015)

S17.04

Automatic sorting of brain magnetic resonance imaging sequences using convolutional neural networks

S. van der Voort, M. Smits, S. Klein
Erasmus MC, Rotterdam, The Netherlands

Purpose/Introduction: When collecting magnetic resonance images (MRI) from clinical practice or from public datasets, usually laborious manual identification of the scan type of the various scans is required. This process is difficult to automate as naming conventions vary, are often unclear, or are even missing due to file format conversions or anonymization. In this work we investigate whether data sorting can be automated using convolutional neural networks (CNN).

Subjects and Methods: We designed a CNN that automatically recognizes different brain MRI scan types based on image appearance and transforms the unstructured dataset into a sorted, standardized format. We developed the CNN to recognize pre-contrast T1-weighted (T1w), post-contrast T1-weighted (T1wC), T2-weighted (T2w), proton density weighted (PDw), T2-weighted FLAIR (T2w-FLAIR), diffusion weighted images (DWI), and derived DWI (DWI-D) such as apparent diffusion coefficient or fractional anisotropy maps. The CNN was trained on 7153 scans of 665 patients from 5 different public datasets. The CNN was then tested on 1700 scans of 207 patients from 4 different public datasets. This training and testing was repeated 5 times to evaluate consistency. We additionally trained a neural network based on six DICOM tags: repetition time (tag 0018, 0080), echo time (tag 0018, 0081), inversion time (tag 0018, 0082), number of averages (tag 0018, 0083), echo train length (tag 0018, 0091) and flip angle (tag 0018, 1314).

Results: The CNN obtained an overall average accuracy of 98.3 ± 0.1% and a per-class average accuracy of 99.1 ± 0.2% (T1w), 98.5 ± 0.7% (T1wC), 99.7 ± 0.4% (T2w), 99.9 ± 0.3% (PDw), 95.9 ± 2.2% (T2w-FLAIR), 98.0 ± 1.8% (DWI) and 96.4 ± 1.5% (DWI-D). By comparison, the neural network trained on the DICOM tags achieved an overall average accuracy of 58.9 ± 1.3%.

Discussion/Conclusion: Our method can automatically sort brain MRI scans into a standardized format with near-perfect accuracy. As evidenced by the poor performance of the DICOM tag-based network, a simple classification based on DICOM tags is not sufficient, due to the fact that DICOM tags are often missing or are not informative enough. For instance, 32% of the T1wC sequence did not have the contrast agent tag (tag 0018, 0010) filled. Furthermore, 8.4% of the six extracted DICOM tags used for training the DICOM tag network was missing. Automating the sorting of scans substantially reduces the laborious manual preparation of datasets and thus allows for large datasets to be more easily used for research purposes.

References:

Clark, K., Vendt, B., Smith, K., Freymann, J., Kirby, J., Koppel, P., Moore, S., Phillips, S., Maffitt, D., Pringle, M., et al.: The Cancer Imaging Archive (TCIA): maintaining and operating a public information repository. Journal of Digital Imaging 26(6), 1045–1057 (2013)

S17.05

Development of a realistic numerical phantom to test and validate CMR feature tracking software

D. Adams, R. Boubertakh, M. E. Miquel
Barts Health NHS Trust, Clinical Physics, London, UK

Purpose/Introduction: Feature tracking (FT) is a relatively recent post-processing technique that uses standard clinical Cardiovascular Magnetic Resonance (CMR) cine images to derive myocardial deformation parameters such as strain for early patient diagnosis and follow-up. However, differences in calculated values between software packages and the lack of absolute validation have hindered its clinical acceptance. Research is active in the development of realistic cine model simulations for which motion deformation parameters are known a priori, to be used as the "gold-standard" to validate CMR-FT packages. The aim of the present work was to use numerical simulation to generate a realistic single slice short-axis bSSFP cine model with known myocardial motion parameters to use as a gold-standard for CMR-FT comparison and validation.

Subjects and Methods: An acquired end-diastole (ED) T1 map, a T2 map, and a proton-density weighted image were used as input to the pulse sequence simulator JEMRIS [1] to simulate a bSSFP sequence. Images were registered to the ED contours of an acquired tagging cine and deformed from ED to simulate the cine frames. The myocardial

deformation was extracted from the tagging cine using CIMTag2D (Auckland MRI Research Group, New Zealand) and merged with deformation outside of the left ventricle extracted from B-spline based non-rigid registration [2] through an acquired FLASH cine (Fig. 1). A zero-end-displacement condition was applied to ensure that the cine start and end displacements were matching. The resulting model was analysed with 2 FT software packages: TomTec 2D CPA MR (TomTec Imaging Systems, Munich, Germany) and cvi42 (Circle Cardiovascular Imaging Inc., Calgary, Canada) and the results compared with the analytical strain values. Analytical values included both 1D and 2D ground-truth strain because the CMR-FT software packages investigated report these differing strain measures [3].

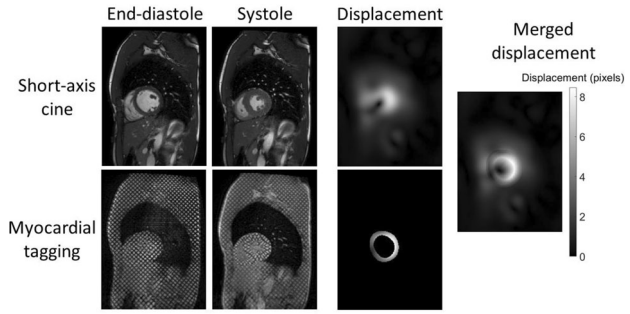

Figure 1: Summary of methodology: The displacement field from the short-axis FLASH cine, obtained using B-spline based non-rigid registration, was merged with the displacement field from the tagging cine, obtained using CIMTag2D software.

Results: The simulated cine showed realistic motion and image texture (Fig. 2). The global strain results of the two FT software packages were comparable to the analytical 1D and 2D ground-truth global strains (Fig. 3). Differences between measured strain and ground-truth strain could be due to regularization.

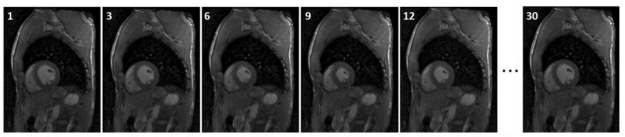

Figure 2: Selected frames of the single-slice short-axis bSSFP cine model (30 frames) simulated using JEMRIS.

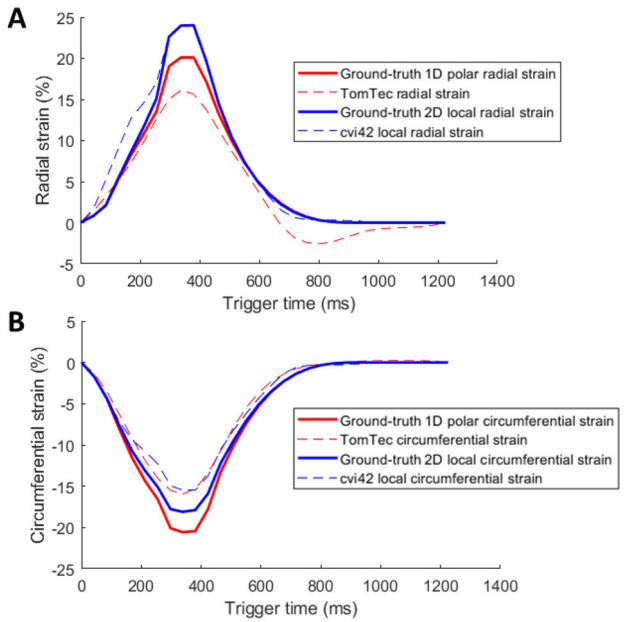

Figure 3: Comparison between the ground-truth global radial strain (A) and global circumferential strain (B) for the cine model with TomTec 2D CPA MR and cvi42 results for 1D and 2D strain (2D uses a local LV coordinate system).

Discussion/Conclusion: This work provides a basis for further work in developing a realistic cine model for CMR-FT validation. The results reaffirm the significance of the effects of regularization and the strain calculation methods on inter-vendor FT strain disagreement. Future work could investigate the effects of spatial and temporal resolutions on measured parameters.

References:

[1] Stöcker, T et al., MRM, vol. 64, no. 1, pp. 186–193, January 2010
[2] Kroon, D J, "B-spline grid, image and point based registration" [Internet], File Exchange MATLAB Central, 2011
[3] Wehner, G J et al., JCMR, vol. 20, no. 1, September 2018

S17.06

Quantification of mitral valve regurgitation from 4D flow MRI using semi-automated flow tracking

C. P. S. Blanken[1], J. J. M. Westenberg[2], J.-P. Aben[3], G. P. Bijvoet[4], S. A. Chamuleau[5], A. J. Nederveen[1], T. Leiner[5], R. N. Planken[1], P. van Ooij[1]
[1]*Amsterdam UMC, location AMC, Amsterdam, The Netherlands*, [2]*LUMC, Leiden, The Netherlands*, [3]*Pie Medical Imaging, Maastricht, The Netherlands*, [4]*MUMC, Maastricht, The Netherlands*, [5]*UMCU, Utrecht, The Netherlands*

Purpose/Introduction: Cardiac 4D flow MRI offers novel possibilities to quantify mitral valve regurgitation (MVR). Retrospective valve tracking enables forward blood flow quantification over the heart valves, taking into account valvular motion[1]. However, quantification of MVR at valve level can suffer from flow incoherency, causing signal loss and underestimation of regurgitant flow. A suggested solution is to measure 1–2 cm proximal to the valve and perpendicular to the regurgitation: flow tracking[2]. The purpose of this study was to compare regurgitant flow over the mitral valve as quantified by semi-automated flow tracking and valve tracking in clinical MRI data.

Subjects and Methods: 26 MVR patients (8 mild-moderate, 8 moderate-severe, 10 severe, as diagnosed by echocardiography[3]) underwent cardiac MRI including 4D flow MRI at 1.5T (30 cardiac phases, free-breathing, retrospective ECG-gating, three-directional VENC of 150–280 cm/s, spatial resolution of $2.89 \times 2.89 \times 3.5$ mm^3 for severe MVR and $1.45 \times 1.45 \times 6$ mm^3 in the other groups. Mitral valve (MV) and aortic valve (AV) flow volumes were quantified from 4D flow MRI by dedicated software (CAAS MR 4D Flow 5v1, Pie Medical Imaging) with through-plane valve motion correction as assessed on two-, three- and four-chamber (2CH, 3CH, 4CH) cine bSSFP.

(1) MV regurgitant flow volume (Rvol) was quantified using flow tracking and valve tracking (Fig. 1). (2) To test inter-valve consistency, MV and AV forward flow were quantified using valve tracking at annulus level. (3) Left-ventricular stroke volume (LVSV) was quantified by short-axis bSSFP volumetry for indirect MVR quantification ($Rvol_{INDIRECT}$ = LVSV − AV flow).

Agreement between MV and AV net flow was evaluated with a Wilcoxon signed rank test, as well as agreement between 4D flow MRI-derived Rvol and $Rvol_{INDIRECT}$. Orthogonal regression and Bland–Altman analysis were performed with $p < 0.05$ considered significant.

Results: Flow tracking measured higher Rvol than valve tracking ($p < 0.001$, Fig. 2). MV net flow turned out higher than AV net flow for valve tracking ($p < 0.001$) but not when Rvol was quantified with flow tracking ($p = 0.97$, Fig. 3). Interestingly, when comparing with indirect quantification (LVSV–AV flow), Rvol measured with flow tracking was higher ($p = 0005$) whereas Rvol measured with valve

tracking was not (p = 0.253), despite a trend towards underestimation of Rvol for severe MVR using valve tracking (Fig. 2).

Discussion/Conclusion: In this study, the application of semi-automated flow tracking provided better quantification of MVR by 4D flow MRI than valve tracking, in particular in severe MVR. Good agreement between MV and AV net flows indicated good accuracy of flow tracking. In conclusion, we found that flow tracking provided more accurate quantification of MVR than valve tracking due to measurement at a location of less incoherent flow.

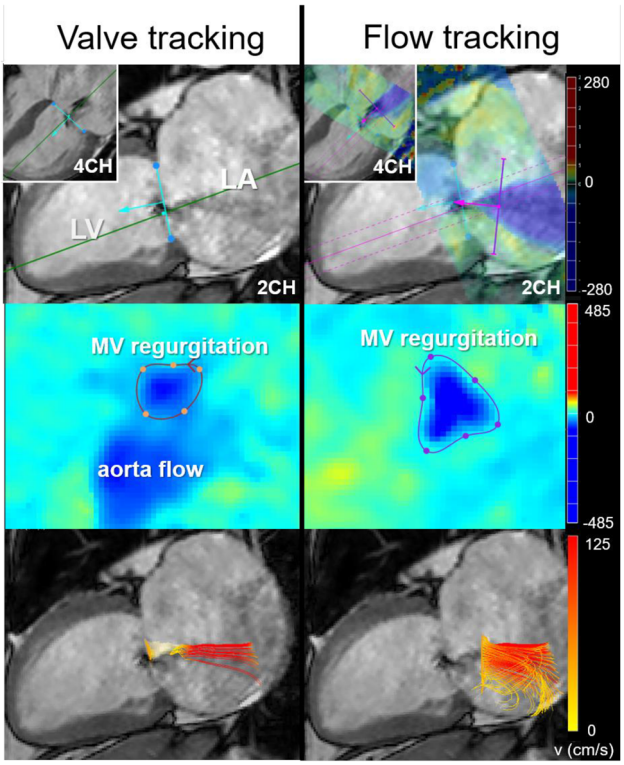

Figure 1: Valve tracking and flow tracking in severe MVR. a-b) Measurement plane initialization. For flow tracking, an additional plane is initialized during regurgitation. c-d) Flow area contouring in 4D flow velocity projection, e-f) streamlines.

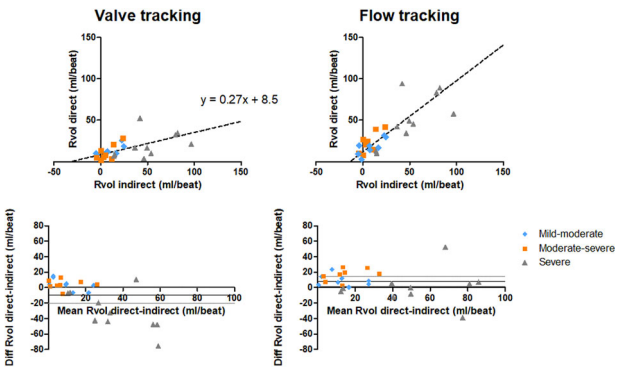

Figure 2: Orthogonal regression (top) and Bland-Altman plots (bottom) of regurgitant volume measured with valve tracking (15±12ml, left) and flow tracking (33±25ml, right) versus indirectly quantified regurgitant volume (Rvol indirect=LVSV-AV flow).

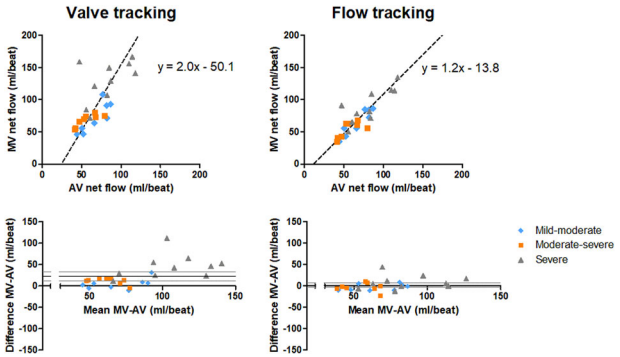

Figure 3: Orthogonal regression (top) and Bland-Altman plots (bottom) of MV and AV net flows (forward – backward flow volume) resulting from valve tracking (left) and flow tracking (right). MV and AV net flows should be the same.

References:

1. Kamphuis, Radiology 2018.
2. Calkoen, JCMR 2015.
3. Vahanian, 2013.

S17.07

Deep learning based processing for quantitative myocardial perfusion MRI

C. M. Scannell[1], M. Veta[2], A. Villa[1], E. Sammut[3], J. Lee[1], M. Breeuwer[4], A. Chiribiri[1]

[1]*King's College London, School of Biomedical Engineering and Imaging Sciences, London, UK,* [2]*Eindhoven University of Technology, Eindhoven, The Netherlands,* [3]*University of Bristol, Bristol Heart Institute and Translational Biomedical Research Centre, Bristol, UK,* [4]*Philips Healthcare, Best, The Netherlands*

Purpose/Introduction: Quantitative myocardial perfusion cardiovascular magnetic resonance (CMR) provides a user-independent assessment of myocardial perfusion status for the non-invasive diagnosis of myocardial ischaemia, with high prognostic value [1]. However, it currently has limited use in clinical practice due to the challenging post-processing required, particularly for the segmentation of the images. We propose an automated method for processing the images prior to quantitative analysis based on deep learning techniques, and in particular convolutional neural networks (CNNs).

Subjects and Methods: A sequence of object detection and image segmentation tasks is performed. There is first a classifier that identifies the time dynamic corresponding to peak enhancement in the left ventricle (LV). A CNN then predicts a bounding box around the LV and myocardium prior to motion correction. After motion correction [2], the myocardium is segmented and the right ventricular insertion point is detected. Due to the use of motion correction, segmentations and landmarks can be propagated to all time dynamics. These are then used in the tracer-kinetic modelling. Each step is assessed individually followed by a comparison of the automated and manually obtained myocardial blood flow (MBF) values on a segmental level. The full pipeline is shown in.

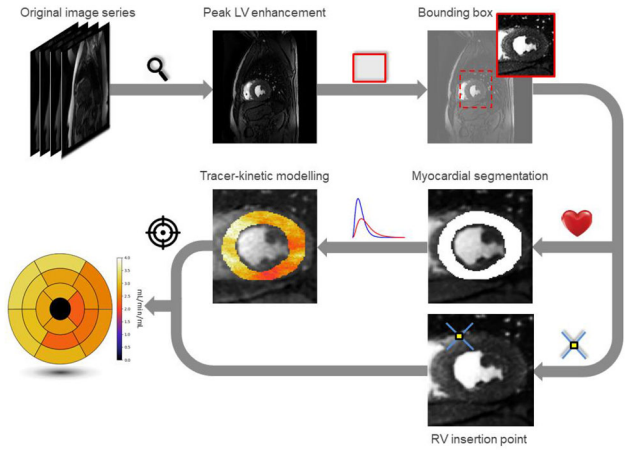

The flow chart representing the pipeline for automated myocardial perfusion quantification.

Results: The respective CNN predicts the correct time of peak LV enhancement with a mean (SD) error of 1.04 (0.72) time dynamic. The mean (SD) Dice similarity coefficient for the bounding box and myocardial segmentation were 0.88 (0.06) and 0.81 (0.08), respectively. The mean (SD) error (voxels) in the RV insertion was 4.2 (3.4). The automated and manually processed MBF values are highly correlated, as evidenced by the slope of the linear relationship (0.94 and 0.99) on a per-scan and per-myocardial segment basis, respectively. The Bland–Altman analysis showed little bias and a good agreement between the automated and manually processed MBF values and there was a high intra-class correlation coefficient of 0.867, 95% confidence interval = [0.829, 0.896].

Discussion/Conclusion: The deep learning-based method is fast and reliable with the MBF values achieved with the automated processing in line with those achieved with manual processing.

References:

[1] Sammut EC, Villa ADM, Di Giovine G, et al. Prognostic Value of Quantitative Stress Perfusion Cardiac Magnetic Resonance. JACC Cardiovasc. Imaging 2017. https://doi.org/10.1016/j.jcmg.2017.07.022.

[2] Scannell CM, Villa ADM, Lee J, Breeuwer M, Chiribiri A. Robust non-rigid motion compensation of free-breathing myocardial perfusion MRI data. IEEE Trans. Med. Imaging [Internet] 2019:1–1. https://doi.org/10.1109/tmi.2019.2897044.

S17.08

Robust quantification of spontaneous muscular activities by simultaneous interpretation of sEMG data

M. Schwartz[1, 2], T. Küstner[1], P. Martirosian[1], J. Machann[1], G. Steidle[1], B. Yang[2], F. Schick[1]

[1]*University Hospital of Tübingen, Section on Experimental Radiology, Tübingen, Germany,* [2]*University of Stuttgart, Institute of Signal Processing and System Theory, Stuttgart, Germany*

Purpose/Introduction: Robust quantification of spontaneous mechanical activities of resting musculature (SMAM[1]) by diffusion-weighted imaging (DWI) is of high interest for the assessment of activity distribution and spontaneous muscle fiber imaging in healthy and non-healthy population. However, detection can be hampered due to varying signal intensity, noise, vessel pulsation and voluntary movement.[2] Strong correlation between simultaneously applied MR-compatible surface EMG (sEMG) and SMAM is utilized to overcome these limitations.[3] A deep learning approach consisting of sEMG classification and DWI activity detection is proposed to enable accurate quantification of SMAMs.

Subjects and Methods: Dataset: DWI parameters are given in Fig. 1a. Images were acquired from 25 subjects (age: 33 ± 12, 9 female) on 3T systems (Trio/Skyra/Prisma[fit]/Vida, Siemens, Erlangen).

Detection: System architecture is depicted in Fig. 1b.

Type	TE [ms]	TR [ms]	TM [ms]	Repetitions	Matrix	FoV [mm²]	Body Region
Spin-Echo	37-53	500	-	100/500	64/80	180-190	Calf/Thigh
Stim. Echo	26-31	500/1000	145	500/1000	64/80	180-210	Calf

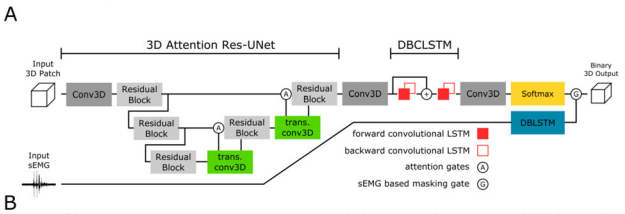

Figure 1: A: MR imaging parameters of the applied spin-echo and stimulated echo sequences. B: Architecture for SMAM detection. A binary segmentation mask depending on the classified sEMG signal is outputted, e.g. voluntary movement: all zero.

It is composed of several building blocks: encoder-decoder structure[4, 5] with residual blocks[6] and attention gates[7] for dense prediction. A deep bidirectional convolutional long short-term memory (DBCLSTM)[8, 9] network is utilized for prediction smoothing by propagating the background class between DWI acquisitions and by that reducing false positive detections. Training data was semi-automatically annotated and revised for supervised learning.[10] Data was augmented by Gaussian noise and random shuffling in time direction. Due to highly imbalanced datasets, a modified Dice loss function considering only present classes in the current patches is utilized. sEMG data were recorded with an MR-compatible system (BrainAmp ExG MR) and MR gradient artifact corrected[3] prior to classification. A pre-trained DBLSTM[11] was applied for sEMG classification (three classes: resting, spontaneous activity and voluntary movement) which prunes the segmentation by gating the output mask. The detection and segmentation pipeline is integrated into the Gadgetron[12] framework enabling a clinical workflow.

Results: Event count maps (ECM) for exemplary subjects are shown in Fig. 2a.

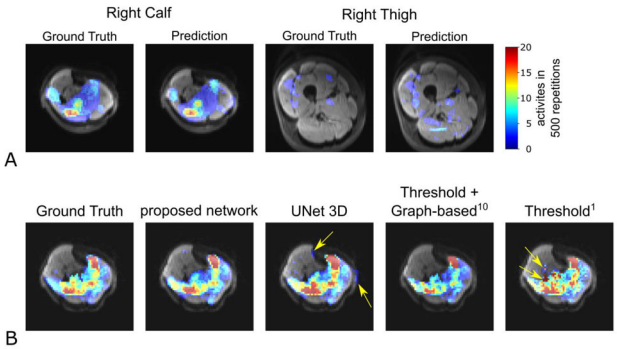

Figure 2: A: ECMs of the ground truth and prediction for two subjects showing only small differences in activation. B: Comparison of different detection approaches. No activations are found in the bone and vessel regions by the proposed network.

Attention and DBCLSTM lead to a reduction of the false positive rate from 56.7[1]/20.4[10] % and 2.4% for UNet3D to 1.3% and avoids misclassification in boundary and vessel regions (Fig. 2b). Reliable quantitative maps can be achieved by discarding the motion-corrupted DWI (Fig. 3).

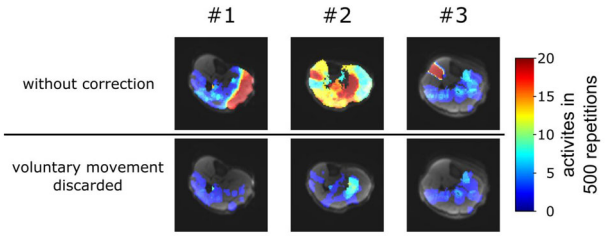

Figure 3: Three subjects where asked for intended movements during examination. ECMs based on sEMG classification are presented, with/-out rejection of motion corrupted data. The importance of subject surveillance during measurements is demonstrated.

Discussion/Conclusion: A reliable and robust assessment of spontaneous activities during DWI measurements was investigated. Furthermore, integration of sEMG information leads to improved activity maps. The proposed method can be easily extended to artifact detection in diffusion-tensor imaging to achieve more robust fiber tractography estimations.

References:

1:Steidle, NMR, 2015.
2:Schwartz, ISMRM, 2018.
3:Schwartz, MRM, 2018.
4:Ronneberger, MICCAI, 2015.
5:Milletari, ArXiv, 2016.
6:He, CVPR, 2016.
7:Oktay, ArXiv, 2018.
8:Hochreiter, Neural Comput, 1997.
9:Shi, ArXiv, 2015.
10:Schwartz, ISMRM, 2016.
11:Schwartz, EMBC, 2019.
12:Hansen, MRM, 2013.

S17.09

Numerical feasibility study of voxel by voxel signal classifications to detect glioblastoma multiforme in mice based on endogenous static BOLD contrast using random forests

A. Hahn[1], S. Schuhegger[2], J. Bode[3], V. J. F. Sturm[1], M. O. Breckwoldt[1], S. Heiland[1], C. H. Ziener[4], M. Bendszus[1], F. T. Kurz[1]

[1]*Heidelberg University Hospital, Department of Neuroradiology, Heidelberg, Germany,* [2]*University of Heidelberg, Department of Physics and Astronomy, Heidelberg, Germany,* [3]*German Cancer Research Center (DKFZ), Schaller Research Group, Molecular Mechanisms of Tumor Invasion, Heidelberg, Germany,* [4]*German Cancer Research Center (DKFZ), Department of Radiology E010, Heidelberg, Germany*

Purpose/Introduction: The microvascular geometry has a strong influence on local T2*-decay due to paramagnetic deoxyhemoglobin [1]. Tumors often produce a convoluted, heterogeneous capillary network, which is presumed to induce characteristic patterns in voxel-intrinsic transverse relaxation.

Subjects and Methods: Intravital fluorescent staining, tissue clearing, and single plane illumination microscopy were combined to image full cerebrovascular networks of, respectively, n = 6 immunodeficient mice with U87 and GL261 glioblastoma, 3 and 4 weeks post intraperitoneal injection of 10^5 tumor cells, as well as n = 3 healthy control mice [2]. The 3D acquisitions were segmented with ilastik [3], post-processed with custom codes in Matlab (Mathworks), and used as a basis for numerical simulations of spin dephasing during FID experiments, implemented in C++ 11. Cubic virtual NMR voxels with side lengths of 100, 200, 300, and 400 µm were extracted from tumors and healthy tissue all over the brain and the FID was simulated with water diffusion at D = 1 μm^2/ms in 0.1 ms time steps up to t = 1 s at a field strength of B_0 = 3 Tesla [4]. The blood composition was modeled to be constant with a homogeneous oxygenation of 60%, leading to microscopic field inhomogeneities due to a paramagnetic vessel architecture [5]. Each signal relaxation was parametrized with linear least square fits assuming different exponential time dependencies; specifically, linear (t), quadratic (t^2), and monomial (t^b) form, respectively, for the entire decay, only the short-time regime ($t < 200$ ms), and subsequent long-time dephasing. Random forest classifiers from the Scikit-learn library [6] were optimized with grid search and trained to detect tumor-specific transverse relaxation after isolating the microvascular impact. Training and testing were conducted on balanced datasets of different size, evaluating the prediction accuracy on samples blinded from prior training.

Results: With training sets attained from our small cohort of mice, considerable prediction accuracies could be achieved with U87 glioblastoma (Fig. 1), and especially with the more angiogenic GL261 tumors (Fig. 2). Both scenarios clearly present a dependence on virtual voxel dimensions, with bigger NMR voxels allowing for better classification. A feature importance analysis revealed that the most influential fit parameter for classification was the short-time Gaussian decay rate, while the relaxation time contribution T_2* was least helpful.

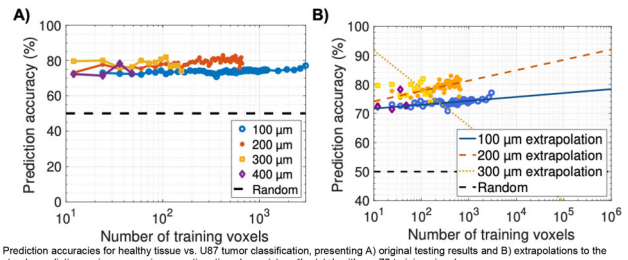

Prediction accuracies for healthy tissue vs. U87 tumor classification, presenting A) original testing results and B) extrapolations to the steady prediction regime, assuming a continuation along y(x) = a*log(x)+b with x ≥ 72 training signals.

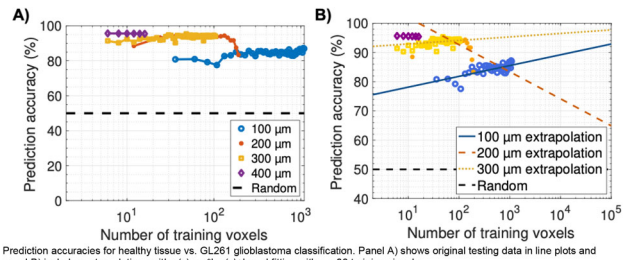

Prediction accuracies for healthy tissue vs. GL261 glioblastoma classification. Panel A) shows original testing data in line plots and panel B) includes extrapolations with y(x) = a*log(x)+b and fitting with x ≥ 36 training signals.

Discussion/Conclusion: A random forest approach for dephasing interpretations toward voxel-wise tumor detection is computationally feasible and delivers motivating results. Larger training sets from extended imaging cohorts should reveal further potential of this method.

References:

1. Magn Reson Med 1994; 32:749–63.
2. Front Neurosci 2019; 12:1004.
3. IEEE Int Symp Biomed Imaging 2011.
4. Neuroimage 2008; 40:1130–43.
5. Magn Reson Med 2001; 45:533–42.
6. J Mach Learn Res 2011; 12:2825–30.

I23 Teaching Session

10:50–11:50 *Room 2 - Van Weelde Zaal*

CEST as an Alternative to Gadolinium

I23.01
Basics of CEST—From Invention to Interpretation in Animal Models

V. Hoerr
Jena University Hospital, Institute of Medical Microbiology, Jena, Germany

Learning Objectives:—Principle of CEST MRI.
- Challenges in quantitative CEST MRI.
- Applications of CEST MRI in animal models in vivo.

Body: In CEST (chemical exchange saturation transfer) experiments, labile protons from molecules with a chemical shift distinct from water are selectively saturated and transfer the saturation by chemical exchange to the bulk water [1–3]. Due to the indirect mode of detection, CEST contrast can lead to a up to 70-fold higher sensitivity compared to localized ^{1}H MRS[4]. CEST developments were originally driven by the research of small molecules and proteins in high resolution ^{1}H NMR spectroscopy; however experiments are meanwhile also well established in ex vivo tissue as well as in vivo. Especially in vivo CEST MRI is a growing field as it is very sensitive to physiological parameters and metabolite levels. Within this frame, besides diamagnetic CEST (diaCEST) approaches using contrast agents, the detection of endogenous glycogen (glycoCEST)[5], glutamate (gluCEST)[6], glycosaminoglycans (gagCEST)[7], glucose (glucoCEST)[8], creatine (CrEST)[4], lactate (LATEST)[9], myo-inositol (MICEST)[10] as well as of amide and amine protons[11] is currently under investigation for imaging of pH, tumor[11], infection[12], inflammation[13] or neuronal function[8]. CEST spectra usually contain the information from different magnetization transfer pathways. Here, magnetization can be physically transferred between protons through space or by dipolar interactions between close spins. Thus the sum of all exchangeable and interacting protons in a molecule or macromolecule are detected in the spectra by corresponding CEST, MT (magnetization transfer) and NOE (nuclear overhauser effect) effects[2], providing sensitive and localized in vivo information from both metabolites and proteins.

Recently, it could be also demonstrated that naturally occurring D-glucose is a suitable biodegradable exogenous MRI contrast agent[14], detectable as glucoCEST contrast, to assess the malignancy of tumors[15] or to monitor treatment responses in zones of inflammation[13].

References:

[1] van Zijl PC, et al., *Magn Reson Med* **2011**, *65*, 927.
[2] Zaiss M, et al., *Phys Med Biol* **2013**, *58*, R221.
[3] Liu G, et al., NMR Biomed **2013**, *26*, 810.
[4] Mohammad H, et al., *Nat Med* **2014**, *20*, 209.
[5] van Zijl PC, et al., *Proc Natl Acad Sci U S A* **2007**, *104*, 4359.
[6] Cai K, et al., *Nat Med* **2012**, *18*, 302.
[7] Ling W, et al., *Proc Natl Acad Sci U S A* **2008**, *105*, 2266.
[8] Roussel T, et al., *Sci Rep* **2019**, 9, 4423.
[9] DeBrosse C, et al., *Sci Rep* **2016**, 6, 21813.
[10] Haris M, et al., *Neuroimage* **2011**, 54, 2079.
[11] McVicar N, et al., *NMR Biomed* **2015**, 28, 566.
[12] Liu J, et al., *NMR Biomed* **2018**, 31, e3942.
[13] Kentrup D, et al., *Kidney Int* **2017**, 92, 757.
[14] Walker-Samuel S, et al., *Nat Med* **2013**, *19*, 1067.
[15] Chan KW, et al. *Magn Reson Med* **2012**, 68, 1764.

I23.02
How Can CEST Reduce Gadolinium Use

M. Zaiss
Max-Planck-Institute for biological cybernetics, Tübingen, Germany

Learning Objectives: Chemical exchange saturation transfer (CEST) MRI is a non-invasive method that enables to indirectly detect metabolites, peptides and proteins via protons in functional groups that are in exchange with the abundant water proton pool (1–2). Principles of the CEST phenomena and efficient sequences will be introduced for endogenous protein CEST, and glucoCEST or dynamic glucose enhancement that utilizes the change in CEST signal after glucose injection. Applications in tumor imaging for these techniques are shown; similarities and differences to Gadolinium enhanced images are discussed.

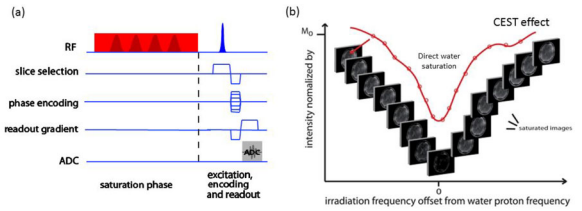

Figure 1: (a) Scheme of CEST sequence: presaturation at a certain irradiation RF frequency offset is followed by a fast image acquisition. Thus is repeated for several frequency offsets to generate the Z-spectrum in each voxel (b).

Body: To generate a CEST contrast a fast MRI readout is used with an RF presaturation module that saturation proton groups nearby the water protons (Fig. 1). Exchanging protons then transport the saturation state to the water pool and generate the CEST effect directly as an image contrast. For endogenous protein and peptide CEST signal the most similar patterns to Gadolinium uptake were achieved using the downfield-NOE suppressed APT signal (3), see Fig. 2.

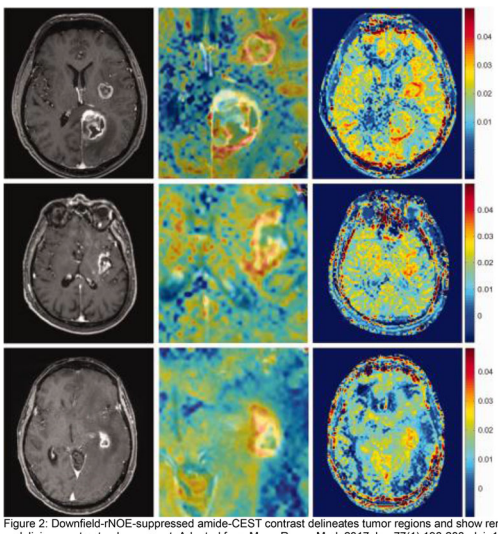

Figure 2: Downfield-rNOE-suppressed amide-CEST contrast delineates tumor regions and show remarkable overlap with the gadolinium contrast enhancement. Adapted from Magn Reson Med. 2017 Jan;77(1):196-208. doi: 10.1002/mrm.

Recently, dynamic glucose enhanced CEST methods using glucose

injection were tested in humans (4, 5, 6). Here a partial overlap with gadolinium could be observed (6), see Fig. 3.

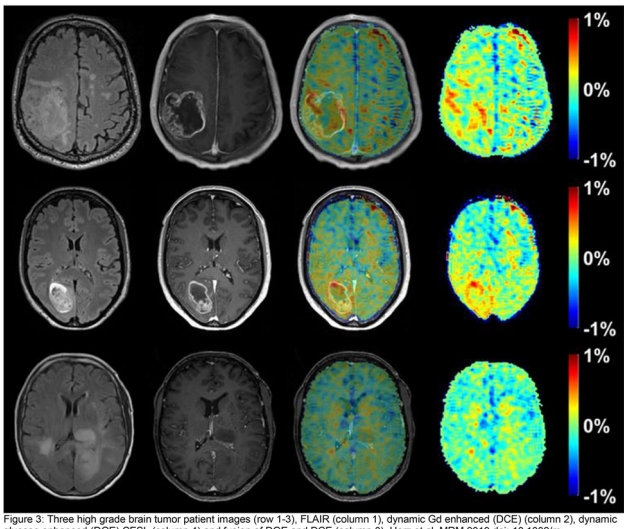

Figure 3: Three high grade brain tumor patient images (row 1-3), FLAIR (column 1), dynamic Gd enhanced (DCE) (column 2), dynamic glucose enhanced (DGE) CESL (column 4) and fusion of DGE and DCE (column 3). Herz et al. MRM 2019 doi: 10.1002/m

Early CEST results shows a great potential of the non-invasive CEST contrast to yield similar information as DCE. If this will translate to all applications of DCE and all types and grades of pathology has still to be investigated.

References:

(1) Zhou J, Payen J-F, Wilson DA, Traystman RJ, van Zijl PCM. *Nature Medicine*. 2003; 9(8):1085–1090. https://doi.org/10.1038/nm907

(2) Zaiss and Bachert *Physics in Medicine and Biology*. 2013; 58(22):R221-R269. https://doi.org/10.1088/0031-9155/58/22/r221

(3) Zaiss M, et al. *Magnetic Resonance in Medicine*. 2016; 77(1):196–208. https://doi.org/10.1002/mrm.26100

(4) Xu X et al. *Tomography*. 2015; 1(2):105–114. https://doi.org/10.18383/j.tom.2015.00175

(5) Schuenke et al. *Magn Reson Med*. 2016; 78(1):215-225. https://doi.org/10.1002/mrm.26370

(6) Herz et al. MRM 2019 https://doi.org/10.1002/mrm.27857

S18 Scientific Session

10:50–12:20 *Room 3 - Ruys & van Rijckevorsel Zaal*

Musculoskeletal Imaging

S18.02
Feasibility of quantitative MRI in eye muscles

K. R. Keene[1], L. van Vught[2], I. A. Ciggaar[2], I. C. Notting[3], S. W. Genders[3], J. J. G. M. Verschuuren[4], M. R. Tannemaat[4], H. E. Kan[5], J. W. M. Beenakker[2]
[1]*Leiden University Medical Center, CJ Gorter center for high field MRI and Neurology, Leiden, The Netherlands,* [2]*Leiden University Medical Center, CJ Gorter center for high field MRI and Opthalmology, Leiden, The Netherlands,* [3]*Leiden University Medical Center, Opthalmology, Leiden, The Netherlands,* [4]*Leiden University Medical Center, Neurology, Leiden, The Netherlands,* [5]*Leiden University Medical Center, CJ Gorter center for high field MRI, Leiden, The Netherlands*

Purpose/Introduction: Quantitative MRI of individual extraocular muscles (EOM) might have diagnostic and prognostic value in myasthenia gravis (MG) and Graves orbitopathy (GO), as conventional neuro/ophthalmic evaluations fail to quantify muscle pathology in EOMs. Since the EOMs are small and prone to eye-motion artefacts they are challenging to image with MRI. We therefore studied the feasibility of Dixon, T2 multi-echo spin-echo (ME-SE) and proton MR-spectroscopy (MRS) to quantify fatty infiltration, volume and inflammation in EOMs in healthy controls (HC) and GO and MG patients.
Subjects and Methods: 9 healthy subjects (36 ± 9yrs, 33% male), 11 MG (52 ± 10yrs, 64% male) and 6 GO patients (47 ± 11yrs, 50% male) were scanned at 7T (Philips Achieva), using a cued-blinking paradigm.[1] A 3-point Dixon scan was acquired (TE/TR/FA/ΔTE:2.4 ms/10 ms/3°/0.33 ms) to determine fat fractions (FF). In a subgroup of 5 MG, 1 GO and 4 HCs a ME-SE of all four recti EOMs (ΔTE/TR:12/4000 ms) and a ^{1}H MRS time series (STEAM, average voxel size: 1 cm^3, TR = 2000 ms, TM = 20 ms, TEs 12, 24, 36, 48, 76, 129, 280 ms) of one EOM were acquired to determine water T2 relaxation time.
For the Dixon, the EOMs were semi-automatically 3D-segmented on the water image, using a seed-growing algorithm in ITK-SNAP (Fig. 1)[2] to determine FF and volumes of the EOMs. The T2 ME-SE data were fitted using Extended Phase Graphing (EPG) in which the FF, fat-T2, water-T2, B1 and the pulse profile were incorporated[3]. The MRS data was analysed in jMRUI. FFs and T2 measurements were compared using T-tests and Pearson correlation to compare ME-SE and MRS.

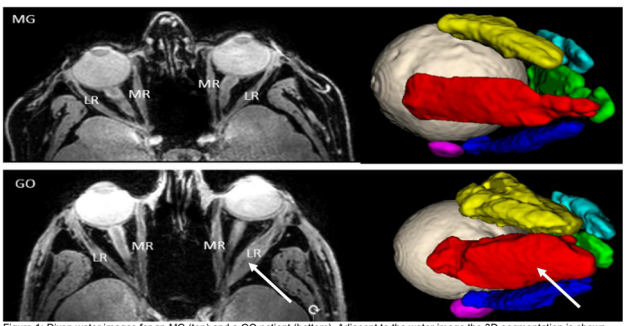

Figure 1: Dixon water images for an MG (top) and a GO patient (bottom). Adjacent to the water image the 3D-segmentation is shown. Notice the enlarged LR muscle in the GO patient (a

Results: Mean FF of the EOMs in MG (14.4 ± 0.5%) and GO patients (13.9 ± 1.8%) was higher than in HC (11.2 ± 0.8%; $p < 0.01$ for MG vs HC and $p = 0.11$ for GO vs HC) and mean muscle volume was higher in GO (1.2 ± 0.17 cm^3) and in MG patients (0.8 ± 0.05 cm^3) compared to the HC (0.5 ± 0.05 cm^3; $p < 0.01$) (Fig. 2).

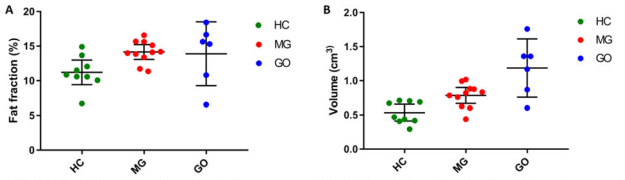

Figure 2-A: Mean fat fraction of all four recti muscles for Myasthenia gravis (MG), Graves' orbitopathy (GO) and healthy controls (HC). Figure 2-B: Mean muscle volume of all four recti muscles for MG, GO and HC.

In 1 MG patient and 1 HC ME-SE of only one eye was obtained due to time constraints. In one subject the MRS data was not analysable due to shimming problems. Although 6 EOMs of the MG patients had elevated T2 (T2 > 35 ms), no differences were seen in the average T2 of all muscles ($p = 0.19$) (Fig. 3). The Pearson correlation between water T2 measured with MRS and T2 ME-SE was 0.64.

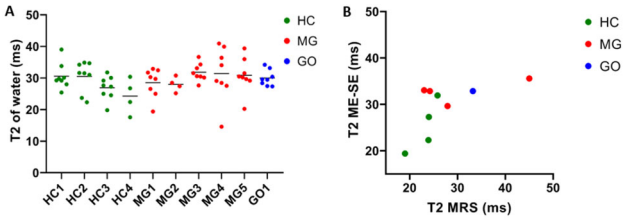

Figure 3-A: T2 of the water component fitted with an EPG model per EOM for 5 MG patients, 1 GO patient and 4 HC. Figure 3-B: Comparison between the T2 of the water component measured with ME-SE and with MR-spectroscopy.

Discussion/Conclusion: It is feasible to perform quantitative MRI of the EOMs in HC and in patients with eye muscle weakness. We were able to 3D-segment the Dixon scans and measure the FFs and volumes of individual EOMs. Contrary to the current pathophysiological knowledge, our results show increased FF and volumes of the EOM's in MG patients. Using ME-SE and EPG analysis we measured T2 values of EOM comparable to the water T2 in skeletal muscle[3]. Mismatches in MRS and T2 ME-SE might be explained by a difference in localization, as the whole muscle is measured with MRS and one slice in ME-SE.

References:

1. Beenakker, et al. (2013)
2. Yushkevich, et al. (2006)
3. Marty, et al. (2016)

S18.03
correlation time as a NEW MRI contrast

H. Elsayed[1], J. Karjalainen[1], N. Hänninen[2], I. Stavenuiter[2], Š. Zbýň[3], H. Henschel[1], M. Nissi[2], M. T. Nieminen[1], M. Hanni[1]
[1] *University of Oulu, Medical Imaging, Physics and Technology, Oulu, Finland,* [2]*University of Eastern Finland, Department of Applied Physics, Kuopio, Finland,* [3]*University of Minnesota, Center for Magnetic Resonance Research, Department of Radiology, Minneapolis, Minnesota, USA*

Purpose/Introduction: Magnetic resonance imaging (MRI) is a well-established tool to study soft tissues affected by osteoarthritis. Magnetic relaxation of nuclear spins is dependent on their local environment and the molecular processes they are involved in. The

purpose of this study is to develop a new MRI contrast for the non-invasive evaluation of the cartilage macromolecular composition. Our aim is to estimate an apparent correlation time (τ_c) of molecular processes in cartilage specimens using dispersion of the relaxation rate in the rotating frame, ($R_{1\rho} = 1/T_{1\rho}$).

Subjects and Methods: Bovine patellar osteochondral plugs ($N = 10$) were imaged using a 9.4 T scanner to obtain T_2—weighted images (TE = 10, 15, 23, 35, 54, 83 and 128 ms) as well as $T_{1\rho}$—weighted images (TSL = 0, 8, 16, 32, 64 and 128 ms) at 15 spin-locking amplitudes (SLA) from 200 to 5000 Hz 0.[1] T_2 and $T_{1\rho}$ maps were obtained by fitting mono exponential model to the corresponding weighted images. The following function[2, 3] was fitted to $R_{1\rho}$ dispersion pixel-by-pixel to create τ_c maps:

$$R_{1\rho} = (3A\tau_c)/(1 + 16\pi^2 f_1^2 \tau_c^2) + B$$

where τ_c, A and B are the fitting parameters, f_1 is the spin locking amplitude (Hz). Least squares method was used for the fitting. The processing of the data was carried out using MATLAB R2017b. Polarized light microscopy (PLM) measurements were used to calculate parallelism index (PI) which is indicative of collagen anisotropy.[4] Digital densitometry was used to calculate optical density (OD) which is a measure of proteoglycan content.[5]

Results: The τ_c maps showed a laminar appearance similar to that of T_2 and $T_{1\rho}$ maps (Fig. 1). τ_c values were in the range of 100–250 μs in the superficial zone, 200–500 μs in the radial zone, and less than 100 μs in the transitional zone. PI and OD maps (Fig. 2) showed depth-wise distribution of collagen anisotropy and proteoglycan content, respectively.

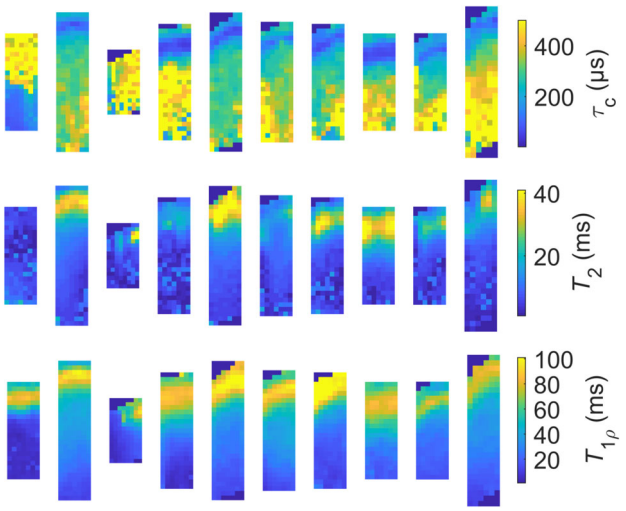

Figure 1: T2 and T1ρ (400 Hz) ROIs of all samples. Cartilage surface is located at the top. Pixel spacing in the x and y directions are 0.56 mm and 0.07 mm, respectively.

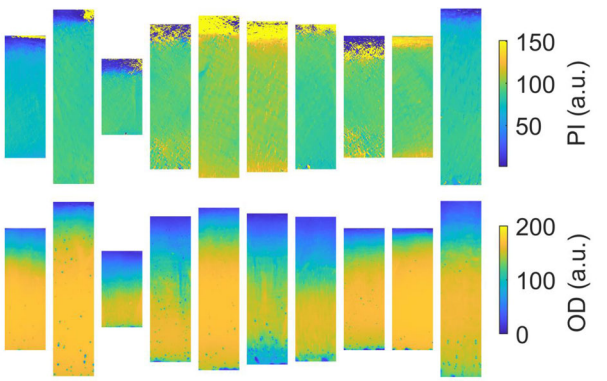

Figure 2: PI and OD ROIs of all samples. Cartilage surface is located at the top. Pixel spacing is 1.4 μm in both x and y directions.

Discussion/Conclusion: Our results suggest that τ_c maps provide information about the structure of cartilage. This initial visual assessment will be followed by quantitative comparisons of τ_c and other fitted parameters against histology.

References:

1- Nissi MJ et al. (2018). Proc. Intl. Soc. Magn. Reson. Med 26 0197.
2- Hanni M et al. (2015). Proc. Intl. Soc. Mag. Reson. Med. 23:117.
3- Elsayed H et al. (2016). Proc. Intl. Soc. Mag. Reson. Med. 24:3003.
4- Rieppo J et al. (2008). Microsc. Res. Tech. 71, 279–287.
5- Király K et al. (1996). Histochem J 28, 99–107.

S18.04

A novel DTI method for quantification of skeletal muscle pennation angles

L. Secondulfo[1], M. Hooijmans[2], M. Froeling[3], V. Mazzoli[4], A. Nederveen[2], G. Strijkers[1]

[1]*Amsterdam University Medical Center, Department of Biomedical Engineering and Physics, Amsterdam, The Netherlands,* [2]*Amsterdam University Medical Center, Department of Radiology and Nuclear Medicine, Amsterdam, The Netherlands,* [3]*Utrecht Medical Center, Department of Radiology, Utrecht, The Netherlands,* [4]*Lucas Center for Imaging, Department of Radiology, Stanford, USA*

Purpose/Introduction: Muscle volume, muscle fiber length and pennation angles (PA) are important characteristics influencing muscle function. PA has shown to change due to training, in muscle injury and in muscle diseases [1]. However, assesment of PA over the full length and volume of an individual muscle is challenging. In this study we propose a diffusion-tensor imaging (DTI) based method to measure the PA and to create PA color maps of the whole muscle volume.

Subjects and Methods: Lower leg MRI datasets of 5 healthy volunteers were acquired twice, using a 16-channel coil and the 12 table top coils. The foot was immobilized in 3 positions: 15°dorsiflexion (D15), 0°neutral position (N0) and 30°plantar flexion (P30). The MRI protocol included a 3-point mDixon scan for anatomical reference (TR/TE/ΔTE = 7.7/2.1/1.7 ms, voxel-seze = 1 × 1 × 2.5 mm^3) and a SE-EPI DTI (TR/TE = 11191/51.63 ms, voxel-size = 3 × 3 × 5 mm^3, b value = 400 s/mm^2, SPAIR). The DT-MRI data were analyzed with DTITools: once they were de-noised with a Rician noise suppression algorithm and registered to the anatomical scans, the tensor was fitted with a WLLS algorithm and the eigenvectors were calculated.

In our method the PA maps are calculated in the entire volume using the eigenvector in each voxel and the vector parallel to a reference line running through 2 points, manually selected on the anatomical scan. Here the reference line was drawn between a point selected mid tibia plateau and the most distal point of the tibia bone. After that, the segmentations, manually drawn on the water images, were used to select the regions of interest.

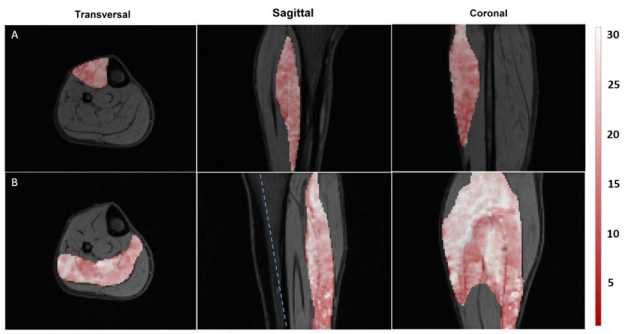

Overlay of the PA color maps over the anatomical images transvers, sagittal, coronal views: (A) for the TA and (B) for the SOL muscles in neutral position. The dashed line is the reference line through the selected points.

Repeatibility of the PA measurements was assessed by Bland–Altman analysis for the Tibialis Anterior (TA) and the Soleus (SOL) muscles.
Results: Our method facilitated visualization and quantification of PA and changes therein with foot position in the whole muscle body of the lower leg. The results show an increased PA average in dorsiflexion for the TA and in plantar flexion for the SOL.

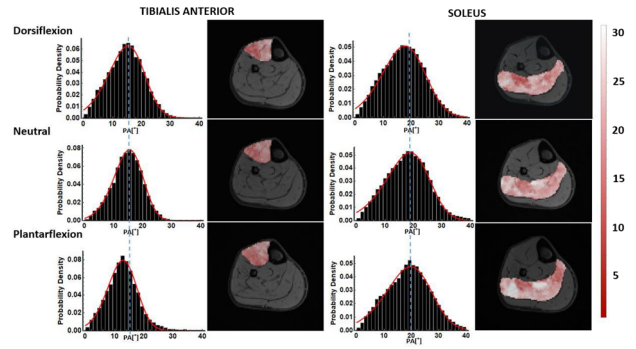

PA distributions and color maps in TA and SOL with three foot positions

Bland–Altman analysis of average PA showed better agreement between repeated measurements for the SOL.

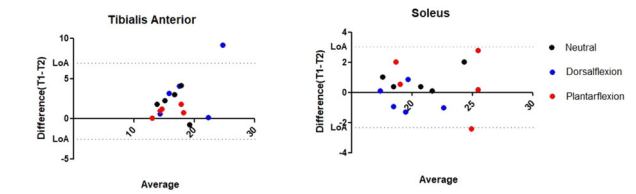

Bland-Altman analysis for the repeated measurements of the PA in the TA and SOL muscles in three foot positions

The coefficients of variation in three positions N0/D15/P30 for the TA and for the SOL were 14.7/18.27/6.47 and 3.81/4.38/7.01, respectively.
Discussion/Conclusion: Our approach facilitates the generation of reproducible PA color maps of leg muscles. Small changes in PA with passive foot stretch can be quantified. The results are in agreement with literature [2]. The different outcome of the repeatibility analysis between muscles could be related to the anatomical location and to some residual unsuppressed fat artefacts in the DTI. The changes in PA distributions with different foot positions for the SOL muscle are minor (Fig. 2), because of its symmetrical anatomy [3]. This method can be applied to study changes in PA with training, injury or disease.
References:
[1] Kellis, 2016
[2] Hudgson, 2006
[3] Bolsterlee B, 2018

S18.05

Muscle usage difference due to laterality–Evaluation by dynamic T2 mapping–

A. Kido[1], S. Shimohara[2], Y. Nitanda[3], M. Tang[1], N. Tawara[4], M. Samukawa[1], T. Yamamoto[1]
[1]*Hokkaido University, Sapporo, Japan,* [2]*Asahikawa Medical College Hospital, Asahikawa, Japan,* [3]*Kin-ikyo chuo Hospital, Sapporo, Japan,* [4]*Japan Health Care Collage, Sapporo, Japan*

Purpose/Introduction: T2 measurement has been used in evaluation of muscle activity because T2-sensitive physiological changes occur in muscles: an increase of blood flow and intracellular water content by an exercise[1]. Although functional and morphological differences due to laterality exist in upper limbs, the difference of usage of arm muscles between dominant and non-dominant arms has been unknown. In this study, we investigated the difference of muscle usage between dominant and non-dominant arms by mapping the T2 values of forearm skeletal muscles dynamically before and after a simple movement exercise.
Subjects and Methods: Seven right-handed male volunteers (23.0 ± 1.3 years) were set a 2-kg nonmagnetic weight on the palm and lay with fixing the forearm on the patient table in a 3-T MRI scanner. An axial slice of forearm at the 35%-proximal position was imaged using SE-EPI by 5 TEs (30, 45, 60, 75, 90 ms) successively with 6-s interval before the exercise. Then, the volunteer repeated the exercise of wrist volar flexion every 1.5 s as long as the volunteer continues maximally within 5 min. After the exercise, the slice was readjusted exactly the same as the slice imaged before the exercise because the arm moved slightly by the exercise. The set of SE-EPI with 5 TEs was repeated every 30 s for 5 min after the readjustment of the slice position. The FLAIR anatomical imaging was also imaged before the exercise. This experiment was carried out first for left arm then for right one. The T2 value of each pixel was calculated and mapped dynamically before and after the exercise. The ROIs ware set on flexor carpi ulnaris (FCU), flexor carpi radialis (FCR) and supinator muscle (SM) on the FLAIR image and the T2 values of these ROIs ware obtained.
Results: The T2 values of all muscles increased significantly after the exercise in both arms: FCR and FCU ($p < 0.05$), SM ($p < 0.001$). These increased T2 values gradually decreased, but they did not recover to the resting T2 values even 10 min even after the exercise. The increase rate of T2 by the exercise in FCU was significantly higher in the left arm than that in the right arm (Fig. 1).

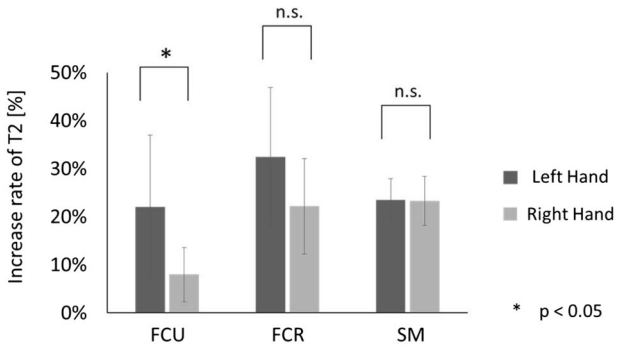

Figure1 The increase rate of T2 values of FCU, FCR and SM in both arms.

Discussion/Conclusion: Although FCR is a predominant muscle for wrist volar flexion, this result suggests that FCU, which is a non-predominant muscle, is used additionally during the exercise for left arm. This result may imply effective control of usage of muscle in the dominant arm. The laterality difference of usage of muscles for a simple movement in dominant and non-dominant arms was demonstrated by measuring the T2 value.
References:
1. Rumeur LE, Certaines DJ, Toulouse P, et al.: Water phases in rat striated muscles as determined by T2 proton NMR relaxation times, Magn. Reson. Imaging. 1987; 5(4): 267–272.

S18.06

Quantitative volume and blood perfusion parameters of the infrapatellar fatpad and the relationship with edema and effusion in patients with patellofemoral pain

R. van der Heijden[1], B. de Vries[1], D. Poot[1], M. van Middelkoop[2], G. Krestin[1], E. Oei[1]
[1]*Erasmus Medical Center, Radiology and Nuclear Medicine, Rotterdam, The Netherlands,* [2]*Erasmus Medical Center, General Practice, Rotterdam, The Netherlands*

Purpose/Introduction: Patellofemoral pain (PFP) is a common knee condition among young people and has been suggested to be a precursor of osteoarthritis. Although the pathophysiology of PFP remains unknown, inflammation, neo-angiogenesis or altered infrapatellar fat pad (IPFP) volume may have causative effects. The aim of this study was to quantitatively evaluate the volume and perfusion parameters of the IPFP in order to unravel PFP pathophysiology. Furthermore, the relationship between these parameters and IPFP edema and joint effusion was studied.

Subjects and Methods: PFP patients and matched healthy control subjects aged 18–40 years were included. Participants underwent MRI including non-fat saturated FSPGR and DCE-MRI. Image registration was used to correct for motion. The IPFP was delineated on the FSPGR sequence using Horos software (Horosproject.org, USA). The volume (body height adjusted) was calculated and quantitative perfusion parameters (Ktrans, Ve and Vp) were extracted by fitting the extended Tofts' pharmacokinetic model. In short, Ktrans represents the inflow, Ve the extravascular extracellular space and Vp vascular fraction of the region.

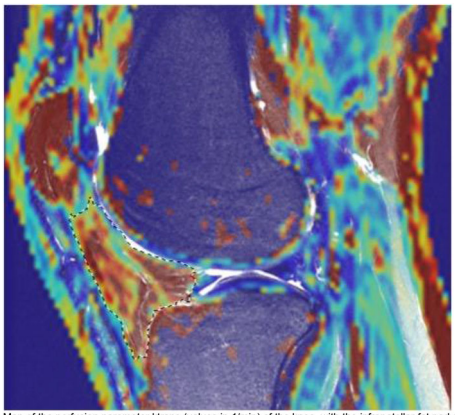

Map of the perfusion parameter ktrans (values in 1/min) of the knee, with the infrapatellar fat pad outlined. Higher perfusion values are depicted in red.

Due to non-normality, log transformation was applied in order to compare these parameters between patients and controls with adjustment for confounders by regression analyses. The same analyses were applied for subjects with and without IPFP edema or effusion.

Results: 43 controls and 35 PFP patients were included. Volume and perfusion parameters were not statistically significantly different between groups and not between subjects with and without edema. In IPFPs with effusion a significantly higher Ktrans was observed and a remarkably higher, but not statistically significant, Vp value was assessed.

	Ktrans (min-1) median	p-value	Ve (unitless) median	p-value	Vp (unitless) median	p-value	Volume (cm3) median	p-value
Control subjects	17.17	0.98	162.37	0.34	0.29	0.10	25.60	0.12
Patiens with PFP	16.49		137.71		0.37		26.56	

Blood perfusion parameters of the infrapatellar fat pad in control subjects and patients with PFP. Perfusion parameters were multiplied by 1000.

Discussion/Conclusion: PFP patients do not demonstrate a significantly different volume or blood perfusion of the IPFP compared to controls. Furthermore, IPFPs with edema did not demonstrate significantly different parameters compared to IPFPs without edema. Subjects with effusion demonstrated a higher inflow of blood and possibly a higher vascular fraction of the IPFP.

References:

-Cowan SM, Hart HF, Warden SJ, Crossley KM. Infrapatellar fat pad volume is greater in individuals with patellofemoral joint osteoarthritis and associated with pain. *Rheumatol Int.* 2015; 35(8):1439–1442.

-Roemer FW, Guermazi A, Zhang Y, et al. Hoffa's Fat Pad: Evaluation on Unenhanced MR Images as a Measure of Patellofemoral Synovitis in Osteoarthritis. *AJR Am J Roentgenol.* 2009; 192(6):1696–1700.

-Ballegaard C, Riis RG, Bliddal H, et al. Knee pain and inflammation in the infrapatellar fat pad estimated by conventional and dynamic contrast-enhanced magnetic resonance imaging in obese patients with osteoarthritis: a cross-sectional study. *Osteoarthritis Cartilage.* 2014; 22(7):933–940.

S18.07

Quantitative MR blood perfusion patterns of infrapatellar fat pad T2 hyperintense lesions on unenhanced MR in patients with and without knee osteoarthritis

B. de Vries[1], R. van der Heijden[1], D. Poot[1], M. van Middelkoop[2], G. Krestin[1], E. Oei[1]
[1]*Erasmus Medical Center, Radiology and Nuclear Medicine, Rotterdam, The Netherlands,* [2]*Erasmus Medical Center, General Practice, Rotterdam, The Netherlands*

Purpose/Introduction: Infrapatellar fat pad (IPFP) T2 hyperintense lesions on unenhanced MR are an important imaging feature of knee osteoarthritis (OA) and are thought to represent inflammation. These lesions are very common, though, also in non-OA subjects, and may not always be linked to inflammation. This leads to the hypothesis that IPFP lesions may have different pathophysiological subtypes. The aim of this study was to evaluate quantitative blood perfusion parameters within T2 hyperintense lesions in patients with knee OA, with patellofemoral pain (PFP) (supposed precursor of OA), and in control subjects.

Subjects and Methods: 43 healthy controls, 35 patients with PFP and 22 patients with knee OA were included. All underwent MRI including T2-mapping and dynamic contrast enhanced (DCE)-MRI. Image registration was used to correct for motion. If present, hyperintense T2 lesions in the IPFP were delineated on T2 maps using Horos software (Horosproject.org, USA). A second region was drawn in an adjacent area without T2 signal intensity alteration. Quantitative perfusion parameters (Ktrans, Ve, Vp) were extracted by fitting the extended Tofts' pharmacokinetic model where Ktrans represents the inflow, Ve the extravascular extracellular space and Vp vascular fraction of the region. A paired Wilcoxon-signed-rank test was used

to compare regions with and without T2 lesions within subjects for each subgroup.

Results: IPFP T2 hyperintense lesions were present in 14 controls, 13 PFP patients and 16 knee OA patients. Perfusion parameters were not statistically significantly different between areas with and without a T2 lesion within controls and PFP patients. In knee OA patients, the lesions demonstrated statistically significantly higher values of Ktrans and Ve compared to an area without a lesion. Remarkably, all regions drawn in knee OA demonstrated higher perfusion parameters, including Vp, compared to the other groups.

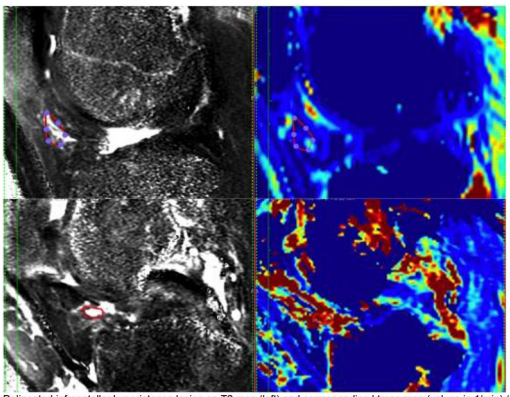

Delineated infrapatellar hyperintense lesion on T2 map (left) and corresponding ktrans map (values in 1/min) (right) in patient with PFP (upper) and patient with OA (lower). Higher values are depicted in red.

	Ktrans (min-1) median	p-value	Kep (min-1) median	p-value	Ve (unitless) median	p-value	Vp (unitless) median	p-value
Control lesion	9.84	0.36	91.00	0.78	160.62	0.51	0.13	0.075
Control no lesion	14.36		122.28		181.53		0.01	
PFP lesion	11.07	0.55	173.41	0.55	143.00	0.92	0.22	0.48
PFP no lesion	13.61		112.86		143.95		0.11	
OA lesion	39.03	0.017	197.57	0.079	157.19	0.010	2.09	0.36
OA no lesion	24.73		163.49		119.18		1.03	

Blood perfusion parameters between areas with and without a T2 hyper intense lesion in different subgroups. Perfusion values were multiplied by 1000.

Discussion/Conclusion: IPFP T2 hyperintense lesions are non-specific. In contrast to morphologically similar lesions in PFP patients and controls in knee OA patients IPFP hyperintense lesions are associated with higher perfusion, suggesting inflammation and neoangiogenesis.

References:

-Roemer FW, Guermazi A, Zhang Y, et al. Hoffa's Fat Pad: Evaluation on Unenhanced MR Images as a Measure of Patellofemoral Synovitis in Osteoarthritis. *AJR Am J Roentgenol.* 2009; 192(6):1696–1700.

-Ballegaard C, Riis RG, Bliddal H, et al. Knee pain and inflammation in the infrapatellar fat pad estimated by conventional and dynamic contrast-enhanced magnetic resonance imaging in obese patients with osteoarthritis: a cross-sectional study. *Osteoarthritis Cartilage.* 2014; 22(7):933–940.

-Wang K, Ding C, Hannon MJ, Chen Z, Kwoh CK, Hunter DJ. Quantitative Signal Intensity Alteration in Infrapatellar Fat Pad Predicts Incident Radiographic Osteoarthritis: The Osteoarthritis Initiative. *Arthritis Care Res (Hoboken)0.*2019; 71(1):30–38.

S18.08

A split-label design for simultaneous measurements of muscle perfusion in distant slices by pulsed arterial spin labeling

T. T. Veeger, C. Baligand, S. L. Franklin, M. J. van Osch, H. E. Kan, L. Hirschler

Leiden University Medical Center, C.J. Gorter Center for High Field MRI, Department of Radiology, Leiden, The Netherlands

Purpose/Introduction: In Arterial Spin Labeling (ASL-)MRI studies of muscle perfusion changes upon or during exercise, single-slice acquisitions (fig. 1a) are commonly used. However, fiber type and oxidative capacity vary along the muscle[1–2] and differences in fatty infiltration along the muscle have been observed in muscular dystrophies.[3–4] Coverage of standard multi-slice pulsed ASL (fig. 1b) is limited by the fact that no label is created between slices. For 10–15 cm long muscles, this implies long transit times to the most distal slice due to slow flow. We propose a split-label design adaptation of FAIR that allows for sufficient labeling for distant slices (fig. 1c).

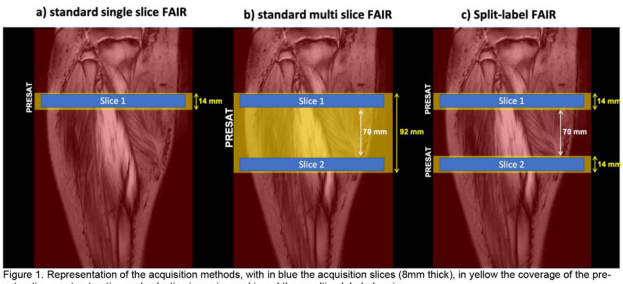

Figure 1. Representation of the acquisition methods, with in blue the acquisition slices (8mm thick), in yellow the coverage of the pre-saturation, post-saturation and selective inversion and in red the resulting labeled regions.

Subjects and Methods: Post-exercise ASL was measured in two slices in the lower leg of three healthy volunteers at 3T (Philips Ingenia) using an 8-elements receiver coil (voxel size = $2.94 \times 2.95 \times 8$ mm^3, slice gap = 70 mm, TR/TE = 3000/20 ms, PLD = 1600 ms) after isometric dorsiflexion against an elastic band until exhaustion. To compare the split-label FAIR (SL-FAIR) with separate single-slice FAIR (SS-FAIR) acquisition in distant slices, we interleaved the acquisitions as described in Fig. 2, resulting in an ASL map approximately every 40 s, for each method. SL-FAIR consisted of the same elements as the SS-FAIR, applied selectively and sequentially for each slice, preserving label between the slices (fig. 1c). To compensate for differences in MT effects, the power of the two selective inversion pulses was half of that of the non-selective pulse. Three QUIPSS-pulses were applied 100 ms before imaging, for both methods. Background suppression was used to improve the perfusion SNR and to act as fat suppression (TIs: 400, 1150, 1400 ms).

Voxel wise ASL maps were calculated as label—control, and the average ASL signal within the Tibialis Anterior (TA) muscle is reported for each dynamic.

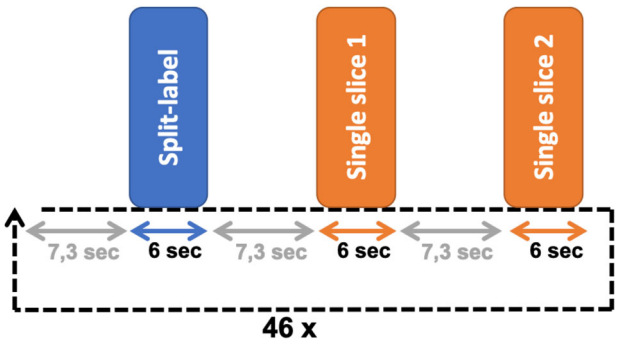

Figure 2. Schematic representation of the scan protocol with the timing and duration of each sequence.

Results: Transient post-exercise hyperemic responses were observed for all participants and the ASL signals were similar with both methods (fig. 3). For comparison between slices, the curves were normalized to their first dynamic. No differences in ASL profiles was observed between the slices.

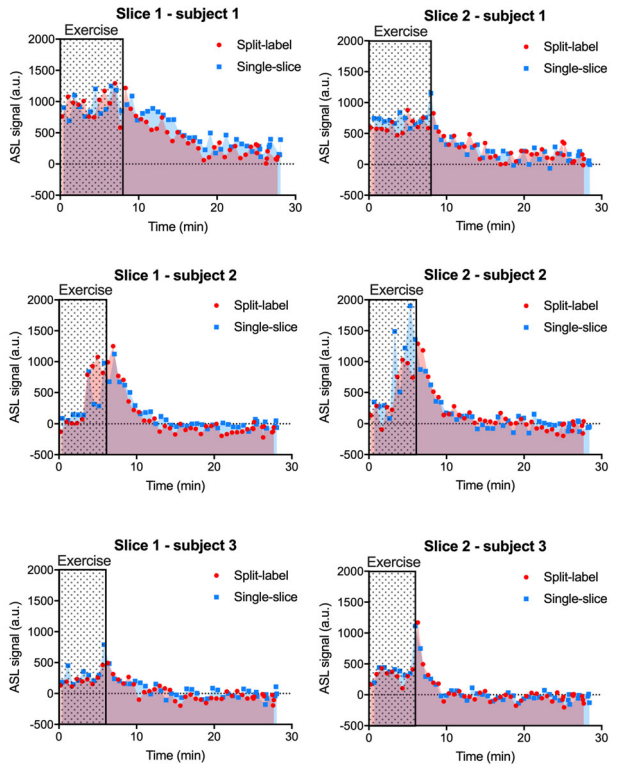

Figure 3. Post-exercise recovery for three subjects, with the block indicating the exercise. The red curves are SL-FAIR and the blue curves SS-FAIR.

Discussion/Conclusion: SL-FAIR yielded similar ASL results to SS-FAIR, suggesting that the saturation generated by one slice minimally affected the other slice. The major advantage of SL-FAIR is the increased time resolution by a factor of 2 compared to interleaved SS-FAIR of two distant slices. This can be increased to 2 ASL measurements every 6 s by calculating $Label_2$-$Control_1$ in addition to $Label_1$-$Control_1$. The inter-individual differences could be due to differences in exercise history and the exercise intensity itself, which were not controlled in this study.

References:

1. PMID:11322722.
2. PMID:29455454.
3. PMID:28302391.
4. PMID:29774305.

S18.09

Mid-term repeatability of sodium levels in skeletal tissue at 3T

T. Gerhalter, L. V. Gast, A. M. Nagel
University Hospital Erlangen, Institute of Radiology, Erlangen, Germany

Purpose/Introduction: Due to its sensitivity to tissue viability and body's homeostasis, ^{23}Na MRI could provide quantitative biomarkers to track pathological changes and response to treatment. The most frequently proposed biomarkers are the total sodium tissue content (TSC) followed by inversion recovery sequences (IR) that suppress the ^{23}Na signal from the fluid environments [1–3].

Any biomarker requires technical and biological validations before being systematically used as clinical outcome measure in longitudinal studies. Therefore, we performed a repeatability study in healthy volunteers, who were rescanned after 6 months, which mimics a normal period of an intervention studies.

Subjects and Methods: Imaging was performed in vivo on the right leg of six healthy subjects (28.6 ± 5.0 years old) with a single-tuned ^{23}Na volume knee coil (Stark Contrast) on a 3T whole-body MR system (Magnetom Skyra, Siemens Healthcare). The rescan was performed after 6 months (27.2 ± 4.8 weeks). TSC was derived from an density-adapted 3D-radial UTE sequence acquired with the following parameters [4]: TE/TR 0.3/50 ms, FA 80°, resolution $3 \times 3 \times 15$ mm^3, 8264 projections, T_{acqu} 6min53sec. An IR sequence was used to reduce ^{23}Na-signal originating from unrestricted environments to achieve an intracellular weighted sodium signal [2]: TE/TR 0.3/124 ms, TI 34 ms, FA 90°, resolution $4 \times 4 \times 20$ mm^3, 4760 projections, T_{acqu} 9min50sec. For ^{23}Na signal calibration, a linear regression based on the signal from the calibration phantoms with 20 mM and 40 mM and 5% agarose was performed. ROIs were drawn on the gastrocnemius medialis (Gas.med.), soleus, and tibialis anterior (Tib. ant.) muscles.

Results: The mean TSC and IR values were measured on the manually traced muscles regions for each volunteer (Fig. 1).

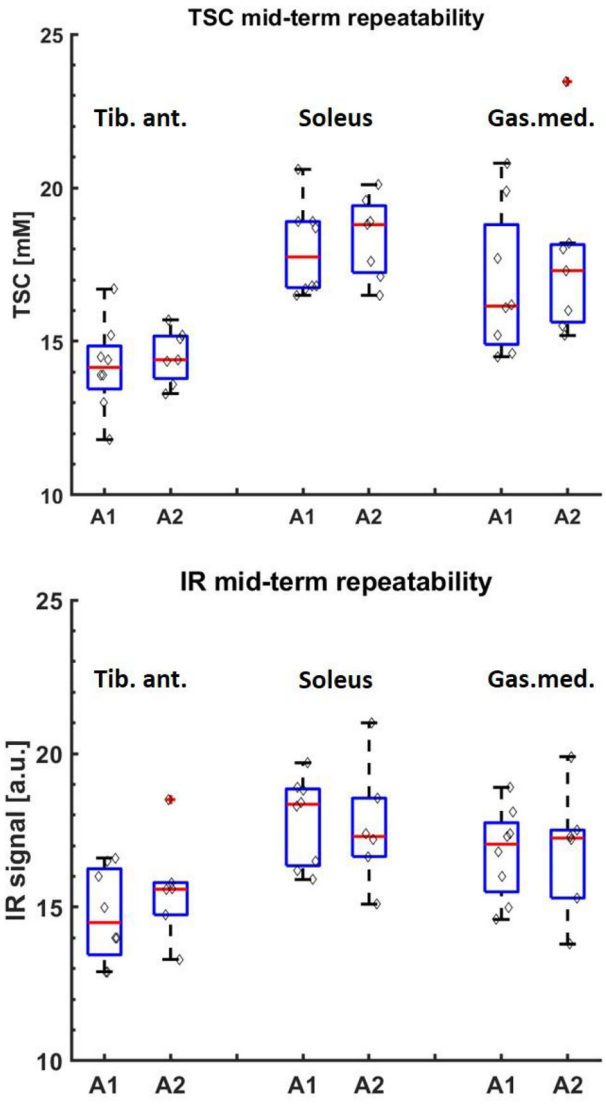

Fig.1: Sodium MR measures at the baseline scan (A1) and the rescan 6 months later (A2) for three different muscles.

The tibialis anterior has systematic lower TSC and IR values as the examined calf muscles.

The reliability of sodium markers is presented with Bland–Altman and correlation plots in Fig. 2.

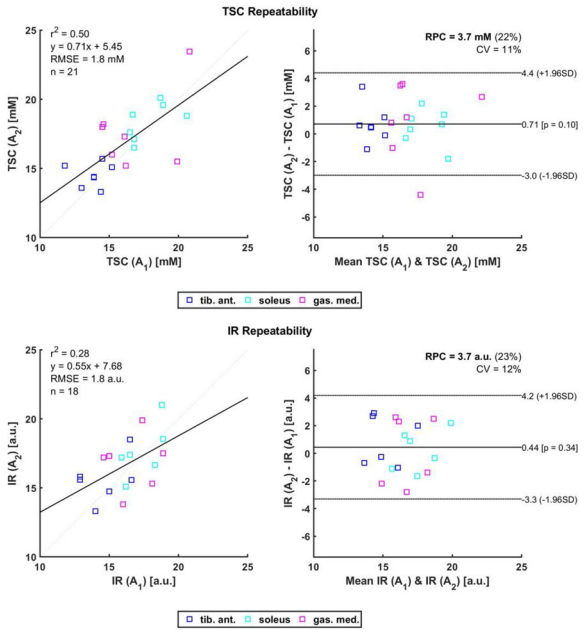

Fig.2: Medium-term repeatability of TSC and IR. On the left side, correlations of the first and second visit is presented. On the right side, the Bland-Altman plots the mean of the TSC between scan 1 and scan 2 against the differences of both scans.

The mean correlation coefficient for mean TSC is 0.5 and 0.28 for IR. The Bland–Altman plot indicated high agreement between the two visits with a mean repeatability coefficient of 3.7 mM and 3.7a.u. for TSC and IR, respectively. For TSC, the limits of agreement at the 95% confidence interval were − 3.0 to + 4.4 mM and the coefficient of variation (CV) over all three muscles is 11%. For IR, the limits of agreement at the 95% confidence interval were − 3.3 to + 4.2a.u. with a CV of 12%.

Discussion/Conclusion: Here, we tested the mid-term variability of quantitative ^{23}Na MRI on skeletal muscle tissue. The TSC as well as the IR measures showed a good reliability and low CV in different muscles of the lower leg.

Thus, TSC and IR measures might be sensitive enough for detecting real changes of the sodium levels of the muscle in longitudinal interventional MRI studies.

References:

1. Weber et al. J Neurol. 2012.
2. Nagel et al. Invest Radiol. 2011.
3. Gerhalter et al. JMRI. 2019.
4. Nagel et al. MRM. 2009.

L06 Lightning Talks

10:50–11:50 *The Stage*

Acquisition, Reconstruction & Quantification

L06.01

An MRI method for the differentiation of mineralized iron in the brain

L. Bossoni, A. Webb, L. van der Weerd
Leiden University Medical Center, Radiology, Leiden, The Netherlands

Purpose/Introduction: Several neurodegenerative diseases feature anomalies in brain iron concentrations. Two particularly relevant iron forms are ferrihydrite, found in the core of the ferritin protein, and magnetite [1, 2]. Since these iron forms affect the proton transverse relaxation, MRI contrast can potentially be used to quantify their concentrations.
Post-mortem studies have shown that tissue R_2^* and susceptibility values correlate with total tissue iron [3, 4]. However, these methods do not offer differentiation between the iron forms.
In this work, we show how an Off-Resonance Saturation (ORS) pulse sequence can be used to quantify ferritin and magnetite-bound iron.
Subjects and Methods: Brain phantoms, one containing different concentrations of magnetite nanoparticles, a second containing different concentrations of ferritin nanoparticles, and a third one containing a mix of both, were studied.
The ORS module, which was implemented on a 7T preclinical scanner, consisted of multiple saturation sech-pulses, followed by a spoiler gradient. The acquisition consisted of a post-excitation steady-state free precession (SSFP) sequence. A control image was acquired without the ORS pulse.
The contrast as a function of the off-resonance frequency (ν_0) was fitted to the analytical model derived in [5] to obtain the absolute iron concentrations ([Fe]).
Results:

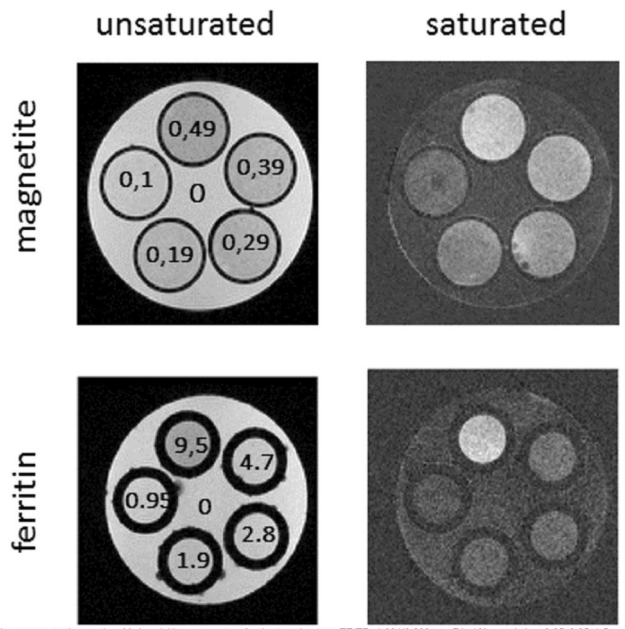

Iron concentration are in mM. Acquisition parameters for the top-phantom: TE/TR=1.634/3.268 ms, FA=10°, voxel size=0.25x0.25x1.5 mm, 3 ORS pulses. Acquisition parameters for the bottom-phantom: TE/TR=20/40 ms, voxel size=0.25x0.25x1mm, 5 ORS pulses.

Fig. 1 shows a comparison between the control (unsaturated) and saturated (at 300 Hz) images. Figure 1a shows the contrast curve acquired after ORS excitation at different frequencies. Results for the magnetite-only and ferritin-only samples are in agreement with the nominal iron concentrations (Fig. 2b–d).

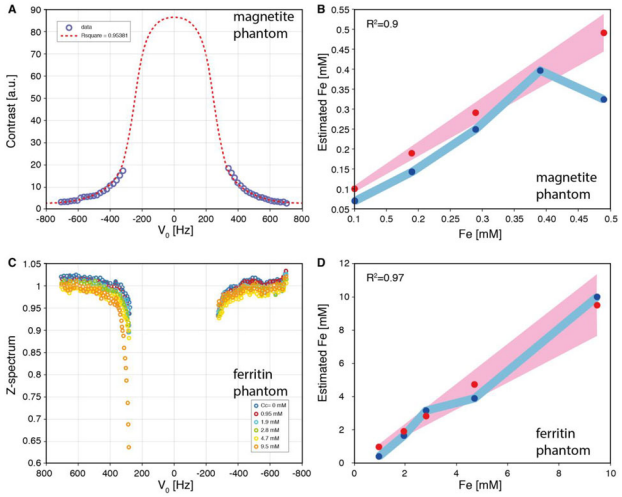

(A) Example of contrast data and fit (red line) for magnetite. (C) Z spectrum for the ferritin phantom. Fitted iron concentration (blue) and nominal iron concentration (red) (C and D). The shaded areas in the figure are the confidence intervals.

In the ferritin sample, the Z-spectrum shows an NOE feature, at negative frequencies (Fig. 2c). For the mixed sample, a weighted-fit was used to extract [Fe] bound to the two minerals (Fig. 3). The latter returned the concentration of magnetite-iron with a high accuracy, while the ferritin-iron fraction was underestimated of ~ 35%.

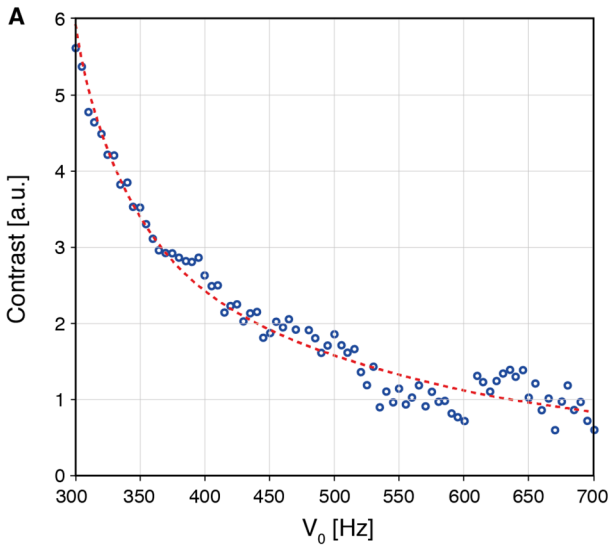

B

[Fe] in magnetite (mM)	Estimated [Fe] in magnetite (mM)
0.185 ± 10%	0,187 (0,1797 0,1940)
[Fe] in ferritin (mM)	**Estimated [Fe] in ferritin (mM)**
4,5 ± 15%	2,858 (2,246 3,470)

(A) Example of contrast data and fit (dashed line) for the mixed sample. (B) Known iron concentration in the two mineral forms, with uncertainty, and fitted (estimated) iron concentration. Numbers in parenthesis refer to the confidence intervals.

Discussion/Conclusion: The ORS method generates positive contrast that is sensitive to superparamagnetic effects [6], therefore it can be applied to detect magnetite and ferrihydrite (ferritin) nanoparticles in brain tissue. The ORS method can use an offset frequency (ν_0) and excitation bandwidth to eliminate MT effects, extrinsic χ-inhomogeneities, and single out the contribution of the nanoparticles, provided that the equatorial field of the iron species is known a priori. While more work is needed to better characterize the contrast of the mixed-sample, our preliminary results show that the ORS method is a promising tool to quantify iron bound to different mineral forms.

References:

[1] Kirshvin et al., PNAS 89, 7683–7687 (1992).
[2] Bulk M et al., Sci. Rep. 8, 6898 (2019).
[3] Langkammer et al., Radiology 257, 455–462 (2012).
[4] Hametner et al., NeuroImage 179, 117–133 (2018).
[5] Delangre et al., JMR 265, 99–107 (2016).
[6] Zurkyia et al., MRM 56:726–732 (2006).

L06.02

Comparing conventional and synthetic 3D T1w MRI for Brain tissue volumes quantification

A. Tisell[1, 2], M. J. B. Warntjes[3], I. Blystad[1], P. Lundberg[1]
[1]*Linköping University, CMIV, Linköping, Sweden,* [2]*Linköping University, Medical radiation physics, Linköping, Sweden,* [3]*Linköping University, CMVI, Linköping, Sweden*

Purpose/Introduction: Atrophy of the brain is a hallmark of a number of neurological diseases such as MS[1], Alzheimer's disease[2]and dementia[3]. Fast, precise and accurate methods for quantification of brain tissue volumes are therefore warranted. Synthetic MRI has received increased attention in recent years. Synthetic MRI has mainly been based on quantitative 2D qMRI methodswith high in-plane resolution, but thick slices[4]. However, a 3D qMRI method (QALAS) has been developed[5, 6]. An advantage of 3D qMRI is that it can be used to generate synthetic MRI with arbitrary image contrast and orientation. Moreover, brain tissue segmentation methods are often based on 3D T1w image volumes. Thus, it might be possible to used 3D QALAS to create synthetic 3D T1w image volume for tissue segmentation. The aim of this work was to compare the accuracy and precision of brain volume quantification using synthetic 3D T1w MRI imaging volumes from QALAS on NeuroQuant.

Subjects and Methods: Twelve volunteers, aged 29 to 74 were examined in a test-re-test procedure using both a 1.5 T and a 3 T MRI systems (Philips Healthcare), using an acquisition protocol that included a 3D T1 W-IR TFE sequence (with the recommended settings from *NeuroQuant*, (CorTechs Labs)) and a 3D QALAS sequence 1.2 mm isotropic resolution, and reconstructed to 1.0 mm resolution. In total 48 QALAS- and 48 T1w-volumes.

Processing of the QALAS data was performed using a prototype version (18Q3v3) of *SyMRI* (SyntheticMR), which generated R_1, R_2 and PD maps and synthetic 3D T1 W-IR images see Fig. 1.

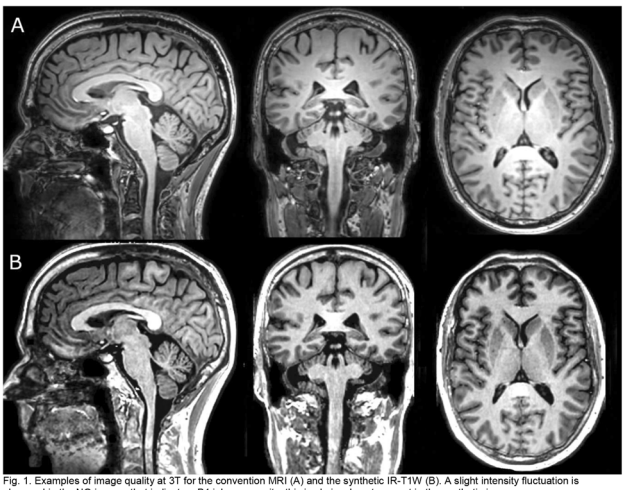

Fig. 1. Examples of image quality at 3T for the convention MRI (A) and the synthetic IR-T1W (B). A slight intensity fluctuation is observed in the NQ images that indicate a B1 inhomogeneity, this is obviously not present in the synthetic images.

Brain tissue volumes were quantified using *NeuroQuant*. The accuracy was then investigated using Pearson-correlation and Bland–Altman statistics. Precision was evaluated as intra-subject-variations using the coefficient of variation (CV %).

Results: High correlations between the methods were observed, with correlation coefficients ranging from 0.78 to 1, with a median 0.97 (1.5 T) and 0.9 (3T) (Table 1).

	1.5 T			3 T		
	r	Bias	SD	r	Bias	SD
Forebrain Parenchyma	1	-38.2*	13.9*	0.98	-80.5*	34.0*
Cortical Grey Matter	0.98	8.3	14.3	0.97	25.5	16.7
Superior Lateral Ventricle	0.99	-2.2	1.4	0.84	0.8	3.7
Inferior Lateral VentricleHippocampus	0.97	0.1	0.2	0.78	-0.1	0.3
Hippocampus	0.97	-0.8*	0.3*	0.94	-0.7*	0.3*
Thalamus	0.90	-0.3	0.9	0.96	-2.1*	0.6*
ICV	1.00	-61.7*	17.4*	1.00	-116.2*	19.3*
Median	0.97	-0.55	0.71	0.90	-1.40	0.62

Table 1: Correlations coefficients r and bias calculated using Bland-Altman method. * Significant bias.

No significant difference in intra-subject-variability (CV %) between the methods were found. However, the group CV % was lower for syMRI at 1.5 T compared to syMRI 3 T (Table 2).

	1.5 T	1.5 T	3 T	3 T
	T1w	syMRI	T1w	syMRI
Forebrain Parenchyma	0.6%	0.7%	36.3%	3.9%
Cortical Grey Matter	1.2%	1.0%	1.5%	4.3%
Superior Lateral Ventricle	1.1%	1.2%	1.0%	24.6%
Inferior Lateral Ventricle	5.3%	4.6%	3.7%	22.2%
Hippocampus	1.2%	1.2%	2.4%	3.7%
Thalamus	3.2%	2.9%	3.2%	5.9%
ICV	0.4%	0.3%	0.3%	1.5%
Median	1.8%	1.3%	2.7%	5.5%

Table 2: Intra-subject variability presented as coefficient of variation (CV%). No significant differences in CV between the methods was observed. However, the group CV% was slightly lower for syMRI at 1.5 T compared to syMRI 3T

4 synthetic volumes and 4 T1w volumes were rejected by NeuroQuant and excluded.

Discussion/Conclusion: High correlations were observed between the estimated tissue volumes using synthetic MRI compared to conventional MRI showing that it is possible to quantify brain tissue volumes using synthetic MRI. However, the tissue volumes were generally smaller for synthetic MRI compared to conventional MRI. We believe that this result was an effect of small contrast differences between the synthetic and conventional MRI. No other significant differences in intra-subject-variations were found between the two methods.

References:

1. Chard,"Brain atrophy…", *Brain*, 2002.
2. Fox,"Brain atrophy…"JMRI, 1997.
3. John"SEMANTIC DEMENTIA…", *Brain*, 1992.
4. Warntjes"Rapid magnetic…."MRM, 2008.
5. Kvernby"Simultaneous"JCMR, 2016.
6. Kvernby"Clinical feasibility…"MRI, 2017.

L06.03

Transverse relaxation time shortening effect of oxygen molecules in cellular mimetic viscous solution

R. Kusumoto, M. Tang, T. Yamamoto
Hokkaido University, Sapporo, Japan

Purpose/Introduction: The oxygen molecule is paramagnetic as well as Gadolinium contrast agents that reduce relaxation times. However, its relaxation time shortening effect has been experimented as too small in water solution such as blood plasma.[1] According to the Bloembergen-Purcell-Pound (BPP) theory, the transverse relaxation time shortening effect is enhanced in viscous solution such as intracellular environment. In this study, we investigated the transverse relaxation time shortening effect of oxygen molecules in cellular mimetic viscous solution.

Subjects and Methods: The viscous solution (75 cP)[2] was made from saline with glycerin 91%(w/w). This solution was sealed in two tubes before (137 mmHg) and after bubbling (233 mmHg) of oxygen. The volume-selected ^{1}H MRS (TR = 2 s) was performed with 10 different TEs (30–48 ms) using 3T MRI while keeping the temperature at 37 °C. The signal of water proton obtained from MR spectra by peak curve fitting (Fig. 1). The rate of MR signal changes (ΔS/S) between different oxygen concentrations was obtained at each TE: [S(137 mmHg)-S(233 mmHg)]/S(233 mmHg). Theoretically, ΔS/S is written as

$$|\Delta S/S| = |(TE \cdot r_2 - TR/(e^{R1 \cdot TR} - 1) \cdot r_1) \cdot \Delta[O_2]|$$

where r_1 and r_2 is the longitudinal and transverse relaxivity, respectively, and $\triangle[O_2]$ is the oxygen concentration difference of the tubes (96 mmHg). The value of r_2 in the viscous solution was obtained from the slope of regression line of the plot ΔS/S versus TE: $r_2\Delta[O_2]$

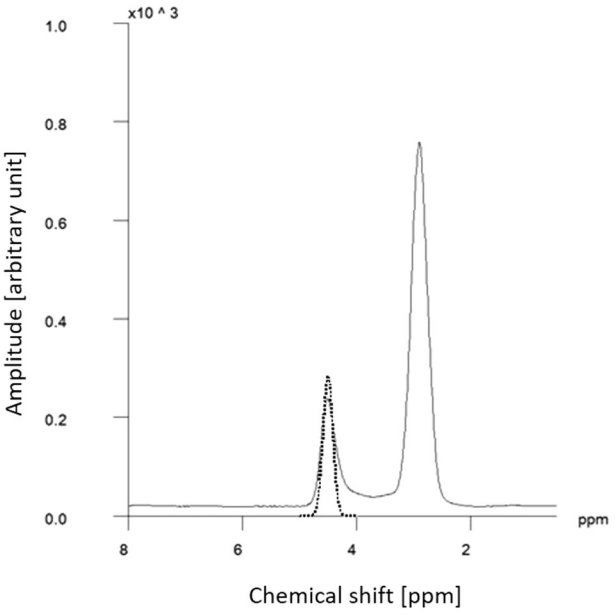

Figure.1 Spectrum of ^{1}H MRS (TR = 2000 ms, TE = 36 ms) of viscous solution. The water signal (left peak) was curve-fitted (dotted line).

Results: The value of ΔS/S increased significantly with TE ($r = 0.85$, $p < 0.05$) (Fig. 2). The theoretically-predicted cross point (TE_0) of the regression line and the abscissa of TE was 22 ms, and r_2 was 3.82×10^{-2} [s mmHg]$^{-1}$.

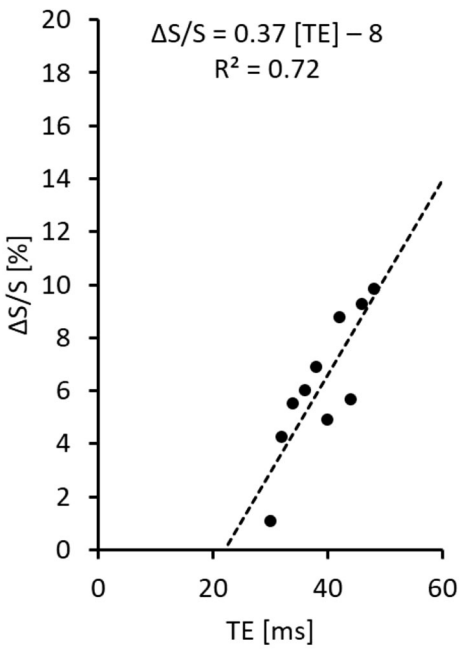

Figure.2 The rate of water MR signal changes (ΔS/S) due to oxygen molecules vs. TE. Dotted line represents the regression line.

Discussion/Conclusion: The r_2 was approximately 158 times larger than that of saline (2.42×10^{-4} [s· mmHg]$^{-1}$) [3] showing that the

relaxation time shortening effect is enhanced in viscous solution. The TE_0 appeared as a result of the counterbalance of the longitudinal and transverse shorting effects. The oxygen concentration at cell membrane is averagely 20 mmHg, and we suppose that the intracellular oxygen concentration fluctuates at this amplitude level; $\triangle[O_2]$ would be 20 mmHg. In this case, intracellular $|\triangle S/S|$ is estimated as 5.2% from the regression line in Fig. 2 for a typical TE (90 ms) of DWI that suppresses the intercellular water signal. This estimation implies that the intracellular oxygen concentration changes would be visible in MRI.

References:

1. Ma Y, Berman AJ, Pike GB. The Effect of Dissolved Oxygen on the Relaxation Rates of Blood Plasma. Implications for Hyperoxia Calibrated BOLD. Magn Reson Med. 75, 363–371, 2016.
2. Kuimova MK, Yahioglu G, Levitt JA, et al.: Rotor measures viscosity of live cells via fluorescence lifetime, J. Am. Chem. Soc. 130, 6672–6673, 2008.
3. Taguchi M, Yamamoto T: Enhancement of the transverse relaxation time shortening effect by oxygen molecules in viscous solution with cellular diffusivity. Jpn. J. Med. Phys. 37S1, 142, 2017.

L06.04

T_1 Bias reduction in the quantification of tissue sodium concentration using flip angle sweep

J. Chacon-Caldera, **A. Adlung**, N. Paschke, R. Hu, L. R. Schad
Heidelberg University, Medical Faculty Mannheim, Computer Assisted Clinical Medicine, Mannheim, Germany

Purpose/Introduction: Tissue sodium concentration (TSC) provides valuable information about tissue viability in pathologies such as ischemic stroke. Here, regions with dead tissue and maximum extracellular space further locally elongate T_1 values. The accuracy of TSC quantification is affected by T_1 contributions. Commonly, they are partially reduced by using relatively long repetition times (TR), restricted by the total measurement times (TA) e.g. TR = 100 ms and TA = 10 min[1]. This approach yields significant local errors in TSC for long T_1 values such as those affected by stroke. In this work, we use a flip angle sweep approach with short TR to reduce T_1 bias in the quantification of TSC.

Subjects and Methods: Measurements were acquired in a 3T MRI scanner (Trio, Siemens Healthineers, Erlangen, Germany) with a birdcage dual-tuned $^{23}Na/^{1}H$ head coil (Rapid Biomedical, Rimpar, Germany). A 3D UTE radial density-weighted sequence was used with 6000 spokes. Three protocols were tested in one healthy female volunteer a) Control, b) Stroke (as used in Ref. 1), c) Sweep. The parameters were: a) TE/TR = 0.2/350 ms, FA = 90°, TA = 35 min to entirely eliminate T_1 bias, b) TE/TR = 0.2/100 ms, FA = 90°, TA = 10 min, c) TE/TR = 0.2/30 ms, FAs = 15, 45, 60 and 84°, TA = 12 min.

Post-processing was done in Matlab (The Mathworks, Nattick, USA). Reconstruction used a convolution-based regridding algorithm and a Hanning filter. A sample slice was chosen and the signal equation $(TSC*\sin(FAs)*(1-\exp(-TR/T_1))/(1-\cos(FAs)*\exp(-TR/T_1)))$ was fitted with a lest-squares approach in a pixel-based with 2 free parameters, representing TSC and T_1 using boundary conditions in T_1 extracted from physiological values (25–80 ms). TSC maps were calculated using a reference vial with a concentration of 100 mmol.

Results:

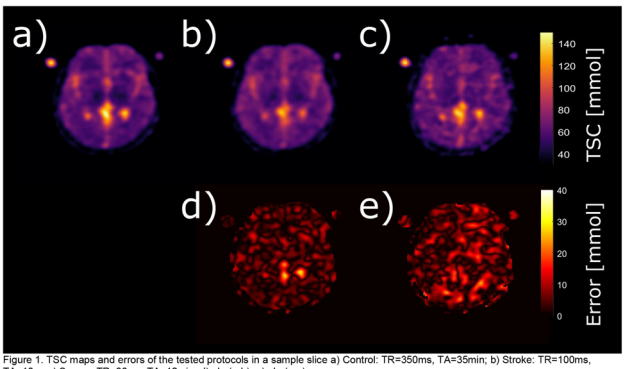

Figure 1. TSC maps and errors of the tested protocols in a sample slice a) Control: TR=350ms, TA=35min; b) Stroke: TR=100ms, TA=10m; c) Sweep: TR=30ms, TA=12min; d) abs(a-b); e) abs(a-c)

In Fig. 1, the Stroke protocol showed errors of up to 27 mmol in the TSC maps compared to the Control protocol. The Sweep protocol reduced the local bias in CSF (T1 $\sim$ 60 ms). The highest errors were approximately 30% lower compared to the hotspots shown in the error-map of the Stroke protocol. However, it showed overall greater variations and errors in TSC and some T_2*-weighting especially at high flip angles (Fig. 2).

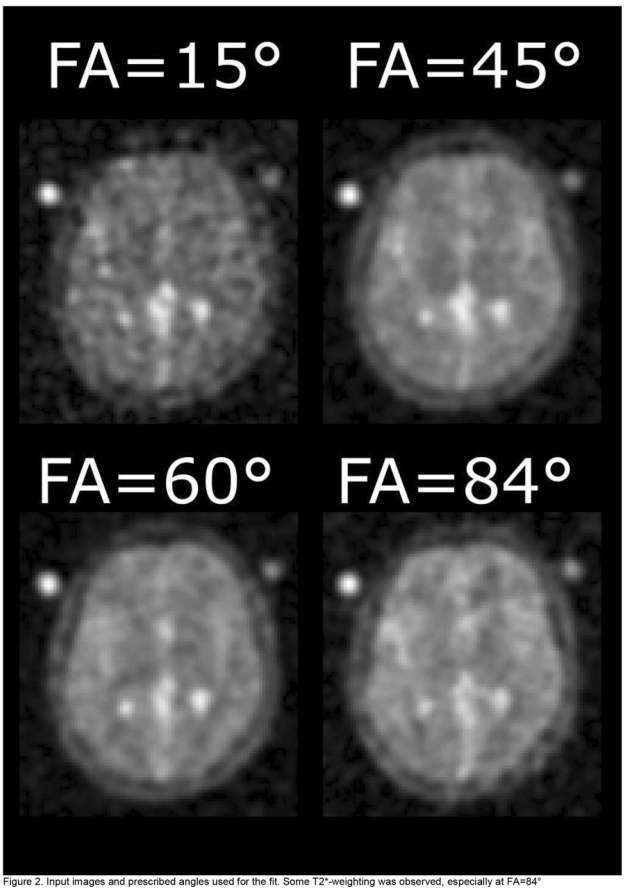

Figure 2. Input images and prescribed angles used for the fit. Some T2*-weighting was observed, especially at FA=84°

Discussion/Conclusion: Using the proposed approach, we reduced local T_1 bias for TSC in vivo while maintaining similar measurement times to previously used protocols in stroke studies. The observed T_2*-weighting suggests the need for signal spoiling. Further

optimization of flip angles and TR will be investigated. However, we expect ^{23}Na studies, in particular those on stroke patients, to benefit from our approach.

References:

1. E. Neumaier-Probst, et al. Int J Stroke (2015), 10:56–61

L06.05

Abdominal magnetic resonance fingerprinting for T_1 and T_2* quantification of the kidneys

I. Hermann[1], I. Brumer[1], B. Rieger[1], J. Chacon-Caldera[1], S. Weingärtner[2], L. Schad[1], F. Zöllner[1]

[1]*Univeristy Heidelberg, University Medical Center Mannheim, Computer Assisted Clinical Medicine, Mannheim, Germany,* [2]*Delft University of Technology, Department of Imaging Physics, Delft, The Netherlands*

Purpose/Introduction: Chronic kidney disease (CKD) is the clinical most significant form of kidney damage and can result from a number of phatological pathways, including, tissue inflammation, fibrosis and oedema. These changes are known to increase T_1[1]. Furthermore in CKD the tissue deoxyhaemoglobin level is decreased which can be monitored by the blood oxygenation level-dependent (BOLD) and therefore the T_2* relaxation time[2].

Magnetic resonance fingerprinting (MRF) is a novel method to quantify multiple parameters simultaneously. Numerous images with pseudo-random contrast weightings are acquired and matched to a dictionary containing different tissue parameters.

In this study we implemented a MRF sequence to quantify T_1 and T_2* relaxation times, to cover multiple slices of the kidneys in a single breath-hold.

Subjects and Methods: A MRF sequence based on echo-planar imaging readouts as proposed by Rieger et al.[3] was used with an online 'on the fly' group matching algorithm[4] at 3T (Magnetom Skyra, Siemens). The sequence parameters were FOV = 350 × 350 mm, matrix size = 192 × 192, slice thickness = 4 mm, bandwidth = 1800 Hz/px, GRAPPA factor = 2, partial fourier = 5/8 and varying flip angle α, TE, TR as shown in Fig. 1. 35 measurements of 4 slices with TR varying between 442 ms and 720 ms, TE between 18 ms and 79 ms and α between 17° and 43° were imaged with a total acquisition time of 17.5 s.

Images were acquired in a phantom and two healthy volunteers in coronal and axial orientation. Region of interests were manually drawn in the kidneys to segment the renal cortex and medulla. Mean values and standard deviations of the T_1 and T_2* times were calculated for each region.

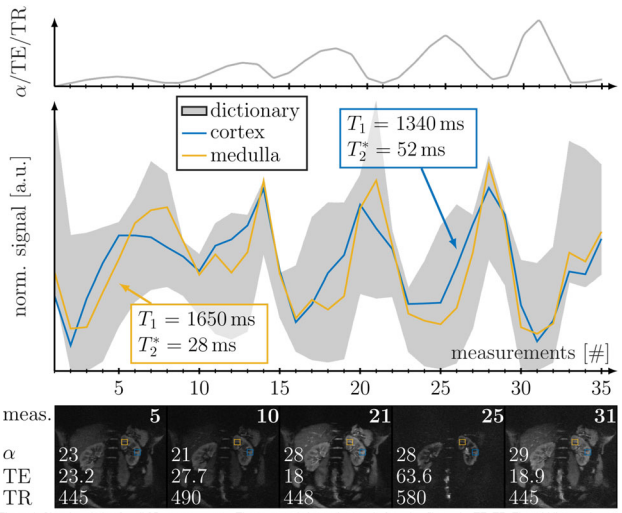

Figure 1: Signal evolution for all 35 measurements. The top panel shows the trend of varying flip angle, TE, TR. The middle panel shows the signal curve of the renal cortex (blue) and medulla (yellow). Example images are provided in the bottom panel.

Results: Our results show that MRF measurements are accurate in the phantom with deviations of less than 5% for T_1 and T_2* relaxation times. Baseline images of the kidneys with various contrast weightings are free of artifacts (Fig. 2). Slight, non-destructive aliasing is observed in axial slice. Mean values and standard deviations of the cortex were T_1 = 1196 ± 81 ms, T_2* = 43 ± 5 ms and in the medulla T_1 = 1493 ± 94 ms, T_2* = 33 ± 3 ms. Online reconstruction was computed in less than 10 s.

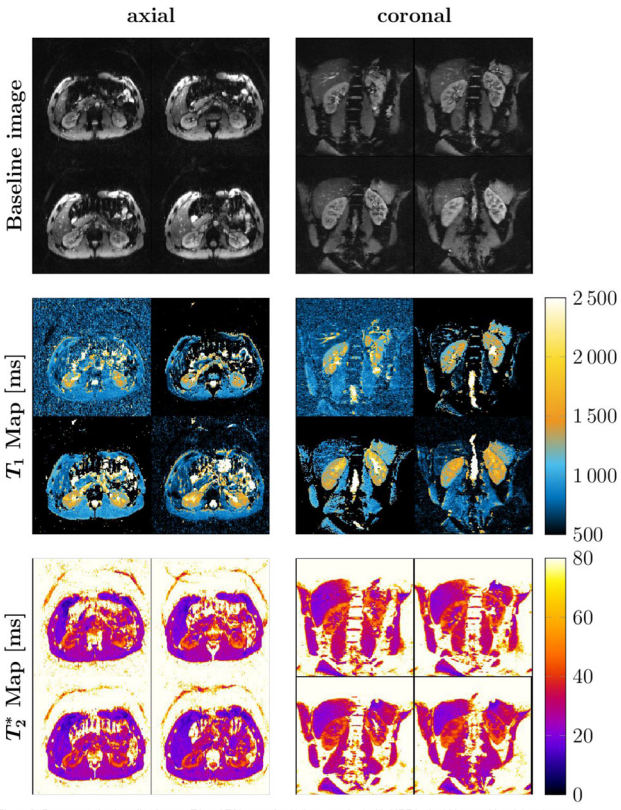

Figure 2: Representative baseline image, T1 and T2* maps for 4 slices acquired with MRF in the kidneys with axial and coronal orentation.

Discussion/Conclusion: A renal MRF sequence was implemented to measure T_1 and T_2* times simultaneously of 4 slices during one

breath-hold. The obtained T_1 and T_2* times of the renal cortex and medulla were comparable to literature values[1, 5]. Our results demonstrate the feasibility of renal T_1 and T_2* mapping with MRF, which can provide a quantitative biomarker for chronic tissue damage.

References:

[1] Wolf, M. et al. *Nephrol. Dial. Transplant.* **33**, ii41-ii50 (2018).
[2] Burnier, M. et al. *Nephrol. Dial. Transplant.* **33**, ii22-ii28 (2018).
[3] Rieger, B. et al. *Magn. Reson. Med.* **78**, 1724–1733 (2016).
[4] Hermann, I. et al. *Proceedings from the 27nd Annual Meeting ISMRM, Montreal, QC, Canada* 4529 (2019).
[5] Hedgire, S. S. et al. *Int. J. Nanomed.* **9**, 2101–2207 (2014).

L06.06

Bi-component fitting for reduced partial volume effects due to fat in MOLLI T1 mapping

A. S. Gaspar[1], A. C. Freitas[1], N. A. da Silva[2], R. G. Nunes[1]
[1]*Instituto Superior Técnico Universidade de Lisboa, ISR-Lisboa/LARSyS and Department of Bioengineering, Lisbon, Portugal,*
[2]*Hospital da Luz Learning Health, Lisbon, Portugal*

Purpose/Introduction: Myocardium T1 quantification allows non-invasive identification of diffuse fibrosis. The Modified Look-Locker Inversion Recovery (MOLLI) sequence is the most clinically applied method due to its high precision [1]. Nevertheless, the standard 3-parameter fitting algorithm (3-param) is vulnerable to partial volume effects (PVE) which can arise from fat infiltration in the myocardium [2–4]. In this work, we propose a 2-component model which accounts for the existence of fat avoiding T1 discrepancies due to PVE.

Subjects and Methods: MOLLI signals using acquisition schemes: 5(3)3, 3(3)3(3)5, and 4(3)3(3)2, with a bSSFP readout (FA = 35°; TI_1 = 100 ms; TR/TE = 2.5/1.25 ms) were simulated using EPG in Matlab2016a. Signals representing pure myocardial (T1/T2 = 1000/50 ms; on-resonance) and fat tissues (T1/T2 = 260/60 ms; 210 Hz off-resonance—Fig. 1) were combined to mimic fat fractions (FF) of [0.00–0.50]. Gaussian noise was added to obtain a typical SNR = 90 at 1.5T.

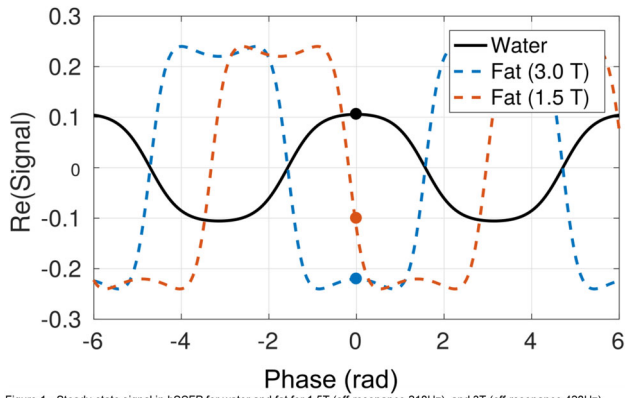

Figure 1 - Steady-state signal in bSSFP for water and fat for 1.5T (off-resonance 210Hz), and 3T (off-resonance 420Hz).

Using the lsqcurvefit function, apparent T1 (T1*) values were estimated with the conventional 3-param (Fig. 2-Eq.1) and the proposed 2-component model which accounts for both fat and water within the pixel (Fig. 2-Eq2).

a. 3-parameter fitting

$$S_{MOLLI}^{3param}(t, A, B, T1^*) = A - B\, e^{-t/T1^*} \quad \text{Eq (1)}$$

b. 2-component fitting

$$S_{MOLLI}^{2comp} = (1-FF)S_W + FF\, S_F = (1-FF)\left(A_W - B_W\, e^{-t/T1_W^*}\right) + FF\left(A_F - B_F\, e^{-t/T1_F^*}\right) \quad \text{Eq (2)}$$

$$S_{MOLLI}^{2comp}(t, A, B_w, T1_w^*, B_F) = A - (1-FF)\, B_w\, e^{-t/T1_w^*} - FF\, B_F\, e^{-t/T1_F^*} \quad \text{Eq (3)}$$

Figure 2 - Fitting algorithms: a. 3-parameter fitting; and b. 2-component fitting model which accounts for the existence of both fat and water within the pixel. where AW, BW, and T1W* correspond to water parameters, and AF, BF, and T1F* to fat.

Results: Figure 3 shows that by fitting the model in Eq. (3), the accuracy of T1 $_W$* is maintained stable at a mean value of 721 ± 190 ms (T1w = 898 ± 299 ms when corrected [5]) in the FF interval tested for MOLLI 3(3)5, while 3-param goes up 2193 ± 455 ms (FF = 0.46). Additional measurements using alternative MOLLI acquisition schemes enabled a more accurate and precise T1 $_W$* estimate, especially when using the scheme 3(3)3(3)5.

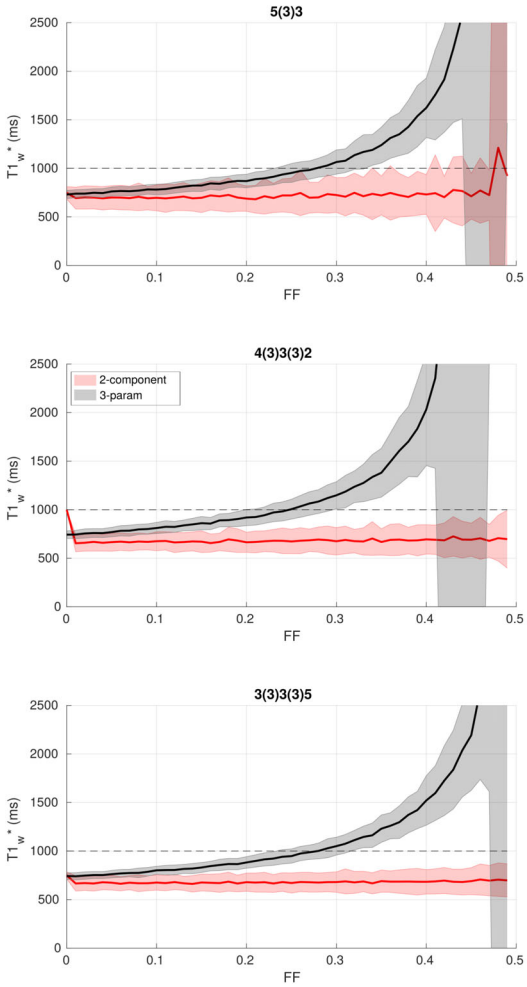

Figure 3 - Mean apparent T1 (T1W*) +/- standard deviation of 200 signal samples, for the 3-parameter fitting (black), and 2-componente model (red) using alternative MOLLI acquisition schemes.

Discussion/Conclusion: The proposed 2-component model enabled to stabilize T1 $_W$* estimates even when the fat fraction within the pixel increased. Although we only compared apparent T1 values, in both cases these could be corrected for afterwards according to [5]. The MOLLI sequence is widely available in the clinical setting but it is known to be very sensitive to fat. To account for its impact,

clinically available methods such as Dixon could be used to measure FF and this information used to estimate accurate T1 $_w$ values with the proposed post-processing 2 component model fitting. Our model should also be compatible with sequences recently proposed for T1 estimation which already include Dixon measurements [6]. Further investigations are underway to include also B0 field variations and to evaluate the impact of errors in the FF estimate on the T1w.

References:
1. McDiarmid AK, et al. Quant Imaging Med Surg. 2015; 5:503.
2. Larmour S, et al. MRM. 2017; 77:237.
3. Kellman P, et al. JCMR. 2015; 17:33.
4. Liu D, et al. MRI. 2017; 37:81.
5. Chow K, et al. ISMRM. 2014; 22:2453.
6. Nezafat N. et al. MRM. 2019; 81:486.

Acknowledgements
FCT (SFRH/BD/120006/2016; UID/EEA/50009/2019); POR Lisboa 2020 (LISBOA-01-0145-FEDER-029686).

L06.07

In vitro and in vivo evaluation of radial turbo-spin-echo-based T_2 mapping of the liver

D. Bencikova[1], S. Kannengieser[2], Y. Natsuaki[3], G. Reiter[4], A. Ba-Ssalamah[1], S. Trattnig[1], M. Kršsák[5]
[1]*Medical University Vienna, Department of Radiology, Vienna, Austria,* [2]*Siemens Healthcare GmbH, Erlangen, Germany,* [3]*Siemens Medical Solutions, Inc., Los Angeles, CA, USA,* [4]*Siemens Healthineers Austria, Graz, Austria,* [5]*Christian Doppler Laboratory for Clinical Molecular Imaging, MOLIMA, MUW, Vienna, Austria*

Purpose/Introduction: Magnetic resonance is a noninvasive modality that can help in the diagnosis of liver disease; it is a potential alternative to liver biopsy. Among other MR parameters, hepatic T_2 relaxation times were reported to be affected by many pathological conditions. The measurement of T_2 values in the human liver is challenging due to the breathing motion in the abdomen. With conventional techniques the measurement takes up to several minutes. A fast radial multi-spin-echo technique was proposed to overcome this problem, being sufficiently fast and motion-insensitive [1].

Subjects and Methods: We compared a prototype radial TSE T_2 mapping (TR/TE = 1500/9.2–266 ms, FOV = 400 × 400 mm^2, matrix = 256 × 256, FA = 180̊, ST = 6 mm, total acq time = 17 s) with conventional Cartesian multi-SE based T_2 mapping (TR/TE = 5000/10–320 ms, FOV = 250 × 250 mm^2, matrix = 256 × 256, FA = 180̊, ST = 8 mm, total acq time > 20 min) in the T_2 array of the NIST phantom (range 8–800 ms) at a 3T scanner (MAGNETOM Prisma Fit, Siemens Healthineers, Erlangen, Germany). In addition we tested the effect of fat signal suppression (FS) on the radial TSE T_2 map in phantoms with variable fat content (0–35%) using the same parameters and compared it to multi-echo single-voxel STEAM spectroscopy (HISTO, 5 TEs = 12, 24, 36, 48 and 72 ms, TR = 3 s) [2]. Finally, we evaluated in a heterogeneous group of 21 patients appointed to clinical abdomen examinations T_2 values obtained via the fat-suppressed radial TSE and HISTO MRS-based sequence.

Results: There was an excellent correlation between T_2 values from the fast radial and the conventional techniques measured in the phantom in the range of T_2s from 260 to 20 ms (r = 0.999, P < 0.0001). Radial TSE T_2 values were higher with a mean difference of 40.49 ± 49.53 ms (P = 0.003), and Bland–Altman plots show a systematic difference. The T_2 values of radial TSE are capped at 400 ms (Fig. 1). The application of FS decreased the T_2 values from radial TSE in samples with fat fraction over 10%, which demonstrates its effect (Fig. 2). The correlation coefficient between T_2 values from HISTO (water only) and radial TSE increased with the application of FS (r = 0.722, P = 0.043 without, r = 0.849, P = 0.008 with FS). Comparison of the in vivo-acquired hepatic radial TSE T_2 map with spectroscopically-obtained T_{2water} values showed a correlation, but higher T_2 values by radial TSE based mapping with a mean difference of 12.38 ± 10.31 ms (P < 0.0001, Fig. 3).

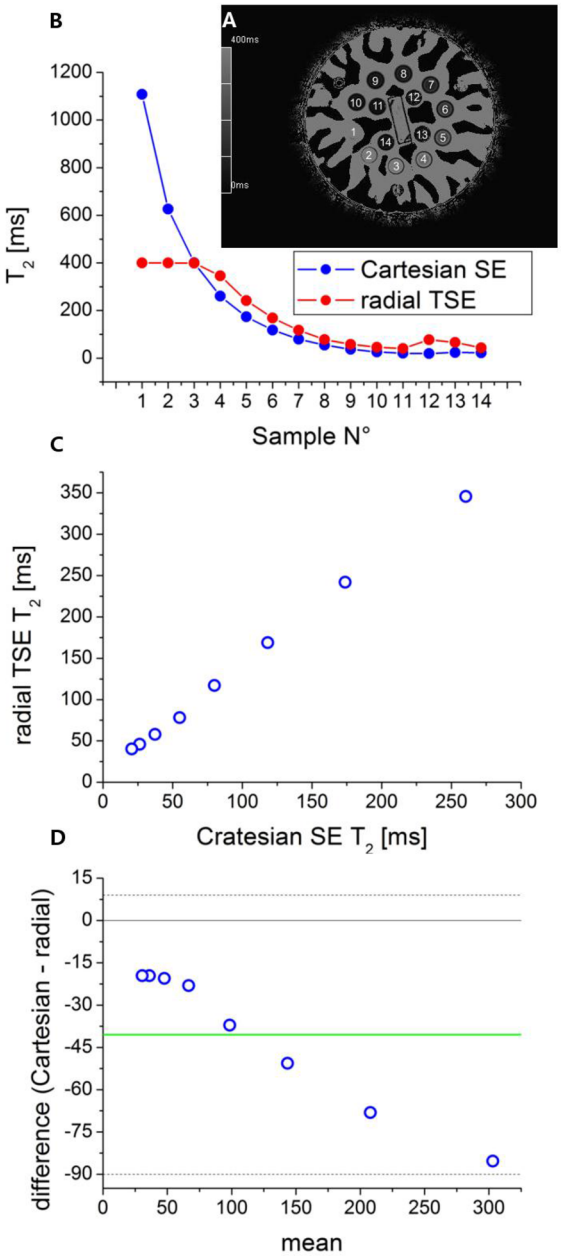

Fig. 1: 14-element T2 array of the phantom (T2 range 8 – 800ms): a) rad TSE T2 map and b) T2 values from all elements. c) Bland-Altman plot and d) correlation from the range of T2s 20 - 260 ms (corresponding to elements 4 – 11) between the two maps.

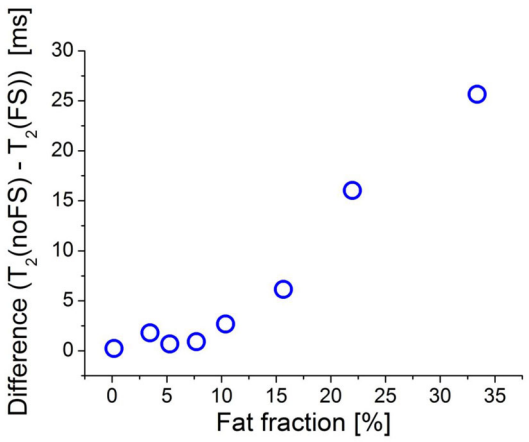

Fig.2: The effect of fat suppression on the T2 values: the difference between T2 values from unsuppressed and suppressed map (y-axis) starts to be obvious in samples with fat fraction (FF) of 10% and more and further increases with increasing FF.

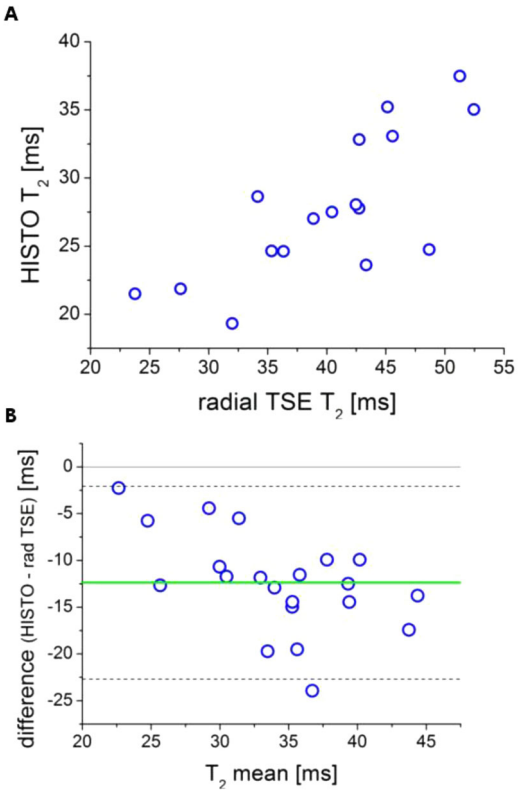

Fig.3: T2 values obtained spectroscopically (HISTO) and from radial TSE map: a) correlation between the two methods, b) Bland-Altman plot.

Discussion/Conclusion: We could show that fast radial TSE T_2 mapping works sufficiently well for in vivo liver data acquisition, and that this method can be used for further characterization of diffuse liver diseases within a clinically acceptable measurement time. In addition, fat signal plays a role in hepatic tissue T_2 mapping and should be considered.

References:

[1] Altbach MI et al., Mag Resn Imaging 2002; 16.2: 179–89.
[2] Sharma P et al., Mag Resn Imaging 2009; 29.3: 629–35.

L06.08

Improving PCASL at 7 T using a VERSE-guided parallel transmission strategy

Y. Tong, P. Jezzard, T. W. Okell, W. T. Clarke
University of Oxford, Wellcome Centre for Integrative Neuroimaging, FMRIB Division, NDCN, Oxford, UK

Purpose/Introduction: Implementing pseudo-continuous arterial spin labelling (PCASL) at ultra-high field is challenging due to increased specific absorption rate (SAR) and B_1^+/B_0 inhomogeneity (1). Parallel transmission (pTx) provides additional degrees of freedom to mitigate B_1^+ inhomogeneity. Among the various pTx strategies, RF shimming is a simple formulation that modulates the complex weights of each RF channel. In addition, Variable-Rate Selective Excitation (VERSE) could also be employed during the labelling period to reduce SAR. VERSE is a technique that reduces SAR without compromising the slice profile (2, 3). In this study, we explored the possibility of using VERSE to further improve PCASL at 7 T and compared the results with 3 T.

Subjects and Methods: Perfusion-weighted images were acquired from five subjects (five male, mean age 33.8, range 27 to 52) on a Siemens (Erlangen, Germany) Magnetom 7 T scanner equipped with an 8 channel pTx system, and a Nova Medical Inc. (Wilmington MA, USA) 8T × 32Rx head coil. To minimise SAR, no background suppression pulses were used. B_1^+ maps were acquired using a DREAM sequence (4, 5) and B_0 maps were acquired using a dual-echo GRE sequence. A time-of-flight (TOF) sequence was used to identify the region-of-interest (ROI) aroud four principal arteries that feed the brain. The flip-angle optimisation strategy was based on a method by Dupas et al. (6). VERSE RF and gradient pulses were obtained using an approach by Hargreaves et al. (3). Cerebral blood flow (CBF) was calculated using a method by Buxton et al. (7). The same subjects were also scanned on a Siemens Prisma 3 T scanner.

Results: In simulation, VERSE shimming improved the flip-angles across the ROIs by 90% compared to CP mode. In experiments, VERSE shimming improved the temporal signal-to-noise ratio in the grey matter by 819% compared to CP mode in 2 subjects with low CP mode perfusion signal, and by 77% in the remaining 3 subjects. However, VERSE shimming did not outperform a matched 3 T sequence with a matched flip-angle.

Discussion/Conclusion: We have demonstrated the feasibility of improving PCASL using VERSE-guided RF shimming on a commercial head coil at 7 T. Unlike dynamic pTx, RF shimming does not involve calculation of a full RF waveform, nor optimisation of the gradient trajectory. Replacing Gaussian RF pulses and trapezoidal gradients with VERSE RF and gradient waveforms further improved the RF efficiency. However, homogenous excitation at the target flip-angle of 20° was not achieved in all subjects. Local SAR monitoring using virtual observation points (VOPs) would allow for less stringent RF power limits, and thus higher and more uniform flip-angles in the labelling vessels.

References:

1. Teeuwisse et al. IJIST, 2010. 2. Conolly et al., MRM, 1988.. 3. Hargreaves et al., MRM 2010. 4. Nehrke et al. MRM, 2012. 5. Tse et al. JMR, 2014. 6. Dupas et al. JMR, 2015. 7. Buxton et al., MRM, 1998.

L06.09

Tradeoff between fat-suppression and partial-voluming in weighted combination alternating repetition-time (ATR) balanced SSFP

M. Shahdloo, T. Çukur
Bilkent University, Electrical and Electronics Engineering Department and National MR Research Center (UMRAM), Ankara, Turkey

Purpose/Introduction: Balanced steady-state free precession (SSFP) imaging yields high SNR efficiency within short scan times. Yet, the undesired fat signal is a major problem. Linear combination SSFP (LCSSFP) was proposed as a multi-acquisition solution to this problem that shapes the spectral response to selectively suppress the fat resonance[1]. The stringent limitations on TR in LCSSFP were later relaxed by a linear combination of multiple alternating repetition-time (ATR) SSFP acquisitions. However, in both cases, the linear combination yields inhomogeneous level of signal suppression within the stop-band. Here, we adopt nonlinear p-norm combinations of multiple ATR-SSFP data to improve fat-suppression efficiency[2]. Note that nonlinear combinations are susceptible to partial-volume effects. To examine this potential issue, we provide a quantitative analysis of the tradeoff between fat-suppression and partial-voluming for a comprehensive set of tissue relaxation times and imaging parameters. We propose a guideline to select the optimal p-norm to yield desired level of fat-suppression while limiting partial-voluming artifacts.

Subjects and Methods: The in-phase and out-of-phase ATR-SSFP profiles have 180° phase difference at the water resonance. Hence, weighted combination of the in-phase (X_I) and out-of-phase (X_O) signals would yield the water-only (D_w) and fat-only (D_f) signals[3]

$$D_w=(|X_I|^pX_I+i|X_O|^pX_O)^{1/1+p}$$
$$D_f=(|X_I|^pX_I-i|X_O|^pX_O)^{1/1+p}$$

where $p\in(-1, 0]$. We quantified a fat-suppression index (FS) as the mean ratio of the pass-band ([− 80, 80] Hz) in the water signal to the mean ratio of it in the fat signal. Linear combination of the phase-cycled datasets ($p = 0$) yields partial-voluming-free reconstruction. Thus, we quantified the level of partial voluming (PV) in terms of deviation from the ideal case of linear combination. We then calculated p that yields specific FS and PV and analyzed its dependence on tissue properties and imaging parameters using a simulated phantom.

Results: Figure 1 shows reconstructions of phantom acquisitions using different p and dependence of FS and PV on p. Fat signal gets more suppressed as $p \rightarrow -1$ at the cost of higher partial-voluming. This assessment is supported by in vivo reconstructions of Fig. 2. Figure 3 shows calculated p using different FS and PV. Optimal p depends on α and T1/T2 but has little dependence on imaging resolution and SNR.

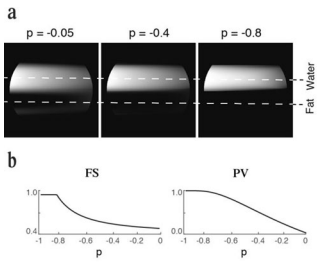

Figure 1. Fat-suppressed reconstructions for the simulated phantom. Phase-cycled ATR-SSFP acquisitions were simulated for a circular phantom for α=45, TR1/TR2/TE = 3.45/1.15/1.7ms, T1/T2 for water = 1000/100ms, T1/T2 for fat= 270/85ms. Ratio of water in voxels varies between 0 to 1 from right to left. Off-resonance varies in [-380,380]Hz from bottom to top. **(a)** Fat-suppressed reconstructions using various p show enhanced fat-suppression at the cost of increased partial-voluming as p approaches to -1. **(b)** Fat-suppression index (FS) and partial-voluming index (PV) calculated using the simulated phantom. Both FS and PV increase as p approaches to -1.

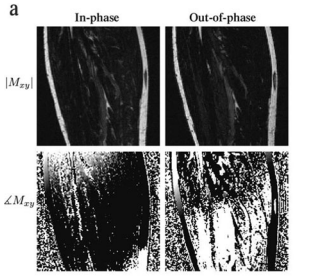

Figure 2. Fat-suppressed reconstructions for the in vivo calf. Phase-cycled acquisitions were performed using a 3D ATR-SSFP sequence with α =60, TR1/TR2/TE = 3.45/1.15/1.7ms, 1mm isotropic resolution. **(a)** Magnitude and phase of in-phase and out-of-phase images of the central coronal slice. **(b)** Fat-suppressed maximum-intensity projection (MIP) reconstructions using various p. Fat-suppression enhances as p approaches to -1 which is reflected as better suppression of the background fat tissue. Partial-voluming also increases as p approaches to -1. This is apparent as degraded depiction of vessels having sub-voxel dimensions (white arrows).

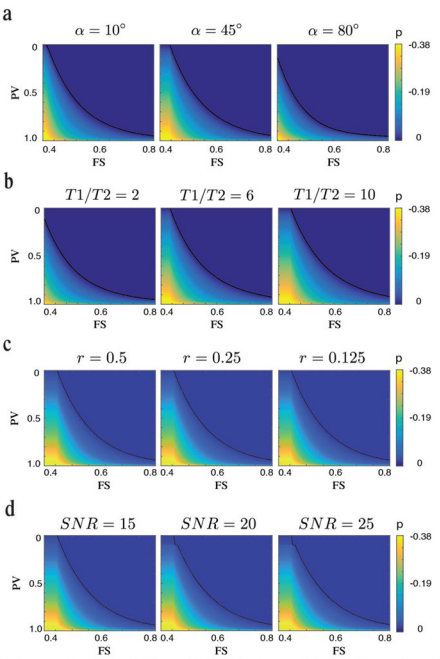

Figure 3. Optimal p as a function of FS and PV. Optimal p was taken as the median of the range of p which is lower-bounded by the allowed PV and upper-bounded by the desired FS for various **(a)** flip angles, **(b)** T1/T2 for the water tissue, **(c)** reduced phantom resolution by a factor of r, and **(d)** SNR. Solid lines specify the boundary of the achievable FS and PV. An intermediate value for flip angle allows for a broader range of achievable fat-suppression for a fixed level of partial-voluming. Achievable fat-suppression for a fixed level of partial-voluming increases with T1/T2 of water tissue. Imaging resolution and SNR have little effect on the applicable range of p.

Discussion/Conclusion: Weighted combination of ATR-SSFP acquisitions with $p \rightarrow -1$ leads to near complete fat-suppression at the cost of enhanced partial-voluming. We provided a comprehensive analysis of this tradeoff. Finally, we proposed optimal p that yields the desired level of fat-suppression while limiting the partial-voluming artifacts.

References:

1. Vasanawala SS, et al. Linear combination steady-state free precession MRI. Magn Reson Med 2000; 43:82–90.
2. Çukur T, et al. Enhanced Spectral Shaping in Steady-State Free Precession Imaging. Magn Reson Med 2007; 58:1216–1223

L06.10

3D heart localization for free breathing cardiac MR navigators in real time at 3T and 7T

T. Körner, S. Wampl, M. Meyerspeer, S. Trattnig, E. Moser, A. Schmid

Medical University of Vienna, Center for Medical Physics and Biomedical Engineering, Vienna, Austria

Purpose/Introduction: A major obstacle for cardiac MRI/MRS is respiratory motion[1, 2]. Many real-time navigators target diaphragm for its better contrast [3, 4], yet its motion is not equal to the heart's [5, 6]. This work evaluates a fast and robust approach for directly detecting cardiac position in real time.

Subjects and Methods: 12 healthy subjects (7 f, 5 m, 25 ± 2 y, 23 ± 2 kg/m2) were examined in supine position on a Prisma 3T and a Magnetom 7T scanner (Siemens, Erlangen, Germany).

Sagittal slices were acquired near the heart's apex and coronal slices posterior to the chest wall (Figs. 1, 2). Different MR sequences (gradient echo—GRE and turbo flash—TFL) and variation of sequence parameters were investigated.

Scan parameters:

· T_E: ∼ 1.4 ms (shortest possible)
· T_R: ∼ 4 ms (shortest possible)
· Flip angle: ∼ 10°–15°
· Slice: ∼ 20 × 20 × 4 cm
· Matrix: 128 × 128

An algorithm was prototyped in PDL (http://pdl.perl.org) and implemented as navigator in the scanner's reconstruction software (ICE). Heart localization was based on the evaluation of signal intensity profiles (Figs. 1, 2).

Features were added to the algorithm to increase detection rates.

Detection efficiency was evaluated by an operator, rating each feature either as "detected" or "missed".

Cranial and caudal edge appeared as minimum and maximum in the respective derivative of mean signal intensity profiles in HF direction (Fig. 1).

In AP direction posterior of the global maximum in median values in readout (HF) direction, intersection of lung tissue signal threshold and median values corresponded to the posterior edge of the heart (Fig. 1).

Lateral detection (Fig. 2) was introduced later, fewer data sets were recorded.

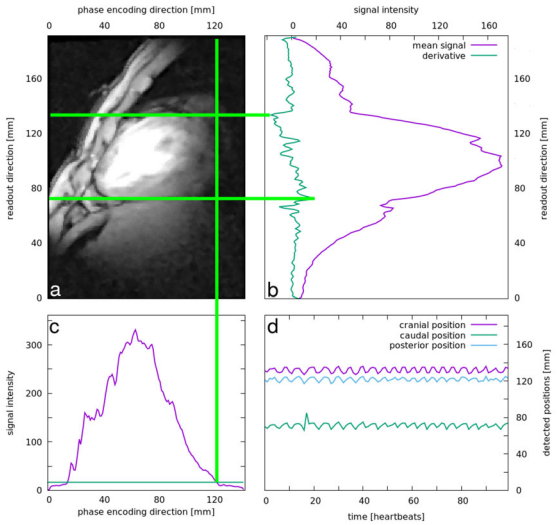

(a) Sagittal cardiac image (7T); detected borders (green lines) correspond to min/max in the derivative of the intensity profile (HF direction) (b), (AP direction) and a lung threshold (c). (d) shows the heart's movement over time.

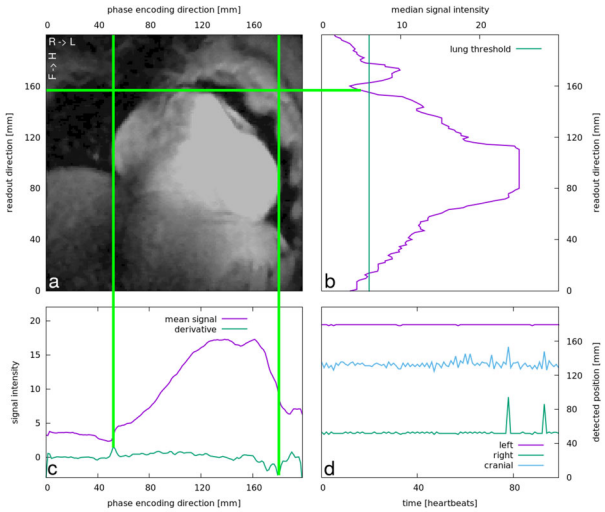

(a) Coronal cardiac image (7T); detected borders (green lines) correspond to (HF direction) and a lung threshold (b),min/max in the derivative of the intensity profile (lateral direction) (c). (d) shows the heart's movement over time.

Results: The algorithm worked equally well on 3T and 7T scanners. No difference was observed for GRE and TFL sequences. Image reconstruction and heart detection on a Magnetom 7T scanner required ∼ 12 ms.

Sagittal (12 subjects)	Coronal (2 subject)
cranial: 98%	cranial: 98%
caudal: 97%	left: 99%
posterior: 98%	right: 99%

Detection efficiency

Discussion/Conclusion: Localizing the heart is feasible using the presented method at 3T and 7T yielding high detection efficiency and sufficient speed, making the algorithm suitable for real-time navigators. Development of anterior heart localization, validation of coronal detection and code optimization for shortening acquisition time are subject to current development.

The big advantage of our approach is that the location of the heart is known. This has the potential to avoid breath-holds, speeding up measurements (high efficiency) thereby significantly enhance cardiovascular MR applications.

References:

1. https://doi.org/10.1148/radiology.159.3.3704156
2. https://doi.org/10.1148/radiology.160.3.3737920
3. https://doi.org/10.1081/jcmr-100107467
4. https://doi.org/10.1002/mrm.10182
5. https://doi.org/10.1002/mrm.23247
6. https://doi.org/10.1002/mrm.1910330517

This work was funded by the Austrian Science Fund project P 28867-B30.

L06.11

Using a field camera to monitor head movement in 7T scanner

L. Bortolotti, J. Smith, P. Gowland, R. Bowtell
Sir Peter Mansfield Imaging Centre, School of Physics and Astronomy, University of Nottingham., Nottingham, UK

Purpose/Introduction: Head movement during MRI produces image artefacts. A variety of motion correction methods have been developed[1]. Here, we evaluate the potential for using measurements of the magnetic field perturbations produced outside the head for monitoring head position inside a 7T MR scanner. This approach could allow contactless motion monitoring without the need for modification of imaging sequences.

Subjects and Methods:

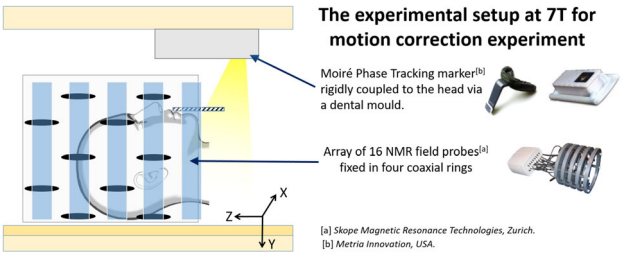

The picture shows a model of the experimental set-up [2]. The 16 NMR field probes are symmetrically placed in a head-coil array support while the optical camera is fixed to the inside of the magnet bore.The system of reference used is also shown.

The set-up of the experiments is shown in Fig. 1. We used a 16-channel field camera in conjunction with an MPT camera system to monitor external field changes and head position. Respiratory and cardiac cycles were also monitored using the scanner's physiological logging system. Data represents four subjects monitored for 60 s-periods corresponding to four different conditions (rest, head-nodding, head-shaking and wiggling the feet) [3] resampled at a common frequency of 10 Hz in post-processing. As expected, chest and head movements cause field fluctuations. Field probe measurements were fitted at each time point to a series of spatial spherical harmonics up to 3rd order. Lower/higher order harmonics best represent the effect of chest/head movements. The 0th and 1st orders were therefore eliminated before reconstituting the signals. A Partial Least Squares (PLS) regression method was used to relate filtered magnetic field data series to the changes in head position.

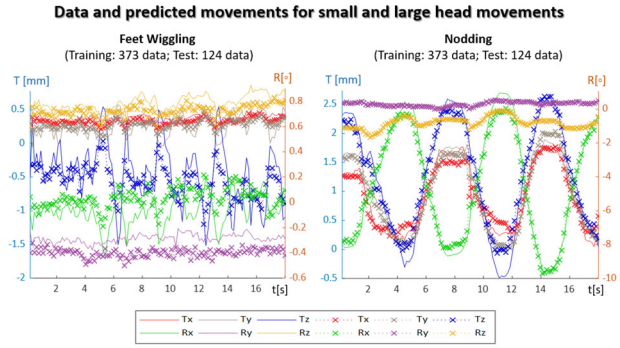

Comparison between the actual (line) and the predicted (crosses) movement derived by applying the PLS regression method to the data from one subject during 35s-segments of the rest and head nodding conditions.

		Tx [mm[	Ty [mm[	Tz [mm]	Rx [o]	Ry [o]	Rz [o]
Feet Wiggling	STD	0.13	0.16	0.45	0.20	0.18	0.18
	RMSE	0.06	0.12	0.32	0.14	0.12	0.08
Head Nodding	STD	0.63	0.68	0.97	3.36	0.37	0.43
	RMSE	0.015	0.11	0.20	0.50	0.09	0.12

Table shows the corresponding values of the standard deviation (Std) of the movements and the ratio of the root mean squared error to Std (Err%). Data are shown for subject 1 (T = translation in mm; R =rotation in degrees).

Results: Figure 2 shows the movement predicted by applying the PLS regression method to the field camera measurements of one subject for the feet wiggling and nodding conditions. The accuracy of the predicted value (Table 1) was evaluated by calculating the Root Mean Squared Error (RMSE) with respect to the MPT-measured parameters, and the ratio of the RMSE with respect to the standard deviation (STD) of the actual position changes.

Discussion/Conclusion: Elimination of the field variations that result from sources other than head movement by spatial filtering improved the predictions of head position using the field camera. The PLS method can identify the relationship between changes in head position and the pattern of field variation from measurements acquired over 45 s. The accuracy of prediction of movement parameters is better for the larger movements, and for the dominant movement parameters for each type of motion. In conclusion, measurements of the changes in the field generated outside the head can be used to estimate head-movement parameters with reasonable accuracy. For practical use it would be necessary to learn the relationship between the field variation and head positions, which requires access to simultaneous measures of head position made using another approach (e.g. MPT).This work provides a step forward towards a non-contact motion monitoring technique.

References:

[1] Aranovitch A. et al., Magn Reson Med. 2018; 79:2046–2056.
[2]Bischoff L. et al., ISMRM 2016; 0303. 2017.**[3]**Bortolotti L. et al. Master's Thesis, University of Bologna, 2017

L06.12

A new generation optical prospective motion correction system: initial results

I. F. Syversen[1], Å. J. Svarliaunet[2], T. N. Schröder[1], P. E. Goa[3]
[1]*Norwegian University of Science and Technology, Kavli Institute for Systems Neuroscience, Trondheim, Norway,* [2]*St. Olavs Hospital, Department of Radiology and Nuclear Medicine, Trondheim, Norway,* [3]*Norwegian University of Science and Technology, Department of Physics, Trondheim, Norway*

Purpose/Introduction: Motion artifacts remain a challenge in MRI, sustaining the need for further development and improvements of motion correction techniques [1]. One promising method is optical prospective motion correction (PMC). This can be realized using optical cameras placed inside the MR scanner bore, to track an adhesive marker attached to the subject's face [2]. Recently, an updated version of this type of system has been developed and commercialized. Here we demonstrate our initial results from using this system.

Subjects and Methods: The optical PMC system (KinetiCor, HI, USA) was installed on a Siemens Skyra 3T scanner (Siemens Medical Solutions, Erlangen, Germany). The version of the tracking software used in this work was 1.2.0. MR images from 5 informed, and consenting healthy volunteers were acquired using the system, with the adhesive marker attached to the volunteers' nasal ridge (Fig. 1). We used the PMC system under two conditions: Scans with deliberate motion, and high-resolution scans without deliberate motion. Protocol parameters: T2 W TSE TIRM, TI/TR/TE = 2594/10240/84 ms, resolution 0.7 × 0.7 × 3.0 mm, acquisition time 3:13 min; T2 W TSE, TR/TE = 5010/93 ms, resolution 0.3 × 0.3 × 3.0 mm, acquisition time 11:28 min.

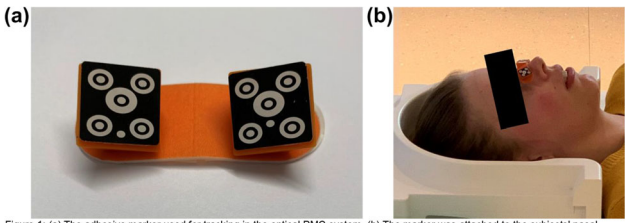

Figure 1: (a) The adhesive marker used for tracking in the optical PMC system. (b) The marker was attached to the subjects' nasal ridge.

Results: Figure 2 shows examples from two different subjects where deliberate motion was performed during scanning. Figure 3 shows examples from two different subjects where no deliberate motion was performed. Across subjects, for scans with deliberate motion present, the image quality is improved using the optical PMC system, although not all motion artifacts are eliminated. For scans without deliberate motion, the image quality is in some cases improved, but also in some cases slightly reduced.

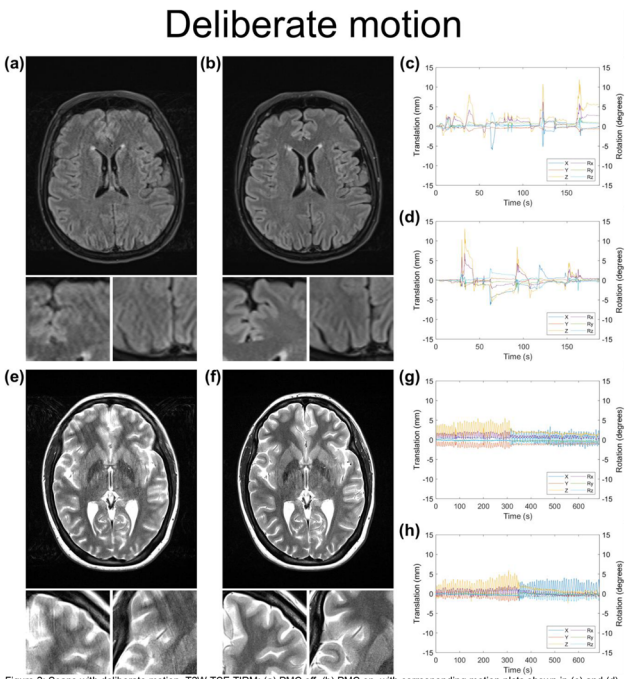

Figure 2: Scans with deliberate motion. T2W TSE TIRM: (a) PMC off, (b) PMC on, with corresponding motion plots shown in (c) and (d), respectively. T2W TSE: (e) PMC off, (f) PMC on, with corresponding motion plots shown in (g) and (h), respectively.

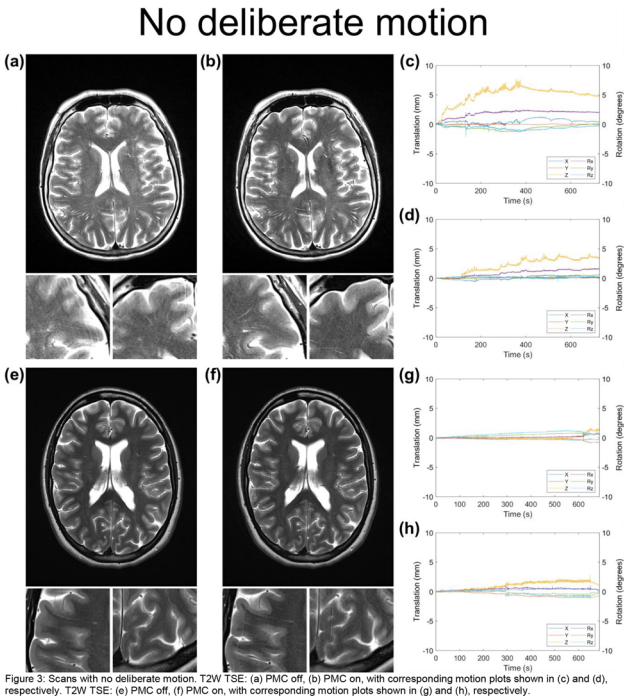

Figure 3: Scans with no deliberate motion. T2W TSE: (a) PMC off, (b) PMC on, with corresponding motion plots shown in (c) and (d), respectively. T2W TSE: (e) PMC off, (f) PMC on, with corresponding motion plots shown in (g) and (h), respectively.

Discussion/Conclusion: In the high-motion cases the optical PMC system generally improves the image quality, although some motion artifacts remain. For the high-resolution images with no deliberate motion, the results are less conclusive. One possible explanation for the mixed results is that the nose marker is not sufficiently rigidly coupled to the skull for this application. An alternative solution where the marker is attached to a bite-bar and fitted to the subject's upper teeth is possibly a more robust approach, but with some added discomfort for the subject. We will perform further work to explore this

solution. In addition, future software updates might improve tracking accuracy and image quality.

References:

[1] F. Godenschweger et al. 2016, *Phys Med Biol* 61(5):R32-R56.
[2] A. Singh et al. 2015, *MAGMA* 28(6):523–534.

Acknowledgements:
Imaging sequences provided by Tobias Kober and Daniel Nico Splitthoff in Siemens Healthineers, and by Maxim Zaitsev at University Medical Center Freiburg. The project has received technical support from KinetiCor, Siemens and Roar Sunde at St. Olavs Hospital, and financial support from Faculty of Medicine and Health Sciences at NTNU.

L06.13

A correction method for susceptibility-induced temperature measurement error during MRI-guided high intensity focused ultrasound treatment

C.-F. J. Huang[1], L.-W. Kuo[2], S.-C. Hwang[3], C. Yao[3], H. Chang[3], W.-L. Lin[1]
[1]*Department of Biomedical Engineering, National Taiwan University, Taipei, Taiwan,* [2]*Institute of Biomedical Engineering and Nanomedicine, National Health Research Institutes, Miaoli, Taiwan,* [3]*MBInsight Technology Corporation, Taipei, Taiwan*

Purpose/Introduction: During MRI-guided high intensity focused ultrasound (MRgHIFU) treatment, the movement of HIFU transducer and the surrounding water bag would lead to susceptibility in the magnetic field and might cause temperature measurement error. To correct this error, conventional correction method uses repetitively scanning before treatment to provide the corresponding baseline for temperature calculation as the transducer repositioned. However, conventional method is cumbersome and time-consuming. Here, we present a novel post-processing algorithm to acquire the corresponding baseline to calculate temperature.

Subjects and Methods: Parameters: Spoiled gradient echo imaging data were acquired on a 1.5T MRI system to calculate temperature map based on proton resonance frequency (PRF) shift method [1]. TR/TE = 37/17.3 ms, FOV = 256 × 256 mm^2, matrix = 128 × 128, slice thickness = 8 mm. Ablation HIFU power was set from 40 to 200 W for in vitro porcine meatwith a heating duration of 30 s for each target and a cooling interval of 60 s for the next [2].

Theory: According to Fourier transform shift theorem, the shift *a*of the signal in time domain corresponds to multiplying signal by e^{-iwa} (hereinafter called shift term) in frequency domain. If the transducer movement-induced shift term in frequency domain can be obtained, then we can acquire the corresponding baseline by multiplying this shift to the initial baseline. Figure 1 shows the procedure to calculate the corresponding baseline and it is described as below.

1) Acquire R map by subtracting P2 from P1, where P1 and P2 are the phase images acquired before and after transducer movement and ablation. R contains phase changes caused by both susceptibility and temperature changes.
2) Acquire R2 map by applying polynomial fitting on R to remove the influence of temperature changes. R2 contains phase changes caused by susceptibility only. With R2 we can calculate the shift matrix Sh in step3.
3) M is the unknown baseline corresponding to P2. Equation 1 can be obtained since susceptibility caused phase change R2 equal to P1 minus M theoretically. Then, equation 1 is converted to frequency domain to get equation 2. Note that shift matrix Sh records the shift term of each point in frequency domain. X1 and V2 in equation2 is known (Fourier transform of P1 and R2, respectively) so that the shift matrix Sh can be obtained.
4) Apply Fourier transform on X1(w)*Sh to obtain the unknown baseline M.
5) Subtract P2 from M to obtain phase changes caused by temperature only. Then calculate temperature rise by PRF method.

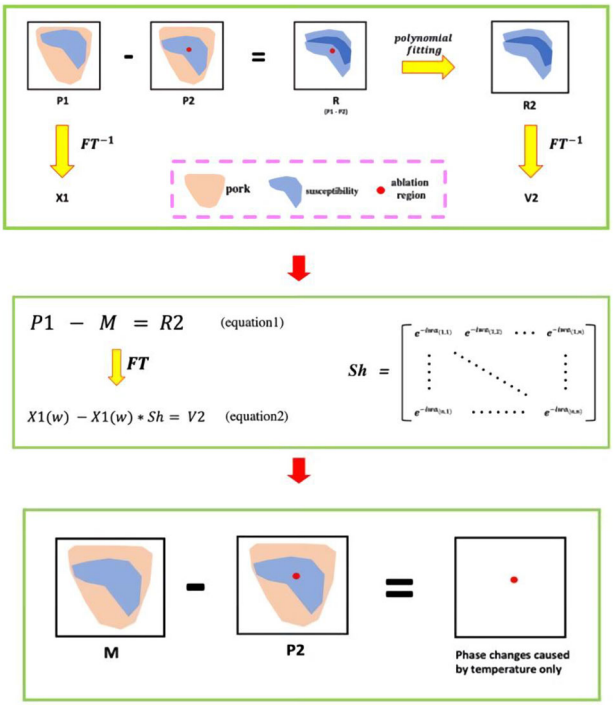

Figure1: The flowchart of the procedure of our algorithm.

Results: The results are shown and described below:

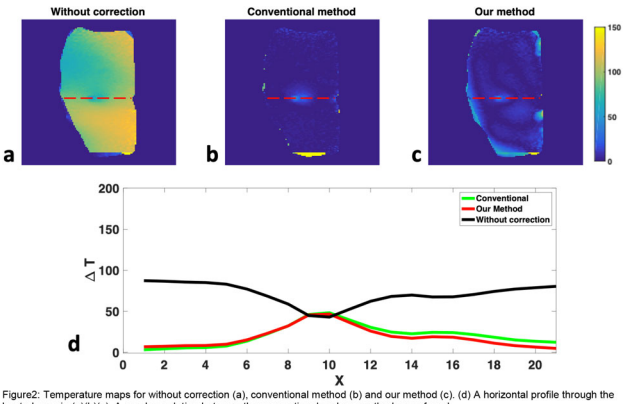

Figure2: Temperature maps for without correction (a), conventional method (b) and our method (c). (d) A horizontal profile through the heated area in (a)(b)(c). A good correlation between the conventional and our methods was found.

Discussion/Conclusion: We proposed a post-processing algorithm method to obtain new baseline for transducer reposition instead of scanning repetitively. The proposed method has the potential to replace the conventional correction method.

References:

1. Peters, R.D. and R.M.J.M.R.I.M.A.O.J.o.t.I.S.f.M.R.i.M. Henkelman, *Proton-resonance frequency shift MR thermometry is affected by changes in the electrical conductivity of tissue.*2000. **43**(1): p. 62–71.
2. Hwang, S.C., et al. *Tissue necrosis monitoring for HIFU ablation with T1 contrast MRI imaging*. in *AIP Conference Proceedings*. 2011. AIP.

L06.14

Optimizing robustness and accuracy of MR elastography for the diagnosis and follow up of glioblastoma patients

M. Yushchenko[1], M. Sarracanie[1], M. Amann[1], R. Sinkus[2], J. Wuerfel[1], N. Salameh[1]
[1]*University of Basel, Department of Biomedical Engineering, Allschwil, Switzerland,* [2]*INSERM, Paris, France*

Purpose/Introduction: Glioblastoma multiforme (GBM) is a malignant brain tumor with a median survival of 15 months, and a 5-year survival rate of less than 10%[1] in treated patients. Although MRI is the gold standard for GBM diagnosis and treatment follow-up, it is not specific to tumor infiltration processes and cannot discriminate treatment response and immune activities from tumor growth. MR Elastography (MRE) is a non-invasive technique estimating the mechanical properties of organs[2, 3] that could appear critical in the proper characterization of tumor response. The goal of this preliminary study is to assess accuracy and robustness of MRE in GBM patients from both simulation and experimental sides while preserving patient's comfort.

Subjects and Methods: Numerical simulations were performed with COMSOL Multiphysics© to produce displacement fields in objects with ground-truth G* values (fig 1a). This synthetic MRE data was then fed to our MRE processing pipeline. Error on the estimated object sizes was obtained from the mean ± SD FWHM calculated from 8 line-profiles drawn across each object.

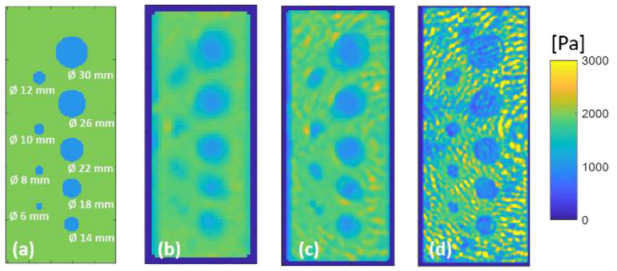

Simulation: ideal Gd distribution at 1 mm resolution (a) & the reconstructed Gd maps, for an isotropic resolution of 3 mm (b), 2 mm (c) & 1 mm (d). The diameter of the inclusions varies from 30 mm to 6 mm, a single frequency of 50 Hz was simulated.

MRE was performed with a fractional encoding GRE-based sequence[4] at 3T. The vibration was produced by a rotating-mass transducer positioned on one side of the head[5]. Parameter optimization was performed on two volunteers to address trade-offs between the acquisition time, patient's comfort, and robustness. Patient's comfort and maintained sensitivity was addressed by using lighter rotating masses and a 3D-printed holder for improved coupling/positioning between the head and the transducer. Positioning of the transducer and the induced wave quality were assessed from waves' amplitude in the brain, absence of contribution from frequencies different from the induced vibration, as well as degree of induced shear waves.

Results: Our simulations show that Gd values of a uniform object are correctly reconstructed (Fig. 1b–d). However, the assumption of mechanical homogeneity along with 3rd derivatives calculations produced blurred contours at interfaces (Fig. 1), leading to errors > 50% in the estimated sizes for objects ≤ 14 mm (Fig. 2).

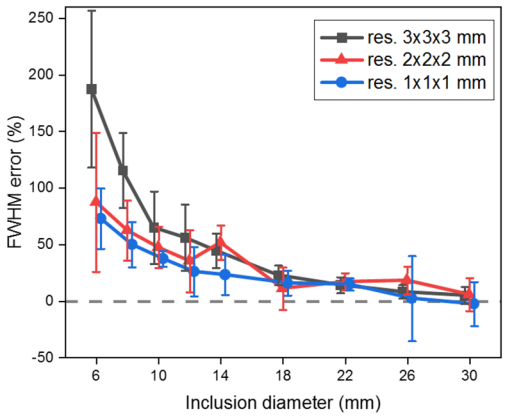

Simulation results: error on the estimated object size calculated from the mean +/- SD FWMH obtained along 8 line profiles crossing each object.

An example of in vivo data with the optimized protocol is shown in fig 3.

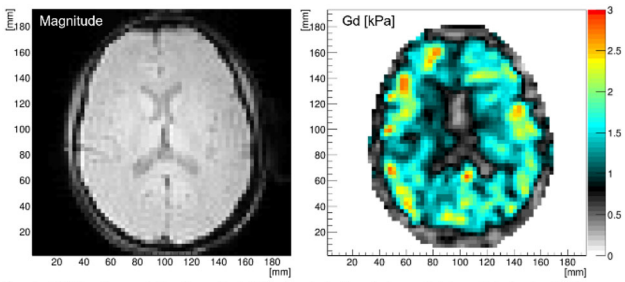

Example of MRE results: magnitude and reconstructed Gd values of a healthy volunteer, central slice, optimized protocol (50Hz-vibration, 60mT/m Motion Encoding Gradients, 3mm isotropic voxel size, 192x192mm FOV, 9 slices, acquisition time 200s).

Discussion/Conclusion: Our protocol provides good wave amplitude inside the brain allowing for successful image reconstruction while maintaining short acquisition times and comfort. As highlighted by our simulations, our protocol enables mapping Gd with confidence in objects larger than 14 mm. This, however, needs to be fully characterized in a larger cohort of volunteers so that clinicians can read the elastograms with certainty. Once this step is validated, the diagnostic performances of MRE in discriminating between tumors' progression or response to treatments will be assessed.

References:

1 Davis 2016 Clin J Oncol Nurs.
2 Simon 2013 New J Phys.
3 Muthupillai 1995 Science.
4 Garteiser 2013 NMR Biomed.
5 Runge 2019 Phys Med Biol.

L06.15

Treatment response assessment maps: towards an acceptance and QA protocol

M. Mills, J. Martin, L. M. Harris
Brighton and Sussex NHS Trust, Medical Physics, Brighton, UK

Purpose/Introduction: Treatment Response Assessment Maps (TRAM) are a high resolution method of differentiating tumour necrosis and cancer progression by displaying the temporal distribution of contrast agent in an enhancing region, as determined by subtraction of two post contrast scans separated by ∼ 1 h [1].

The current literature does not reference any guidance on a validation/QA to test this technique.
Using an in-house Matlab program to produce TRAMs, we aimed to quantitatively test the repeatability of the technique.
Subjects and Methods: A Eurospin TO5, with 8 test vials (T1 and T2 times similar to common brain tumours, white/grey matter and oedema/water at 1.5T and 3.0T [2, 3]), was scanned using a clinical 3D-MPRAGE sequence in the configurations shown in Fig. 1. Figure 2 shows an example TRAM.

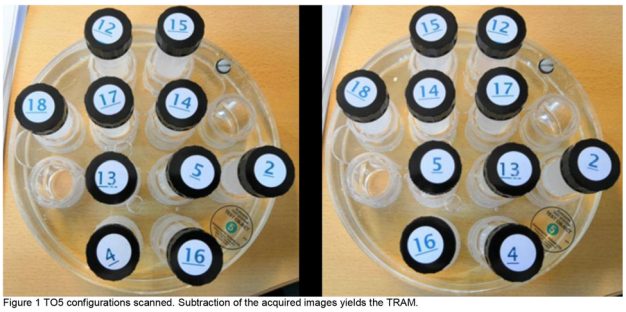

Figure 1 TO5 configurations scanned. Subtraction of the acquired images yields the TRAM.

TRAM signals were measured using 6 mm ROIs (chosen to minimize signal variation, see Fig. 3) using IQWorks.

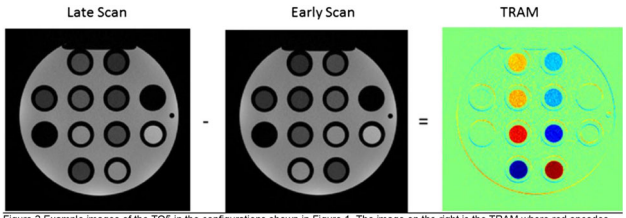

Figure 2 Example images of the TO5 in the configurations shown in Figure 1. The image on the right is the TRAM where red encodes an increase in signal in the late scan compared to the early scan, and blue the opposite.

Repeatability was measured:
- Across 9 central imaging slices for one TRAM (inter-slice).
- Over 5 repeat scans (inter-scan).
- Across 3 imaging sessions with at least 1 day between them (inter-session).
- Across three 1.5T Siemens Aeras (inter-scanner).
The effect of field strength and conversion of 16bit greyscale to 8bit magnitude RGB data was also investigated.
Statistical testing was performed using SPSS23.
Results: Repeatability was generally high, however the similarity of absolute values appears contingent on having identical imaging parameters.

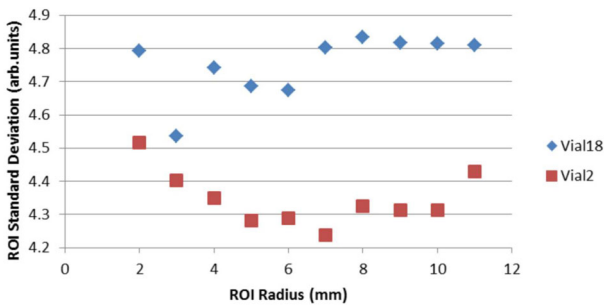

Figure 3 Standard deviation within the ROIs of the stationary TO5 vials (vials 2 and 18). The minimum variability occurs at approximately 6mm.

Inter-slice repeatability was high: the maximum coefficient of variation (CoV) was 1.4% across 9 slices.
Inter-scan repeatability yielded an average CoV of $\sim$ 2% (slice matched ROIs across repeats); the largest was 8.0%. ANOVA showed significant differences ($p < 0.05$) between repeats however.
Inter-session repeatability was also high: average CoV was measured at $\sim$ 3% and the largest at 5.7%. Again, ANOVA showed significant differences between repeats.
Inter-scanner testing shows that when scanning parameters are kept identical a high degree of agreement is found, while small changes result in substantial differences.
Initial testing suggests a similar level of repeatability is observed at 3T, but values differ from those obtained at 1.5T.
T testing of the background signals showed no significant difference compared to the hypothetical value ($p = 0.318$), suggesting no impact from converting to 8bit data.
Discussion/Conclusion: We have demonstrated a high level of repeatability of TRAMs across the imaging volume, between repeats and across scanners. Separate baselines may be required at different field strengths and where sequences differ. These tests may be used for acceptance andongoing QA testing for sites producing TRAMs.
References:
1 Zach, Leor, et al. "Delayed contrast extravasation MRI…" PloS one 7.12 (2012): e52008.
2 https://mri-q.com/why-is-t1–t2.html
3 Badve, Chaitra, et al. "MR fingerprinting of adult brain…" American Journal of Neuroradiology 38.3 (2017): 492–499.

L06.16
Beyond high resolution: denoising during image reconstruction to improve image quality

F. Luesebrink[1], F. Luesebrink[2], H. Mattern[2], S. Oeltze-Jafra[1], S. Oeltze-Jafra[3], O. Speck[2], O. Speck[3], O. Speck[4], O. Speck[5]
[1]*Otto-von-Guericke University, Department of Neurology, Medicine and Digitalization, Magdeburg, Germany,* [2]*Otto-von-Guericke University, Institute for Physics, Biomedical Magnetic Resonance, Magdeburg, Germany,* [3]*Center for Behavioral Sciences, Magdeburg, Germany,* [4]*German Center for Neurodegenerative Disease, Magdeburg, Germany,* [5]*Leibniz Insitute for Neurobiology, Magdeburg, Germany*

Purpose/Introduction: Each MRI acquisition is contaminated by thermal noise. Its spectrum is white, its amplitude distribution is Gaussian, and it is additive to the MR signal[1, 2]. Various steps in image reconstruction alter the noise distribution and removal of non-Gaussian noise is more challenging. Therefore, in this study we applied a state-of-the-art non-local means filter, BM4D[3], and a pre-trained neural network, DnCNN[4], to reduce the Gaussian distributed noise in channel-wise complex image data during image reconstruction.
Subjects and Methods: Data of one healthy male Caucasian subject (34 years old) were acquired using a whole-body 7 T (Magnetom, Siemens Healthineers Erlangen, Germany) with a 32-channel receive head coil (Nova Medical, Wilmington, Massachusetts, USA). The local ethics committee approved the study and the subject gave written informed consent.
An MPRAGE sequence was employed (TR: 2500 ms, TE: 2.55 ms, TI: 1050 ms, BW: 320 Hz/px, no partial Fourier, 0.7 mm isotropic resolution, TA: 800 s) to acquire nine volumes: 4 high SNR volumes (FA: 5°), 4 low SNR volumes (FA: 1°), and 1 noise volume (FA: 0°). All datasets were acquired using prospective motion correction[5]. The noise volume was used to decorrelate the data. The high SNR volumes were rigidly registered and averaged. These averaged data

served as a reference for validation of denoising performance by calculating PSNR and SSIM[6].

We have written a reconstruction pipeline in MATLAB (Fig. 1) to denoise during reconstruction. Parametrization of BM4D is set either very conservatively or strong.

After extraction of raw data (mapVBVD [7]), the channels are prewhiten. Then the data are denoised (BM4D or DnCNN) and filtered in k space (3D Tukey window [8]). After iFFT, the channels are combined by adaptive combine [9], and output as NIfTIs.

Results: In all cases denoising with BM4D results in higher SSIM and PSNR (except Fig. 2d). Conservative filtering does not introduce any drawbacks visually. Conservative filtering during reconstruction yields better results than after reconstruction (Fig. 2, b, g, l vs. c, h, m). Strong filtering of BM4D results in removal of small structures (Fig. 2, d) and blurring of the image (Fig. 2i, n).

Application of DnCNN leads to blurring of the lateral temporal lobes (Fig. 2 j, o). In Fig. 2e SSIM is reduced after application of DnCNN for unknown reasons—visual inspection does not show a decline in image quality.

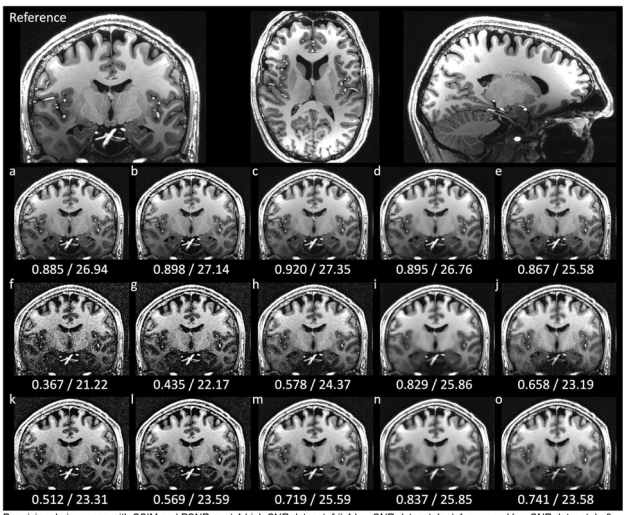

Denoising during recon with SSIM and PSNR. a-e) 1 high SNR dataset. f-j) 1 low SNR dataset. k-o) 4 averaged low SNR dataset. Left to right: No denoising, denoising after recon, denoising during recon with BM4D conservative, BM4D strong, and DnCNN.

Discussion/Conclusion: Fine-tuning of BM4D parametrization may lead to better denoising while preserving sharpness. Training the neural network on 3D data instead of 2D images only may improve denoising results[10].

This method could be applied to ultrahigh resolution images to improve image quality of existing data, e.g. our 250 µm dataset[11, 12], to reduce the number of averages in future studies, or to improve image resolution even further with the same amount of averages.

The technique is not limited to structural data, but is applicable to all data with Gaussian distributed noise and can be extended to most denoising algorithms from computer vision readily as they are typically designed for Gaussian noise only.

References:

1. Aja-Fernández, S. & Vegas-Sánchez-Ferrero, G. *Statistical Analysis of Noise in MRI* (Springer International Publishing, Cham, 2016).
2. Hansen, M. S. & Kellman, P. Image reconstruction: an overview for clinicians. *Journal of magnetic resonance imaging : JMRI* **41,** 573–585 (2015).
3. Maggioni, M., Katkovnik, V., Egiazarian, K. & Foi, A. Nonlocal transform-domain filter for volumetric data denoising and reconstruction. *IEEE transactions on image processing : a publication of the IEEE Signal Processing Society* **22,** 119–133 (2013).
4. Zhang, K., Zuo, W., Chen, Y., Meng, D. & Zhang, L. Beyond a Gaussian Denoiser: Residual Learning of Deep CNN for Image Denoising. *IEEE transactions on image processing : a publication of the IEEE Signal Processing Society* **26,** 3142–3155 (2017).
5. Maclaren, J. *et al.* Measurement and correction of microscopic head motion during magnetic resonance imaging of the brain. *PloS one* **7,** e48088 (2012).
6. Wang, Z., Bovik, A. C., Sheikh, H. R. & Simoncelli, E. P. Image Quality Assessment: From Error Visibility to Structural Similarity. *IEEE Trans. on Image Process.* **13,** 600–612 (2004).
7. Ehses, Philipp,DZNE Bonn, personal communication.
8. Tukey JW. An introduction to the calculations of numerical spectrum analysis. *Spectral Analysis of Time Series* **1967,** 25–46.
9. Walsh, D. O., Gmitro, A. F. & Marcellin, M. W. Adaptive reconstruction of phased array MR imagery. *Magn. Reson. Med.* **43,** 682–690 (2000).
10. Jiang, D. *et al.* Denoising of 3D magnetic resonance images with multi-channel residual learning of convolutional neural network. *Japanese journal of radiology* **36,** 566–574 (2018).
11. Lüsebrink, F., Sciarra, A., Mattern, H., Yakupov, R. & Speck, O. T1-weighted in vivo human whole brain MRI dataset with an ultrahigh isotropic resolution of 250 µm. *Scientific data* **4,** 170032 (2017).
12. Lüsebrink, F., Sciarra, A., Mattern, H., Yakupov, R. & Speck, O. Raw data from: T1-weighted in vivo human whole brain MRI dataset with an ultrahigh isotropic resolution of 250 µm.

L06.17

High-resolution real-time phase contrast flow imaging using sparse sampling, k-t regularization and shared velocity encoding

A. Greiser[1], M. Schmidt[1], N. Jin[2], R. Wassmuth[3], C. Tillmanns[3], C. Forman[1]

[1]*Siemens Healthcare GmbH, Erlangen, Germany,* [2]*Siemens Medical Solutions, Chicago, USA,* [3]*Diagnostikum Berlin, Berlin, Germany*

Purpose/Introduction: MR Phase-Contrast Flow imaging is widely available, but significant acceleration is needed for real-time performance with high resolution. Various methods have been proposed [1, 2], but robustness and image quality are typically limited. We demonstrate the feasibility of L1-regularized wavelet-based compressed sensing acceleration [3, 4] in combination with shared velocity encoding (SVE) [5] for Real-Time Flow Imaging (CS RT). Quantitative flow results are checked for reproducibility and agreement in a flow phantom and in healthy volunteers. Finally, the real-time protocol is also applied in arrhythmia patients.

Subjects and Methods: CS Flow was implemented in clinical 1.5T and 3T scanners (MAGNETOM Aera and Prisma, Siemens Healthcare, Erlangen, Germany) using pseudo-random sampling [1] and shared velocity encoding [2] in a 2D k-t-sparse cine phase contrast prototype sequence. Aortic flow was acquired (n = 8) in the aorta for 3 protocol variants (conventional: TE 2.5 ms, temp. res. 37.1 ms, res. $1.8 \times 2.0 \times 6$ mm^3, 18 heartbeats; CS segm.: TE 2.7 ms, temp. res. 28.5 ms, res. $1.4 \times 2.0 \times 6$ mm^3, $R_{eff} = 7.5$, 7 heartbeats; CS RT: TE 2.3 ms, temp. res. 45.8 ms, res. $1.7 \times 2.6 \times 10$ mm^3, $R_{eff} = 8.8$) and also in a phantom with steady or pulsatile flow. Analysis was performed using commercial software (Argus Flow, Siemens Healthcare GmbH, Erlangen, Germany).

Results: Iterative CS Flow reconstruction could be performed in-line at $\sim$ 1 s/frame. In vivo results showed high to moderate reproducibility (conv.: FV/v_{max} stdev. 3.8/3.9%; CS segm.: FV/v_{max} stdev. 3.5/3.5%; CS RT: 8.9/6.7%) and low to moderate bias vs. conv. (FV/v_{max} CS seg: − 1.96 ml/− 4.6 cm/s; CS RT: − 7.5 ml/ − 13.5 cm/s). In the steady-flow phantom results were more consistent (FV/v_{max} stdev. conv.: 2.2/0.6%; CS segm.: 3.6/0.31%; CS RT: 1.5/0.6%) and also showed low bias vs. conv. (CS seg: − 4.1 ml/ − 0.9 cm/s; CS RT: − 1.1 ml/–2.0 cm/s). In the pulsatile phantom reproducibility

was 4.6/2.2% for FV/$v_{max.}$. Background phase was slightly higher in CS RT (conv./CS segm./CS RT: 1.3/1.5/2.6 cm/s). Fig. 1 shows volunteer results; Figs. 2 and 3 show flow in patients.

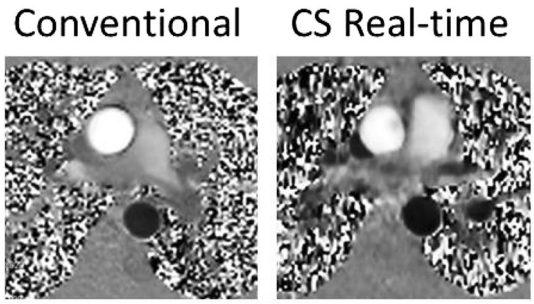

Fig.1: Systolic aortic flow measured with the conventional and the CS RT Flow protocol in a healthy volunteer.

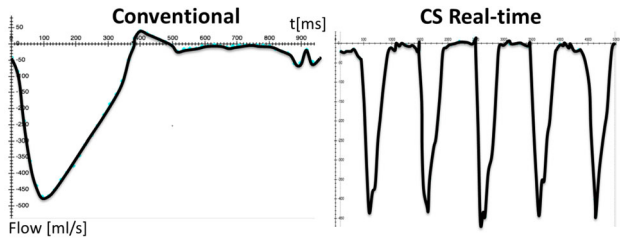

Fig.2: Flow measured with the CS RT Flow protocol in an arrhythmic patient; top left: anatomical image; top right: phase difference image of peak flow in the shortened heartbeat; bottom: flow rate measured over 5 seconds.

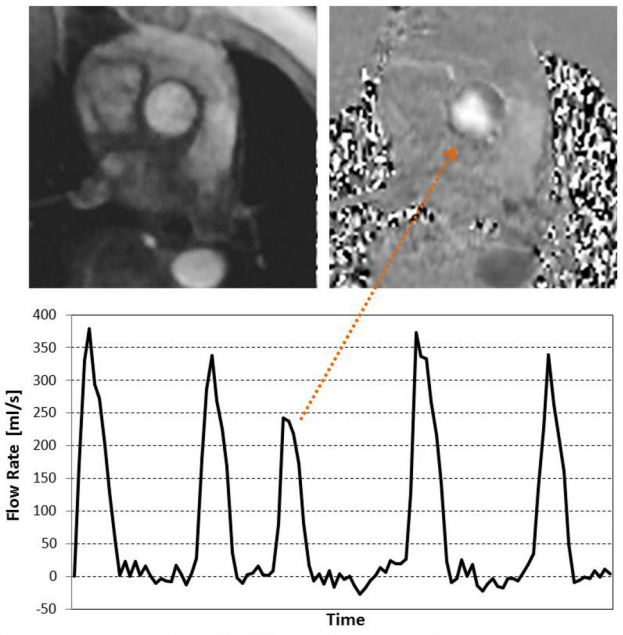

Fig.3: Flow measured with the conventional and the CS RT protocol in 73y male patient with atrial fibrillation.

Discussion/Conclusion: CS Flow enables high-resolution phase contrast flow in patients with low breath-holding capabilities and arrhythmia. Underestimation of flow in particular in the RT protocol may result from sub-optimal regularization. Evaluation tools are needed for robust segmentation and to handle data from multiple heartbeats. Further adaptation and wider clinical evaluation are needed to find the best compromise between acceleration and data quality. Due to the high integration and fast inline reconstruction the presented CS Flow can easily replace the current standard.

References:

[1] Hulet J et al., JMRI 2013, https://doi.org/10.1002/jmri.24160.
[2] Kim D et al., MRM 67, pp. 1054–1064 (2011).
[3] Schmidt M et al., J CMR 2013. 15(Suppl. 1):P36.
[4] Liu J et al., #4249 Proc. ISMRM 20 (2012).
[5] Lin H et al., MRM 68(3) pp. 703–710 (2012).

L06.18

Efficient sparse image reconstruction using $l_{1/2}$-regularization for cardiac MRI

T. Khan[1], O. Inam[2], Z. Abid[2], H. Omer[2], M. Qureshi[2]
[1]*Bahria University, Computer Engineering, Islamabad, Pakistan,* [2]*COMSATS University Islamabad, Electrical & Computer Engineering, Islamabad, Pakistan*

Purpose/Introduction: Compressed Sensing (CS) [1] is used in MRI for accelerating the imaging speed by highly under-sampling the acquired data. Sparsity in CS is used for finding a unique solution to the ill-conditioned problem of equations, caused by the compressive under-sampling of data. In the recent past, various approaches have been proposed for sparsity minimization using different $l_p (0 \leq p \leq 1)$ norms. In this paper, $l_{1/2}$-regularization based CS reconstruction algorithm for MR images is proposed.

Subjects and Methods: An $l_{1/2}$-regularization for tangent-vector-based gradient (TVBG) algorithm [2] is proposed for finding a unique solution for the sparsity constrained optimization problem. The acquired images are represented in wavelet domain using Daubechies wavelet transform for promoting sparsity and $l_{1/2}$-norm is used in TVBG algorithm to reconstruct the highly under-sampled MR images. The proposed method is tested using (i)1-D sparse signal (ii) 30-channel cardiac array coil data (Cartesian) acquired using 3.0T scanner with the parameters: matrix size = 256 × 135, FOV = 300 mm^2, slice thickness = 5 mm, flip angle = 44°, TR/TE = 2.97/1.6, Total acquisition time = 14 s. PSNR and root mean square error (RMSE) are used to estimate the quality of the reconstructed images.

Results: The images reconstructed using the proposed method ($l_{1/2}$ -regularization for TVBG) are compared with the l_1-regularization based CS reconstruction [1]. Figure 1a compares the effect of using different step sizes on the proposed method and the conventional (l_1-regularization based CS) reconstruction. The results show that $l_{1/2}$-regularization converges earlier while minimizing the error. RMSE and PSNR values for the images reconstructed with AF = 2 and 4, plotted in Fig. 1b, also show that the proposed algorithm provides a better estimation of the sparse signal and improves the reconstruction quality by 19% in terms of RMSE and 14% in terms of PSNR. Figure 2 provides a visual comparison of the fully sampled reference images that is images reconstructed using the proposed method and

the conventional method. This comparison also shows that the proposed method results in better image reconstruction quality as compared to the conventional l_1-regularization technique.

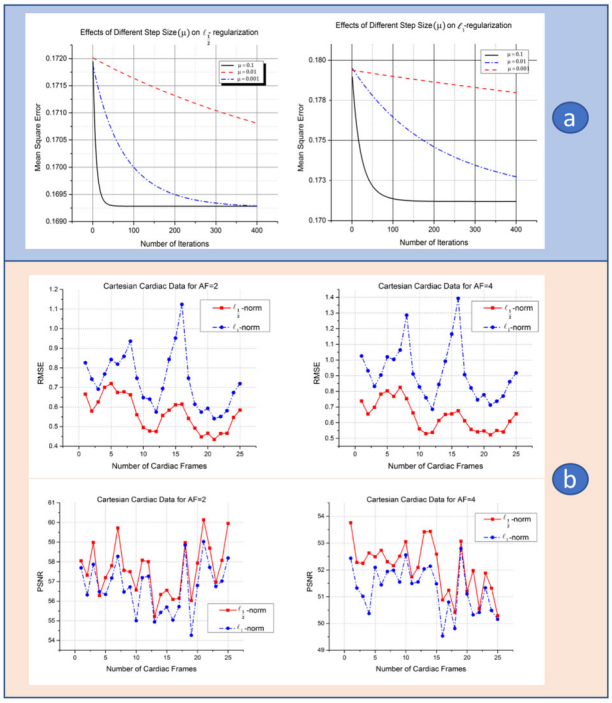

Figure 1. (a) The effect of step sizes on l_(1/2)- regularization and l_1-regularization. (b) Plot of RMSE and PSNR for difference acceleration factors (i.e. 2 and 4)

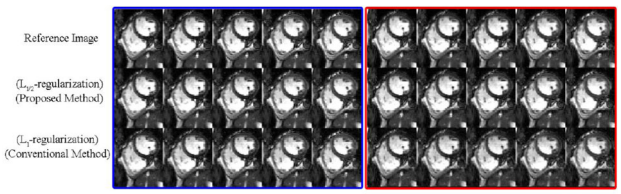

Figur 2. Reconstruction results of the first five frames from cardiac dataset with acceleration factors of 2 and 4

Discussion/Conclusion: $l_{1/2}$-regularization, used as a thresholding technique for TVBG algorithm is proposed for solving the sparsity-based optimization problem. The results show that the proposed algorithm successfully reconstructs images from sparse signals, converges better and low RMSE values indicate that $l_{1/2}$-regularization is a promising technique for successful reconstruction of MR images as compared to the conventional CS based regularization algorithm.

References:

[1] M. Lustig, D. Donoho, and J.M. Pauly, *Sparse MRI:The Application of Compressed Sensing for Rapid MR Imaging*, MRM, 58(2007), 1182–95

[2] S.C. Douglas, S.I. Amari, S.Y. Kung, IEEE Trans. Signal Process. 48(6), 1843–1847 (2000)

L06.19

Feasibility of compressed sensing reconstruction for glutamate and myo-inositol detection using optimized TE-averaged PRESS spectral editing technique in human brain at 3T

G. H. Hatay[1], A. Dincer[2], E. Ozturk-Isik[1]

[1]*Bogazici University, Institute of Biomedical Engineering, Istanbul, Turkey,* [2]*Acibadem Mehmet Ali Aydinlar University, Department of Radiology, Istanbul, Turkey*

Purpose/Introduction: MR spectral editing techniques, such as 2D J-resolved point resolved spectroscopy (PRESS) [1] and TE-averaged PRESS [2], are used to separately quantify glutamate (Glu), glutamine (Gln) and myo-Inositol (mI) metabolite peaks. However, TE-averaged PRESS technique requires a long scan time that is proportional to the number of TE's. Optimized TE-averaged PRESS technique has been proposed for scan time reduction [3]. This study aims to investigate the feasibility of compressed sensing (CS) technique [4] for further scan time reduction of optimized TE-averaged PRESS in human brain at 3T.

Subjects and Methods: ^{1}H-MRSI of eight healthy volunteers were acquired at 3T Siemens Prisma scanner using four different TEs that were determined by using Monte Carlo simulations [3] (TR = 2000 ms, TE = 35, 37, 40, 42 ms, 1200 Hz, 1024points, FOV = 120 × 120 mm, NSA = 1, 16 × 16 array, total scan time = 20 min). The raw ^{1}H-MR spectral data of each TE was exported offline, and undersampled with a pseudorandom pattern. After compressed sensing reconstruction [5], data acquired at four TEs were averaged to create TE-averaged PRESS spectra.

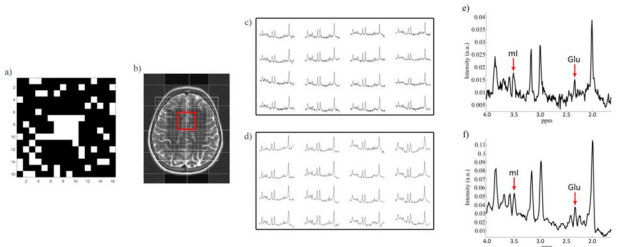

Undersampling pattern (R=4) (a), T2-weighted MR image of a healthy volunteer (b), and full (c) and CS accelerated (d) 35 ms PRESS data at the voxels within red box. Full (e) and accelerated (f) TE-averaged PRESS spectra.

The area under the peak was estimated for choline (Cho, 3.2 ppm), creatine (Cr, 3 ppm), Glu (2.35 ppm), Gln (2.43 ppm), mI (3.52 ppm) and N-acetyl aspartate (NAA, 2 ppm) using MATLAB (MathWorks Inc., Natick, MA). Metabolite peak intensities were then normalized by the Cr intensity of the same voxel. A Bland–Altman statistical test was used to detect if there were any bias between the full and compressed sensing accelerated TE-averaged PRESS data of healthy volunteers.

Results: Glu and mI metabolites were clearly separated in both full and CS accelerated data. Gln/Cr, mI/Cr and Cho/Cr ratios of full and accelerated TE-averaged PRESS data were similar ().

	Glu/Cr	Gln/Cr	mI/Cr	NAA/Cr	Cho/Cr
F	0.52±0.03	0.16±0.05	0.94±0.09	2.06±0.05	0.86±0.04
CS	0.48±0.03	0.18±0.07	0.95±0.12	1.94±0.06	0.86±0.04

Mean (±std) metabolite to Cr ratios for the full and compressed sensing accelerated TE-averaged PRESS data of eight healthy volunteers.

Lower Glu/Cr and NAA/Cr ratios were observed in CS accelerated

data than full data. According to the Bland–Altman test results, mean difference was close to zero for all metabolite ratios ().

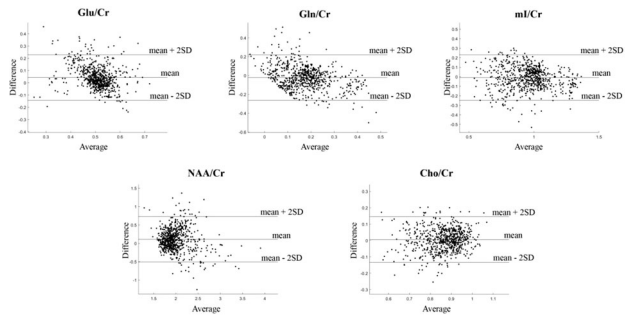

Bland Altman test results for the differences of metabolite peak ratios of all the healthy volunteers estimated from the full and CS accelerated TE-averaged PRESS data.

Although there were a few outliers in metabolite ratios, the standard deviation of the difference was small in all metabolite ratios. The largest number of outliers were observed in NAA/Cr (47/800 voxels).

Discussion/Conclusion: The results of this study showed that compressed sensing accelerated optimized TE-averaged PRESS spectral editing technique could be used for quantification of Glu, Gln and mI metabolites in human brain at 3T. In future studies, regularization parameters of compressed sensing reconstruction will be optimized and its pulse sequence will be implemented.

Acknowledgement

This study was supported by Bogazici University BAP grants 10844SUP and 13260D, and the Turkish Directorate of Strategy and Budget under the TAM Project number DPT2007K120610.

References:

[1] Ryner et al. MRI, 1995.13(6):p.853–69.
[2] Hurd et al. MRM, 2004.51(3):p.435–40.
[3] Hatay et al. Conf Proc ISMRM, 2018. Paris, France.
[4] Lustig et al. MRM, 2007.58(6):p.1182–95.
[5] Hatay et al. MBEC, 2017.55(8):p.1303–15.

L06.20
MAP reconstruction in single inversion dual slice acquisition

J. Bibiano, A. Slawig, T. Wech, H. Köstler
University Hospital Würzburg, Department of Diagnostic and Interventional Radiology, Würzburg, Germany

Purpose/Introduction: Inversion recovery sequences are frequently used for quantification of the longitudinal relaxation times. Conventionally, such measurements require multiple repetitions using different TI. To overcome the increase in the scan time, a model-based reconstruction (MAP) was proposed [1]. The aim of this work is to further improve the acquisition by using a simultaneous dual slice acquisition and spiral readout gradients.

Subjects and Methods: An IR prepared spoiled gradient echo sequence with spiral readouts was developed. A dual-band pulse was used to excite two slices simultaneously. The RF-phase difference between two slices was alternated between 0° and 180°. The trajectories followed a TWIRL (twisting of the radial trajectory [2]) approach with a double golden angle increment between consectuive spiral arms. Additionaly, it was corrected using a gradient system transfer function (GSTF) based pre-emphasis [3]. The sequence was tested in a healthy volunteer at 3T (Magnetom Prisma, Siemens Healthineers, Germany). The acquisition parameters were: 1280 spiral arms, each with 512 read out points, TE: 1.7 ms, TR: 3.3 ms, flip angle: 10°, slice thickness: 6 mm, resolution: 1.2 × 1.2 mm. The entire IR-prepared dataset was binned into packs of 8 consecutive spiral arms each and was reconstructed using MAP. For this purpose, the algorithm was adjusted such that phase pattern of the dual slice acquisition was considered in each iteration.

Results: Figure 1 depicts the undersmapled in vivo images of both slices after reconstruction combining the spiral arms into packs groups of 8. Figure 2 shows in vivo images after the fith MAP iteration. Images are shown at TI = 407, 803, 3971 ms after the inversion.

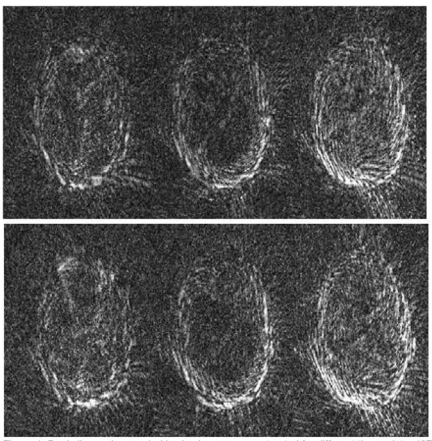

Figure 1: Dual slice undersampled in vivo images reconstructed for different time points, 407 ms, 803 ms, 3971 ms after the inversion for slice 1 (upper row) and slice 2 (bottom row).

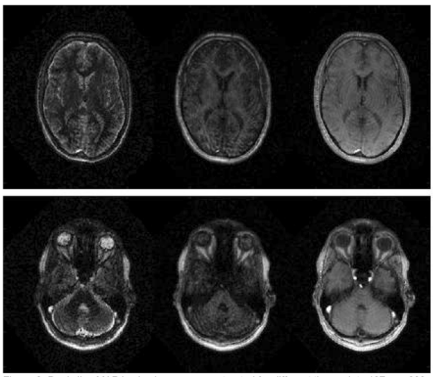

Figure 2: Dual slice MAP in vivo images reconstructed for different time points 407 ms, 803 ms, 3971 ms after the inversion for slice 1 (upper row) and slice 2 (bottom row).

Discussion/Conclusion: The study demonstrated that it is possible to perform a MAP reconstruction on dual slice acquisitions using a spiral trajectory. The reconstruction provides a time series of images showing the relaxation process in both slices.

References:

[1] Tran-Gia, J. et. al. Model-Based Acceleration of Parameter Mapping (MAP) for Saturation Prepared Radially Acquired Data. MRM 2013; 70: 1524–1534.

[2] Jackson, J. I. et. al. Twisting radial lines with application to robust magnetic resonance imaging of irregular flow. MRM. 1992; 25(1):128–139.
[3] Stich, M. et. al. Gradient waveform pre-emphasis based on the gradient system transfer function. MRM, 2018; 80:1521–1532.

L06.21

Performance of PEAR reconstruction of fMRI data using Cartesian Poisson under-sampling schemes

M. Pinto, P. Figueiredo, **R. G. Nunes**
Instituto Superior Técnico - Universidade de Lisboa, ISR-Lisboa/ LARSyS and Department of Bioengineering, Lisbon, Portugal

Purpose/Introduction: Accelerating fMRI acquisitions by under-sampling the k-t space can improve temporal resolution. By taking advantage of prior information regarding the fMRI signal within the compressed sensing framework[1, 2], the PEAR algorithm is capable of reconstructing under-sampled data. We evaluated the performance of PEAR when using Cartesian-Poisson distribution schemes and varying acceleration factors.

Subjects and Methods: Synthetic fMRI datasets were generated using as baseline a real 2D EPI image of the brain, by adding 10 time series representing activation regions (ARs) with an "L" shape (see Fig. 1): a sinusoid, S1; a 2 sinusoids combination, S2; an aperiodic signal, A; and an aperiodic-sinusoid combination, A + S1.

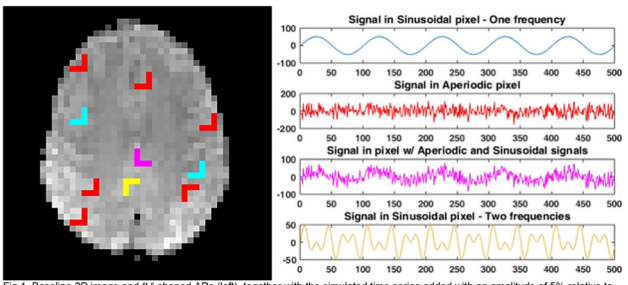

Fig.1. Baseline 2D image and "L" shaped ARs (left), together with the simulated time series added with an amplitude of 5% relative to the average baseline signal in grey matter (right).

A Cartesian-Poisson distribution scheme was then considered to perform the k-space under-sampling along the phase-encoding direction and the sampling mask was randomly varied across 500 time points. Three target acceleration factors (R) were tested with ten synthetic datasets each: R = 3, 5 and 8. A 32-elements coil array was simulated and Gaussian noise added to achieve SNR = 25 dB. The algorithm was implemented in MatlabR2016b, using $\lambda = 0.9$ (selected based on tests with different SNRs) and r = 5 (selected to match the rank of the simulated data) as regularization parameters[1]. To detect activations in the reconstructed fMRI data, a general linear model (GLM) was fitted to the data, F-tests were applied to the relevant contrasts of parameter estimates and converted to Z-scores, subsequently thresholded with $Z > 4$ (using FEAT, fsl.fmrib.ox.ac.uk, see Fig. 3). To assess its sensitivity and specificity, the true positive rate (TPR) and false positive rate (FPR) were calculated (see Fig. 2).

Results: High sensitivity (TPR $\sim$ 100%) was obtained for all types of temporal variation patterns and acceleration factors considered, with only R = 8 performing worse for the case of the combination of sinusoids (TPR $\sim$ 80%). Specificity was generally high for the periodic signals (FPR $< 2\%$), but it deteriorated for the aperiodic signals (FPR $\sim$ 40% for R = 3 and FPR $\sim$ 20% for R = 5 and 8)—Fig. 2.

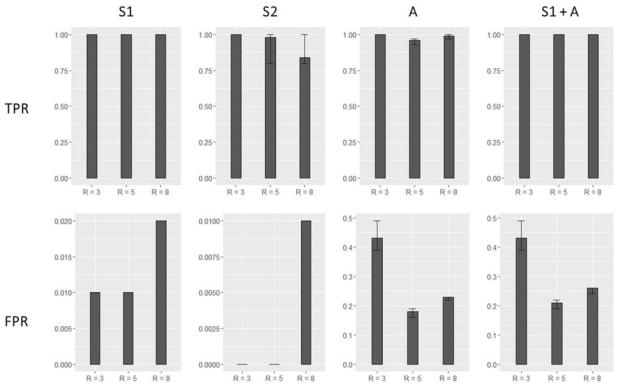

Fig.2. Activation detection results for each temporal variation pattern considered (S1, S2, A, S1+A), using acceleration factors R=3, 5, and 8: average TPR (top), FPR (bottom) and standard deviation (error bars) across the 10 repetitions.

A more modest performance for aperiodic signals was also observed in the original report proposing PEAR[1]. The poorer results obtained in our study for aperiodic signal can probably be explained by a sub-optimal selection of regularization parameters, which hindered the distinction between aperiodic signals and noise—Fig. 3.

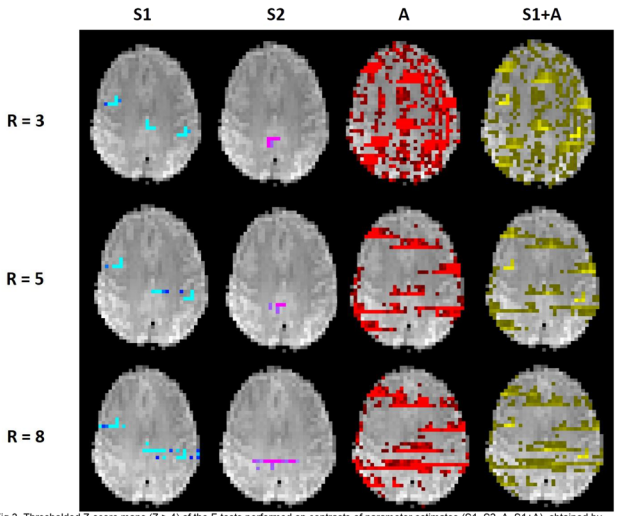

Fig.3. Thresholded Z-score maps (Z > 4) of the F-tests performed on contrasts of parameter estimates (S1, S2, A, S1+A), obtained by GLM analysis of the reconstructed data using acceleration factors R=3, 5, and 8.

Discussion/Conclusion: Our results indicate that using Cartesian under-sampling schemes up to an acceleration factor R = 8 allows sensitive detection of fMRI activation but with considerable false positives in the case of aperiodic signals—Fig. 3. Further optimization is needed before the algorithm can be successfully applied to ultrafast fMRI acquisitions using Cartesian sampling.

References:

1. Weizman L, et al. Med Phys. 2017; 44(12):6166–6182.
2. Chiew M, et al. Magn Reson Med. 2015; 74(2):353–64.

L06.22

Reconstruction of all offresonance states in DYPR bSSFP using an elliptical signal model

A. Slawig, T. Wech, H. Köstler
University Hospital Würzburg, Department of Diagnostic and Interventional Radiology, Würzburg, Germany

Purpose/Introduction: An elliptical signal model was proposed to describe the signal behavior of the bSSFP signal with changing offresonance(1). The model can be fitted to data from phase-cycled bSSFP acquisitions and was so far utilized for the reconstruction of banding free images (2), estimating underlying tissue parameters(3) and to create artificial contrasts based on these parameters(4). All procedures are based on the acquisition of multiple phase-cycled measurements, which significantly increases scan time. As shown before a frequency-modulated acquisition can acquire the same information in a single measurement(5) and a multifrequency reconstruction enables banding free images with high SNR from such data(6). Here, the elliptical signal model is employed to reconstruct multiple offresonance images from one single frequency-modulated acquisition.

Subjects and Methods: A frequency-modulated bSSFP measurement of the lower leg in a healthy volunteer was performed at a 1.5T MR system (MAGNETOM Aera, Siemens Healthcare) using a radial golden-angle trajectory.

One 2D slice was acquired using the following sequence parameters: slice thickness: 8 mm, flipangle: 40°, resolution: 0.6×0.6 mm^2, radial spokes:1000. A long TR value of 13.8 ms as well as a linear offset in the shim enforced banding artifacts. Initially undersampled images were reconstructed using GROG resulting in a stack of 100 images representing different offresonances. The elliptical signal model was used in a MAP-like algorithm(7) to iteratively reconstruct fully sampled images of all offresonance states. Resulting images can then be combined using standard combination techniques like sum of squares or maximum intensity projection.

Results: Initially reconstructed images show strong undersampling artefacts and no anatomical details are discernable. Examples for two different offresonances are shown in Fig 1a.

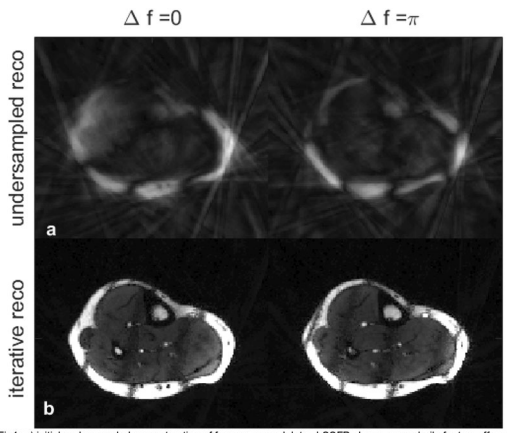

Fig1: a) initial undersampled reconstruction of frequency-modulates bSSFP shown exemplarily for two offresonances, b)images after iterative reconstruction using the elliptical signal model in a MAP approach

In the results after 20 iterations of the reconstruction algorithm no undersampling artefacts remain and a good anatomical representation is given (examples in Fig 1b). The combination of the 100 reconstructed images can then reliably remove all banding artifacts (Fig 2).

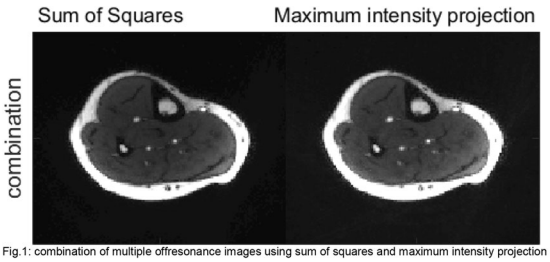

Fig.1: combination of multiple offresonance images using sum of squares and maximum intensity projection reconstruction

Discussion/Conclusion: Frequency-modulation allows the acquisition of the bSSFP signal over a wide range of offresonances in one single measurement. Here, the elliptical signal model was successfully applied to the reconstruction of images representing multiple offresonance states as well as banding free images. Limitations arise, as the frequency modulation needs to be limited to small steps to retain high signal and the validity of the signal model. The proposed technique is therefore especially suited to high resolution or 3D acquisitions.

References:

1. Xiang et al. MRM2014; 71:927–933
2. Hoff et al. MRM2017; 77:644–654
3. Shcherbakova et al.MRM2018; 79:711–722
4. Hilbert et al. MRM2018; 79:1901–1910
5. Benkert et al. MRM2015; 73:182–194
6. Slawig et al. MRM2017; 78:2226–2235
7. Tran-Gia et al. MRM2013; 70:1524–1534

L06.23

Evaluating compressed SENSE acceleration for quantitative mapping of longitudinal relaxation rate R1

R. Berg[1], S. Kaczmarz[1], T. Leutritz[2], C. Preibisch[1]
[1]*Technical University of Munich, Klinikum rechts der Isar, Department of Neuroradiology, Faculty of Medicine, Munich, Germany,* [2]*Max Planck Institute for Human Cognitive and Brain Sciences, Department of Neurophysics, Leipzig, Germany*

Purpose/Introduction: Absolute measurements of the longitudinal relaxation rate R1 (= 1/T1) potentially have a high value for diagnostic applications because, in contrast to conventional magnetic resonance imaging (MRI), they allow to grasp disease related systemic changes. Moreover, measured values are assumed to be sequence and hardware independent[1, 2].

When using R1 mapping with the variable flip angle approach, the protocol duration increases compared to conventional T1-weighted (T1w) MRI. Acceleration techniques such as Compressed SENSE[3] (CS) can be used to speed up acquisition but might compromise precision. Therefore, the aim of our study was to investigate the effect of CS acceleration on the fidelity of R1 mapping.

Subjects and Methods: Five healthy subjects were scanned on a Philips 3T Ingenia Elition. The MRI protocol consisted of B1 mapping and two T1w sequences with different flip angles. Measurements

were performed with either standard SENSE (S = 2.5, scan time: 11 min) or two different compressed SENSE acceleration factors CS = 4 (9.5 min) and CS = 6 (6 min). R1 maps were computed using the in vivo histology toolbox[4, 5], correcting for B1-inhomogeneities and insufficient RF spoiling[1, 2]. Gray matter (GM) and white matter (WM) segments were obtained using SPM12[6]. R1 maps with different accelerations were compared visually and quantitatively by extracting R1 values and their variances from GM and WM volumes-of-interest (VOI)s.

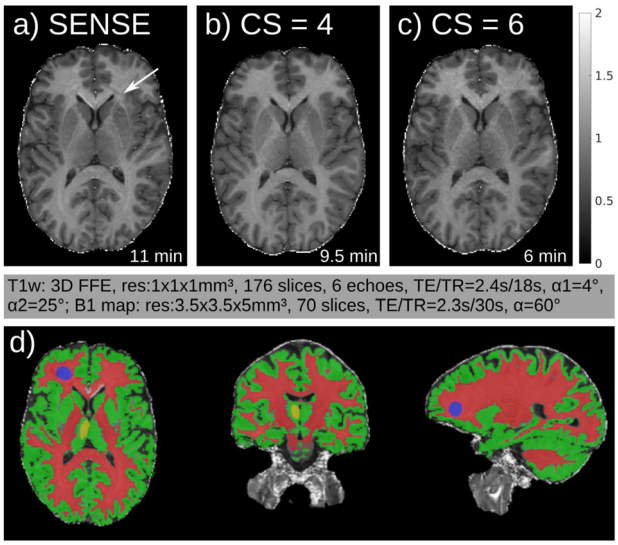

Fig1: Exemplary data of a single subject. R1 maps for different imaging accelerations: a) SENSE and CS with factor b) CS=4 and c) CS=6. d) Exemplary segmented GM (green), WM (red) and manually selected VOIs in GM (Thalamus, yellow) and WM (purple).

Results: Visually, R1 maps obtained with different accelerations are very similar (Fig. 1). Slight artifacts from standard SENSE reconstruction (arrow Fig. 1a) were eliminated by CS (Fig. 1b, c). Subject average R1 values in GM, WM, and manually defined VOIs (Fig. 1d) agree well between the three scan protocols (Fig. 2). The largest variance of R1 values across subjects is found with SENSE, while CS reduces R_1 value variations across subjects (Fig. 2). Both CS protocols show comparable results. Overall, the standard deviation of R1 values is very similar across accelerations (Fig. 3).

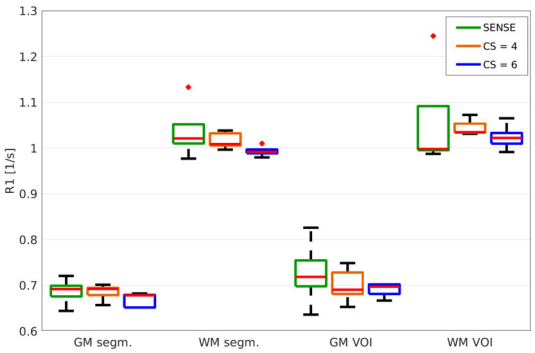

Fig2:Comparison of subject average quantitative R1 values. R1 values within automatically segmented and manually selected VOIs in GM and WM show similar results for different accelerations (SENSE vs. CS). Error bars indicate variance across subjects

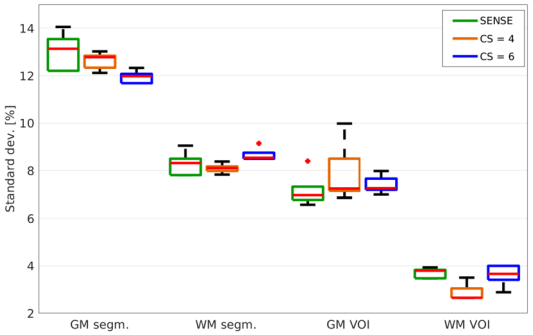

Fig3: Subject average standard deviations of R1. Standard deviations across automatically segmented and manually selected VOIs in GM and WM show similar results for different accelerations (SENSE vs. CS). Error bars indicate variance across subjects.

Discussion/Conclusion: Our comparison of R1 mapping protocols with different accelerations reveals R1 maps with comparable quality. Quantitative R1 values depend neither on acceleration technique (SENSE vs. CS) nor factor (CS = 4 vs. CS = 6) and agree well with the literature[1, 7–8]. Our results suggest that compressed SENSE, with acceleration factors up to at least 6, can be used for quantitative R1 mapping without loss of fidelity. These findings are in good accordance with studies investigating the impact of CS acceleration on other imaging sequences[9–11].

To conclude, CS is highly promising to establish quantitative R1 mapping within clinically feasible scan times.

References:

1. Preibisch 2009 MRM
2. Baudrexel 2018 MRM
3. Geerts-Ossevoort 2018 Philips
4. Tabelow 2019 Neuroimage
5. Weiskopf 2015 CurrOpinNeurol
6. www.fil.ion.ucl.ac.uk/spm
7. Weiskopf 2013 FrontNeurosci
8. Wright 2008 MAGMA
9. Vranic 2019 AJNR
10. Eichinger 2019 InvestRadiol
11. Nam 2019 KoreanJRadiol

L06.24

FPGA based SENSE coprocessor for high speed cardiac MR image reconstruction

A. Basit[1], **O. Inam**[2], M. Qureshi[3], H. Omer[3]
[1]*Khwaja Fareed University of Engineering and Information Technology, Computer Engineering, Rahim Yar Khan, Pakistan,* [2]*Comsats University Islamabad, Electrical and Computer Engineering, Islamabad, Pakistan,* [3]*Comsats University Islamabad, Electrical and Computer Engineering, islamabad, Pakistan*

Purpose/Introduction: Field-Programmable-Gate-Arrays (FPGAs) have recently emerged as a viable solution to meet the rising demands of fast data processing in MRI using pMRI techniques e.g. SENSE [1]. This paper presents a 32Bit floating point FPGA-based coprocessor design for SENSE reconstruction optimized for efficient cardiac MR image reconstruction. The proposed coprocessor employs Conjugate Gradient for Least Squares (CGLS) method to efficiently solve the complex matrix inversions in SENSE for unfolding the multi-channel aliased signals.

Subjects and Methods: FPGA-based architecture of SENSE reconstruction has been implemented on Zynq development board of Xilinx-FPGA family using advanced high-level synthesis tool named as vivado-HLS [2]. The design flow of vivado-HLS, reduces the

design efforts by many folds as compared to the Register Transfer Logic (RTL) level design. The proposed FPGA based coprocessor for SENSE reconstruction is features the use of CGLS to perform complex matrix inversions for unfolding multi-channel aliased images. HLS directives are used to achieve optimizations (e.g. pipelining and loop unrolling) in the proposed design. Also, the coprocessor works in coordination with the ARM processor, where arbitration logic is controlled by the ARM processor and application specific processing (i.e. SENSE reconstruction) is performed by the coprocessor (Fig. 1). Moreover, the proposed design is featured with Direct Memory Access Controller (DMAC) to expediate the memory transactions required to perform SENSE reconstruction. The performance of the FPGA-based coprocessor is evaluated on 11 frames of cardiac MRI data set acquired using 3.0T Siemens Skyra scanner (Table 1).

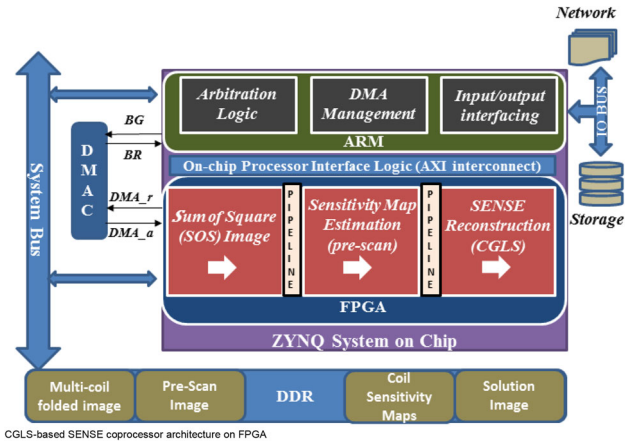

CGLS-based SENSE coprocessor architecture on FPGA

Data Acquisition details	
Scanner	3.0 *T* Siemens
No of receiver coils	30
Matrix Size	512 *x* 252
FOV	$300mm^2$
TR	$2ms$
TE	$0.8ms$
Slice thickness	$8mm$
Flip angle	50^0

Summary of Data Acquisition details for cardiac MRI dataset

Results: For a performance comparison between the proposed design, single-core CPU and multi-core CPU based SENSE reconstruction, the computation time and reconstruction accuracy of the MR images are evaluated for acceleration factor (Af) 2 (Fig. 2). The results show that the combination of HLS design, debug, and analysis environment leverages optimizations in the proposed design, thereby resulting in 8x to 14x speed-up in the reconstruction time in our experiments without compromising the image reconstruction accuracy.

(a)

Features	CPU	FPGA
Model	DellOptiPlex7050	Xilinix Zynq UltraScale ZCU102
Cores	4	4
Clock Speed	3.6GHz	1GHz
Memory (On-Chip)	8MB	4MB (Block RAM + 64KB cache)

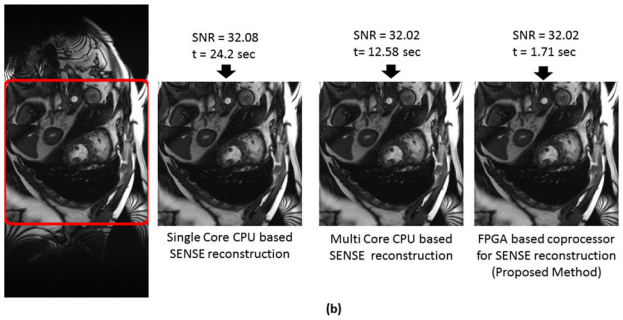

(b)

Quantitative and Qualitative comparisons of the reconstructed images using the proposed architecture and CPU based SENSE reconstruction for A_f= 2; (a) Hardware Specification (b) Reconstruction results of 30 channel (frame No.1) cardiac data set

Discussion/Conclusion: A novel FPGA-based 32Bit floating point coprocessor for SENSE reconstruction is proposed. The proposed coprocessor has been optimized using HLS framework for high speed cardiac MR image reconstruction without degrading the reconstruction accuracy.

References:

[1] Siddiqui et al.," Magnetic resonance imaging 44 (2017): 82–91.
[2] Winterstein et al.," International Conference on Field-Programmable Technology (2013): 362–365.

L06.25
Optimized CG-SENSE using GROG for radial MRI

I. Aslam[1], K. Afsar[2], F. Najeeb[2], I. Ullah[2], H. Omer[2]
[1]*Hospital University of Geneva, Department of Radiology and Medical Informatics, Geneva, Switzerland,* [2]*COMSATS University Islamabad, Electrical and Computer Engineering, Islamabad, Pakistan*

Purpose/Introduction: Conjugate Gradient SENSE (CG-SENSE)[1] is a leading scheme used to recover the unaliased images from undersampled *k*-space data. In literature, a combination of GRAPPA Operator Gridding (GROG) with NUFFT based CG-SENSE[2] has been proposed to recover the artefact free images from the accelerated radially encoded data. However, it requires gridding and de-gridding of the *k*-space repeatedly between iterations, thereby significantly increasing the computational cost.

This paper proposes an optimized implementation of CG-SENSE using GROG, which performs gridding operation only once in the whole set of iterations to recover the un-aliased MR images. Experiments on human head data confirms that the proposed scheme offers better results (e.g. 64%, 37%, 5% improvement in AP, RMSE, PSNR respectively and 4x speed up in reconstruction time at AF = 4) than the conventional method[2].

Subjects and Methods: GROG[3] is a method which transfers the radially encoded data onto a Cartesian grid and leaves some vacant points in the gridded *k*-space.

In recent past, GROG based CG-SENSE[2] has been proposed that requires forward and reverse gridding of the *k*-space data in each iteration, where gridding has been performed using GROG[3] while de-gridding has been done using NUFFT[4] approach.

This paper proposes an optimized CG-SENSE with GROG to find the un-aliased image from under-sampled radial *k*-space data iteratively without to perform gridding and de-gridding operations in each iteration. Figure 1 shows a schematic illustration of the proposed scheme.

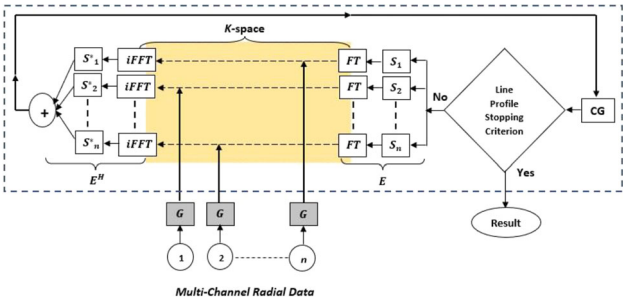

Figure 1: A schematic depiction of 'optimized CG-SENSE using GROG' (proposed method).

In this work, a correlation value (i.e. 0.9995 empirically selected) among the three different central lines is used as stopping criteria[5].
Results: The proposed scheme is verified on 1.5T human head data (GE scanner, St. Mary's Hospital, London), with dimensions 256 × 256 × 8. Initially, the Cartesian human head data is converted into the fully sampled radially encoded data using the following formula: (π/2) × FOV.
Figure 2 displays 'Optimized CG-SENSE using GROG' (proposed method) and conventional GROG with CG-SENSE[2] reconstruction results at AF = 4, 6 & 9.

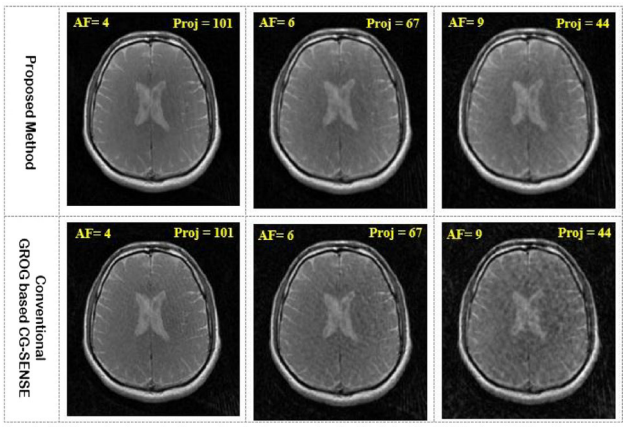

Figure 2: 1.5T Human head reconstruction results using the proposed method (Optimized CG-SENSE using GROG) and the previously suggested 'GROG based CG-SENSE' at acceleration factors 4, 6, and 9 with 101, 67 and 44 radial projections respectively.

Table 1 presents the results w.r.t RMSE, AP, PSNR and reconstruction time. The results show that the proposed scheme gives better outcomes in terms of quantifying parameters (i.e. 64% improvement AP, 37% improvement in RMSE, 5% improvement in PSNR and 4x speed up in reconstruction time at AF = 4) than conventional GROG based CG-SENSE[2].

	Optimized CG-SENSE using GROG (Proposed Algorithm)					Conventional GROG based CG-SENSE				
Acceleration Factor	Iteration	AP	RMSE	PSNR (dB)	Recon. Time (sec)	Iteration	AP	RMSE	PSNR (dB)	Recon. Time (sec)
AF = 4	4	0.006	0.0199	82.167	2.559	5	0.0166	0.0317	78.135	10.996
AF = 6	3	0.0156	0.0308	78.395	1.968	5	0.0265	0.0401	76.102	8.470
AF = 9	4	0.0311	0.0435	75.403	2.531	7	0.0600	0.0603	72.557	9.713

Table 1: Reconstruction results of 1.5T human head data using the proposed method and GROG based CG-SENSE in terms of number of iterations, AP, RMSE, PSNR(dB) and reconstruction time.

Discussion/Conclusion: This work presents a novel method 'Optimized CG-SENSE using GROG' to get the final MR image. Results show that the proposed scheme gives good reconstruction results at a low computational cost as gridding operation is performed only once.
References:
1. K. P. Pruessmann et al. *MRM 2001*. 638–651
2. I. Aslam et al. *ESMRMB* 2017. 136
3. N. Seiberlich et al, *MRM 2008*. 930–935
4. J. A. Fessler et al. IEEE 2003. 560–574
5. M. Khan et al. APMR 2007. 227–240

L06.26

In vivo quantitative detection of tumour associated macrophages (TAM) in mice melanoma models, by relaxation measurements (T_1) at low magnetic fields with Ferumoxytol

S. Geninatti Crich, M. R. Ruggiero, S. Baroni, S. Rapisarda, S. Aime
University of Torino, Torino, Italy

Purpose/Introduction: Tumour associated macrophages (TAM) are forced by cancer cells to adopt an anti-inflammatory phenotype and secrete factors to promote angiogenesis and tumor invasion. For these reasons, sensitive, non invasive, methods to obtain a quantitative TAM detection are needed for tumour classification and individual patient stratification to stronger or targeted therapies. To this purpose, the use of Ultra Small Iron Oxides nanoparticles (NPs) has been already proposed as they are taken up by TAM generating a detectable contrast in T_2 weighted images. However, the main drawback of this approach relies on the fact that the observed contrast is not dependent on the effective intracellular localization of the NPs with the possibility of a number of false positives. Thereafter, new methods are needed not only for TAM detection and, in general, for a number of "cell tracking" applications. Herein we tested the T_1 measurements at low field (0.01–1 MHz) to assess the localization of ferumoxytol (FE) (clinical approved NPs) in TAM in melanoma tumours.
Subjects and Methods: NMRD profiles were acquired on a Fast Field Cycling relaxometer (Stelar) implemented with a 40 mm widebore magnet and a 11 mm solenoid detection coil placed around the anatomical region of interest[1] (Fig. 1). The tumour xenografts were prepared by injecting melanoma cells in the hindlimb muscle. FE was injected at a 0.5 mmol/kg dose of Fe. R_1 measurements were carried out before, 3 and 24 h after the injection.
Results: R_1 measured at low fields of FE labelled macrophages (J774) differs markedly from the one obtained from ferumoxytol particles suspended in aqueous solution. Likely, this is the consequence of a substantial relaxivity "quenching" when the magnetic particles are compartmentalized in intracellular vesicles such as endosomes or lysosomes. On the basis of these observations, the $1/T_1$ low field profiles of melanoma tumours implanted in mice were acquired in vivo. This tumour is characterized by a high amount of macrophages infiltrating the stroma. T_1 measured (0.01–1 MHz) 3 h and 24 h after the injection were significantly different (Fig. 2). At 24 h they displayed an increasing behavior similar to one found for FE labelled J774 macrophages whereas at 3 h, when the FE distribution is extracellular, the R_1 behavior is opposite. This finding clearly indicated the intracellular localization of ferumoxytol as confirmed by histological analysis (Pearls).
Discussion/Conclusion: A new sensitive imaging method capable of a quantitative TAM detection is herein proposed. R_1 at low magnetic fields appear highly dependent on the intra or extra cellular localization of the NPs thus allowing an unambiguous TAM quantification.

This information could be hardly achievable from the measurements at single magnetic field and open new horizons for the field of cell tracking applications using FFC-MRI.

References:

1. Ruggiero et al. Angew Chem.2018, 57:7468.

L06.27

Solution pH affects the sodium triple-quantum signal of bovine serum albumin

D. Kleimaier, R. Hu, L. R. Schad
Heidelberg University, Computer Assisted Clinical Medicine, Mannheim, Germany

Purpose/Introduction: Sodium triple-quantum(TQ) signal, which depends on the protein and sodium concentration, has a higher intracellular sensitivity than sodium single-quantum(SQ) signal[1–3]. The interaction of sodium ions with negatively charged e.g. carboxyl groups(COO^-) of proteins results in a TQ signal[4]. The pH of the protein solution affects the charges of the amino acid residues of proteins and therefore the negatively charged carboxyl groups[5]. Thus, we hypothesize that the TQ signal strength depends on the solution pH.

TQ and SQ signal were simultaneously measured with a spectroscopic TQ sequence(TQTPPI)[4]. The TQ FID is described by the difference of two exponential decays resulting from the slow and fast transversal relaxation time. The TQTPPI FID was nonlinearly fitted to determine the contribution of the transversal relaxation times and of the TQ amplitude to the TQ signal[4].

To test the hypothesis, we measured the TQ signal of the protein bovine serum albumin(BSA) in a pH range of[4.86 9.64] with constant protein and sodium concentration.

Subjects and Methods: Measurements were carried out on a 9.4T preclinical MRI(Bruker, Germany) with a $^{1}H/^{23}Na$ volume coil. A $T_R = 5T_1$ was used for the TQTPPI sequence (Fig. 1) by measuring T_1 with an inversion recovery. The TQTPPI FID was nonlinearly fitted to obtain the SQ and TQ amplitude(A_{SQ} and A_{TQ} respectively) as well as the transversal relaxation times. The A_{TQ} was normalized to the A_{SQ}.

A pH range of [4.86 9.64] was non-equidistantly covered by 19 phantoms consisting of 154 mM NaCl solution with 10%w/v BSA. To adjust the pH amounts of the 154 mM NaCl solution were replaced by a solution containing 154 mM NaOH or 100 mM HCl with 154 mM NaCl. This resulted in a constant protein and sodium concentration for all phantoms.

Pearson correlation coefficient(PCC) and linear fitting were used as the measurement parameters showed a linear correlation with pH.

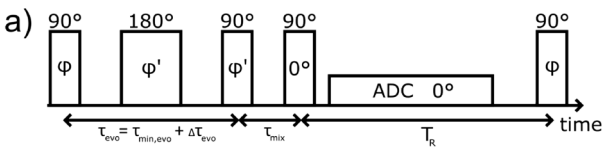

b)

Sequence	Sequence parameters
TQTPPI	$T_R = 5T_1$, 7 Repetitions, 3 Averages, 1024 points, $\Delta\tau = 25\,\mu s$, $\Delta\tau_{evo} = 200\,\mu s$, 8 phase steps, 100 phase cycles
Inversion Recovery	$T_R = 5T_1$, 3 Repetitions, 8 Averages, 1024 points, $\Delta\tau = 25\,\mu s$, 125 inversion times

Fig.1: a) The TQTPPI sequence for the simultaneous acquisition of SQ and TQ signal is shown. b) The sequence parameters for the TQTPPI sequence and the inversion recovery sequence are listed.

Results: The T_1 and T_{2S} had a linear relationship with pH up to 8.84 reaching a constant value for higher pH while T_{2F} showed a linear decrease in the pH range of[4.86 9.64] (Fig. 2):

· T_1: PCC = −1.00; linear slope: − (2.5 ± 0.2)ms.
· T_{2S}: PCC = −0.99; linear slope: − (2.9 ± 0.2)ms.
· T_{2F}: PCC = −0.99; linear slope: − (3.5 ± 0.3)ms.

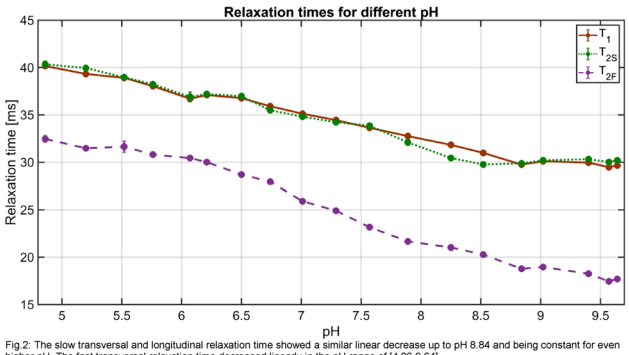

Fig.2: The slow transversal and longitudinal relaxation time showed a similar linear decrease up to pH 8.84 and being constant for even higher pH. The fast transversal relaxation time decreased linearly in the pH range of [4.86 9.64].

The A_{TQ}/A_{SQ} ratio was constant below pH6.50 and above pH8.84. Between pH[6.50 8.84] the A_{TQ}/A_{SQ} ratio increased linearly(PCC = 0.99, linear slope of(1.6 ± 0.2) %), Fig. 3.

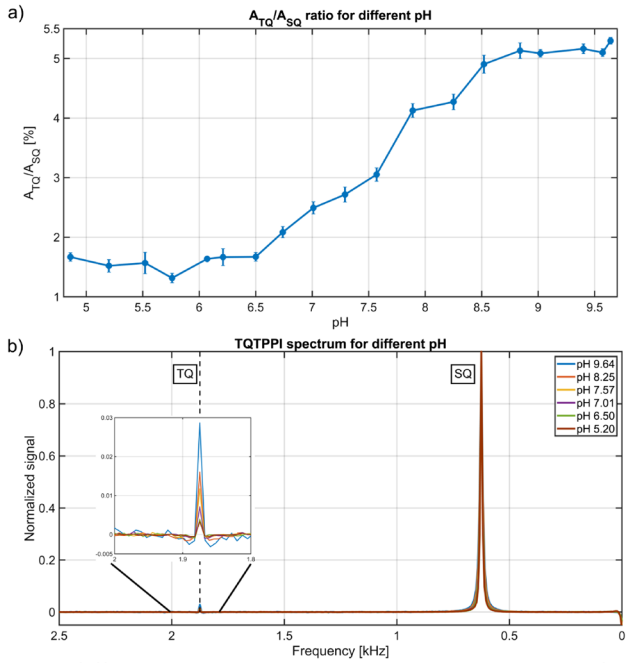

Fig.3: a)The ATQ/ASQ ratio is constant below pH6.50 and above pH8.84 while linearly increasing between pH[6.50 8.84]. b)The TQ spectral appearance changes in different pH caused by different transversal relaxation times and a different TQ amplitude

Discussion/Conclusion: A higher pH increases the total number of accessible negatively charged interaction sites for sodium ions[5]. In accordance with the measurement results a higher pH reduced the relaxation times and the A_{TQ}/A_{SQ} ratio increased substantially in the pH range of [6.50 8.84].

In conclusion, our results indicate a TQ signal dependency on pH. This additional dependence should be considered when the TQ signal is applied as an intracellular sensitive parameter.

References:

[1]FiegeMRM2013.
[2]SchepkinMRM1998.

[3]TorresMRC2005.
[4]SchepkinJMR2017.
[5]HeinrichSpringer2014.

L06.28

Longitudinal (T_1) relaxation times of 1-^{13}C glycogen at 3T and 11.7T

M. Jonuscheit, M. Rothe, F. Wickrath, D. Markgraf, M. Roden, J.-H. Hwang
Institute for Clinical Diabetology, German Diabetes Center at Heinrich Heine University, Leibniz Institute for Diabetes Research, Düsseldorf, Germany

Purpose/Introduction: Glycogen is a complex hydrated polymer of glucose and the major storage of carbohydrates in mammals. Studies on glycogen metabolism are essential to understand carbohydrate metabolism. Since ^{1}H MRS cannot resolve glycogen peaks well, ^{13}C MRS is a proper choice to detect the 1-^{13}C glycogen peak at around 100 ppm noninvasively in humans and animal models. However, due to its intrinsically low SNR of natural abundant ^{13}C MRS, optimization of pulse sequence to improve SNR is crucial for successful detection of glycogen. Since T_1 values are important in optimization of ^{13}C MRS parameters, this study was aimed to measure T_1 relaxation times of 1-^{13}C glycogen at 3T and 11.7T.

Subjects and Methods: An aqueous solution of 250 mM oyster glycogen (Sigma-Aldrich) was used for natural abundant ^{13}C MRS. Inversion recovery (IR) experiments employing 8 different IR times were conducted and each study was repeated three times. All spectra were processed with Nuts® (Acorn NMR, USA). The time series of peak integrals were fitted to a 3-parameter mono-exponential recovery function, $S = S_0\ (1 + A\ \exp(-TI/T_1))$.

Study at 3T: ^{13}C MRS was performed on a 3T Philips Achieva X-Series human scanner using a ^{13}C (7 cm i.d.) surface coil with a ^{1}H quadrature coil. A non-localized pulse-acquire scheme with an inversion recovery was used to determine T_1 (TR = 1100 ms, NSA = 800, CW proton-decoupling, excitation block pulse = 160 µs, FA = 90°, adiabatic inversion pulse = 4.173 ms, TIs = 5/22/42/66/97/141/214/550 ms). The excitation pulse power was calibrated to be approximately 90° at the center of the coil plane where a ^{13}C labeled formic acid microsphere was placed. The FWHM of the water peak was less than 20 Hz.

Study at 11.7T: Experiments were performed on an 11.7T Bruker BioSpec 117/16 USR with a cylindrical ^{13}C/^{1}H volume resonator (40 mm i.d.). A 3D ISIS sequence with an inversion recovery was used to determine T_1 (TR = 4250 ms, voxel size = 25 × 25 × 45 mm^3, NSA = 256, broadband proton-decoupling, excitation block pulse = 64 µs, FA = 90°, 180° inv. block pulse = 114.3 µs, TIs = 12/77/154/248/368/537/822/2125 ms). The FWHM of the water peak was less than 7 Hz. Temperature was monitored and adjusted by a heating pad.

Results: T_1 of 1-^{13}C glycogen was found to be 95 ± 10 ms ($R^2 > 0.962$) at 3T (21 °C, Fig. 1). At 11.7T, 513 ± 18 ms ($R^2 > 0.991$) and 507 ± 47 ms ($R^2 > 0.990$) of T_1s were assessed at 25 °C and 37 °C, respectively (Fig. 2). There was no detectible change in T_1 at 25 °C and 37 °C at 11.7T.

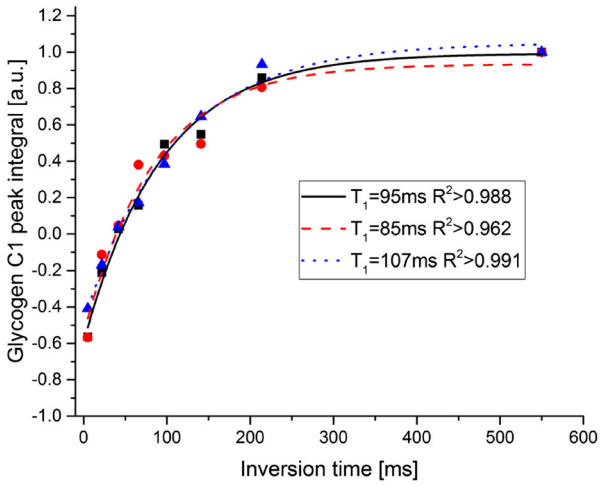

Figure 1: Results of inversion recovery experiments at 3T (21°C).

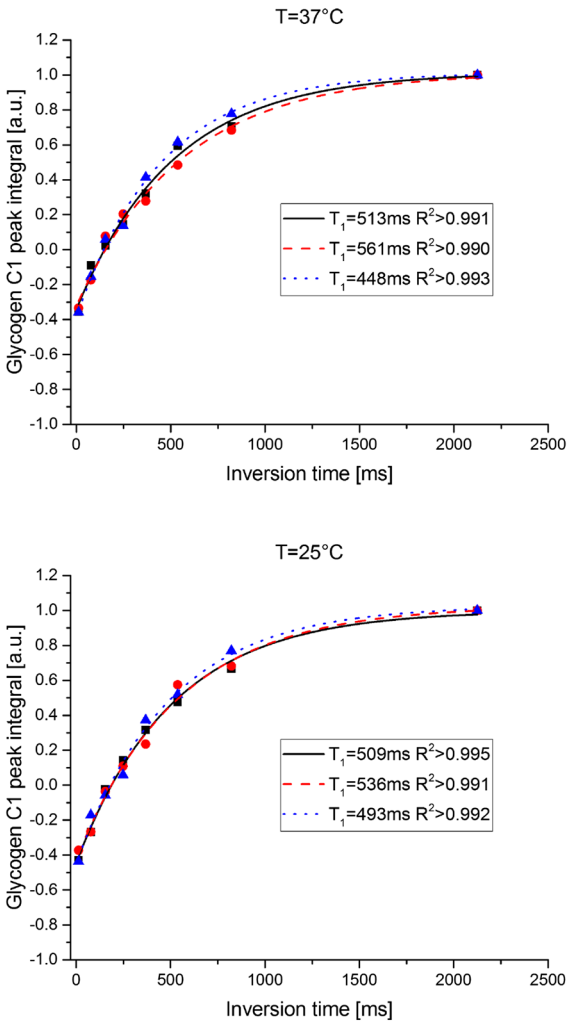

Figure 2: Results of inversion recovery experiments at 11.7T and 37°C or 25°C, respectively.

Discussion/Conclusion: All T_1s at 3T and 11.7T in this study are within the range of previously reported values from in vivo and

in vitro studies (Table 1). At 25 °C and 37 °C, no discernible difference in T_1 was detected at 11.7T as similar to a previous study at 4.7T (2).

B_0 [T]	T_1 [ms]	Temperature [°C]	Reference
2.1	65 ± 5	22	1
3	95 ± 10	21	this study
4.7	142 ± 10	22	1
	164 ± 4	23	2
	162 ± 6	37	2
	158 ± 15*	37	1
8.4	300 ± 10	22	1
	310 ± 6	23	2
	220 ± 10	27	3
	310 ± 10	37	1
	304 ± 5	37	2
9.4	332 ± 15*	37	4
	340 ± 20	37	5
	310 ± 10*	37	5
11.7	513 ± 18	25	this study
	507 ± 47	37	this study
14.1	521 ± 34*	37	4

*in vivo

Table 1: Summary of current and previously reported T1 values of 1-13C glycogen.

References:

1 Zang LH et al. *Biochemistry* 1990.
2 Overloop K et al. *Magn. Reson. Med.* 1996.
3 Sillerud LO et al. *Biochemistry* 1983.
4 van Heeswijk RB et al. *Magn. Reson. Med.* 2012.
5 Choi IY et al. *J. Neurochem.* 1999.

L06.29

Investigation on the effects of the macromolecular signals in quantification of high-field and short-echo-time in vivo proton magnetic resonance spectroscopy

C.-H. Yoo[1], H.-M. Baek[2], D.-C. Woo[3], B.-Y. Choe[1]
[1] *The Catholic University of Korea, Seoul, South Korea,* [2]*Gachon University, Department of Health Sciences and Technology, Incheon, South Korea,* [3]*Asan Medical Center, Asan Institute for Life Sciences, Seoul, South Korea*

Purpose/Introduction: The aim of this study was to investigate the effect of the macromolecular (MM) signals on quantification, and to assess the efficiency of the handling for the MM signals using high-field and short-TE MRS obtained in the prefrontal cortex and hippocampus of the rats.

Subjects and Methods: *In vivo* ^{1}H MRS spectra of two voxels were obtained in the brain of eight Sprague–Dawley rats using a point-resolved spectroscopy sequence with the following parameters: TR/TE, 5000/16.3 ms; average, 192; spectral bandwidth: 5000 Hz. For quantification, the jMRUI-QUEST and LCModel software was used with the basis-sets simulated by the Vespa software. For handling of the MM signals, the spline-based mathematical estimation was performed by the LCModel, while without any handling (no-handling), and truncation-subtraction based handling (Sub) was used for the jMRUI.

Results:

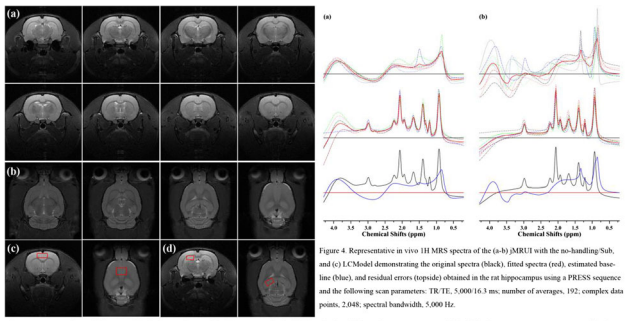

Figure 4. Representative in vivo 1H MRS spectra of the (a-b) jMRUI with the no-handling/Sub, and (c) LCModel demonstrating the original spectra (black), fitted spectra (red), estimated baseline (blue), and residual errors (topside) obtained in the rat hippocampus using a PRESS sequence and the following scan parameters: TR/TE, 5,000/16.3 ms; number of averages, 192; complex data points, 2,048; spectral bandwidth, 5,000 Hz.

Figure 1. Representative multislice (a) axial and (b) coronal T2-weighted MRI scans obtained in the rat brain with the TurboRARE sequence with the followings: TR, 4,000 ms; TE, 11 ms; effective TE, 33 ms; RARE factor, 8; averages, 2; FOV, 30 × 30 mm²; matrix size, 256 × 256; slice thicknesses, 1.5 mm (axial) and 1 mm (coronal). The T2-weighted images (axial/sagittal) are shown with the voxel of in vivo 1H MRS (red box), located in the (c) prefrontal cortex and (d) hippocampus.

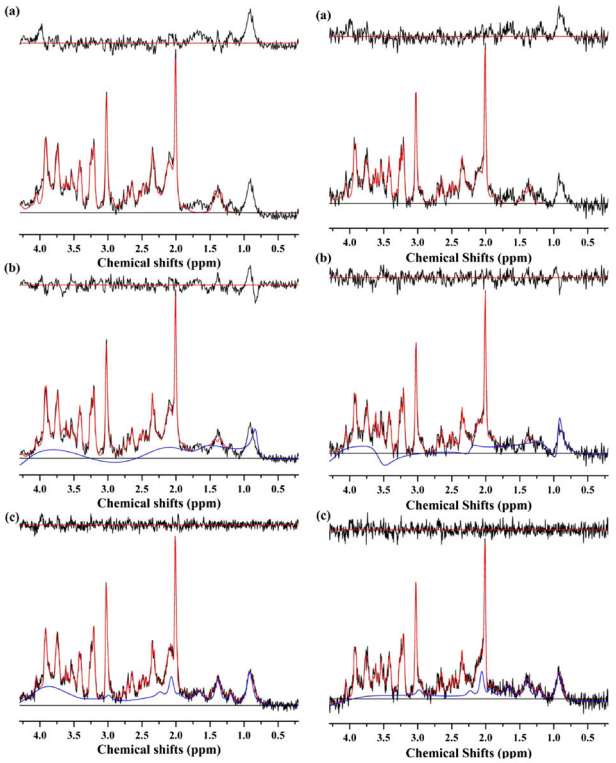

Figure 2. Representative in vivo 1H MRS spectra of the (a-b) jMRUI with the no-handling/Sub, and (c) LCModel demonstrating the original spectra (black), fitted spectra (red), estimated baseline (blue), and residual errors (topside) obtained in the rat prefrontal cortex using a PRESS sequence and the following scan parameters: TR/TE, 5,000/16.3 ms; number of averages, 192; complex data points, 2,048; spectral bandwidth, 5,000 Hz.

Figure 3. Representative in vivo 1H MRS spectra of the (a-b) jMRUI with the no-handling/Sub, and (c) LCModel demonstrating the original spectra (black), fitted spectra (red), estimated baseline (blue), and residual errors (topside) obtained in the rat hippocampus using a PRESS sequence and the following scan parameters: TR/TE, 5,000/16.3 ms; number of averages, 192; complex data points, 2,048; spectral bandwidth, 5,000 Hz.

The highest residual error of the jMRUI no-handling was significantly reduced by using the Sub. Although the fitted data of the jMRUI Sub were similar to the LCModel, its residual error was relatively higher. Generally, the spectra of the hippocampus showed decreased SNR for all methods compared to the PFC.

Table 1. The mean concentrations and CRLB value of the metabolites measured by *in vivo* ^{1}H MRS with (a-b) the jMRUI with the no-handling and Sub, and (c) LCModel in the prefrontal cortex of the animals.

			Metabolites											
			NAA	Glu	Gln	Glc	GABA	GSH	mIns	Tau	tCho (GPC/PCh)	tCr (Cr/PCr)	Glx (Glu/Gln)
Conc. (μmol/g)	jMRUI	no-handling	12.39 ± 0.78	17.92 ± 0.64	3.61 ± 1.00	3.64 ± 0.66	3.14 ± 0.69	1.60 ± 0.25	4.53 ± 0.47	6.49 ± 0.56	2.07 ± 0.25	10.41 ± 0.59	21.53 ± 1.18
		Sub	12.42 ± 0.81	13.86 ± 0.80	2.27 ± 0.34	1.56 ± 0.50	2.87 ± 0.58	3.21 ± 0.33	4.26 ± 0.42	8.69 ± 0.42	2.86 ± 0.79	10.54 ± 0.51	16.13 ± 0.65
	LCModel		10.02 ± 0.57	12.54 ± 0.60	3.96 ± 0.43	1.82 ± 0.53	2.70 ± 0.45	1.50 ± 0.15	3.99 ± 0.12	6.66 ± 0.43	1.43 ± 0.07	7.73 ± 0.17	16.51 ± 0.75
CRLB (%SD)	jMRUI	no-handling	2.17 ± 0.21	4.07 ± 0.52	18.73 ± 4.33	7.19 ± 1.28	13.96 ± 2.88	17.37 ± 1.71	6.81 ± 0.65	6.47 ± 1.57	(11.18 ± 2.88 / -)	(8.59 ± 0.67 / 15.20 ± 1.91)	(4.07 ± 0.52 / 18.73 ± 4.33)
		Sub	1.63 ± 0.19	2.98 ± 0.48	15.69 ± 2.20	10.66 ± 3.54	11.65 ± 3.10	8.47 ± 0.81	5.08 ± 0.38	5.14 ± 1.50	(13.15 ± 2.90 / -)	(5.89 ± 0.63 / 12.87 ± 1.94)	(2.98 ± 0.48 / 15.69 ± 2.20)
	LCModel		2.13 ± 0.35	2.75 ± 0.46	8.63 ± 1.06	12.38 ± 3.62	13.00 ± 2.88	10.75 ± 1.16	5.75 ± 0.46	3.63 ± 0.52	3.88 ± 0.64	2.38 ± 0.52	3.00 ± 0

Table 2. The mean concentrations and CRLB value of the metabolites measured by *in vivo* ^{1}H MRS with (a-b) the jMRUI with the no-handling and Sub, and (c) LCModel in the hippocampus of the animals.

			Metabolites										
			NAA	Glu	Gln	Glc	GABA	GSH	mIns	Tau	tCho	tCr	Glx
Conc. (μmol/g)	jMRUI	no-handling	11.30 ± 0.60	14.68 ± 1.45	1.59 ± 0.66	3.16 ± 0.77	1.88 ± 1.14	1.53 ± 0.38	5.22 ± 1.04	5.58 ± 0.61	2.38 ± 0.52	9.89 ± 0.79	16.27 ± 1.15
		Sub	11.71 ± 0.66	10.18 ± 1.39	1.29 ± 0.91	2.80 ± 0.95	4.12 ± 2.18	2.23 ± 1.08	5.98 ± 1.07	7.24 ± 3.18	3.65 ± 0.84	8.35 ± 1.10	11.46 ± 1.11
	LCModel		9.03 ± 0.50	9.59 ± 0.87	3.37 ± 0.66	2.28 ± 0.38	2.77 ± 0.40	1.84 ± 0.40	5.26 ± 0.39	6.23 ± 0.47	1.44 ± 0.11	7.65 ± 0.42	12.96 ± 1.07
CRLB (%SD)	jMRUI	no-handling	3.15 ± 0.46	6.02 ± 0.95	44.85 ± 14.07	12.44 ± 4.25	39.92 ± 27.29	25.41 ± 5.36	8.41 ± 0.98	9.38 ± 2.29	(22.67 ± 5.10 / -)	(16.00 ± 2.38 / 15.45 ± 7.17)	(6.02 ± 0.95 / -)
		Sub	2.51 ± 0.39	6.26 ± 2.12	58.12 ± 34.72	10.60 ± 4.40	16.40 ± 7.68	20.26 ± 16.38	6.03 ± 0.73	8.43 ± 4.73	(- / 18.03 ± 9.22)	(13.57 ± 3.49 / 13.13 ± 3.33)	(6.26 ± 2.12 / -)
	LCModel		3.75 ± 0.46	4.63 ± 0.52	15.00 ± 3.78	11.25 ± 2.49	18.13 ± 3.94	12.38 ± 2.20	5.88 ± 0.35	5.38 ± 0.92	5.38 ± 0.52	3.50 ± 0.53	5.00 ± 0.76

For the PFC, the percentage difference of the concentration of the jMRUI no-handling/Sub to the LCModel were similar in NAA (23.65/23.95%) and tCr (34.67/36.35%). For the jMRUI Sub, these percentage differences were reduced in Glu (42.90–10.53%), Glc (100 to − 14.29%), GABA (16.30–6.30%), mIns (13.53–6.77%), and Glx (30.41 to − 2.30%), while those of Gln (− 8.84 to − 42.68%), GSH (6.67–114.00%), Tau (− 2.55 to 30.48%), and tCho (44.76 to 100.00%) were increased compared to no-handling. For hippocampus, the percentage difference of the concentration of the jMRUI no-handling/Sub to the LCModel were similar in NAA (25.14%; 29.68%). For the jMRUI Sub, these percentage differences were reduced in Glu (53.08–6.15%), Glc (38.6–22.81%), tCr (29.28–9.15%), and Glx (25.54 to − 11.57%), while those of mIns (− 0.76 to 13.69%), Tau (− 10.43 to 16.21%), and tCho (65.28–153.47%) were increased compared to no-handling.

Discussion/Conclusion: Our findings suggested that the effects of the MM signals can cause substantial error to the quantification of high-field and short-TE MRS. By applying the handling for the MM signals, the SNR of the jMRUI can be improved, and overestimations compared to the LCModel can be reduced. However, the estimated baseline of the jMRUI and LCModel showed conspicuous inconsistency in 3.3–2.5 ppm, suggested as the cause of inconsistency for tCho, Tau and GSH. The estimated baseline contributed by the MM signals may complicatedly affect quantification related with not only the ppm range of main resonances of metabolites and its signal intensity.

References:

Ratiney H, et al., (2005) Time-domain semi-parametric estimation based on a metabolite basis set. NMR Biomed.

I25 Teaching Session

13:50–15:20 *Room 1 - Willem Burger Zaal*

Accelerated MRI

I25.01
Parallel imaging

M. Blaimer
Fraunhofer Institute for Integrated Circuits (IIS), Magnetic Resonance and X-Ray Imaging, Würzburg, Germany

Learning Objectives:- To review acceleration strategies in MRI
To learn the basic principles of the most popular reconstruction methods (SENSE and GRAPPA).
To understand limitations and future directives of current state-of-the art algorithms.
Body: During the last 20 years there has been amazing progress in the development of accelerated MRI methods. A major breakthrough was the introduction of multi-coil receiver arrays in the 1990 s which enabled the parallel acquisition of MR signals with improved signal-to-noise ratio (SNR). Parallel imaging algorithms such as SMASH, SENSE or GRAPPA were introduced and made use of the additional spatial information inherent in the receiver arrays to reconstruct image from sub-sampled data sets.
This presentation will give a short introduction to parallel imaging. The basic concepts will be described in detail with focus on the most widely used techniques SENSE and GRAPPA. Limitations including noise amplification (i.e. g-factor) and reconstruction artifacts will be discussed. After the presentation of applications there will be an outlook, e.g. the extension of parallel imaging and machine learning.
References: The following review articles are recommended:
1. Heidemann et al. A brief review of parallel magnetic resonance imaging. Eur Radiol. 2003 Oct; 13(10):2323–37.
2. Blaimer et al. SMASH, SENSE, PILS, GRAPPA: how to choose the optimal method. Top Magn Reson Imaging. 2004 Aug; 15(4):223–36.
3. Larkman DJ, Nunes RG. Parallel magnetic resonance imaging. Phys Med Biol. 2007 Apr 7; 52(7):R15–55.
4. Deshmane A et al. Parallel MR imaging. J Magn Reson Imaging. 2012 Jul; 36(1):55–72.
5. Hamilton J et al. Recent advances in parallel imaging for MRI. Prog Nucl Magn Reson Spectrosc. 2017 Aug; 101:71–95

I25.02
SMS Imaging, CAIPIRINHA, and multi-slice excitation

J. Schulz
Radboud University Nijmegen, Donders Institute for Brain, Cognition and Behaviour, Nijmegen, The Netherlands

Learning Objectives:—SMS imaging enables the acceleration along the slice direction without the penalty of a sqrt(R)-reduction in SNR.

- A SMS pulse consists of complex-summed individual pulses with a specific linear phase ramp.
- SMS pulses are demanding and its amplitude is limited by the maximal transmit voltage of the system.
- (Blipped-)CAIPIRINHA shifts individual slices in the FOV to improve image reconstruction.
- PINS-pulses yield a periodic excitation profile with a low power deposition which is independent of the number of slices.

Body: Simultaneous multi-slice (SMS) imaging enables an acceleration along the slice direction. Proposed by Larkman [1], SMS (also called multiband (MB)) imaging provides the possibility to accelerate acquisition in the slice direction by exciting and acquiring N slices simultaneously without the penalty of a sqrt{R}-reduction in signal-to-noise ratio [2, 3]. The superimposed slices can be reconstructed using a SENSE [4] or slice-GRAPPA [5] algorithm.
To excite multiple slices simultaneously, a linear phase ramp is applied to an individual RF-pulse to shift the slice to the desired location. All individually modified RF-pulses are subsequently complex-summed [3] to form the SMS RF-pulse. Both, the power deposition and amplitude of the RF-pulse, depend linearly on the number of simultaneously excited slices making SMS pulses rather demanding. The RF amplitude is limited by the maximal transmit voltage of the system and different techniques have been developed to maintain an acceptable range [6–9].
With power independent of number of slices (PINS) [10] pulses, the number of simultaneously excited slices is only limited by the dimensions of the RF coils or the size of the body. PINS pulses have a low power deposition and are especially suited for SE-based sequences at high field strength [11–13]. A combination of SMS and PINS, MultiPINS pulses, has been developed taking advantage of both characteristics [14].
A limitation of SMS imaging lies in the ability to properly disentangle the aliased slices as reconstruction is dependent of the coil sensitivity profiles. To improve image quality, CAIPIRINHA [15] has been introduced. By alternating the phase of the individual RF-pulses in a defined order, individual slices are shifted within the FOV and enlarge the distance between similar voxels. For acquisitions acquiring more than one ky-line per excitation, the shift can also be evoked by gradient blips along the slice direction, called blipped-CAIPIRINHA.[5].
References:
[1] Larkman, JMRI, 2001.
[2] Feinberg, PLoS One, 2010.
[3] Moeller, MRM, 2010.
[4] Pruessmann, MRM, 1999.
[5] Setsompop, MRM, 2012.
[6] Hennig, MRM, 1992.
[7] Goelman, MRM, 1997.
[8] Wong, In Proceedings of ISMRM 2012.
[9] Auerbach, MRM, 2013.
[10] Norris, MRM, 2011.
[11] Koopmans, Neuroimage, 2012.
[12] Eichner, MRM, 2014.
[13] Norris, NeuroImage, 2012.
[14] Eichner, MRM, 2014.
[15] Breuer, MRM, 2005.

I25.03
Sparse imaging

S. Kozerke
University and ETH Zurich, Zurich, Switzerland

Learning Objectives: Upon completion of the lecture, attendees should be able to:
(1) Quantify sparsity of objects.
(2) Select and apply appropriate sparsifying transforms.
(3) Design suitable sparse sampling patterns.

(4) Sketch non-linear reconstruction algorithms for image recovery.
(5) Name applications as well as identify benefits and limitations.

Body: Compressed sensing (1–3) aims to reconstruct MR images from fewer measurement samples than traditionally required. In order for compressed sensing to work, three requirements have to be fulfilled.

The first requirement relates to *compressibility* or *sparsity* of object images in a suitable domain. While angiographic scans already provide a sparse representation of the object i.e. only few image pixels contain information different from noise, other imaging modes require dedicated transforms to represent the object in a compact fashion. The Wavelet transform has been shown efficient for compressing image data of various anatomies, i.e. only few Wavelet coefficients are significant while the others contain noise and hence can be discarded.

As a second condition, compressed sensing requires *incoherence* between the sparse representation of the object and the data points picked in the sensing domain. For example, if an angiographic image is considered then only vessels provide information significantly different from noise. While such an image is sparse in itself, its Fourier transform i.e. its representation in the sensing domain cannot be sparse at the same time. Accordingly, the sampling or sensing pattern is required to be dense in the domain the object of interest is represented in. It has been proven that this requirement can be well approached by using random sampling patterns in the sensing domain. In practice this is achieved by randomly picking m measurement points in k-space where m is smaller than the full matrix dimension n. It has been found that the object can be recovered to good approximation if m is chosen to be about 4x the number of significant pixels of the object or its transform representation. Assuming that only 32 out of a total of 256 points are different from noise than the object can be recovered from as few as 128 measurements and hence the imaging process can be accelerated by a factor of 2.

The third ingredient includes deployment of *non-linear reconstruction* methods to select among all possible images i the one that is most probable and closest to the desired object within error bounds.

Today, a wide range of different implementations of the fundamental compressed sensing concept is found for various applications. It is the purpose of this talk to review most important variants and their applications following the introduction of the underlying basic concept.

References:

(1) Candes E et al. IEEE Trans Inform Theory 2006, 489–509.
(2) Donoho D. IEEE Trans Inform Theory 2006, 1289–1306.
(3) Lustig M et al. Magn Reson Med 2007, 1182–1195.

S19 Scientific Session

13:50–15:20 *Room 2 - Van Weelde Zaal*

Gadolinium-free Imaging: Why & How?

S19.02
Gadolinium retention in RBCs and WBCs from human and murine blood treated with GBCAs

E. Gianolio, E. Di Gregorio, C. Furlan, S. Atlante, R. Stefania, S. Aime
University of Torino, Molecular Biotechnologies and Health Science, Torino, Italy

Purpose/Introduction: The assessment of Gd-retention in brain tissues of patients who received multiple administrations of GBCAs still is a topic of major concern. At the preclinical level, it was demonstrated that GBCAs may distribute in all tissues they enter in contact.[1] The tissue which GBCAs first experience is blood. The changes in Gd concentration in plasma allow to establish the GBCA's excretion time. However, the contiguity of GBCAs (at high concentration) and cellular membranes may yield to internalization processes thus removing part of the GBCA from the filtration process occuring at the glomerular level. Moreover, Gd entrapped into RBCs and WBCs may be the source for supplying organs such as spleen and liver. Herein we report results that show that indeed GBCAs enter RBCs and WBCs thus introducing new items in the complex excretion and retention pathway of administered GBCAs.
Subjects and Methods: Two independent experiments were carried out: i) human blood was incubated in vitro with GBCAs (gadoteridol, gadobenate dimeglumine, gadodiamide and gadopentetate dimeglumine) 5 mM for variable times (30 min, 1, 2 and 3 h) at 37 °C. Then, blood cell components were isolated by using Ficoll Histopaque method, washed three times, and analyzed by ICP-MS for total Gd quantification. Blood components derived from human blood incubated with gadodiamide or gadoteridol underwent the UPLC-MS analysis for the determination of the amount of intact Gd-DTPA-BMA and Gd-HPDO3A; ii) the distribution of Gd in the blood components of mice administered with gadodiamide and gadoteridol was carried out: a single dose of GBCA (1.2 mmol/kg) was iv administrated to healthy CD-1 mice and blood was recovered at different time points: 24 h, 48 h, 96 h and 10 days. As for human blood, the procedure of separation of blood components, ICP-MS quantification of the total Gd and UPLC-MS determination of the amount of intact GBCAs was carried out.
Results: GBCAs enter RBCs and WBCs at quantities well detectable by ICP-MS. The structure of the different GBCAs are not relevant to determine the amount of Gd internalized in the cells. Whereas the amount of Gd steadily decreases in the case of gadoteridol-labelled cells, in the case of gadodiamide, the amount of Gd in the cells is preserved also 10 days from the administration of the GBCA. Moreover, whereas gadoteridol maintains its structural integritty, upon the cellular uptake, gadodiamide largely transforms upon time.
Discussion/Conclusion: The detection of significant amounts of Gd in RBCs and WBCs indicates that GBCAs can cross also blood cellular membranes. Before this observation, GBCAs were scrutinized only for their ability to escape from the vascular bed but this new finding opens new questions on the involvement of cells in the process that lead to accumulation of Gd in the tissues of patients undergone to the administration of GBCAs.
References:
E Gianolio et al. Eur. J. Inorg. Chem. 2019, 137–151

S19.03
Combining qMRI parameters for Gd-free evaluation of Gd-enhanced lesions

S. Berman[1], Y. Backner[2], N. Levin[2], P. Petrou[3], D. Karussis[3], A. Mezer[4]
[1]*The Hebrew University of Jerusalem, The Edmond and Lily Safra Center for Brain Science., Jerusalem, Israel,* [2]*Hadassah Hebrew University Hospital, MS Center and the fMRI unit, Jerusalem, Israel,* [3]*Hadassah Hebrew University Hospital, MS Center, Jerusalem, Israel,* [4]*The Hebrew University of Jerusalem, The Edmond and Lily Safra Center for Brain Science, Jerusalem, Israel*

Purpose/Introduction: MRI is a valuable tool for the clinical diagnosis and monitoring of Multiple Sclerosis (MS), a neurological disease that causes damage to white matter. Currently, Gadolinium (Gd) enhancement is the clinical standard for detecting inflammatory activity in MS patients, but it is known to be a toxic substance (Cacheris et al., MRI, 1990), and its sensitivity is limited to the time window of the blood brain barrier breakdown (Tourdias et al., Radiology, 2012). Thus it would be of great value to develop imaging techniques that accurately reflect the underlying pathophysiologic information to monitor MS progression, without the need for Gadolinium.
In this study we use multiple quantitative MRI maps to detect Gd-enhanced lesions, without the use of Gd (Chen et al., Radiology, 2014).
Subjects and Methods: The subjects for this study were part of clinical trials of a new MS therapy at the Hebrew University Hadassah Medical Center. The trial, a longitudinal mesenchymal stem-cell-therapy study, included 48 progressive MS patients. Trial inclusion criteria include disease duration above 3 years, EDSS score of 3.5–6.5, and failure of currently available treatments. The patients were monitored monthly by EDSS records.
The patients were scanned prior to and following two treatment sessions, giving 6 MRI scans. The MRI scans included protocols designed to evaluate changes in the lesion volume and brain atrophy (FLAIR, T2-weighted, T1-weighted, and Gd enhanced T1-weighted). For most scans (N = 193) we also used protocols designed for analysis of qMRI parameters: T1 and proton density mapping (Mezer et al., HBM, 2016) and diffusion tensor imaging (Pierpaoli et al., Radiology, 1996).
Results: The T1-weighted and T2-weighted were used to create an automatic segmentation of the lesions for all scans (Dadar et al., NeuroImage, 2017), with some manual corrections. Then, a Gd-enhanced image was used to calculate detect enhanced lesions. Figure 1 shows an example of the segmentations outline for a single subject.

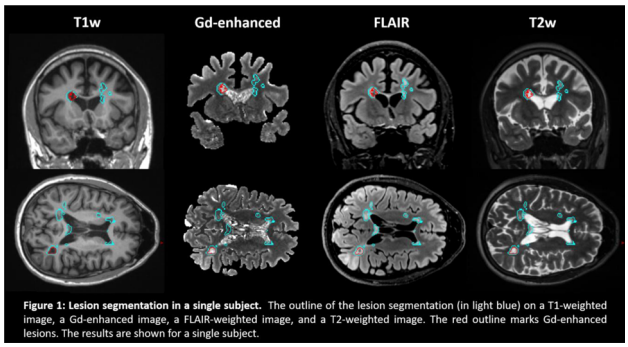

Figure 1: Lesion segmentation in a single subject. The outline of the lesion segmentation (in light blue) on a T1-weighted image, a Gd-enhanced image, a FLAIR-weighted image, and a T2-weighted image. The red outline marks Gd-enhanced lesions. The results are shown for a single subject.

We then calculated, for each scan, the mean values of quantitative T1, PD and MD, and their linear relationships, in the enhanced lesions, non-enhanced lesions, and the normal appearing white matter. The differences between the tissue types can be seen in Fig. 2. We find the qMRI estimates reveal differences between ehanced and non-enhanced lesions, without requiring Gd.

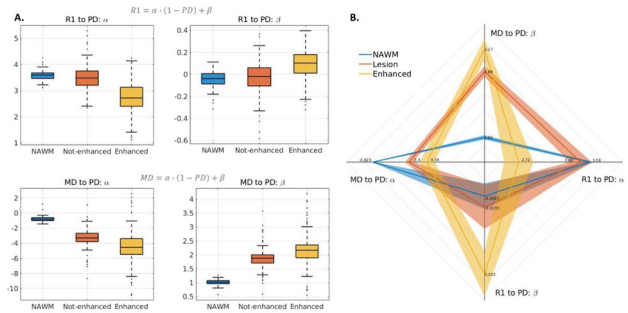

Figure 2: qMRI in MS tissue types. (A) Boxplots of the coefficients in the linear relationships between R1 (and MD) to (1-PD), in NAWM (blue), non-enhanced lesions (red) and Gd-enhanced lesions (yellow). **(B)** A spider plot summarizing the data in (A), showing combined qMRI parameters could separate Gd-enhanced lesions from non-enhanced lesions.

Discussion/Conclusion: Our preliminary results suggest qMRI is valuable in characterizing Gd-enhanced lesions, thus shedding more light about the molecular composition of these lesions, as well as potentially allowing to monitor the lesion progression without using Gd. We plan to test whether the qMRI information is enough to perform a within scan classification of active lesions.

References: The references are in the text.

S19.04

Voxelwise correlation between vascular parameters obtained with ASL and DSC in non-enhancing glioma

E. A. H. Warnert[1], F. Incekara[1], A. J. P. E. Vincent[2], M. J. van den Bent[3], P. J. French[3], H. J. Dubbink[4], J. M. Kros[4], J. A. Hernandez-Tamames[1], M. Smits[1]

[1]*Erasmus MC, Radiology & Nuclear Medicine, Rotterdam, The Netherlands,* [2]*Erasmus MC, Neurosurgery, Rotterdam, The Netherlands,* [3]*Erasmus MC, Neurology, Rotterdam, The Netherlands,* [4]*Erasmus MC, Pathology, Rotterdam, The Netherlands*

Purpose/Introduction: Comparative studies of dynamic susceptibility contrast (DSC) based measurement of cerebral blood volume (CBV) or cerebral blood flow (CBF) and arterial spin labelling (ASL) based measurement of CBF have previously shown good correlation of these parameters in human glioma[1]. However, these studies were mostly done before inclusion of the mutation status of the isocitrate dehydrogenase (IDH) encoding gene in brain tumour classification[2]. In light of the call for gadolinium-free imaging, here we investigate the effect of IDH-mutation status on the correlation between ASL and DSC-based perfusion measurements in non-enhancing glioma.

Subjects and Methods: Twenty-two patients with non-enhancing glioma and confirmed IDH-mutation status (next generation sequencing, 6 IDH-wildtype and 16 IDH-mutated) underwent 3T MRI scanning (GE, Milwaukee, WI, USA). Image acquisition included a 3D spiral pseudocontinuous ASL with time-encoded labelling (7 effective label delays from 0.8 to 2 s, reconstruction matrix $128 \times 128 \times 42$, resolution $1.9 \times 1.9 \times 3.5$ mm^3), and 2D DSC imaging (122 TRs, TR/TE 1500 m/18.6 ms, 15 slices, voxel size: $1.88 \times 1.88 \times 4$ mm^3) in which a bolus of 7.5 ml of gadolinium-based contrast agent (Gadovist, Bayer, Leverkussen, GE) was injected. A pre-load bolus of equal size was given 5 min prior to DSC imaging.

DSC and ASL images were motion corrected and linearly registered to high resolution FLAIR images (FSL, version 5.0.9, Oxford, UK). DSC-relative CBV (rCBV), DSC-relative CBF (rCBF), and ASL-CBF maps were calculated via previously described methods[3–5].

The glioma region of interest (ROI) was determined via manual segmentation on the FLAIR images. Voxel-wise Pearson's linear correlation coefficients (ρ) within this ROI were calculated between ASL-CBF and DSC-rCBV, and between ASL-CBF and DSC-rCBF.

Results: Normalised histograms (Fig. 1) indicate that IDH-wt glioma has higher values for ASL-CBF, DSC-rCBV, and DSC-rCBF than IDH-mutated glioma. IDH-wildtype glioma has a significantly lower $\rho_{\text{ASL-CBF vs DSC-rCBV}}$ and $\rho_{\text{ASL-CBF vs DSC-rCBF}}$ than IDH-mutated glioma (two-sample t tests $p < 0.05$, Figures 2 & 3).

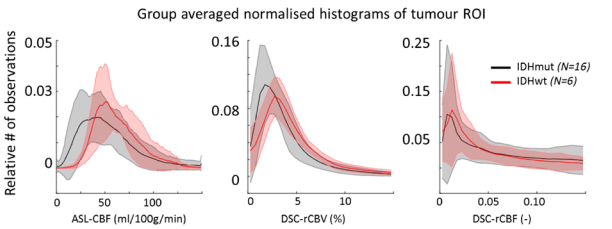

Figure 1. Group averaged histograms across the tumour ROI for IDH-mutated (black lines) and IDH-wildtype (red lines) non-enhancing gliomas. The shaded errorbars indcate the standard deviation across the groups.

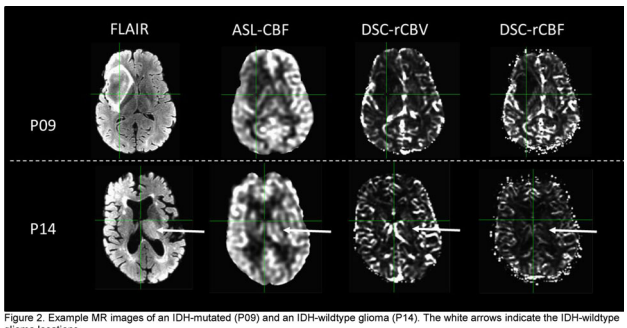

Figure 2. Example MR images of an IDH-mutated (P09) and an IDH-wildtype glioma (P14). The white arrows indicate the IDH-wildtype glioma locations.

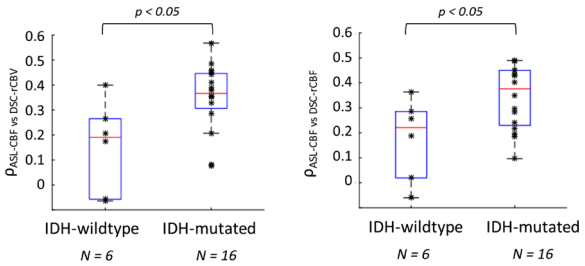

Figure 3. Correlation coefficients for ASL-CBF and DSC-rCBV (l) and DSC-rCBF (r) within non-enhancing gliomas. The spatial correlation between ASL-CBF and DSC-rCBF and DSC-rCBV are lower for the IDH-wt tumours (two-sample t-tests, $p < 0.05$).

Discussion/Conclusion: IDH-mutation status of non-enhancing glioma potentially affects the correlation between ASL-CBF and DSC-rCBF/rCBV and should be taken into account when moving towards ASL-only imaging. The decreased correlation between ASL and DSC-based vascular parameters in IDH-wt gliomas may be due to more aggressive vasculature in subtypes of IDH-wt tumours[6]. Future work includes expansion of the current patient cohort (part of the ongoing iGENE study).

References:

1. Grade M et al. NeuroRad. 2015.
2. Louis DN et al., Acta Neuro Patho. 2016; 131:803–20.
3. Kellner E et al. JMRI. 2015; 42(4):1117–25.
4. Chappell MA et al. MRM. 2015; 74(1):280–90.
5. Dai W et al. MRM. 2013; 69(4):1014–22. **6**. Zhang L et al. Neuro Oncol. 2018

S19.05

Recent advances in flow-based arterial spin labeling techniques: comparing velocity selective, acceleration selective, multiple-velocity selective, velocity-selective inversion and pseudo-continuous arterial spin labeling

S. Franklin[1], A. Monteiro Paschoal[1], C. Bos[2], M. van Osch[1], S. Schmid[1]

[1]*Leiden University Medical Center, C.J. Gorter Center for High Field MRI, Leiden, The Netherlands,* [2]*University Medical Center Utrecht, Center for Image Sciences, Utrecht, The Netherlands*

Purpose/Introduction: Arterial Spin Labeling (ASL) is a non-contrast enhanced MRI method to measure tissue perfusion. Pseudo-continuous ASL (pCASL) is the recommended method[1]. However, it is associated with transit-time artefacts[1] and difficulties planning the labeling slab. Flow-based spatially non-selective techniques overcome these issues, since they do not require a labeling slab and they also label within the imaging region, reducing transit-time artifacts. The first was velocity-selective ASL (VSASL)[2], where label is created by saturating spins flowing above a certain cutoff-velocity. Shortly after, acceleration-selective ASL (AccASL)[3], using labeling based on acceleration of spins, multiple velocity-selective ASL[4] (mm-VSASL), using two VS-labeling modules, and velocity-selective inversion (VSI)[5], using Fourier-transform based velocity-selective inversion, were presented to increase SNR. In this study we compared these flow-based ASL methods to pCASL, in the brain, based on temporal signal-to-noise (tSNR) as well as their ability to measure increases in perfusion.

Subjects and Methods: Five subjects were scanned (24–60 years) on a 3T Philips scanner using a multi-slice EPI readout and 32ch-head coil, technique-specific scan parameters were chosen based on previous research[1, 2, 3, 4, 5], see Table 1. AccASL, VSASL, mm-VSASL, VSI, and pCASL -scans were acquired twice in random order, first while watching a cartoon and later with eyes closed. T_1 and M_0 scans were acquired for post-processing.

All ASL scans were realigned, co-registered to T_1, transformed to MNI space, and smoothed (SPM12). Perfusion-weighted signal (PWS) maps were normalized by dividing by M_0, and tSNR (= S/std(S)) was calculated. Gray matter masks were segmented from the T_1-scan. PWS map during the visual task and rest were subtracted to create activation maps.

Scan parameter	AccASL[2]	VSASL[5]	mm-VSASL[3]	VSI[1]	pCASL[4]
Voxel size (mm)	3x3x7	3x3x7	3x3x7	3x3x7	3x3x7
Slices	17	17	17	17	17
Recovery after presaturation (ms)	2000	2000	2000	2000	-
TR (ms)	4260	4260	4610	4160	4170
Repetitions	28	28	28	28	28
Total scan duration (min)	4:07	4:07	4:27	4:01	4:01
Post-label delay (PLD)	1600	1600	1150/820	1500	1800
Background suppression (ms)	50/1150	50/1150	20/620	560/580/1140	112/1350
Cut-off velocity or acceleration	1.8m/s^2	2cm/s	2cm/s	2.8cm/s	-
Duration labeling module (ms)	50	50	50	48	1800
# labeling modules	1	1	2	1	1
VS-crushing at acquisition in z-dir	-	2cm/s	2cm/s	3cm/s	-

Table 1. Scan parameters ASL scans.

Results: PWS maps are shown in Fig 1A. As expected, mm-VSASL and to a lesser extent VSASL and AccASL show some T_2- and/or diffusion-weighting[2, 3, 4]. Fig 1B shows the tSNR in gray matter; VSI has a significantly higher tSNR compared to all other ASL techniques, and variation over volunteers comparable to pCASL. VSASL and mm-VSASL show a higher variation in tSNR over volunteers. The perfusion increase in an area associated with the visual cortex during the visual task is most clearly shown in the activation maps of VSI and pCASL, see Fig 2.

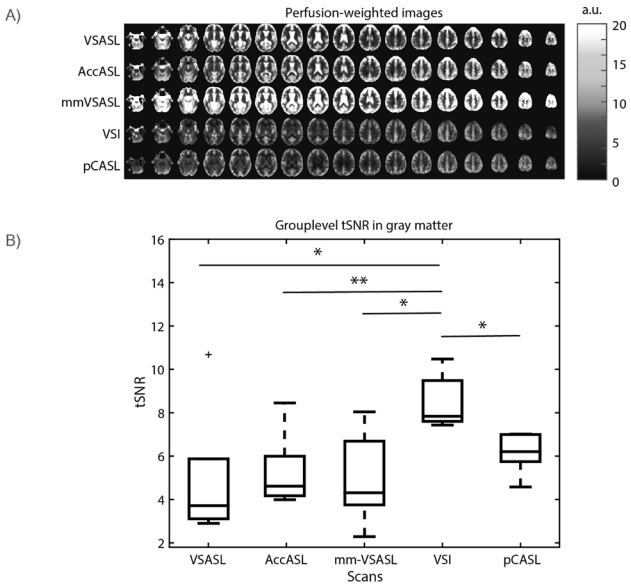

Fig.1 A) Perfusion-weighted images of a representative volunteer, normalized by M0. From top to bottom: AccASL, VSASL, mm-VSASL, VSI, pCASL (only 17 slices shown). B) Group-level temporal SNR (tSNR) in gray matter, * = p<0.05, ** = p<0.001.

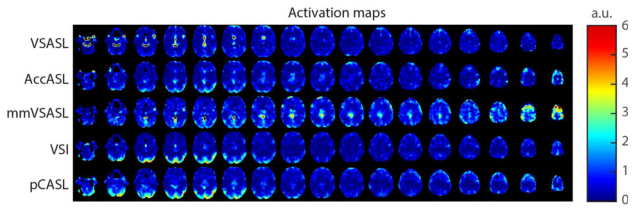

Fig.2 Activation maps for the visual task for all ASL images (only 17 slices shown). Maps are averaged over all volunteers.

Discussion/Conclusion: Our results show potential for VSI, both in terms of tSNR and the ability to pick up increases in perfusion. tSNR in gray matter of VSI was higher than the reference pCASL, this is especially notable since Qin (2016) [5] reported a similar tSNR between pCASL and VSI. In future work similar comparisons will be done in kidneys to see which technique is most suited for measuring renal perfusion.

References:

1. Alsop DC, *Magn Res Med* 2015.
2. Wong EC, *Magn Res Med* 2006.
3. Schmid S, *Magn Res Med* 2014.
4. Guo J, *Magn Res Med* 2015.
5. Qin Q, *Magn Res Med* 2016.

S19.06

Clinical plasma volume expanders as potential MRI-CEST blood pool agents for tumor perfusion imaging

L. Consolino[1], P. Irrera[2], A. Anemone[3], F. Romdhane[3], S. Aime[3], D. Longo[4, 5]

[1]*University of Torino, Dept of Molecular Biotechnologies and Health Sciences, Torino, Italy,* [2]*University of Campania "Luigi Vanvitelli", Torino, Italy,* [3]*University of Torino, Dept of Molecular Biotechnologies and Health Sciences, Turin, Italy,* [4]*National Research Council of Italy (CNR), Institute of Biostructures and Bioimaging (IBB), Turin, Italy,* [5]*National Research Council of Italy (CNR), Institute of Biostructures and Bioimaging (IBB), Torino, Italy*

Purpose/Introduction: Clinical low-molecular weight Gd-based contast agents (CAs) exhibit non-specific accumulation in tumors due to their passive diffusion across the vascular endothelium, making them not optimal agents for the accurate assessment of tumor perfusion properties by MRI. By contrast, macromolecular CAs provide more reliable measurements of tumor permeability thanks to the enhanced permeability and retention effects [1]. However, this advantage is counterbalanced by their reduced blood pool clearance, hence in safety-related issues, due to increased risk of Gd accumulation in tissues, with critical limitation for their translational application. Therefore, looking for alternatives to common Gd-blood pool agents is currently deemed of interest. Two macromolecular systems with size comparable to albumin and clinically used as plasma volume expanders, Voluven and Dextran70 [2], can be exploited by the MRI-CEST approach owing to the presence of hydroxyl protons. In this work we aimed to investigate their CEST properties and evaluate their potential as blood pool perfusion agents in comparison to an albumin-binding agent, Gd-AAZTA Madec [3].

Subjects and Methods: *In vitro* CEST properties were measured in phantoms containing 6% p/v Voluven or Dextran70 in the pH range of 5.5–7.9 and irradiation power of 1–2–3 μT on a 7T Bruker MRI scanner at 37 °C. *In vivo* MRI experiments were carried out in a murine breast tumor model (n = 6). CEST spectra and T_{1w}-images have been sequentially acquired, in the same tumor region, before and after i.v. injection of Voluven/Dextran70 (250 μl) and Gd-AAZTA Madec (dose = 0.03 mmol Gd/kg bw). Contrast enhancement maps were calculated for both CEST and T_{1w} images and tumor perfusion was quantified in term of the extravasation fraction and their similarity was calculated spatially.

Results: *In vitro* studies demonstrate similar size to human serum albumin (Fig. 1b) and different CEST contrast dependency on pH for voluven and dextran70 (Fig. 1c).

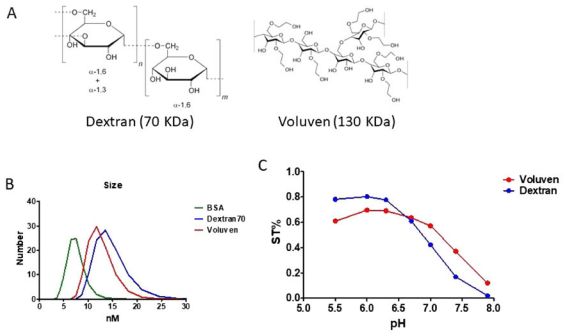

Figure 1. Chemical structure (A), size (B) and CEST contrast pH dependence measured in vitro at 37°C (C) for Voluven and Dextran70.

Both agents can generate in vivo similar increase in ST contrast (3%) inside the tumor region up to 30 min (Fig. 2), with lower extravasation fraction (30%) in comparison to a small-size CEST perfusion agent (iopamidol: 80%).

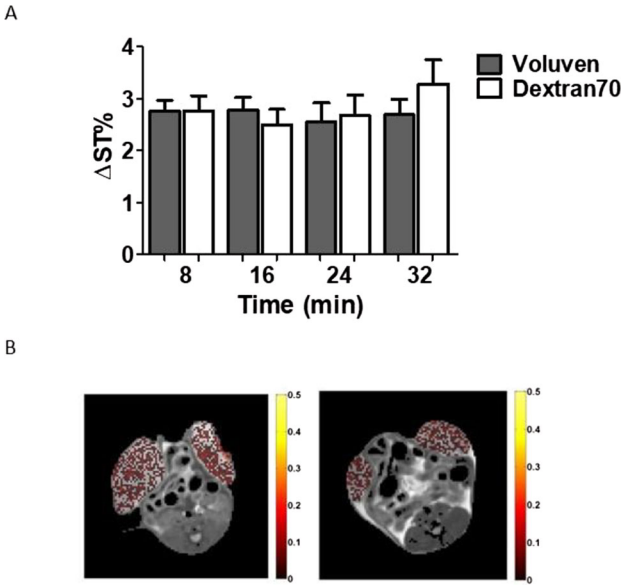

In mice receiving both CEST and T_{1w} agents, voxel-wise analysis shows a better spatial correlation in perfusion maps (Fig 3A;B) between Voluven (60%) and Gd-AAZTA Madec than for Dextran70 (40%), suggesting that differences in size and in molecular conformation may influence the spatial distribution of the molecules in the tumor. Moderate spatial similarity was observed in contrast enhancements maps inside the tumor region (Fig 3C).

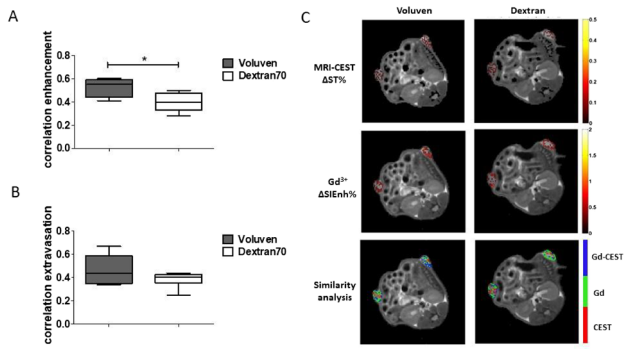

Figure 3. Pixel-by-pixel similarity measured as CEST contrast (A) or as extravasation (B) between voluven or dextran and the Gd-based agent. Represenative maps of spatial correlation with that of Gd-AAZTA Madec in the same tumor region (C

Discussion/Conclusion: Voluven and Dextran70 can be positively considered as potential blood pool MRI-CEST agents to accurately measure tumor permeability/perfusion properties.

References:

[1] Turetschek K et al.; J Magn Reson 2004.
[2] Dubniks. et al.; Journal of Trauma. 2009.
[3] Longo D et al.; Biomaterials 2016, 75, 47.

S19.07

Hyperpolarized ^{129}Xe dissolved-phase magnetic resonance imaging detects heterogeneity of lung perfusion in paediatric cystic fibrosis patients

A. L. Kern[1], A. Voskrebenzev[1], M. Gutberlet[1], G. Pöhler[1], F. Wacker[1], J. Hohlfeld[2], A.-M. Dittrich[3], J. Vogel-Claussen[1]
[1]*Hannover Medical School, Institute for Diagnostic and Interventional Radiology, Hannover, Germany,* [2]*Fraunhofer Institute for Toxicology and Experimental Medicine, Clinical Airway Research, Hannover, Germany,* [3]*Hannover Medical School, Clinic for Paediatric Pneumology and Neonatology, Hannover, Germany*

Purpose/Introduction: Cystic fibrosis (CF) is the most common lethal inherited disease among Caucasians and affects more than 30,000 patients in Europe [1]. Computed tomography and dynamic contrast-enhanced (DCE) MRI are often performed for assessment of lung structure and perfusion, bringing about risks due to ionizing radiation and contrast agent side effects, especially in the paediatric setting. Purpose of this study was to investigate the potential of hyperpolarized ^{129}Xe dissolved-phase MRI for the assessment of altered lung structure and impaired perfusion in paediatric CF patients and to compare the results to DCE MRI.

Subjects and Methods: 9 CF patients and 9 healthy volunteers underwent MRI at 1.5T (Avanto, Siemens). Subjects inhaled 1L of gas containing 450 ml (CF patients) or 800 ml (healthy volunteers) hyperpolarized ^{129}Xe (polarization $\sim$ 25%) from functional residual capacity and held their breath. Imaging of ^{129}Xe in tissue/plasma (TP) and red blood cells (RBC) was performed using a multi-echo sequence similar to [2]. High-resolution spectra of the dissolved phase were obtained and two Lorentzians were fitted for lineshape analysis. TP and RBC were normalized on voxel basis by the gas signal and averaged in the ventilated area. For quantification of heterogeneity, each coronal slice was normalized by the slice median to remove gravitational gradients, and the interquartile range of all voxels was computed. DCE MRI was performed in CF patients after injection of 0.025 mmol/kg Dotarem and data were analyzed by model-free deconvolution [3].

Results: Results are summarized in Table 1 and exemplary images are given in Figs. 1 and 2. Heterogeneity was significantly increased in CF patients in the case of the RBC signal, $p = 0.048$, but not in the case of the TP signal, $p = 0.130$. No significant differences were found for the whole lung values of RBC and TP, $p = 0.436$ and $p = 0.863$. A good visual correlation of RBC signal with blood volume from DCE-MRI was apparent in the ventilated area, Fig. 1. T_2^* of the TP phase was significantly reduced in CF patients, $p = 0.011$.

CF patients	Age/Sex	RBC heterogeneity	TP heterogeneity	TP T2* (ms)	Healthy volunteers	Age/Sex	RBC heterogeneity	TP heterogeneity	TP T2* (ms)
CF1	12/f	0.428	0.229	2.044	HV1	53/m	0.551	0.338	2.147
CF2	13/m	0.529	0.299	2.117	HV2	50/m	0.365	0.258	2.407
CF3	16/f	0.432	0.258	2.140	HV3	30/f	0.289	0.154	2.281
CF4	17/f	0.314	0.206	2.152	HV4	25/f	0.309	0.235	2.289
CF5	14/f	0.451	0.212	2.258	HV5	22/f	0.286	0.181	2.367
CF6	18/f	0.313	0.254	2.231	HV6	21/f	0.360	0.224	2.352
CF7	16/f	0.503	0.290	2.265	HV7	22/f	0.444	0.212	2.213
CF8	13/f	0.539	0.252	2.134	HV8	31/f	0.289	0.194	2.209
CF9	13/f	0.370	0.268	2.127	HV9	44/m	0.274	0.223	2.246

Subject demographics and main results.

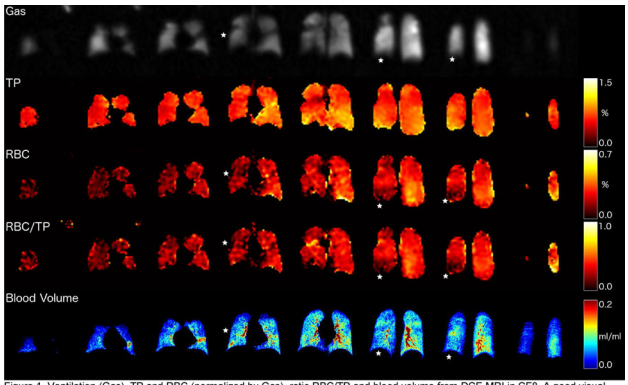

Figure 1. Ventilation (Gas), TP and RBC (normalized by Gas), ratio RBC/TP and blood volume from DCE MRI in CF8. A good visual correlation of RBC with blood volume in the ventilated area is given. Wasted ventilation is seen in right lung (asterisks).

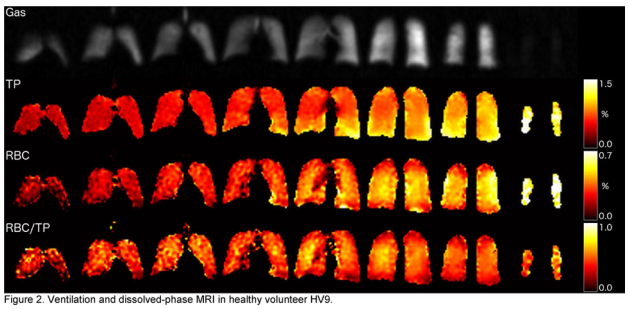

Figure 2. Ventilation and dissolved-phase MRI in healthy volunteer HV9.

Discussion/Conclusion: The more heterogeneous ^{129}Xe RBC signal in CF is likely due to mosaic perfusion frequently found in CF. Comparison with ventilation imaging enables the assessment of wasted ventilation.

The lineshape of dissolved ^{129}Xe is broadened by the microscopic heterogeneity of magnetic flux density in the lung parenchyma and the broadening increases with lung air content [4]. Hence, the reduced T_2^* in CF could be associated with hyperinflation or parenchymal changes.

In conclusion, hyperpolarized ^{129}Xe MRI enables the assessment of regional lung perfusion, tissue density as well as ventilation in a single breathhold, without the need for Gadolinium-based contrast agents or ionizing radiation.

References:

1. Bell SC et al. J Pharm Thera 145; 2015.
2. Qing K et al. JMRI 39; 2014.
3. Østergaard L et al. MRM 36; 1996.
4. Christman RA et al. MRM 35; 1996.

S19.08

Non-invasive assessment of CSF movement in paravascular spaces of the entire human brain

L. Hirschler[1], K. Lønning[2], L. Gottwald[3], M. J. van Osch[1], M. W. Caan[4]

[1]*Leiden University Medical Center, Radiology, Leiden, The Netherlands,* [2]*The Netherlands Cancer Institute, Amsterdam, The Netherlands,* [3]*Amsterdam University Medical Center, Radiology, Amsterdam, The Netherlands,* [4]*Amsterdam University Medical Center, Biomedical Engineering & Physics, Amsterdam, The Netherlands*

Purpose/Introduction: The flow of cerebrospinal fluid (CSF) has been shown to play an important role in the transport of brain metabolites, ushering in the concepts of glymphatics[1] and intramural periarterial drainage[2]. Failure of waste-drainage has been linked to several neurodegenerative diseases[3]. The lack of non-invasive imaging techniques for the investigation of drainage mechanisms in the human brain greatly hinders our understanding of brain clearance in humans. Here, we follow up on our recent work[4] where we non-invasively measured CSF-flow for the first time along paravascular spaces in the human brain. However, the readout used in the latter study was limited to a thin 3D-slab. To increase the coverage while maintaining reasonable acquisition time, we implemented a compressed sense sampling (CS) scheme, enabling full brain coverage.

Subjects and Methods: Two subjects were scanned at 7T (Achieva, Philips, The Netherlands) using a 32-channel head-coil and 8-channel parallel transmission.

We first adapted the parameters of our original thin-slab turbo spin echo sequence[4] to reach a full brain readout, while maintaining optimal parameters to select only the CSF signal with a very high resolution (0.45 mm^3 isotropic, TSE factor = 146, acquisition time T_{acq} = 8 min) (Fig. 1). The total acceleration (SENSE + partial Fourier) was 13x. To further accelerate imaging, we introduced a pseudo-random undersampling scheme. We acquired and evaluated the image quality from 11, 14 and 17 times CS-accelerated scans. Reconstruction was performed using BART[5] with an L1-norm and optimized by comparing 4 regularization values (r).

Subsequently, a T_2 prep-module with velocity-encoded gradients of 3 mm/s was included in the 17x scan and seven scans were acquired, including one without velocity-encoding (total T_{acq} = 40 min). Images were registered using Elastix[6]. Flow was modelled by a rank-two positive definite tensor, analogous to Diffusion Tensor Imaging (DTI).

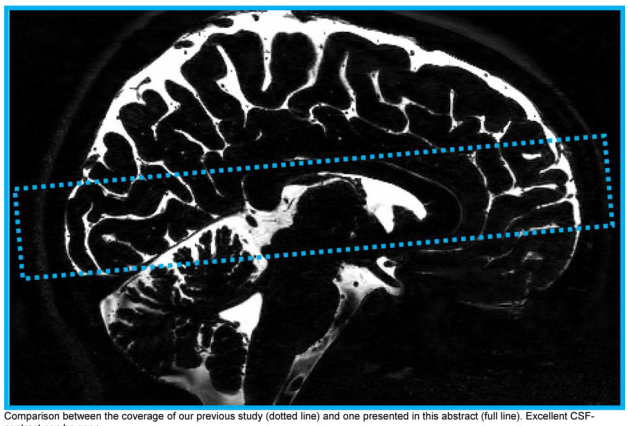

Comparison between the coverage of our previous study (dotted line) and one presented in this abstract (full line). Excellent CSF-contrast can be seen.

Results: Higher CS-factors improved image quality: signal leakage artefacts present for 11x acceleration disappeared for 14x and 17x. r = 0.005 was optimal: lower r lead to increased background noise; higher r to more blurring. The optimal choice appeared to be 17x accelerated CS with r = 0.005, as it enabled full brain coverage in only 5min30, while keeping a very good CSF-contrast and image quality (Fig. 2).

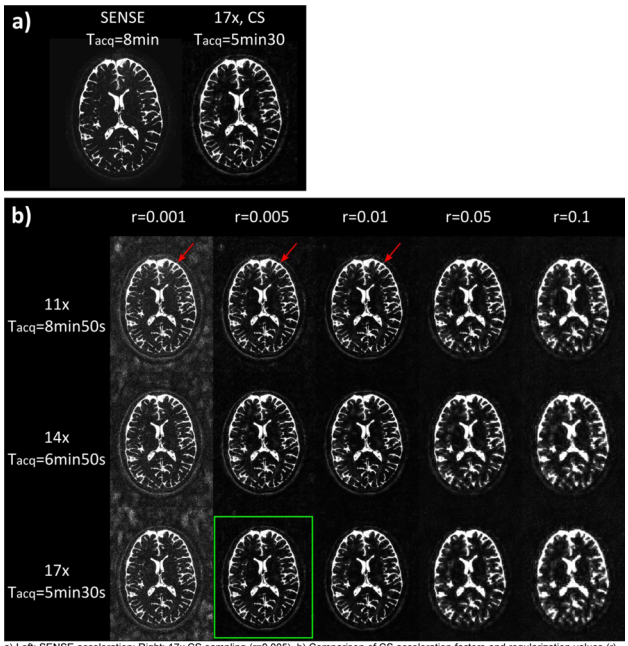

a) Left: SENSE acceleration; Right: 17x CS sampling (r=0.005). b) Comparison of CS acceleration factors and regularization values (r). Red arrows indicate signal leakage artefacts, the green box the optimal parameter combination.

This readout enabled to measure CSF-flow in different brain regions in reasonable scan time (Fig. 3).

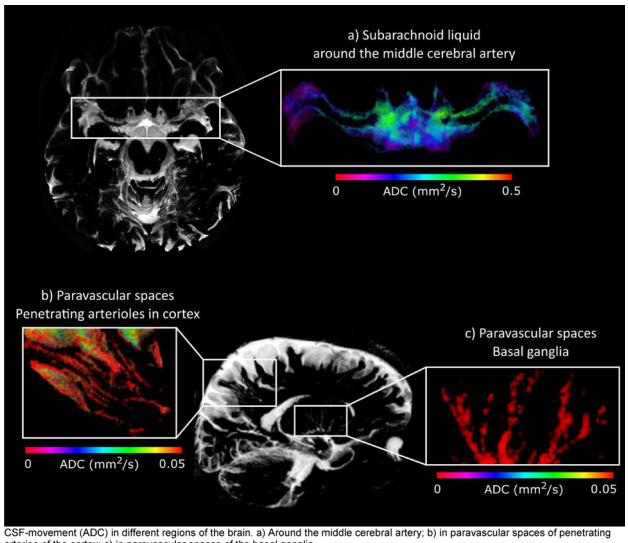

CSF-movement (ADC) in different regions of the brain. a) Around the middle cerebral artery; b) in paravascular spaces of penetrating arteries of the cortex; c) in paravascular spaces of the basal ganglia

Discussion/Conclusion: CSF-movement was measured non-invasively in the full human brain. The 3D-dataset consists of a huge amount of data that calls for more extensive exploration, especially in the paravascular spaces of smaller arteries.

References:

1. Iliff *Sci.Transl.Med.*2012
2. Albargothy, *Acta Neurop.*2018
3. Tarasoff-Conway, *Nat. Rev. Neuro.*2015
4. Hirschler, *ISMRM 2019; 5. Lustig, MRM 2010;* 6. Klein, *IEEE Trans. Med. Imaging* 2010

S19.09

Test–retest reliability of perfusion assessment using BOLD delay

A. Khalil[1], A. C. Tanritanir[1], U. Grittner[2], A. Villringer[3], J. Fiebach[1], R. Mekle[1]
[1]*Charité – Universitätsmedizin Berlin, Center for Stroke Research Berlin, Berlin, Germany,* [2]*Charité – Universitätsmedizin Berlin, Institute of Biometry and Clinical Epidemiology, Berlin, Germany,* [3]*Max Planck Institute for Human Cognitive and Brain Sciences, Department of Neurology, Leipzig, Germany*

Purpose/Introduction: In this study, we assess the test–retest reliability of perfusion values measured using a perfusion imaging method based on resting-state functional MRI (rsfMRI), termed BOLD delay[1], which does not require the use of contrast agents.

Subjects and Methods: Six different openly available data sources[2–7] (healthy individuals) and one study conducted at the Charité Universitätsmedizin Berlin (healthy individuals and stroke patients without perfusion deficits) were analyzed. All subjects were scanned at rest using an rsfMRI sequence (TR = 0.4–3 s, scan length = 4–30 min, depending on the data source; six datasets acquired at 3T and one at 7T). Intervals between the first and second scan ranged from 30 min to 3 months (depending on the data source). rsfMRI data was bandpass filtered (0.01–0.15 Hz), spatially smoothed (4 mm FWHM Gaussian kernel), and realigned to the mean. Using rapidtide[8], the time shift to maximum cross-correlation between the BOLD signal in each voxel and in the venous sinuses was calculated to generate BOLD delay maps. To evaluate their reproducibility, these maps were registered to a custom EPI template[9] and the voxelwise absolute differences between the maps from the first and second scans were calculated (excluding the ventricles). A linear mixed model (with random intercepts for subjects) was used to investigate the association between motion (framewise displacement[10]), scan parameters, age, and absolute differences.

Results: Data from 138 individuals was analyzed. Figure 1 shows the spatial distribution of the absolute differences in BOLD delay values between the study time points, averaged across subjects. Table 1 shows the effect of each independent variable on the absolute differences in BOLD delay, as well as the mean absolute difference (intercept) after accounting for these effects. A mean absolute difference of 2.91 s (95% CI = 1.91–3.89 s) between time points was found.

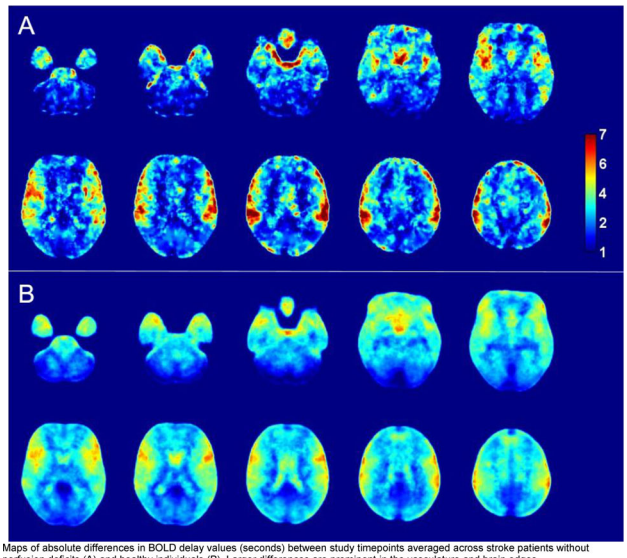

Maps of absolute differences in BOLD delay values (seconds) between study timepoints averaged across stroke patients without perfusion deficits (A) and healthy individuals (B). Larger differences are prominent in the vasculature and brain edges.

Variable	Estimate	Standard error of estimate	P-value
Intercept (mean absolute difference)	2.91	0.5042	<0.0001
Age	0.007	0.0103	0.4995
Framewise displacement	0.009	0.4638	0.5762
Repetition time	-0.102	0.2153	0.6379
Scan length	-0.00012	0.000269	0.6618
Interval between scans	0.0096	0.003901	0.0155

Results of the linear mixed model (dependent variable: BOLD delay absolute differences between study timepoints).

Discussion/Conclusion: Absolute differences in BOLD delay values over time are in the range of $\sim$ 3 s, substantially smaller than changes associated with hypoperfusion seen in cerebrovascular diseases ($>$ 10 s)[11]. The largest differences were in the major cerebral arteries and the edges of the brain. This may reflect subtle changes in cardiorespiratory function or cerebral blood flow between the study time points.

References:

1. Lv, Y. et al. *Ann. Neurol.* (2013).
2. Noble, S. et al. *Cereb. Cortex* (2017).
3. Gordon, E. M. et al. *Neuron* (2017).
4. Dobrushina, O. R. et al. https://openneuro.org/datasets/ds001408/versions/00001.
5. Cera, N. et al. *PLoS One* (2014).
6. Roy, A. et al. *PLoS One* (2017).
7. Gorgolewski, K. J. et al. *Sci. Data* (2015).
8. Erdoğan, S. B. et al. *Front. Hum. Neurosci.* (2016).
9. Khalil, A. A. et al. *Stroke* (2017).
10. Power, J. D. et al. *Neuroimage* (2012).
11. Khalil, A. A. et al. *J. Cereb. Blood Flow Metab.* (2018).

S20 Scientific Session

13:50–15:20 *Room 3 - Ruys & van Rijckevorsel Zaal*

New Technical Applications in Neuroradiology

S20.01

Effect of lactate administration on cerebral blood flow during hypoglycaemia

L. van Meijel[1], E. Wiegers[2], **J. van Asten**[2], C. Tack[1], A. Heerschap[2], M. van der Graaf[2], B. de Galan[2]
[1]Radboud University Medical Center, Internal Medicine, Nijmegen, NETHERLANDS, 2Radboud University Medical Center, Radiology and Nuclear Medicine, Nijmegen, NETHERLANDS

Purpose/Introduction: Impaired awareness of hypoglycaemia (IAH), clinically reflected by the inability to timely detect hypoglycaemia, affects ~ 25% of people with type 1 diabetes (T1DM). Both altered brain lactate handling (including greater transport) and increased cerebral blood flow (CBF) during hypoglycaemia are thought to be involved in the pathogenesis of IAH [1, 2, 3]. It is unknown whether these two effects are linked in patients with diabetes. The aim of the present study was to examine the effect of lactate on CBF and to test if hypoglycaemia has an additional effect.
Subjects and Methods: This was a randomized single-blind, placebo-controlled cross-over intervention study. Eight patients with type 1 diabetes and normal awareness of hypoglycaemia were included (age 22.3 ± 3.0 years, 5 female participants, HbA1c 55.4 ± 10.6 mmol/mol (7.2 ± 1.0%)). They underwent two hyperinsulinaemic euglycaemic-hypoglycaemic glucose clamps in a 3T MR system, once with sodium lactate infusion 50% (600 mmol/l) and once with saline infusion. First, 3D T1-weighted MRI's were acquired. During euglycaemia (25 m), transition (* 25 m) andhypoglycaemia (45 m), CBF-weighted images were acquired continuously using pseudo-continuous ASL (pCASL) with 3D-GRASE read-out and whole-brain coverage (Fraunhofer MEVIS, Germany)with a time resolution of 7 min. Image analysis (i.e., motion correction, susceptibility correction and subtraction of label and control images) was performed in FMRIB Software Library (FSL). CBF was quantified according to the equations and parameters described in Alsop et al. [4], and normalized per subjects to baseline values.
Results: Mean CBF maps during euglycaemia and hypoglycaemia of one participant are depicted (Fig. 1). Glucose levels during euglycaemia and hypoglycaemia averaged 4.6 ± 0.6 and 3.0 ± 0.0 mmol/l versus 4.7 ± 0.4 and 3.0 ± 0.1 mmol/l for the lactate and placebo studies, respectively. Plasma lactate levels during euglycaemia and hypoglycaemia averaged 3.2 ± 0.3 and 3.5 ± 0.6 mmol/l, respectively. Global CBF significantly increased in response to intravenous lactate infusion when compared to placebo infusion (17.6 ± 4.3% vs. - 2.6 ± 2.5%, respectively, change from baseline, p = 0.001) (Fig. 2), but did not further increase upon achieving hypoglycaemia (p = 0.50).

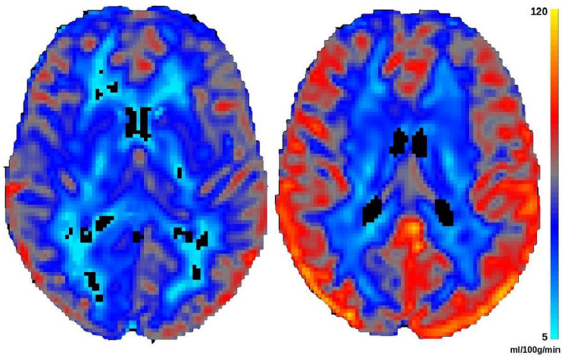

Figure 1. Mean CBF of one participant with lactate infusion during euglycaemia (left) and hypoglycaemia (right)

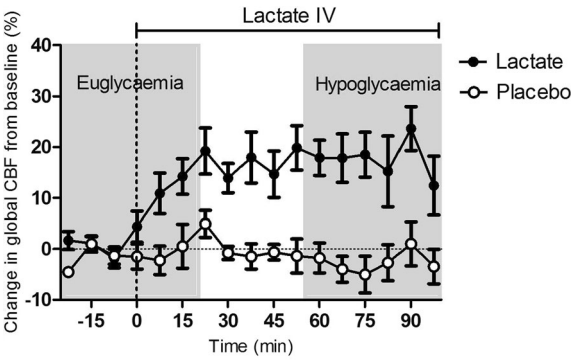

Figure 2. Change in global CBF from baseline (%) during lactate and placebo infusion

Discussion/Conclusion: Lactate infusion caused a marked increase in global CBF in people with T1DM. However, there was no additional effect of hypoglycaemia on global CBF during lactate infusion.
References:
[1] Teves D, et al. 2004, Proc Natl Acad Sci USA 101:6217–6221.
[2] Mangia S, et al., 2012, J Cereb Blood Flow Metab 32:2084–2090.
[3] Wiegers EC, et al. 2018, J Cereb Blood Flow Metab 0:1–9.
[4] Alsop DC, et al. 2015, Magn Reson Med 73: 102–116

S20.02

Fast field-cycling MRI identifies ischaemic stroke at ultra-low magnetic field strength

J. Ross[1], L. Broche[1], M. J. MacLeod[2], D. Lurie[1]
[1]*University of Aberdeen, Aberdeen Biomedical Imaging Centre, Aberdeen, UK,* [2]*Aberdeen Royal Infirmary, Acute Stroke Unit, Aberdeen, UK*

Purpose/Introduction: Fast Field-Cycling MRI[1] (FFC-MRI) is a novel MRI technique in which the external magnetic field is switched rapidly between levels during the imaging experiment. In this way, FFC-MRI gains access to information which is invisible to conventional MRI scanners, especially the variation of T_1 with magnetic field, known as "T_1 dispersion". By performing signal measurements at a relatively high magnetic field, FFC-MRI allows relaxation times below below 1 mT to be probed without the excessive loss of SNR usually incurred at ultra low field. The T_1 values corresponding to these ultra-low magnetic fields are associated with slow molecular

motion with long correlation times, which may have diagnostic value in a wide range of pathologies.

In this work we aimed to assess whether we can identify recent cerebral infarcts at ultra-low field strength, when compared with conventional imaging.

Figure 1: The FFC-MRI system

Subjects and Methods: After informed consent, a group of patients (n = 22) with ischemic stroke were scanned using FFC-MRI within 24–96 h of presentation. Initial diagnosis was performed using CT and/or 3T MRI.

The FFC-MRI scans were performed a home-built field-cycling scanner (Fig. 1) comprised of a resistive magnet with a maximum field strength of 0.2 T. Sets of images from five different evolution fields ranging from 200 mT to 0.2 mT were obtained using a spin-echo readout. The FFC-MRI imaging parameters were: Matrix size 128 × 128, FOV = 280 mm, THK = 10 mm, TE = 24 ms. Total scan duration, including setup time, was approximately 45 min.

Results: In patients with sub-acute ischaemic stroke, T_1-weighted FFC-MRI images exhibited hyper-intense regions, with contrast increasing markedly as the evolution magnetic strength field decreased, to a maximum at the lowest field used (0.2 mT). The infarct region measured by FFC-MRI correlated well with the abnormality in CT and/or DWI images (Examples in Figs. 2, 3).

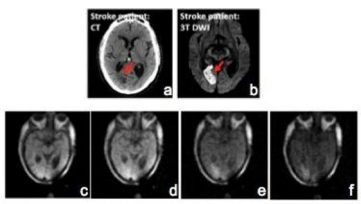

Figure 2: CT, 3T DWI MRI and FFC-MRI images from a patient admitted with a right occipital infarct. a) CT at 24 hours after onset, b) 3T DWI images at 78 hours after onset. c-f) FFC-MRI images at 200 mT, 20 mT, 2mT and 0.2 mT

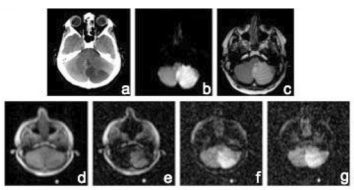

Figure 3: CT, 3T DWI MRI and FFC-MRI images from a patient admitted with a posterior inferior cerebral artery territory infarct. a) CT b) 3T DWI, c) 3T T2 weighted image at 96 hours after onset. d-g) FFC-MRI images at 200 mT, 20 mT, 2 mT and 0.2 mT

Discussion/Conclusion: This is the first-ever clinical application of this new modality, proving that FFC-MRI can generate diagnostic-quality images of ischaemic stroke at ultra-low magnetic fields (e.g. 0.2 mT), with significantly enhanced endogenous T_1-contrast compared to conventional MRI. These findings have implications for future development of a new and safe imaging modality not only for stroke but many other clinical conditions.

References:

Lurie, D. J. et al. Fast field-cycling magnetic resonance imaging. *Comptes Rendus Phys.* **11,** 136–148 (2010).

S20.03

Multiple quantum filtered sodium MRI as a marker for IDH mutational status of cerebral gliomas

W. A. Worthoff[1], A. Shymanskaya[2], G. Stoffels[1], J. Lindemeyer[1], B. Neumaier[3], P. Lohmann[1], N. Galldiks[4], K.-J. Langen[1], N. J. Shah[1]

[1]*Forschungszentrum Jülich, Institute of Neuroscience and Medicine - 4, Jülich, Germany,* [2]*Forschungszentrum Jülich, Institute of Neuroscience and Medicine - 11, Jülich, Germany,* [3]*Forschungszentrum Jülich, Institute of Neuroscience and Medicine - 5, Jülich, Germany,* [4]*Forschungszentrum Jülich, Institute of Neuroscience and Medicine - 3, Jülich, Germany*

Purpose/Introduction: The isocitrate dehydrogenase (IDH) mutation status is an important molecular marker for the classification of brain tumors. In this study, its relationship to restricted and unrestricted sodium signals from multiple quantum filtered sodium MRI data was explored and compared with [^{18}F]-FET-PET.

Subjects and Methods: Ten untreated cerebral gliomas patients (5 IDH wildtype, 5 IDH mutated) underwent dynamic [^{18}F]-FET-PET and sodium MRI using an enhanced SISTINA sequence [1]. Total (NaT), weighted non-restricted (NaNR) and restricted (NaR) sodium in tumors and normal brain tissue was estimated and compared to [^{18}F]-FET uptake in tumors with different IDH mutational statuses. Full neuropathological information, including the IDH mutational status, was available for each patient.

Sodium MRI experiments were carried out at 4T with a dual tuned Na/H birdcage coil for full brain coverage with 10 mm isotropic resolution. The enhanced SISTINA sequence was used [1], yielding multiple quantum filtered (MQF) sodium data in approximately 8 min acquisition time.

FET-PET data were acquired on an ECAT EXACT HR + scanner in 3-dimensional mode (32 rings; axial field of view of 155 mm) up to 50 min after intravenous injection of ~ 200 MBq [^{18}F]-FET. Data were corrected for attenuation, deadtime, as well as for random and scattered coincidences. The reconstructed image resolution is approximately 5.5 mm [2]. Mean and maximum tumor-to-brain ratios (*TBR*) were calculated on summed [^{18}F]-FET-PET images obtained 20–40 min post injection by dividing the mean or the maximal ROI value of the lesion by the mean ROI value of normal brain tissue. If the TBR exceeds a threshold of 1.6, the lesion was considered [^{18}F]-FET positive [3].

Results: IDH mutated gliomas show significantly elevated NaT, NaT/NaR, TBRs of NaT and NaNR, as well as reduced NaR, compared to IDH wildtype gliomas (Fig. 1). [^{18}F]-FET parameters (TBRmean, TBRmax and time-to-peak) did not relate to IDH status or sodium distribution in this group of patients.

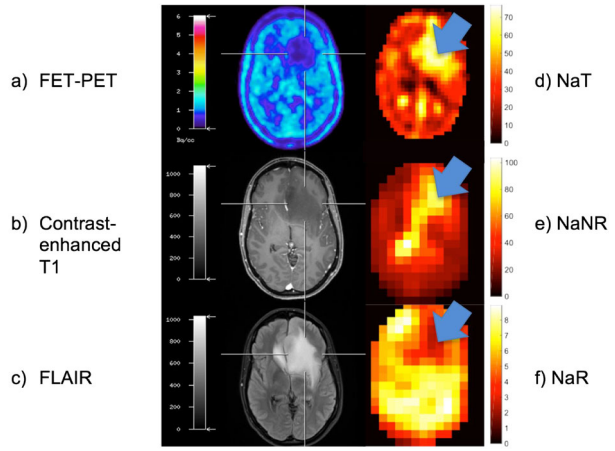

Fig. 1: IDH mutated astrocytoma grade III. a) FET-PET shows no significant tracer uptake. b) little contrast enhancement in the T1-weighted MRI. c) Clearly delineation in FLAIR. d-f) Increased NaT, increased NaNR, and decreased NaR (blue arrow).

Discussion/Conclusion: A strong relationship between sodium MRI and IDH mutational status is apparent in this study, while [^{18}F]-FET-PET does not discriminate between IDH mutated and IDH wildtype gliomas. It can, therefore, be hypothesised that sodium signal and amino acid transport reflect different metabolic properties and, thus, carry complimentary information.

References:

1. Worthoff, Shymanskaya, Shah. MRM 2019; 81(1):303–315.
2. Herzog et al. IEEE T Nucl Sci 2004; 51:2662–9.
3. Pauleit et al. Brain 2005; 128:678–87.

S20.04

Multiscale fMRI entropy declines with age and is greater in women

C. de Vries[1], R. Staff[2], G. Waiter[1], M. Sokunbi[3], A. Sandu[1], A. Murray[1]
[1]*University of Aberdeen, Aberdeen Biomedical Imaging Centre, Aberdeen, UK,* [2]*NHS Grampian, Imaging Physics, Aberdeen, UK,* [3]*De Montfrot University, Faculty of Health and Life Sciences, Leicester, UK*

Purpose/Introduction: Lipsitz and Goldberger hypothesised that ageing and diseased systems lose complexity inherent to healthy systems[1]. Higher resting-state fMRI brain entropy, a measure of complexity, has been observed in younger, more intelligent individuals[2, 3]. Here, we examined the association between multiscale entropy and age and sex for a large Scottish sample (N = 715).

We have previously shown that simple corrections for patient movement do not fully account for the possible confounding effect of motion on fMRI brain entropy measures[4]. In addition, most entropy analyses have been performed at a single time scale. Multiscale entropy, which considers multiple time scales, is a more complete measure of entropy/complexity.

Using multilevel mixed modelling, we considered the time-scales and their trajectory in one model, while stringently correcting for head motion. We hypothesised that entropy declines with age after correction for movement and sex.

Subjects and Methods: Multiscale brain entropy (scale 1–5) was calculated for the STRADL sample, which consists of individuals born in Aberdeen between 1950 and 1956 (aged 58–65; N = 281), their first degree relatives (aged 26–85; N = 260), and individuals born in Dundee (aged 48–77; N = 174). The resting-state fMRI scans were realigned, followed by nuisance regression of the head motion parameters. Fuzzy approximate entropy with high-pass filter (0.008 Hz) and fuzzy sample entropy with band-pass filter (0.008–0.1 Hz) were calculated for every voxel. Next, the mean entropy in 95 AAL regions was extracted.

Multilevel mixed modelling was employed to examine associations between multiscale entropy and age and sex. Six log-transformed measures of head motion during acquisition (mean displacement and rotation in 3D) were included in the model to correct for the effect of motion. The relationship between scales and entropy was modelled as a reciprocal for fuzzy approximate entropy (1/scale), and as a quadratic (scale^2) for fuzzy sample entropy.

Results: Sex and age were associated with multiscale entropy for both methods at multiple locations throughout the brain ($p < 0.001$). Age showed a negative association with entropy. In addition, women had greater entropy than men.

Discussion/Conclusion: These results support the Lipsitz/Goldberger hypothesis that biological systems lose complexity with age[1]. Here, we show a decline in brain entropy with age, after stringent motion correction. This decline likely reflects the neuro-degeneration inherent in ageing. Furthermore, these findings show that women have greater brain complexity than men. This has previously been observed when examining the effect of smoking on brain entropy[5].

References:

[1]Lipsitz (1992) Jama
[2]Sokunbi (2011) IEEE Transactions on Biomedical Engineering
[3]Sokunbi (2014) Frontiers in neuroinformatics
[4]de Vries (2019) IEEE JBHI
[5]Li (2016) Scientific reports

S20.05

Quantitative susceptibility mapping (QSM): Echo time dependence in the human and nonhuman primate brain

R. Dadarwal, A. Moussavi, S. Boretius
German Primate Center, Functional Imaging Laboratory, Goettingen, Germany

Purpose/Introduction: Quantitative Susceptibility Mapping (QSM) has been shown to be sensitive to local variations in tissue structure and chemical composition of the brain[1, 2]. These local variations at the sub-voxel level affect both the magnitude and phase of the measured gradient echo signal[3]. Recent studies have shown that gradient echo reconstructed QSM maps are extremely sensitive to the acquisition parameters which is true especially for the echo time (TE), where a small change may produce drastic differences in the resultant magnetic susceptibility values[4, 5]. This study is aimed to assess TE dependence of magnetic susceptibility for brain areas in humans and long-tailed macaques (*Cynomolgus monkey*).

Subjects and Methods: Data acquisition: 6 healthy adult female volunteers (age:23–29 years) and 5 healthy adult female monkeys (age:7–9 years) were scanned at a field strength of 3T (MAGNETOM Prisma, Siemens) using a 3D multi-echo gradient echo (GRE) sequence with almost identical acquisition parameters: $(TE)_1$/spacing/TE_9/TE_{10} = 3.7/4.9/43/50.4 ms, repetition time (TR) = 57 ms, flip angle (FA) = 20°, and spatial resolution of 0.75 × 0.75 × 0.75 mm^3 and 0.312 × 0.312 × 0.310 mm^3 for humans and monkeys, respectively.

Data analysis: QSM data analysis pipeline, applied likewise for humans and monkeys, is schematically illustrated in Fig. 1. To discern QSM TE dependence, single echo QSM maps were reconstructed using QSMbox[6] and were referenced to whole brain magnetic susceptibility. Segmented brain areas on QSM template are shown in Fig. 2.

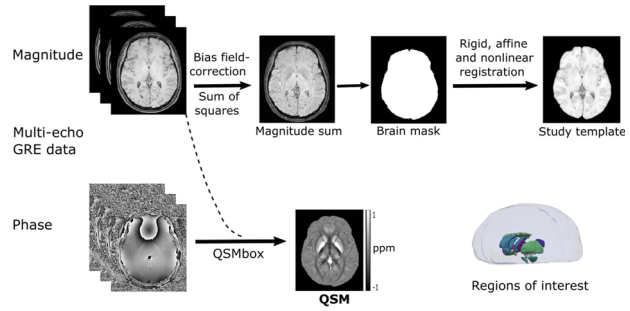

Figure 1. Schematic illustration of the data analysis pipeline.

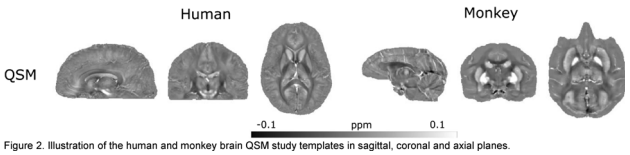

Figure 2. Illustration of the human and monkey brain QSM study templates in sagittal, coronal and axial planes.

Results: Humans and monkeys revealed susceptibility TE dependence in grey and white matter, although to a different extent and the respective profiles varied between brain regions (Fig. 3). Larger structures such as corpus callosum showed stronger heterogeneity within the structure, reflected by different TE profiles of its substructures like the genu, splenium, and body. The middle thalamus, external globus pallidus, red nucleus, internal capsule, anterior commissure, habenula tract and parts of the corpus callosum revealed the same shape of the TE-profile in humans and monkeys but a shift towards higher susceptibility values in humans. In contrast, the putamen, substantia nigra, insula, internal globus pallidus, and cingulum showed similar temporal susceptibility profiles in humans and monkeys.

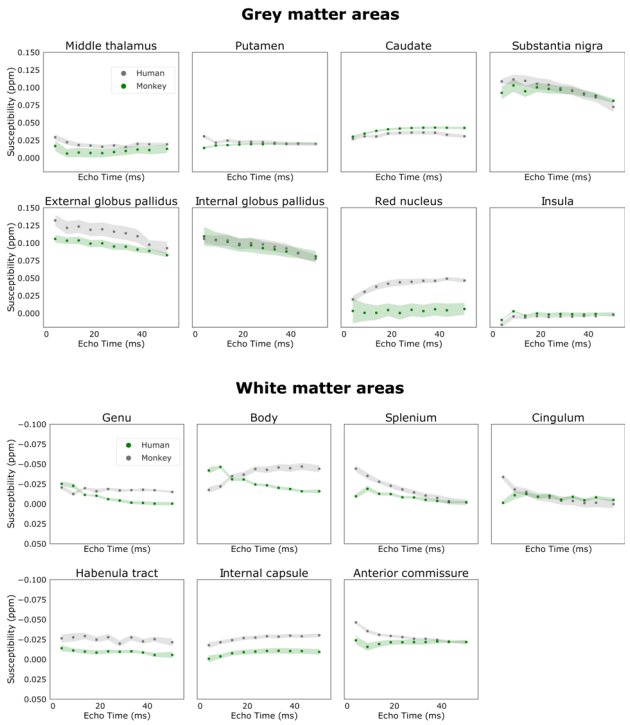

Figure 3. Susceptibility values as a function of echo time for different brain areas. Individual plots show the susceptibility temporal response for the group mean (thin dotted line) and confidence interval (shaded area).

Discussion/Conclusion: The observed species and structure-dependent influence of TE on the susceptibility values may provide important insight into the tissue microstructure of the brain. However, the underlying mechanism is still hardly understood and further studies comparing QSM results with quantitative histology are required.

References:

1. Acosta-Cabronero et al., PLOS ONE; 2013.
2. Haacke et al., Magn. Res. Imaging; 2015.
3. Cronin and Bowtell et al., Scientific Reports; 2018.
4. Sood et al., Magn. Res. in Medicine; 2017.
5. Cronin et al., NeuroImage; 2017.
6. Acosta-Cabronero et al., NeuroImage; 2018.

S20.06

qMRI grey matter microstructural changes predict healthy aging and identify Multiple Sclerosis

A. Erramuzpe[1], R. Schurr[2], A. Mezer[2]
[1]*Hebrew University of Jerusalem, ELSC, Jerusalen, Israel,* [2]*Hebrew University of Jerusalem, ELSC, Jerusalem, Israel*

Purpose/Introduction: Aging is a dynamical process that encompasses a systemic time-dependent decline on multiple scales. Individuals with the same chronological age (ChA, time past since being born) might exhibit different trajectories of the biological age. Being able to build an accurate prediction model of healthy aging has been proposed to be useful to identify cases where the biological age has been altered due to a disease or external biomarkers. Quantitative MRI (qMRI) can provide additional and accurate information (with respect to biophysical properties). qMRI is also changing as a function of a disease state such as multiple sclerosis (MS). It has been shown that qMRI parameters are sensitive to brain changes in MS even in cases where the tissue appear normal using conventional MRI (Mezer, 2013).

In this study, we make use of qMRI to predict healthy aging using a linear model of T1 values along multiple cortical regions and we use the same model to predict the age of MS patients. Importantly, we find that MS patients are predicted to be older even when the areas used are free of visible MS lessons.

Subjects and Methods: We used the dataset from (Yeatman, 2014) ($N = 86$, $7 < age < 85$). In addition, we included 9 patients with MS acquired in the same scan. The analysis pipeline for producing the unbiased T1 maps is an open source tool available at (https://github.com/mezera/mrQ). FreeSurfer was used to segment the cortex in 148 regions and T1 mean values were extracted for each individual, used as features for the linear regression model.

Results: A linear model was built and age was estimated splitting the data into two subsets (young and adults). After cross-validation, the young group ($N1 = 41$, $7 < age < 22$) obtained a mean absolute error (MAE) of 0.81 years and the group of adults ($N2 = 45$, $22 <= age <= 85$) MAE equal to 3.3 years. Finally, the MS group (using only the normal appearing brain regions) was tested against the trained model of adult subjects, obtaining a MAE of 30.7 years.

Discussion/Conclusion: Quantitative T1 enables to model subject age very accurately. The key to our study is not only maximizing the model performance but showing that we can estimate age using qMRI features from multiple cortical regions. Thus, we are able to link the process of aging and the change of cortical tissue properties obtained from qMRI parameters that are thought as in vivo histological tools. Finally, we are able to demonstrate that MS patients are predicted older than their real age; using qMRI we are showing that their cortical microstructural composition changed, whilst these changes cannot be perceived with standard imaging techniques.

References:
Yeatman, J. D., Wandell, B. A., & Mezer, A. A. (2014). Lifespan maturation and degeneration of human brain white matter. NatCom, 5, 4932.
Mezer, A., et al. (2013). Quantifying the local tissue volume and composition in individual brains with magnetic resonance imaging. NatMed, 19(12), 1667.

S20.07

Resting state BOLD signal, functional connectivity, and neural dynamics modeling

M. E. Archila-Meléndez, C. Sorg, C. Preibisch
Technische Universität München, Department of Diagnostic and Interventional Neuroradiology, Klinikum rechts der Isar, Fakultät für Medizin, Munich, Germany

Purpose/Introduction: Brain activity can be evaluated non-invasively by the blood oxygenation level dependent (BOLD) signal. BOLD signal's capabilities to report the underlying neuronal activity relies on the assumption of a tight coupling between neuronal activity and subsequent vascular-hemodynamic processes. This neurovascular coupling is especially dependent on changes in cerebral blood flow (CBF) and cerebral metabolic rate of oxygen (CMRO2). The precise mechanisms responsible for neurovascular coupling are matter of continuous debate and research as well as the influence of impairments of those parameters on the BOLD signal. Especially, the precision with which the ongoing neuronal activity is reflected by the BOLD signal during 'rest' and derived BOLD-based measures is not completely understood. Therefore, in this study we aimed to investigate the influence of CBF and CMRO2 amplitude changes on the measured BOLD signal, and particularly on BOLD functional connectivity at rest by modeling.

Subjects and Methods: To explore the influence of neurovascular coupling on functional connectivity, BOLD signals were simulated using a dynamic model based on the balloon model assuming tight coupling,[1, 2] for different combinations of normalised CBF and CMRO2 amplitude changes, f1 (1.0–1.75) and m1 (1.0–1.375), respectively. The neural input was modeled as a dynamic relationship (amplitude-amplitude coupling) between gamma (60 Hz), alpha (10 Hz) and ultra-slow modulatory (0.05 Hz) oscillations[3]. Different SNR levels (1000–125) were modeled by adding random noise to the simulated BOLD signal (S_{BOLD}). Finally, we calculated correlation coefficients (CC) between S_{BOLD} with different f1 and m1 for all SNR levels to get insight into the interaction between vascular components influencing the BOLD signal (Fig. 1).

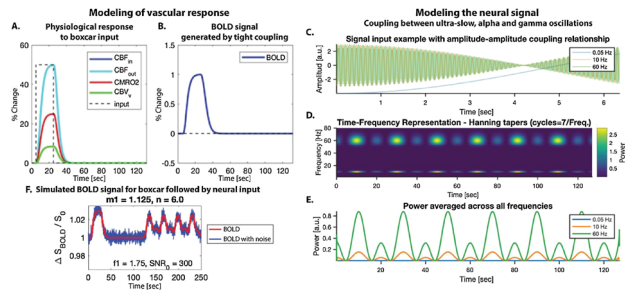

Fig. 1. A) Physiological response. B) BOLD signal. C) Simulated neural signal input. D) Time-frequency representation. E) Power used as the input for the BOLD simulations. F) BOLD signal for boxcar followed by neuronal input with and without noise.

Results: S_{BOLD} reflected the amplitude modulation in power generated by ultra-slow oscillations. S_{BOLD} evolved from negative responses for all CMRO2 amplitudes (m1 = 1.0–1.375) at constant CBF, i.e., f1 = 1.0, to positive responses for all CMRO2 amplitudes at max. CBF change amplitude, f1 = 1.75 (Fig. 2). Accordingly, the CC varied between negative and positive values for different SNR levels (Fig. 3). For SNR between 150 and 250, correlation coefficients ranged between 0.4 and 0.3, as commonly found in rs-fMRI connectivity analyses.

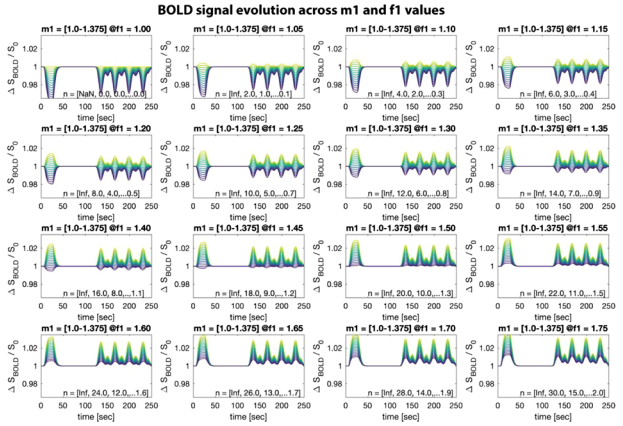

Fig. 2. Evolution of the simulated BOLD signal for different m1 and f1 combinations. Each plot shows the BOLD signal for all values of m1 at a fixed value of f1. The BOLD signal varied from all negative (top left) to all positive (bottom right).

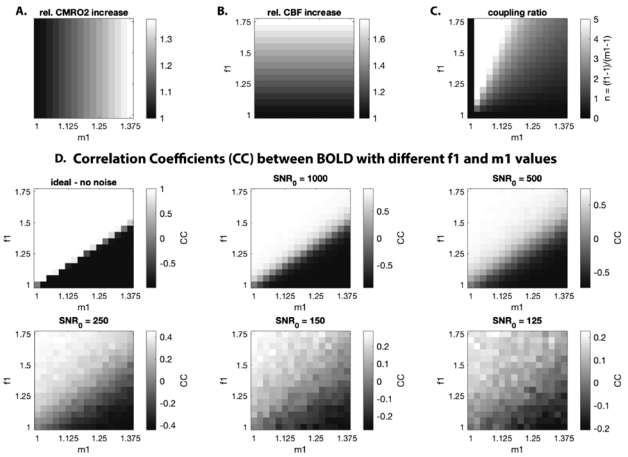

Fig.3. Range of investigated m1 (A), and f1 amplitude changes (B) and their coupling ratio n=(f1-1)/(m1-1) (C). D) Correlation coefficients between simulated BOLD signals depending on m1 (A) and f1 (B) at different SNR levels between 1000 and 125.

Discussion/Conclusion: Our results show the importance of neurovascular coupling for an adequate reflection of the underlying neuronal input and therefore the meaningful estimation of intrinsic functional connectivity analysis. Accurate modeling of the hemodynamic coupling can help to gain insights on the crucial interplay between vascular-hemodynamic components that should be taken into account when estimating intrinsic functional connectivity, especially in patients with potential vascular pathologies.

References:
1. Simon and Buxton, NI, 2015
2. Chu et al., NI, 2018
3. Michalareas et al., Neuron, 2016

S20.08

A BIDS compliant automated CSD fiber tracking pipeline for presurgical white matter mapping

A. Radwan[1], J. Blommaert[2], S. Kovacs[3], R. Peeters[1], S. De Vleeschouwer[4], P. Dupont[5], T. Theys[4], S. Sunaert[1]
[1]*KU Leuven, Department of Imaging & Pathology, Translational MRI, Leuven, Belgium,* [2]*KU Leuven, Department of Oncology, Gynaecological Oncology, Leuven, Belgium,* [3]*UZ Leuven, Department of Radiology, Leuven, Belgium, Belgium,* [4]*KU Leuven, Department of Neurosciences, Research group experimental neurosurgery and neuroanatomy, Leuven, Belgium,* [5]*KU Leuven, Department of Neurosciences, Laboratory for Cognitive Neurology, Leuven, Belgium*

Purpose/Introduction: Current clinical presurgical white matter mapping relies on Diffusion Tensor imaging (DTI) with manual deterministic fiber tractography. This approach has several drawbacks, among which the inability to resolve different fiber orientations inside a single voxel. Furthermore, the manual nature of this workflow introduces user bias, requires experienced personnel and is labor-intensive. In this work we introduce a brain imaging data structure (BIDS) compliant subject specific automated fiber tracking pipeline using Constrained spherical deconvolution (CSD).

Subjects and Methods: We included 10 novel neurosurgery patients in need of a presurgical fMRI and DTI mapping scan. T1 images (isotropic 0.9 mm) and diffusion images (b values: 0, 1200, 2500 with resp. 7, 128, 128 directions and 4 reversed phase b0 s, $2 \times 2 \times 2$ mm voxels) were acquired on a Philips 3T Achieva scanner and were preprocessed using Freesurfer and MRtrix respectively. Brain parcellation of the T1 was performed by Freesurfer, diffusion preprocessing included denoising, correction of eddy currents, susceptibility distortion, and bias. The resulting anatomical labels informed the probabilistic CSD tractography (iFOD2, MRTrix) for specific fiber bundles relevant to presurgical planning (see Fig. 1). Spurious fibers were removed when passing through voxels where less than 0.3% of streamlines traverse.

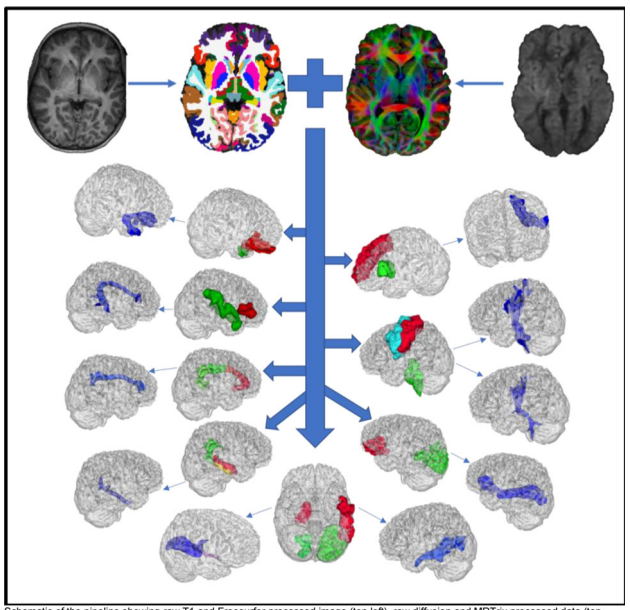

Schematic of the pipeline showing raw T1 and Freesurfer processed image (top left), raw diffusion and MRTrix processed data (top right), & the resulting VOIs used as seeds for CSD iFOD2 tractography with the reconstructed fiber bundles shown in blue

Results: A BIDS compliant automated CSD fiber tracking pipeline ran successfully in 10 patients with varying pathologies. Compared with the manual DTI tractography based method, our results show that CSD allows more accurate representation of the tracked bundles as it can resolve multiple fiber orientations within a single voxel, thus reconstructing fiber bundles that pose a challenge to the DTI approach, such as the optic radiations[1] and the temporo-insular bundles[2]. Figure 2 shows an example from a patient with a left thalamic lesion, where manual DTI tractography failed to identify an anatomically sound trajectory for the optic radiation on the healthy side and heavily underestimated the streamline count (SC) on the diseased side (DTI SC = 3 and CSD SC = 5032).

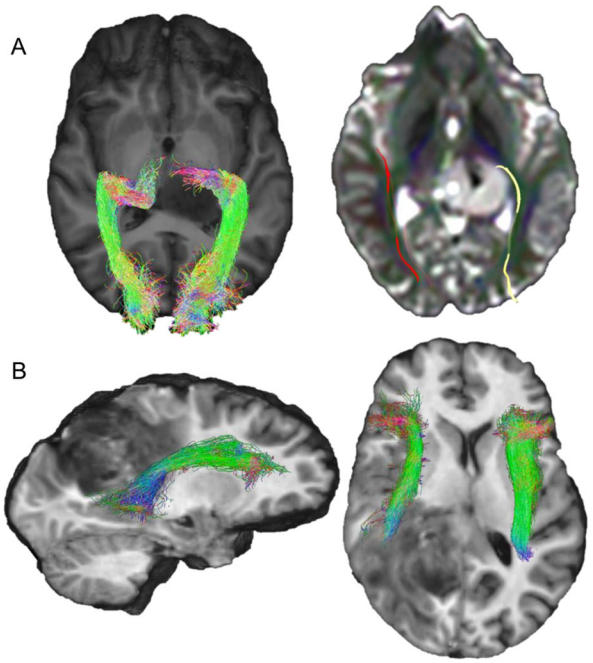

A) ORs using the proposed CSD based method (L) & standard DTI method (R) in a patient with a left thalamic central neurocytoma. B) Arcuate fasciculus with CSD in a patient with an anaplastic oligodendroglioma DTI failed to produce the right AF.

Discussion/Conclusion: The proposed method has several advantages over manual DTI tractography. First it is fully automated, precluding the need for manual intervention and thus avoiding user bias. Next, it uses state-of-the-art preprocessing and is largely stable in the presence of pathology. However, the Freesurfer parcellation may fail in the presence of large lesions. Future work will allow a more quantitative comparison of CSD to DTI results, as well as developing a strategy to avoid Freesurfer parcellation failure in the presence of large lesions. Finally, increasing the sample size will allow statistical group wise comparison of both methods.

References:

1. Winston GP, et al. *Epilepsy Res*. 2011; 97(1–2):124–132.
2. Nachtergaele P, et al. *J Neurosurg*. 2019; 22:1–9.

S20.09

Characterization of in utero brain development after fetal surgery using super-resolution reconstruction

K. Payette[1], R. Tuura[2], M. Meuli[3], A. Jakab[4]
[1]*University Children's Hospital Zurich, Center for MR Research, Zurich, Switzerland,* [2]*University Children's Hospital Zurich, Center for MR-Research, Zurich, Switzerland,* [3]*University Children's*

Hospital Zurich, Spina Bifida Center, Zurich, Switzerland, [4]*University Children's Hospital Zurich, Center for MR-Research, Zurich, Switzerland*

Purpose/Introduction: Fetal MRI is increasingly important for prenatal counselling, particularly in neural tube defects that result in spina bifida myelomeningocele (MMC). In specialized centers, in utero repair of the MMC shows clear benefits by improving postnatal neurological outcomes[1]. Our purpose was to characterize the longitudinal morphological changes that the fetal brain undergoes postoperatively, and evaluate if lesion size, type, location, or age of the fetus at surgery have an impact on brain growth.

Subjects and Methods: Surgical repair of MMC lesions was carried out in 85 subjects with pre- and post-operative MRIs. MRI was acquired on 1.5T and 3T whole-body scanners using a T2-weighted single-shot fast spin echo sequence (SSFSE). We reconstructed multiple orthogonal SSFSE images into high resolution 3D volumes using the total variation super-resolution (SR) reconstruction algorithm[2]. 43 cases had high quality pre and post op images, while the remaining cases were excluded due to poor SR reconstructions. Brain growth between the images was determined using voxel-based morphometry. The average age of the subjects is as follows: pre-op scans: 23.6 $\pm$ 1.4 gestational weeks (GW); surgery: 25.1 $\pm$ 0.8 GW; post-op scans: 27.5 $\pm$ 1.0 GW. The effect of lesion size (area), lesion type (MMC or Myeloschisis), lesion location, and GW at operation on regional brain growth was analyzed using a general linear model[3].

Results: Lesion size was significantly associated with the variability of fetal brain growth in the brain parenchyma around the midline, in the anterior part of the lateral ventricles, posteriorly, as well as in the external CSF spaces ($p < 0.05$, see Fig.). We found differences in growth when comparing MMC (n = 27) vs Myeloschisis (n = 15), mostly in the right lobar gray and white matter, as well as posteriorly ($p > 0.1$). No differences in brain growth were found in GW at surgery, or lesion location.

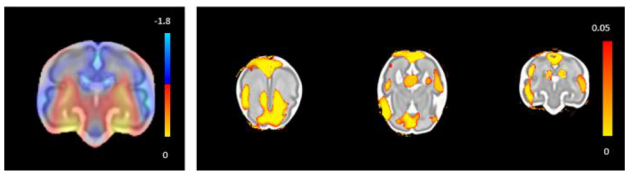

Left: Average growth map Right: Areas of brain growth affected by lesion size ($p<0.05$)

Discussion/Conclusion: We revealed a characteristic link between regional brain growth patterns and MMC size during the crucial perioperative fetal period in cases undergoing fetal surgery. Cystic lesions and myeloschisis affected growth patterns differently, however, there was an unequal sample size between the two groups. No differences were found when looking at lesion location or gestational age at operation. A larger sample size is needed before it can be confirmed a link between age at operation and brain growth patterns.

References:

1. Meuli, M. & Moehrlen, U. Fetal surgery for myelomeningocele is effective: a critical look at the whys. *Pediatr. Surg. Int.* **30**, 689–697 (2014).

2. Tourbier, S. et al. An efficient total variation algorithm for super-resolution in fetal brain MRI with adaptive regularization. *NeuroImage* **118**, 584–597 (2015)

3. Winkler, A. M., Ridgway, G. R., Webster, M. A., Smith, S. M. & Nichols, T. E. Permutation inference for the general linear model. *NeuroImage* **92**, 381–397 (2014)

S21 Scientific Session

13:50–15:20 *Room 4 - Plate & Van der Vorm Zaal*

Quantitative MRI

S21.01
Quantification of sodium T1 in abdominal tissues at 3 Tesla

R. Gomolka, A. Meier, A. Ciritsis, C. Rossi
University Hospital Zurich, Department of Diagnostic and Interventional Radiology, Zurich, Switzerland

Purpose/Introduction: Introduction:
Sodium (^{23}Na) is the second most common magnetic resonance (MR) active nucleus in the human body and is involved in multiple endocrine pathways controlling the blood pressure, and the osmotic and electrolyte balance [1]. Hence, ^{23}Na imaging method of choice is desired in biomedical applications [2–4]. Although relevant for the accurate assessment of sodium dysfunction in multiple endocrine pathways, ^{23}Na-T1 quantification is challenging due to technical limitations (SAR, B1 inhomogeneity), and to the influence of tissue's local molecular dynamics. Hereby, we propose T1 quantification of ^{23}Na-MRI signal acquired over the abdomen using a centric reordered 3D saturation-recovery (SR) true fast imaging with steady state precession (TrueFISP) sequence.
Subjects and Methods: Subjects and Methods:
Sodium signal measurements were performed at 3 T using a dual-tunable ^{23}Na/^{1}H coil in 10 healthy volunteers, by means of 3D TrueFISP (TR/TE = 1300/1.5 ms; flip angle = 90°; bandwidth = 450 Hz/px; voxel size = 5 × 5 × 10 mm^3). Variable T1-weighting was achieved by non-selective saturation pre-pulses delayed from the centre of the k-space acquisition by 25, 50, 70, 180 and 300 ms. T1 measurements were also performed in an in-house phantom (distilled water solution of 0.6% NaCl + 0.004% $CuSO_4$) using prepulses of 25, 50, 120, 300 and 500 ms. Biexponential fitting was performed to account for quadrupole interactions in the renal parenchyma, the spinal cord, as well as in the phantom.
Results: Minimal average of residuals was computed for a relative ratio of $T1_{slow}/T1_{fast}$ components of 0.65/0.35 forming biexponential curve, for both tissues. Mean ± standard deviation (SD) of $T1_{slow}$ component was 37 ± 17 ms for the renal parenchyma and 52 ± 17 ms for the spinal cord. In the water solution, the ratio was found as 0.8/0.2 and mean ± SD $T1_{slow}$ time calculated slice-wise was 51 ± 19 ms.
Discussion/Conclusion: Conclusion:
^{23}Na-T1 quantification using a SR-TrueFISP is feasible in clinical settings and biexponential fitting accounts for tissue-specific differences in molecular dynamics.
References:
1. Patel S, Rauf A, Khan H, Abu-Izneid T (2017) Renin–angiotensin–aldosterone (RAAS): The ubiquitous system for homeostasis and pathologies. Biomed Pharmacother 94:317–325.
2. Madelin G, Regatte RR (2013) Biomedical applications of sodium MRI in vivo. J Magn Reson Imaging 38 (3):511–529.
3. Thulborn KR (2018) Quantitative sodium MR imaging: A review of its evolving role in medicine. Neuroimage 168:250–268.
4. Bottomley PA (2012) Sodium MRI in Man: Technique and Findings. In: Harris RK, Wasylishen RE (eds) Encyclopedia of Magnetic Resonance (eMagRes), vol 1. Wiley: Chichester, pp 353– 366.

S21.02
A simplified approach to quantification of multiple contrasts from time-encoded ASL

L. Vaclavu[1], C. Falcon[2], J. Domingo[2], P. Montesinos Suárez de la Vega[3], M. J. van Osch[1]
[1]*Leiden University Medical Center, Department of Radiology, Leiden, The Netherlands,* [2]*BarcelonaBeta Brain Research Center, Barcelona, Spain,* [3]*Philips Iberia, Madrid, Spain*

Purpose/Introduction: Time-encoded ASL (TE-ASL) allows quantification of multiple contrasts such as arterial transit time (ATT), arterial blood volume (aBV) as well as cerebral blood flow (CBF). However, the dependence on offline post-processing could be considered a barrier to clinical implementation of the technique. The aim of this study was to develop a simplified method of quantifying multi-contrast maps from TE-ASL data. We hypothesised that this could be achieved by isolating the macrovascular and microvascular components of the arterial signal using a two-step fitting method, similar to what is implemented in the BASIL toolbox.
Subjects and Methods: TE-ASL images were acquired on a 3T clinical MR system (Philips Healthcare, Best, The Netherlands) with a 32-channel head coil and body coil transmission. The sequence parameters were: 2D GE EPI read-out to capture of time-course of images at 7 inversion times (35–3800 ms following labelling.

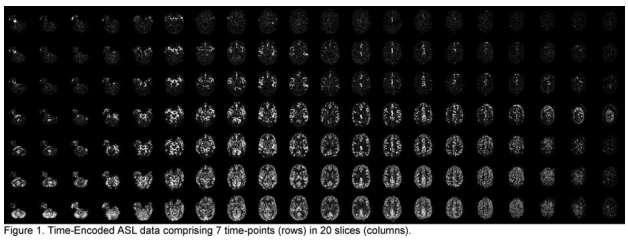
Figure 1. Time-Encoded ASL data comprising 7 time-points (rows) in 20 slices (columns).

two background suppression pulses; TR/TE 4496/12.53 ms; 96 × 96 matrix; field of view 220 × 220 × 120, voxel size 2.29 × 2.29 × 6 mm; flip angle 90°; 20 slices. After subtraction with the Hadamard matrix, ASL images were processed in BASIL FSL (FMRIB, Oxford) to obtain reference CBF, ATT and aBV maps. For the proposed two-step method, a Buxton curve was first calculated in the image with the longest PLD (bottom row in Fig. 1), and subtracted from the initial time-curve. A macrovascular model (Chappell et al. 2010) was fitted to this resulting 'non-perfusion' signal to isolate the intravascular blood volume component (aBV). After subtraction of this macrovascular signal from the initial time-curve, a Buxton-curve was fitted to obtain the CBF and ATT.
Results:

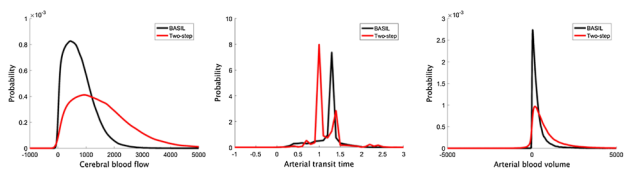

Figure 3. Histograms of CBF, ATT and aBV comparing the two-step method to BASIL in 5 volunteers. CBF was overestimated in the Two-step method with more variation and a longer trailing edge reflecting the higher values not removed by the macrovascular fit. The ATT from the two-step method showed two distinct peaks, one at an early arrival time around 1 second, possibly reflecting the macrovascular signal arrival time. The blood volume showed more variation in the two-step method and a longer trailing edge reflecting higher values in the two-step method

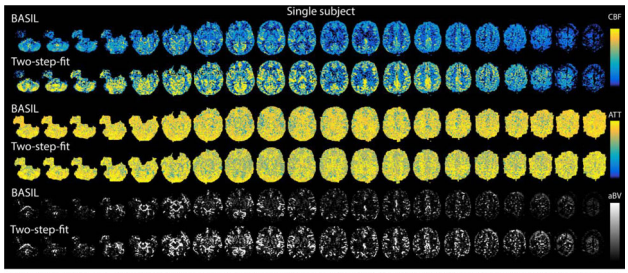

Figure 2. Examples of CBF, ATT and aBV maps processed in BASIL and using the proposed two-step fitting procedure. The two-step method produced similar CBF maps to the BASIL method albeit quantitatively overestimated CBF and aBV compared to BASIL. The CBF showed a longer trailing edge on histogram analysis with more variation than BASIL.

In general, the two-step method and BASIL produced visually similar maps (**Fig. 2**). Histogram analysis showed that variation was higher and that there was a longer trailing edge particularly for CBF. The two-step method assigned more voxels to macrovascular signal than BASIL, resulting in less zero voxels in the aBV maps form two-step (n = 130,309) compared to BASIL (n = 155,357, $P < 0.01$). Results from the 5 volunteers also showed higher CBF and aBV i the two-step method, and showed two distinct arrival times for the two-step method (**Fig. 3**).

Discussion/Conclusion: Both CBF and aBV were quantitatively higher for the two-step method but showed visually similar results to BASIL. The higher aBV in the two-step method could have been due to false assignment of tissue signal to macrovascular signal or inclusion of noise. In BASIL, the use of Bayesian inference may minimise these errors, as well as minimise variation. In conclusion, a simplified two-step method was feasible to quantify multiple contrasts which were visually similar to the parameters quantified from BASIL.

References:

Chappell et al. Magnetic Resonance in Medicine 63:1357–1365 (2010)

S21.03

MESMERISED: super-accelerated 7T STEAM imaging for quantitative T_1 and diffusion MRI

F. J. Fritz, B. A. Poser, A. Roebroeck
Maastricht University, Cognitive Neuroscience, Maastricht, The Netherlands

Purpose/Introduction: There is an increasing interest in quantitative imaging (qMRI) of T_1, T_2 (qT_1 and qT_2) and diffusion contrast due to greater robustness against bias fields and artefacts, as well as better biophysical interpretability. However, acquisition time constraints increase when combined T_1/T_2/ADC measurements are needed. Although UHF ($\geq$ 7T) has desirable properties for many MR modalities, the shortening T_2s and the high SAR load of inversion/refocusing pulses bring challenges for qMRI. It is well known that STEAM has advantages that can overcome some of those limitations but it results in long TRs and acquisition times which severely restricts time efficiency. In this work, we present the MESMERISED (**M**ultiplexed **E**cho **S**hifted **M**ultiband **E**xcited and **R**ecalled **I**maging of **S**team **E**ncoded **D**iffusion) sequence to achieve super-accelerated 7T STEAM imaging, by combining echo shifting[1] (ES) and multi-band (MB) acceleration. This leads to very high multiplicative acceleration factors and time efficiency for 7T T_1-weighted (T_1w) and diffusion (dMRI) imaging.

Subjects and Methods:

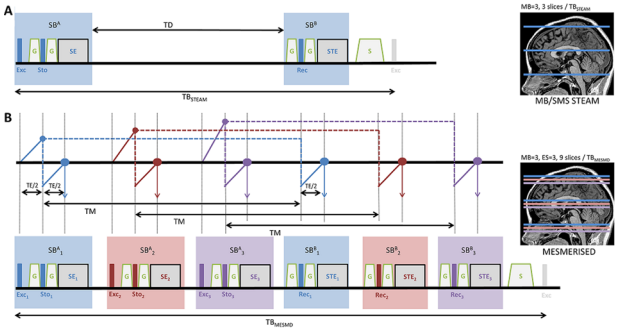

MB-STEAM (A) vs MESMERISED (B). MB-STEAM acquires MB slices per block, leaving considerable dead-time (TD). In contrast, MESMERISED sequence utilizes this TD by echo shifting one or more SB^A blocks (here ES = 3), acquiring MBxES slices per block

Fig 1 shows the MESMERISED sequence in comparison to MB-accelerated STEAM. MESMERISED combines blipped-CAIPI MB-EPI[2] with ES of multiple stimulated-echoes (STEs). The ES is independent of MB acceleration and allows high multiplicative ESxMB acceleration factors. MESMERISED was implemented and tested on one healthy subject on a Magnetom Siemens 7T human MRI system using several resolutions (from 2.0 to 1.5 mm isotropic) for different modalities (T_1w and dMRI) and ESxMB combinations. Fat-unfocussing was achieved by appropriate pulse lengths and BWTP combination[3]. T_1w relaxometry and dMRI data were distortion corrected, and dMRI was analyzed using DTI, BallStick$_{r2}$ & NODDI.

Results:

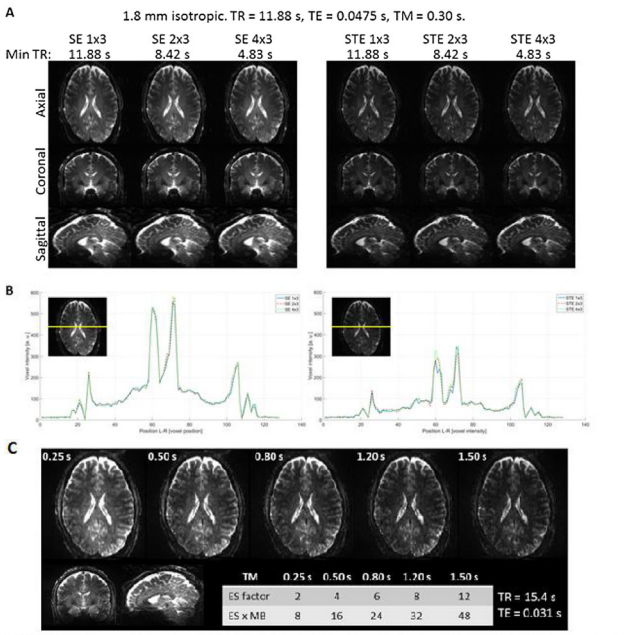

A. MESMERISED images at 1.8 mm iso. with ESxMB=(1,2,4)x3. (B) Signal line plots (see insert) for SE/STE (left/right) show no loss in signal fidelity at increasing ES. C. T1w relaxometry at different TM/ES at MB=4 and matched TR/TE

Figure 2a, b shows a comparison between image and signals obtained using MESMERISED with ESxMB = (1—no ES, 2, 4) $\times$ 3 for the spin-echo (SE) and STE which shows that echo-shifted interleaving does not affect the acquired signals. Figure 2c shows MESMERISED T_1w data at 1.5 mm isotropic which illustrates that TR/TE can remain constant at different TMs by increasing the ES factor proportionally which highlights its super-acceleration capability. Figure 3 shows high b value 2&3-shells MESMERISED dMRI data, illustrating that ESxMB = 3 $\times$ 4 and b5000 are possible for 1.7 mm isotropic in whole brain volume at TR = 4.9 s. The multi-shell diffusion data is

suitable for modeling with standard DTI and biophysical multi-compartment (e.g. NODDI & Ball&Stick$_{r2}$ models).

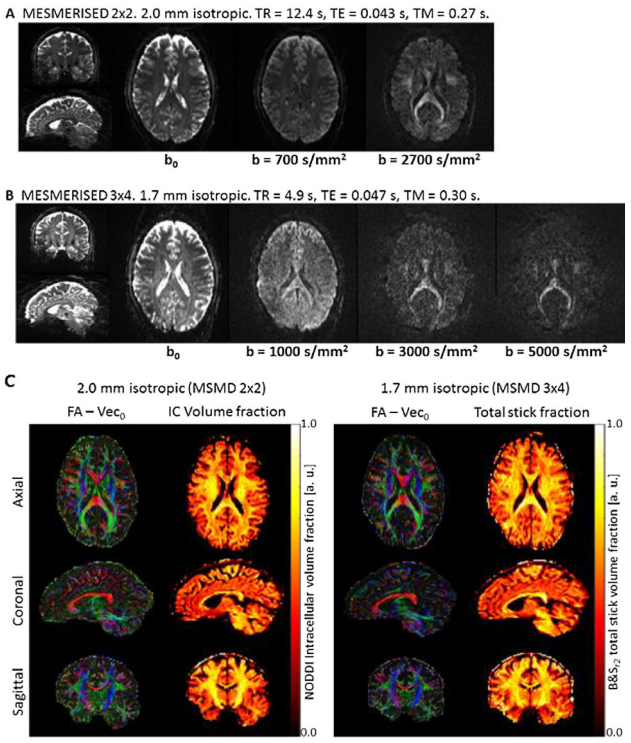

dMRI multishell MESMERISED acquisitions at 2.0 (A) and 1.7 (B) mm iso. Corresponding NODDI and B&Sr2 analysis results respectively (C).

Discussion/Conclusion: MESMERISED achieves super-accelerated 7T STEAM imaging by combining ES—MB acceleration leading very high time efficiency of qT$_1$/qT$_2$ and dMRI. Future combination with PINS[4] will allow high data quality with lower SAR.

References:

1 Setsompop et al. Magn. Reson. Med., 2011; 67:1210–24.
2 Gibson et al. Magn. Reson. Imag., 2006; 24:433–42.
3 Ivanov et al. Magn. Reson. Med., 2010;64:319–26
4 Norris et al. Magn. Reson. Med. 2011;66:1234–40

S21.04

Generalized model-based reconstruction for quantitative MRI using the Bloch-Equations

N. Scholand, X. Wang, S. Rosenzweig, M. Uecker
University Medical Center Göttingen, Institute for Diagnostic and Interventional Radiology, Göttingen, Germany

Purpose/Introduction: Model-based reconstruction techniques enable highly accelerated quantiative MRI by extracting the parameter maps directly from undersampled k-space data [1, 2].
We propose a generic model-based reconstruction technique, which includes the full Bloch equations. The technique is demonstrated for a phantom study by estimating T$_1$, T$_2$, M$_0$ and the coil sensitivities with one 5 s single-shot IR bSSFP acquisition.

Subjects and Methods: The proposed method combines calibrationless parallel imaging and quantitative MRI by treating the calculation of all parameter maps and coil sensitivities as a single non-linear inverse problem which includes the Sobolev norm as a smoothness penalty for the coil sensitivities and a joint-sparsity model as regularization term. The time development of the magnetization is obtained by solving the ordinary differential-equation (ODE) using a Runge–Kutta 5(4) method (RK5(4)) within the forward operator.
To calculate the derivatives a direct sensitivity analysis (DSA) of the Bloch equations is performed that yields a set of ODEs for the partial derivatives. Those are solved simultaneously with the signal model using a RK5(4). The full non-linear inverse problem is solved using the IRGNM-FISTA algorithm [1].
In this proof-of-principle study we applied the proposed method to simultaneously map T$_1$ and T$_2$ of a phantom with a 5 s single-shot IR bSSFP scan (TE/TR: 2.25/4.5 ms, FA: 45°, BR: 192) and compared it to reference measurements based on single-echo spin-echo sequences. Measurements are performed on a SIEMENS Skyra 3T scanner using a 20 channel head coil. The method is implemented in BART [3].
Additionally, a B$_1$-map is acquired using a vendor-proved method based on the Bloch-Siegert shift. The effects from an imperfect slice profile are corrected by reducing the flip-angle by an empirically determined factor of 0.7 in the forward model.

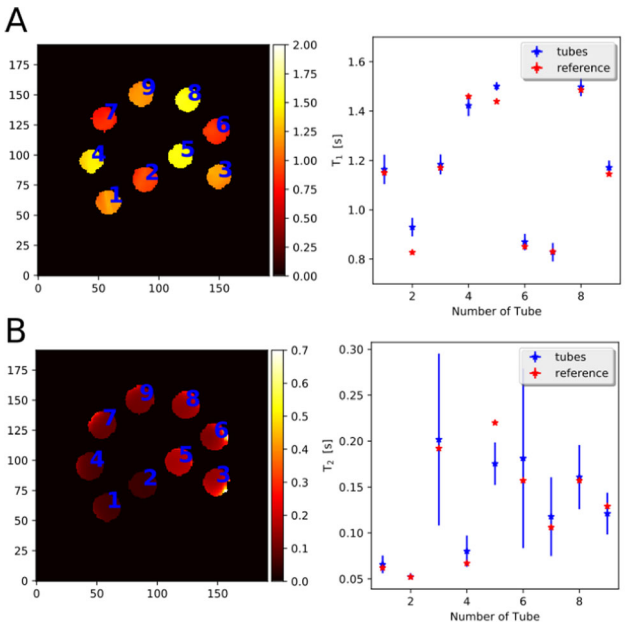

Figure 1: Visualization of the extracted ROIs on the left side and the corresponding relaxation parameters on the right. The results demonstrate T1 in A and T2 in B. The reference values are estimated using gold-standard single-echo spin-echo se

Results: Figure 1 visualizes the extracted ROIs for T$_1$ and T$_2$, their relaxation parameters, and standard deviations (SD) together with the results of the reference measurements.
The reconstructed tubes have accurate relaxation parameters. Tube 2, 4, and 5 show some deviations. They might result from an inaccurate B$_1$-compensation. Additionally, some brightening effects occur on the edges of the phantom, which increase the SD.

Discussion/Conclusion: We described a new method which combines calibrationless parallel imaging with a generic technique for quantitative MRI that makes use of a model-based reconstruction approach based on a DSA of the Bloch equations.
In this first proof-of-principle study, the method was used to extract T$_1$ and T$_2$ from a single-shot IR bSSFP measurement. Because it is

based on a generic model, it can be used with any sequence which is sensitive to the parameters of interest.

References:
[1] Wang X., et al., Magn. Reson. Med.79, 2. 2017
[2] Sumpf TJ, et al., J. Magn. Reson. Imaging.34, 2. 2011
[3] Uecker M, et al. ISMRM Workshop, Sedona. 2013

S21.05

Accuracy and repeatability STUDY of MAGiC and MR fingerprinting

L. Núñez González[1], G. Kotek[1], R. Schulte[2], P. Gómez[3], M. Vogel[4], G. Buonincontri[5], J. A. Hernández-Tamames[1]
[1]Erasmus Medical Center, Radiology & Nuclear Medicine, Rotterdam, The Netherlands, [2]General Electric, GE Global Research, Munich, Germany, [3]Technische Universität München, Computer Science, Munich, Germany, [4]General Electric, GE Healthcare, Hoevelaken, The Netherlands, [5]IMAGO7 Foundation, Pisa, Italy

Purpose/Introduction: We evaluate different 'Quantitative MR' methods in a standardized phantom for MRF[1], MRF-vFA[2], and MAGiC[3].

Subjects and Methods: The experiments were carried out with a phantom from Leeds Test Objects[4] on two different scanners: a 1.5T GE MR450 and a 3.0T GE MR750. MR Fingerprinting (MRF) and MR Fingerprinting variable flip angle only (MRF-vFA) were acquired with the implementation described in Gómez[2]. The third method is the Magnetic Resonance Image Compilation utility (MAGiC, GE Healthcare). On both systems, the acquisitions were repeated 10 times. To reconstruct and to estimate with MRF and MRF-vFA, a high-resolution dictionary was built using EPG formalism[2]. For numerical comparison, a mean value inside an ROI for each tube was calculated. The average and standard deviation of the 10 acquisitions were computed.

Results:

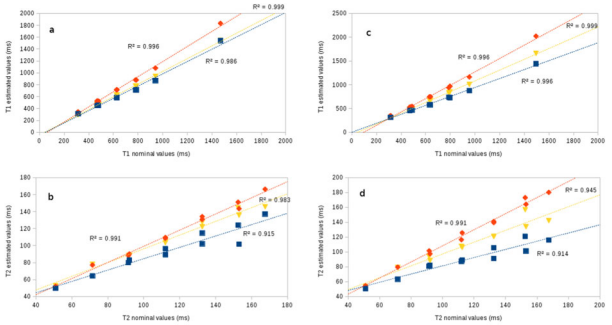

Correlation plots comparing estimated values and reference values with MAGiC (blue), MRF (red) and yellow (MRF-vFA). T1 (a) and T2 (b) on a 1.5 T system. T1 (c) and T2 (d) on a 3 T system.

All methods provide estimations close to nominal values. The correlation is higher for T1 values than for T2. The repeatability of the measurement is calculated as the ratio of the standard deviation to the average value[5]. It means that a lower percentage corresponds to better repeatability. T1 variations are below 5%. T2 variations are higher than in T1 but in agreement with previous reports (below 10%) [6]. On the 3.0 T system, MAGiC shows larger variation for long T1 and T2 and MRF-vFA shows more variability than MRF.

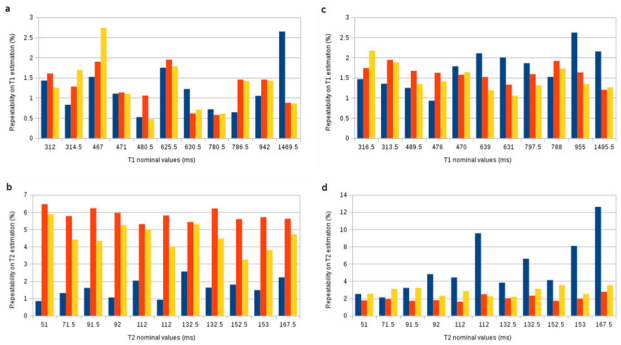

Repeatability on 1.5 T (a, b) and 3 T (c, d) of MAGiC (blue), MRF (red) and MRF-vFA (yellow). Lower percentage means better repeatability.

Discussion/Conclusion: All the methods show good accuracy and consistency with the literature[5, 6]. T2 estimation is less accurate due to B0 and B1 inhomogeneities. The accuracy and repeatability are influenced by the quantitative MR method, the range of T1 and T2 values, and the strength of the magnetic field. This should be taken into account when applying in population and longitudinal studies.

References:
1. Jiang, Y., Ma, D., Seiberlich, N., Gulani, V., Griswold, M.A.: MR Fingerprinting Using Fast Imaging with Steady State Precession (FISP) with Spiral Readout. MRM (2014)
2. Gómez, P.A., Buonincontri, G., Molina-Romero, M., Sperl, J.I., Menzel, M.I., Menze, B.H.: Accelerated parameter mapping with compressed sensing: an alternative to MR Fingerprinting. Proc Intl Soc Mag Reson Med (2017).
3. Warntjes JB, Leinhard OD, West J, Lundberg P. Rapid magnetic resonance quantification on the brain: Optimization for clinical usage, Magn Reson Med 2008, 60:320–9
4. Leeds Test Objects. http://www.leedstestobjects.com/index.php/phantom/t1-t2-gels/
5. Yun Jiang, Dan Ma, Kathryn E. Keenan, Karl F. Stupic, Vikas Gulani, Mark A. Griswold. Repeatability of magnetic resonance fingerprinting T1 and T2 estimates assessed using the ISMRM/NIST MRI system phantom. Magn. Reson. Med. 2016. https://doi.org/10.1002/mrm.26509
6. Guido Buonincontri, Laura Biagi, Alessandra Retico, Michela Tosetti, Paolo Cecchi, Mirco Cosottini, Pedro A Gomez, Rolf F Schulte, Mary McLean, Frank Riemer, Ferdia Gallagher, Martin J Graves, Joshua D Kaggie. Repeatability of 2D FISP MR Fingerprinting in the Brain at 1.5 T and 3.0T. ISMRM 2018

S21.06

Accuracy of the T1 measurements with variable flip angle in vivo and in vitro

C. Lavini, E. M. Akkerman
Amsterdam University Medical Centers, Radiology and Nuclear Medicine, Amsterdam, The Netherlands

Purpose/Introduction: VFA (Variable Flip angle) T1 mapping is a method widely used to allow quantification of Gd concentrations in DCE MRI.

A recent study highlighted the poor reproducibility of the VFA T1 mapping method in vitro, showing variations of up to 30% in the same phantom when measured with different scanners [1].

We postulate that better reproducibility results can be expected in vivo due to a more homogeneous B1 field.

Subjects and Methods: The right knee of a healthy volunteer and one row of the HPD Quantitative MRI (qMRI) System phantom

(consisting of rows of 14 spheres with different T1 and T2 s) were scanned with the same VFA protocol on 5 different scanners (three Philips 3T scanners -named scanner 1, 2 and 3, and two Siemens 1.5 Tesla scanners—named scanner 4 and 5). IR-derived T1 maps and B1 maps were acquired as well.

VFA-derived T1 values were compared with those published by the phantom manufacturer in the 14 spheres of the middle row, as well as with the IR-derived T1 values. Fourteen ROIs were drawn on the knee, and VFA-derived T1 values were compared with IR-derived values.

Results: IR-derived T1 maps of the phantom were consistent across scanners, even though in the case of the three 3T scanners they were not accurately replicating the published phantom values, systematically underestimating the T1 s, especially at short (< 0.3 s) and large (> 1 s) T1 values.

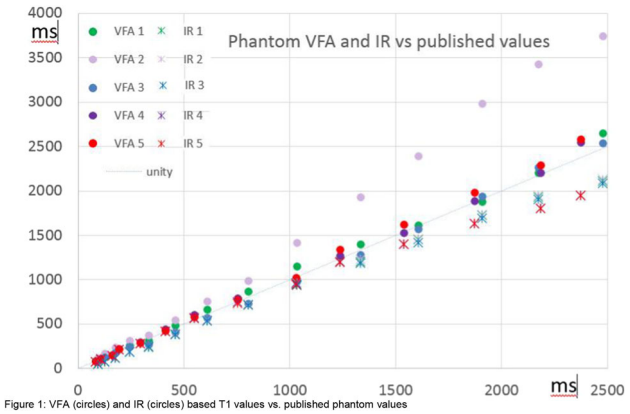

Figure 1: VFA (circles) and IR (circles) based T1 values vs. published phantom values

%	Sc. 1 (3T)	Sc. 2 (3T)	Sc. 3 (3T)	Sc. 4 (1.5T)	Sc. 5 (1.5T)
Av Rel Err IR	-19.5	-18.8	-19.9	-4.9	-6.3
Max Rel Err IR	-44.9	-44.5	-45.1	-18.0	-18.0
Av Rel Err VFA	4.68	36.2	3.36	3.54	3.97
Max Err VFA	11.2	51	-18.6	15.5	12.9

Table 1: Average and max relative errors of the measured T1 value in the 14 vials

VFA maps of the phantom were not always consistent across scanners: in most cases they approximated the published T1 values better than the IR derived T1 maps, but in one case (scanner 2) the VFAs performed very poorly.

In the knee VFA values could only be compared to the IR-derived T1 values. VFA T1 values and IR T1 values correlated better in the knee than in the phantom (Fig 2). Also in the scanner with poor phantom T1 VFA accuracy (i.e. scanner 2), the VFA derived T1 values in the knee reproduced well the IR-derived values. B1 maps in the knee revealed consistently better B1 homogenity than in the phantom.

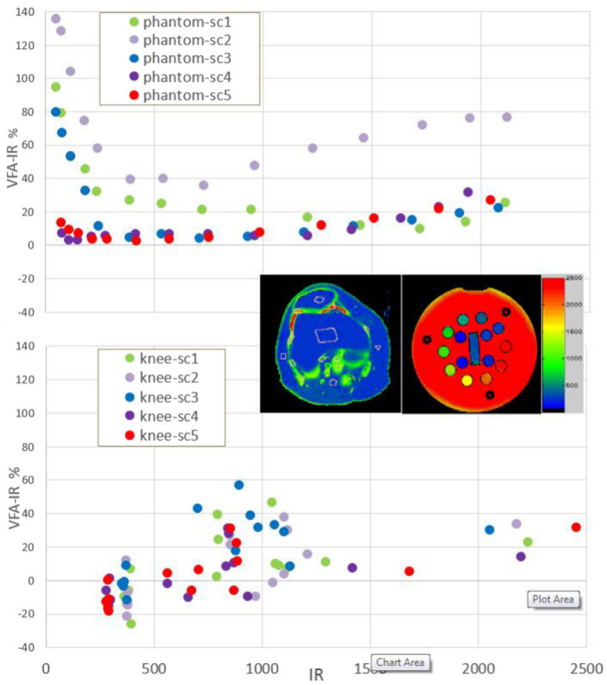

Figure 2: Relative difference (VFA-IR)/IR vs IR T1 values in the Phantom (above) and knee (below). Inset: the VFA T1 image of the knee with the 14 ROIs, and the phantom.

Discussion/Conclusion: VFA-derived T1 measurements in the knee reproduce the IR derived values better than in the phantom. However, especially at low T1, IR T1 maps did not perform well at 3T in the phantom, causing the mismatch between VFA and IR in Phantoms in the spheres with short T1 s.

The better performance of VFA in vivo appears to be related to the better B1 homogeneity in the knee than in the phantom.

References:

1. Bane O. et al. Magnetic Resonance in Medicine 79:2564–2575 (2018).

S21.07

A bi-compartmental model to resolve R2* relaxometry

M. Michaud, G. Arribarat, S. Boucher, P. Péran
Université Paul Sabatier/Inserm-ToNIC, Toulouse, France

Purpose/Introduction: The quantification of intracerebral iron content in vivo is an objective of modern imaging. Iron quantification is used to study pathophysiological mechanisms of neurodegenerative diseases [1]. For this aim, one method used to quantify iron content is the R2* relaxometry [2]. This approach extracts one parameter, the relaxation rate (R2*) for each voxel. The calculation of R2* is mainly conducted by fitting a mono-exponential signal decay curve, which assume a single tissue in the voxel (mono-compartmental). However, the tissue within a large voxel can be heterogeneous (e.g. iron, myelin). Our work aims to develop a fitting of a bi-exponential curve to address a bi-compartmental resolution of R2* relaxometry. We tested this approach to measure iron-content increase related to normal aging [2].

Subjects and Methods: First we conducted a phantom study, realised on 3D print, to implement and check a bi-exponential equation. The phantom contains three tubes with three fillings. Multi echo gradient and multi echo spin echo were acquired, to calculate R2 and R2* maps. For the post-treatment, we selected voxels inside tubes and voxels between tubes. We analysed images (3D T1-FFE, TE: 6–12–

20–30–40–55 ms) from 40 young subjects (mean = 29 ± 6 years) and 37 older subjects (mean = 68 ± 6 years). Image processing was performed using ANTs and FSL, and image filtering for noise reduction has been applied with NESMA filter [3].

Results: The phantom study demonstrated that it is possible to evaluate the number of components from R2 relaxometry: one component from homogeneous tube and two compartments between two tubes.

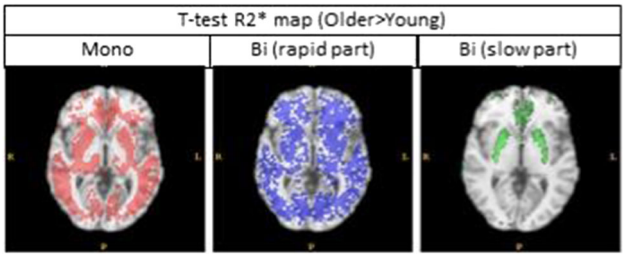

The figure showed significant R2* voxels higher in older subjects group than in younger one using *t* test. Result showed that we can distinguish two age-related spatial patterns using with bi-compartmental method. The difference of rapid component concerns mainly white matter region. The difference of slow component concerns mainly the putamen.

Discussion/Conclusion: Our results showed the feasibility to calculate bi-compartment maps from R2* relaxometry. Our age-reated results can be interpreted by a better sensitivity to myelin for the rapid component and a better sensitivity to iron-content for the slow component. Bi-R2* relaxometry could be used to better distinguish the respective contribution of iron and myelin.

References:

[1] Altamura et Muckenthaler, 2009. JAD [2] Péran & al, 2007. JMRI [3] Bouhrara & al, 2019, MRI

S21.08

Estimation of microstructure parameter from ex vivo data using realistic WM models

R. Hedouin, K.-S. Chan, R. metere, J. marques
Donders Institute, Nijmegen, The Netherlands

Purpose/Introduction: The gradient echo (GRE) MRI signal evolution is affected both in magnitude and in phase depending on the magnetic susceptibility of its various compartments with respect to the main static field B0. In this study, we present methods to: (i) create realistic WM models from electron microscopy data and use these models to simulate GRE signal; (ii) train a deep learning network and recover parameter map from ex vivo data.

Subjects and Methods: WM Model creation: Real myelinated axon shapes, obtained from an electron microscopy image, were used to create WM models including 3 compartments (intra-axonal, myelin, extra-axonal), with different fiber volume fraction (FVF) and g-ratio, using an in-house developed axon packing algorithm derived from [1]. Myelin sheaths susceptibilities (isotropic Xi and anisotropic Xa) were used to compute the field perturbation [2]. The complex signal evolution as a function of TE was derived (see Fig 1) assuming relaxation times (T2*), and relative weight (ρ) specific to each compartment [3].

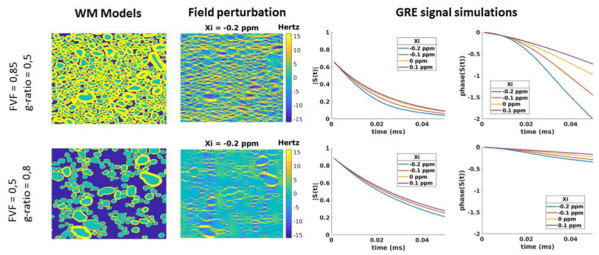

Fig1. Each row represents a WM model with specific FVF and g-ratio values. Second column: corresponding field under a perpendicular B0 orientation with Xi = -0,2 ppm. Two last columns : magnitude and phase of the GRE signal for different Xi values.

Acquisition: A fixed ex vivo human brain was scanned on a 3T scanner using 6 multi-echo GRE sequence (TR/TE1/TE12 = 46/1.7/35.2 ms, 1.8 mm isotropic, fa = 5/10/15/20/35/60) the protocols were repeated for 9 orientations of the brain with respect to B0. A DWI was also performed to estimate main fiber orientations.

Deep learning: A dictionary of GRE signal, defined by microstructure (FVF, g-ratio) and tissue related (T1, T2*, ρ, Xi, Xa) parameters, was created. Each vector is the concatenation of fiber orientations, normalized magnitudes and phases along the 9 orientations of the ex vivo acquisition (see Fig 2). This signal vector is defined by 5 parameters (the remaining parameters been fixed): FVF, g-ratio, T2_IntraExtraAxonal, ρ, and Xi. Deep learning was performed on the dictionary using Keras [4].

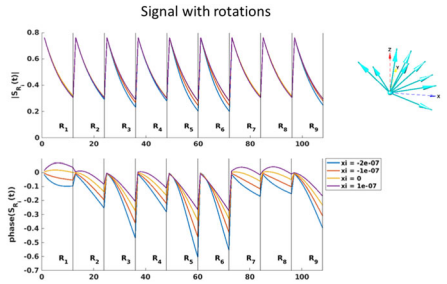

Fig2. Entire signal simulation of the same 12 TE with 9 different B0 orientations (represented at the top right) for several Xi values. The difference of signal behavior between orientations provide valuable additional information.

Results: For each fa, the parameter map was estimated from the ex vivo data. These maps were then used to compute the mean and standard deviation along with the different flip angles (see Fig 3). The mean parameter maps of FVF and T2 are compatible with literature values. The relative weight of intra/extra compartment compare to myelin is decreasing with higher flip angles as expected. The standard deviation of the T2 across flip angles is almost null. However, the FVF parameter is still sensitive showing that improvements in the model are necessary to enforce robustness.

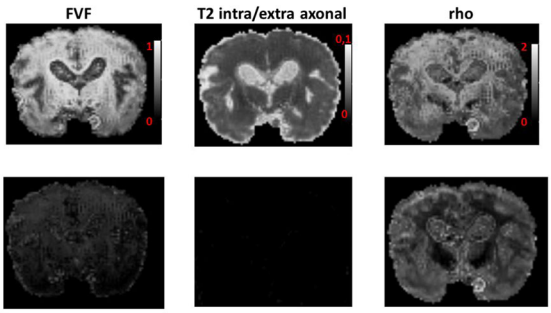

Fig3. Column 1,2: Parameter maps from ex-vivo data. Top mean across flip angles, bottom standard deviation. Column 3: Relative weight of intra/extra compartments compare to myelin compartments, top flip angle 10, bottom flip angle 35

Discussion/Conclusion: We have shown that some microstructural

properties are recoverable using multiple orientation GRE data combined with prior axonal orientation knowledge. Future work will be devoted to develop quantified evaluations of this method.

References:
[1] Mingasson, Tom, et al. 2017
[2] Liu, Chunlei. 2010
[3] Wharton, Bowtell. 2012
[4] Chollet, François, et al., https://keras.io/

L07 Lightning Talks

13:50–14:50 *The Stage*

Machine Learning, Image Analysis & their Application

L07.01

Deep learning for classification of Alzheimer's disease: is MRI pre-processing required?

J. Linders, V. Venkatraghavan, W. J. Niessen, E. E. Bron
Erasmus MC, Biomedical Imaging Group Rotterdam, Department of Radiology & Nuclear Medicine, Rotterdam, The Netherlands

Purpose/Introduction: Machine learning methods for classification of Alzheimer's disease (AD) based on MRI have shown promising results. While conventional machine learning often requires excessive pre-processing of the data, it is thought that deep learning (DL) can extract the relevant features itself, due to a deep hierarchy of non-linear transformations. Nevertheless, previous studies using DL for MRI-based AD classification show a large variability in pre-processing methods before feeding the data into the model. Most commonly observed, studies used T1-weighted (T1w) images or grey matter (GM) modulated images since AD is characterized by reduced GM volume. The current study aims to investigate the effects of this prior feature engineering of MRI data on performance of a DL model.
Subjects and Methods: This study used data from the Alzheimer's Disease Neuroimaging Initiative (ADNI), containing MRI scans of AD patients (N = 334), cognitively normals (CN; N = 520), mild cognitive impaired (MCI) patients who converted to AD within 3 years of baseline measurement (N = 231) and who did not convert (N = 628). Two types of voxel-wise features were evaluated: T1w images, which were affinely registered to MNI space, and GM modulated maps. The GM modulated maps were created using previously described methodology [1]. In short, T1 images were first non-rigidly registered to a group template. Probabilistic GM segmentations were subsequently transformed to this template and modulated using the Jacobian determinant of the deformation field, to compensate for compressions and expansions.

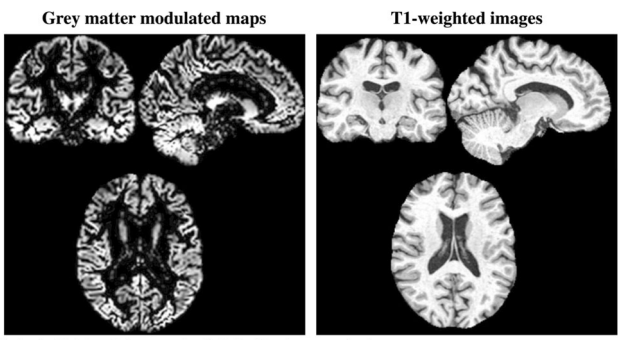

The two input data types to be compared, subjected to different pre-processing steps.

For computational efficiency all data was down sampled with factor 4. A classifier was trained on the AD and CN data and tested on two classification tasks: AD vs. CN (tenfold cross-validation) and MCI converters vs. MCI non-converters. For classification, a fully convolutional neural network (CNN) was used, consisting of 5 blocks including 3D convolutional layers, drop-out, batch-normalization, relu activation and stride 2 pooling. The last layers of the network were a conv layer with 2 kernels and a softmax.

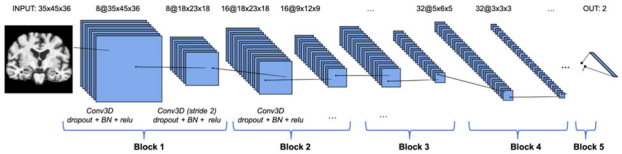

The CNN architecture used for classification. Per block, the number of kernels increases from 8 to 32, in steps of 8. The output shapes of each layer are visualized.

The CNN architecture used for classification. Per block, the number of kernels increases from 8 to 32, in steps of 8. The output shapes of each layer are visualized.
Results: For classification of AD, the area under the curve (AUC) of a CNN trained on GM modulated images (92%) was significantly higher ($p < 0.001$, based on the McNemar test) than the CNN trained on T1w images (88%). A network pre-trained on the AD task was used for classification of MCI conversion, which also yielded a significantly higher AUC ($p = 0.04$) for the network trained on GM modulated images (74%) than the network trained on T1w images (70%).

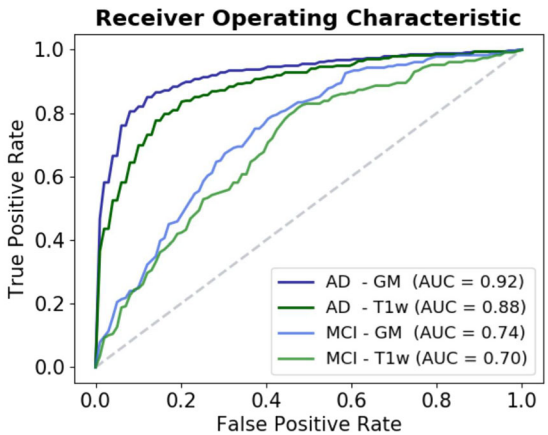

The area under the receiver operating characteristic curve of the diagnosis and prognosis of AD, comparing the results of GM and T1w input data.

The area under the receiver operating characteristic curve of the diagnosis and prognosis of AD, comparing the results of GM and T1w input data.
Discussion/Conclusion: These results indicate that prior extraction of voxel-wise GM density information is beneficial for CNN performance in diagnostic and prognostic AD classification. This indicates that most relevant features are embedded in the GM structures of the brain and that the CNN is not able to automatically extract this information from the raw T1w images.
References:
[1] Bron, E., et al. (2014). *HBM*

L07.02

Voxelwise harmonisation of FA on a cohort of 605 healthy subjects using ComBat: an exploratory study

M. Siqueira Pinto[1], R. Paolella[2], T. Billiet[2], P. Van Dyck[1], P.-J. Guns[3], B. Jeurissen[4], A. Ribbens[2], A. J den Dekker[4], J. Sijbers[4]
[1]Antwerp University Hospital, Antwerp, Belgium, [2]Icometrix, Leuven, Belgium, [3]University of Antwerp, Pharmacology Department, Antwerp, Belgium, [4]University of Antwerp, imec Vision Lab, Antwerp, Belgium

Purpose/Introduction: Fractional Anisotropy (FA) maps are dependent on MR hardware and acquisition parameters (scanner model, field strength, echo time (TE), repetition time (TR), and diffusion protocol). As a result, a quantitative comparison of FA across sites may suffer from high variability and low statistical power[1]. In this study, ComBat, a robust and fast harmonisation method[2], was used to recalculate diffusion FA maps taking into account possible confounding factors. For a large multi-center cohort of healthy subjects, we investigated which factors are relevant for reducing intra and inter-site variability in FA maps while maintaining the biological information.

Subjects and Methods: Diffusion Tensor Images of 605 healthy subjects (aged 8–86 years; 327 males) were acquired using a variety of MRI scanners (3 vendors, 2 field strengths and 11 models) and acquisition schemes (7 TEs, 9 TRs and 2 diffusion shells). An in-house diffusion pipeline was used to estimate FA maps of white matter (WM) in MNI space. We implemented ComBat harmonisation with associated confounding factors for harmonisation, and biological covariates. Mean FA per subject and population variance were calculated for statistical comparison. First, different factors for harmonisation were evaluated at the population level. Next, similar analysis was performed for different age groups (bin size of 10 years).

Results: The effect of different harmonisation factors on the variability of FA is shown at population-level and for different age groups in Figs. 1 and 2, respectively. Except for TR and field strength, accounting for confounding factors reduces population variance ($p < 0.05$) while maintaining the biological information. The factor model demonstrated to reduce variation of FA best. Stepwise adding in other factors did not significantly reduce variation further. A t test of FA between young and old groups (aged 25–35 and 55–65) confirms that the decrease in FA is preserved ($p < 0.001$). The t statistic slightly increased after harmonisation, showing greater evidence of ageing effect in FA.

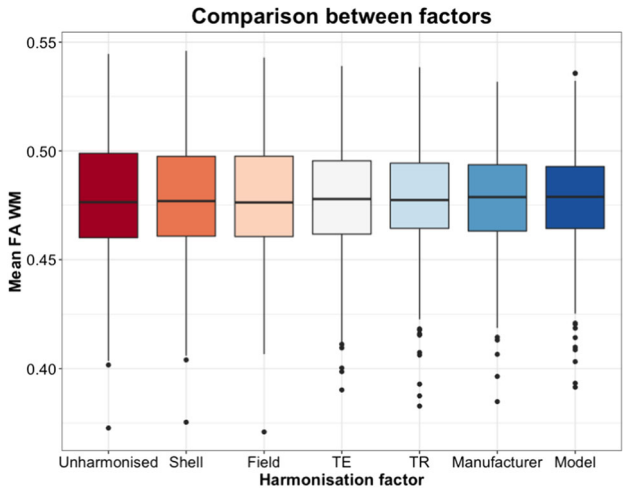

Figure 1. Mean FA of WM of the population before and after ComBat harmonisation, considering the following factors: diffusion shell, field strength, TE, TR, MR system, manufacturer, and scanner model.

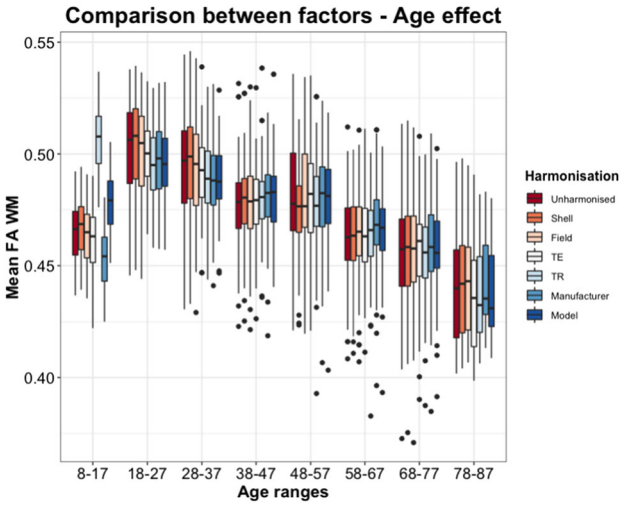

Figure 2. Mean FA of WM of the population divided by age groups before and after ComBat harmonisation, considering the different factors of harmonisation: shell, field strength, TE, TR, MR system manufacturer and scanner model.

Discussion/Conclusion: In this study, harmonisation using ComBat with scanner model as confounding factor reduced the population variability, while preserving the known trend for age-related changes in FA[3]. However, the harmonisation has decreased the mean FA difference between the first two age bins (Fig. 2). This effect may be due to the fact that all subjects within the younger group were scanned in the same MR system model, but this needs further analysis. Our findings suggest the effectiveness of ComBat as a harmonisation method in multi-center studies.

This research was partially funded by the B-Q Minded EU H2020 project under grant agreement No. 764513.

References:

1-Vollmar C, et al., https://doi.org/10.1016/j.neuroimage.2010.03.046
2-Fortin JP, et al., https://doi.org/10.1016/j.neuroimage.2017.08.047
3-Westlye LT, et al., https://doi.org/10.1093/cercor/bhp280

L07.03

Spurious group effects may be caused by increased connectivity between odd or even slices in resting state fMRI data

R. Yakupov, C. Metzger, A. Cardenas-Blanco, E. Duezel
DZNE, Magdeburg, Germany

Purpose/Introduction: In our preliminary resting state fMRI connectivity analysis (rs-fMRI FC) we encountered a persistent artifact exhibited as increased connectivity between odd or even slices, which was not caused or addressed by preprocessing, and which was also observed in data from another independent study. In this study we present the results of our investigation into this artifact.

Subjects and Methods: 212 healthy subjects were scanned on 3T Siemens scanners. Each fMRI dataset went through standard preprocessing steps and FC calculation.

Examining individual FC maps revealed layered structure of increased connectivity corresponding to EPI acquisition slices (Fig. 1). Furthermore, FC calculated from raw data showed the same artifact, which showed that preprocessing neither introduced nor sufficiently corrected this artifact.

In order to enhance artifact appearance, brain slices were used as ROIs. This approach drastically improved artifact detectability, which in severe cases looked like Fig. 2.

All 212 subjects were checked visually and artifact grades from 0 (no artifact) to 3 (strong correlation) were assigned. Based on this grade subjects were divided into 4 groups and dependence on motion, i.e. motion parameters and derived values, was investigated. Also, the effect of data scrubbing was investigated with removing up to 6 volumes for each high-motion volume.

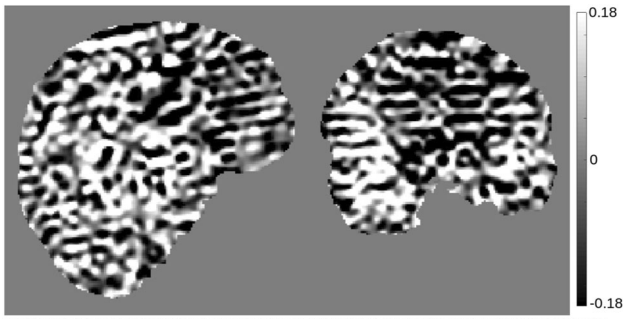

Figure 1. The artifact as seen in pre-processed (standard pipeline without smoothing) and registered to study-specific template data.

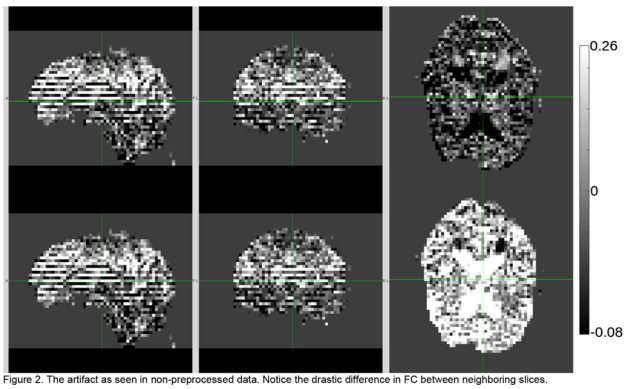

Figure 2. The artifact as seen in non-preprocessed data. Notice the drastic difference in FC between neighboring slices.

Results: Two-way ANOVA with motion parameters showed no significant results. However, checking for dependence on frame-wise displacement (FD) showed that mean FD (Fig. 3) and number of volumes with FD over 0.5 were statistically significant between groups.

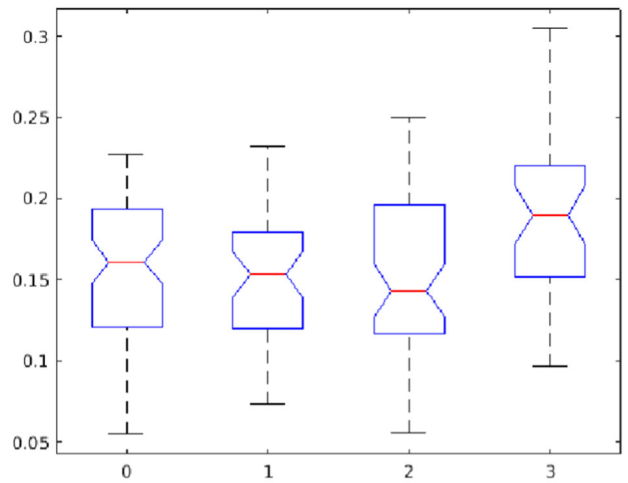

Figure 3. ANOVA results of mean FD dependence on artifact severity

Discussion/Conclusion: Motion can adversely affect FC analysis, e.g. introduce variance and reduce statistical power, as well as introduce spurious activations[1] and inflate correlations[2]. Our investigation showed existence of increased FC between odd or even slices and its dependence on motion, which even strictest motion-scrubbing techniques were unable to correct.

One suggestion why extended motion-scrubbing did not help is that perturbations to steady-state EPI acquisition last longer than 4 repetitions. Another is that it is indeed caused by motion, but during acquisition of auto calibration scan (ACS). It has been shown before[3] that even small motion, e.g. breathing, can lead to big tSNR differences between slices. However, we could not find prior investigations of such FC differences between slices. As spatial smoothing masks the artifact, this gives a hint to why this has not been detected before. Further investigation of effect of motion during ACS acquisition is necessary. It is also important to determine whether it can inflate connectivity thus introducing spurious effects due to motion. This could be important for studies involving subjects prone to motion, e.g. Parkinson's disease patients or children.

References:

1. Friston et al., 1996
2. Power et al., 2012
3. Polimeni et al., 2016

L07.04

Spatial and temporal connectivity between networks from low and high dimensionality independent component analysis

R. Tudela[1], R. Sala-Llonch[2], E. Muñoz-Moreno[3], G. Soria[3]
[1]CIBER-BBN, Barcelona, Spain [2]University of Barcelona, Department of Biomedicine, Barcelona, Spain [3]Institut d'Investigacions Biomèdiques August Pi I Sunyer (IDIBAPS), Experimental 7T MRI Unit, Barcelona, Spain

Purpose/Introduction: Functional Connectivity (FC) brain networks based on resting state functional MRI (rs-fMRI) reveal biomarkers of neurological conditions such as Alzheimer's disease (AD). While low dimensionality independent component analysis (ICA) can depict the main resting state networks (RSNs), high dimensionality ICA offers a more detailed parcellation of functional networks. Our goal was to automatically select the networks from a high dimensionality ICA based on the RSNs obtained from a low dimensionality ICA. We studied inter- and intra-network connectivity using temporal and spatial correlation. Our method was applied to study an AD model of TgF344-AD rats [1, 2].

Subjects and Methods: Rs-fMRI were acquired in TgF344-AD (n = 9) and Fischer control (n = 10) rats at 5 time points (5, 8, 11, 15 and 18 months), in a 7T scanner with a single-shot gradient echo EPI sequence: 600 volumes of $64 \times 64 \times 34$ voxels, $0.4 \times 0.4 \times 0.6$ mm^3/voxel, TR = 2 s and TE = 10.75 ms.

After image preprocessing 2 ICAs were performed using FSL MELODIC [3] for the whole cohort: ICA_L with 30 independent components (ICs) and ICA_H with 150 ICs. 10 ICs from ICA_L were classified as RSNs based on their anatomical structures.

Dual regression was performed for both decompositions to find subject- and network-specific time-series and spatial maps. Temporal correlations between ICA_L and ICA_H were computed with FSLNets. The Matthews spatial correlation coefficients were obtained from the flattened and binarized spatial maps. The networks from ICA_H were automatically selected using thresholds for the time correlation and the Matthews correlation by minimizing the mean square error

between the added masks of the networks from both ICAs. Finally, hierarchical clustering was computed for both connectivities.

Results: 25 components from the ICA_H were automatically identified in correspondence with the main RSNs by combining the temporal and spatial thresholds. Temporal and spatial connectivities between these 25 networks and the 10 RSNs of the whole cohort showed similar behavior as observed from the hierarchical clustering. When considering each group and time point separately, we observed differences in connectivity.

Discussion/Conclusion: With the proposed method the relevant networks from a high dimensional ICA were automatically selected based on the main RSNs also obtained from ICA, using temporal and spatial criteria. From the hierarchical analysis of the connectivities between both ICAs, we define new insights in the relationship between functional networks for the TgF344-AD and control groups at the different time points.

References:

[1] Muñoz-Moreno et al. Alz. Res. & Ther. 2018. 10:16
[2] Cohen et al. J. Neurosci. 2013. 33:6245–6256.
[3] Beckman & Smith. NeuroImage 2005. 25(1):294–311

L07.05

Ultra-high temporal resolution on the inversion recovery curve: new insight into T1 relaxometry of the human brain

A.-M. Oros-Peusquens, A. Weglage, N. J. Shah
Research Centre Juelich, INM-4, Juelich, Germany

Purpose/Introduction: T2 relaxometry in human white matter is able to reproducibly detect a fast-relaxing component (15 ms) attributed to myelin water (MW) [1] and validated histologically as a myelin marker. Conventionally, T1 relaxation is considered monoexponential, assuming that exchange between different water pools in tissue is fast on the T1 time scale, although the residence time of myelin water **in vivo** is unknown.

We hypothesized that a spatially-resolved investigation of the T1 relaxation curve with ultra-high temporal resolution might reveal previously unidentified characteristics of a fundamental NMR parameter.

Subjects and Methods: Ten healthy volunteers (5 female, 32.4 ± 0.3 years old) were measured on a 3T MR scanner using a bird-cage transmit and an 8-element receive head coil following prior, written informed consent. Quantitative MRI was performed using a Look-Locker sequence named TAPIR [2] with sequence parameters including: $\alpha = 10$, TR = 17 ms, TI = 20 ms, TE = 6.62 ms, $\tau = 2$ s, BW = 898 Hz, EPI-factor = 3, 460 timepoints, in plane resolution 1×1 mm, 2 mm single-slice acquisition. The total acquisition time, including mapping of the inversion efficiency [ref], was just below 4 min.

Analysis of signal characteristics and denoising of magnitude and phase data was performed using principal component (PCA) decomposition of the complex data, retaining only 3–5 components out of 460.

Results: The original and denoised signal from a single WM voxel, the original and denoised magnitude and phase images at a given time point and the T1 and M0 maps obtained by monoexponential fitting of the original and denoised data are compared in Figs. 1 and 2.

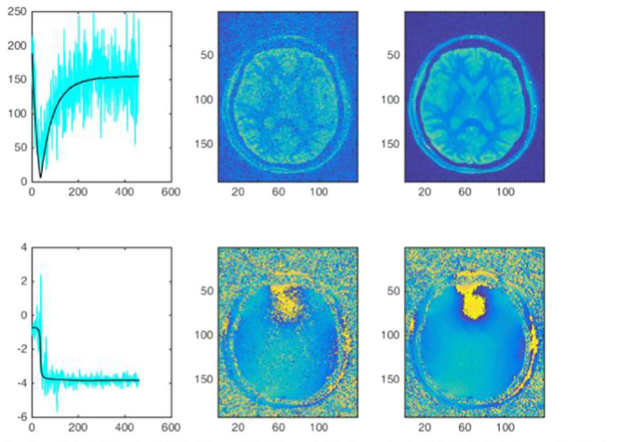

Denoising effects. Left: the signal obtained from a single GM voxel (original, cyan; denoised, black). Right: the images at a given time point, before and after denoising - magnitude on top, phase on bottom row.

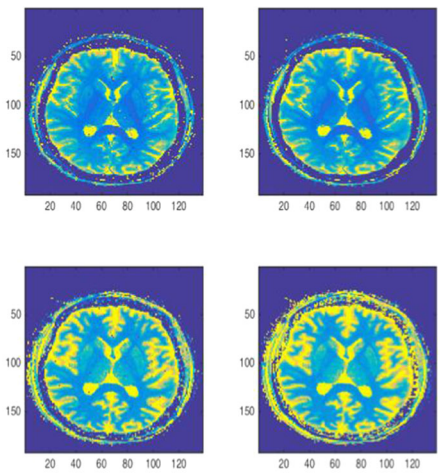

T1 (top) and M0 (bottom) maps obtained by monoexponential fitting of the original (left) and denoised data (right). The similarity of the maps reflect the tremendous noise reduction already obtained by fitting a simple model with many data.

Figure 3 shows the results of NNLS analysis of the original and denoised data, with and without Tikhonov regularisation (chi2 < 1.025*chi2_orig), in spectra and image form.

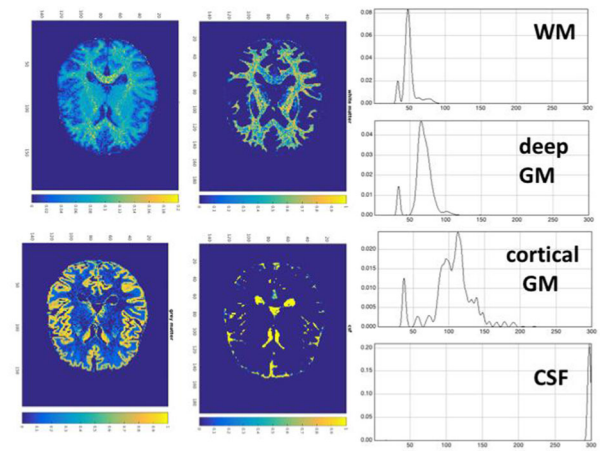

2 Multicomponent T1 information. Spectra from ROIs characteristic of WM, GM (deep and cortical) and CSF are shown on the right. The maps of the different components are shown on the left: myelin water, white matter, grey matter, CSF.

2 Multicomponent T1 information. Spectra from ROIs characteristic

of WM, GM (deep and cortical) and CSF are shown on the right. The maps of the different components are shown on the left: myelin water, white matter, grey matter, CSF.

Discussion/Conclusion: In all volunteers and practically all WM and GM voxels, a moderately-short T1 component was identified, with T1 $\sim$ 400 ms (WM) and $\sim$ 500 ms(GM), and attributed to the presence of myelin. The component is robustly identified also when using the original low-SNR data. In the absence of regularisation, an additional, even shorter component, possibly related to MT effects, might be present; however, only the longer short component survives regularisation. The maps reflecting its spatial distribution (tentatively called 'myelin water maps') show unprecedented SNR and detail, even when NNLS analysis is performed on the original (SNR = 10) data. While in WM a single additional peak was identified in most cases, GM shows a more complicated T1 spectrum. The precise nature of the observed components will be further investigated.

References:

[1] A. MacKay et al. Magn. Reson. Med., 31(1994)
[2] Shah NJ et al. Neuroimage. 14 (2001).

L07.06

Fully Convolutional Neural Network Segmentation of Multiple Sclerosis Lesions using T1 and T2* Maps

A.-K. Schnurr[1], I. Hermann[1], R. Schmidt[2], A. Gass[2], F. G. Zöllner[1], L. R. Schad[1]
[1]*Heidelberg University, Computer Assisted Clinical Medicine—Medical Faculty Mannheim, Mannheim, Germany,* [2]*Heidelberg University, Department of Neurology—Medical Faculty Mannheim, Mannheim, Germany*

Purpose/Introduction: For the therapeutic management of multiple sclerosis (MS) the detection of brain lesions is highly important. Manual delineation is time-consuming and suffers from high inter- and intraobserver variability [1]. Automatic and reproducible segmentation with Fully Convolutional Neural Networks (FCNNs) may be useful to overcome these problems. In this initial configuration study we compare different architectures and loss functions for this task.

Subjects and Methods: Eleven MS patients were examined on a 3T scanner using magnetic resonance fingerprinting with fast group matching [2] with parameters FOV = 240 $\times$ 240 mm, matrix size = 240 $\times$ 240, 60 slices of 2 mm thickness, GRAPPA R = 2, partial fourier 5/8, bandwidth = 998 Hz/px and varying flip angle, TE and TR. Reconstructed T1 and T2* maps were of size 240 $\times$ 240 $\times$ 60 voxels.

We compared an extended U-Net [3] architecture which receives the two parametric maps as a combined input versus a Siamese Network [4] which first processes each parametric map in separate pathways and then combines the feature maps (Fig. 1). Each architecture was used with three loss functions: Tversky with alpha = 0.3 (TV3), Generalized Dice (GDL) and Cross Entropy (CEL). Due to the small sample size we performed Leave-One-Out-Cross-Validation. Therefore, 66 networks were trained. The Adam optimizer was used with learning rate 0.001, 100 training epochs, batch size = 8 and patch size 192 $\times$ 192.

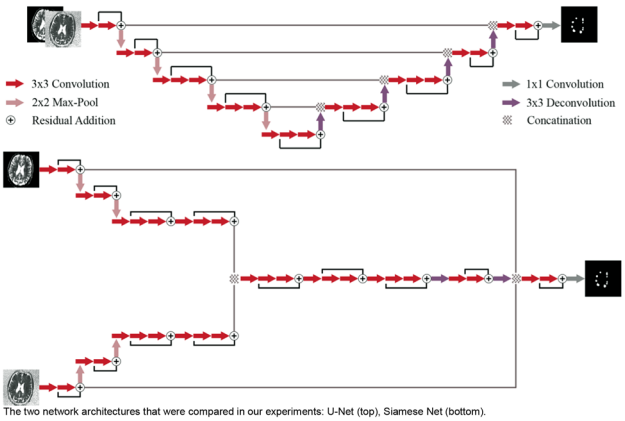

The two network architectures that were compared in our experiments: U-Net (top), Siamese Net (bottom).

MS lesions were identified and manually outlined by a trained reader also considering information from matching FLAIR images. Evaluation was performed by calculation of the Dice Similarity Coefficient (DSC) and the Lesion Detection Rate (LDR) comparing segmentation outcomes of the different networks to the manual segmentations.

Results: Segmentation quality was significantly ($p < 0.05$, paired t test) increased using TV3 in comparison to CEL and GDL (Figs. 2, 3). The best DSC was achieved using it in combination with the Siamese network (0.431 ± 0.127), however the difference to the U-Net (0.424 ± 0.171) was not significant. Nonetheless, the U-Net achieved a significantly higher LDR. Segmentation of each image volume took 1.5 s.

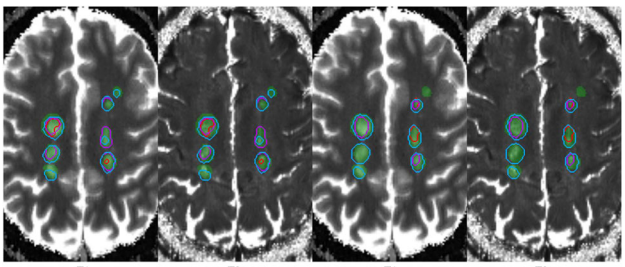

Segmentation results (contours: red=CEL, violet=GDL, blue=TV3) of the different configurations in comparison to manual annotation (overlay: green) superimposed to the respective parametric maps.

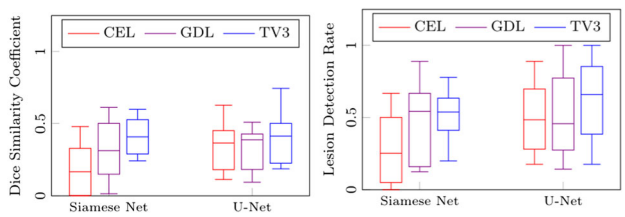

Comparison of DSC and LDR (fraction of lesions which have been detected by at least one voxel) between the different network configurations.

Discussion/Conclusion: In this study, we showed that using a FCNN with the Tversky loss function had the best ability to segment MS lesions in quantified T1 and T2* maps. While both architectures performed similar, the U-Net was able to detect more lesions. This configuration is therefore promising to be used in future for

automated MS lesion segmentation. With an increased study size the segmentation quality is expected to improve.

References:
1. Ashton, EA et al., J Magn Reson Imaging, 17: 300–308 (2003).
2. Rieger, B et al., Magn Reson Med 78, 1724–1733 (2016).
3. Ronneberger, O., et al. In Proc. MICCAI, 234–241 (2015).
4. Roy, S., et al.,. arXiv preprint arXiv:1803.09172(2018).

L07.07

PSIR segmentation robustness at 7T: a travelling head study

O. Mougin[1], W. Clarke[2], C. Rua[3], I. Driver[4], A. Morgan[5], R. Wise[4], S. Clare[2], C. Rodgers[3], **R. Bowtell**[1]
[1]University of Nottingham, SPMIC, Nottingham, UK, [2]University of Oxford, Wellcome Centre for Integrative Neuroimaging, Nuffield Department of Clinical Neurosciences, Oxford, UK, [3]University of Cambridge, Wolfson Brain Imaging Centre, Department of Clinical Neurosciences, Cambridge, UK, [4]Cardiff University, Cardiff University Brain Research Imaging Centre, School of Psychology, Cardiff, UK, [5]University of Glasgow, Institute of Neuroscience & Psychology, Glasgow, UK

Purpose/Introduction: Ultra-high magnetic field (7T) MRI scanners provides high spatial resolution images and excellent contrast for classifying brain tissue, but robustness of tissue segmentation across sites is key for multi-site studies. Here, we present a subset of the main UK7T travelling-head study focusing on harmonized T_1-weighted images acquired on six subjects at 0.7 mm^3 isotropic resolution across three 7T sites, with five repeats at one site. The aim is to assess the harmonisation of the MP_2RAGE sequence across sites, by focusing on segmentation reproducibility.

Subjects and Methods: Acquisition:
The data used in this work was collected as part of the UK7T Network's travelling head study. Six subjects (4 male, 34 ± 6y) underwent structural neuroimaging scans at three of the five 7T-capable UK sites. Each subject was scanned at each away site (N_a = 3), and a further four times at their designated home site (N_h = 4, N_t = 7 scans per subject). A standardised 3D-MP_2RAGE acquisition was implemented on all sites using the following parameters: 0.7 × 0.7 × 0.7 mm^3, FOV = 224 × 224 × 157 mm^3, GRAPPA/SENSE = 3, TR = 3500 ms, echo spacing = 6.3 ms, FAs = 5/2̊ and $TI_{1/2}$ = 725/2150 ms f. Acquisition time = 6min14 s/7min51 s (SENSE/GRAPPA).
Processing: Offline PSIR reconstruction[1] was carried out on all MP_2RAGE data, including a simple method to denoise non-tissue pixels[2]. Additionally, the MP_2RAGE data was segmented using the Freesurfer longitudinal stream after inhomogeneity correction using spm. The cortical thickness was compared using a 3-way analysis of variance (ANOVA), looking at the effect of sites, subjects and repeats on the individual subject segmentations. Additionally, coefficients of variation (CoV) and Intraclass Correlation Coefficients (ICC) were computed for each region outputted from the DKT Atlas. Dice Similarity Coefficients (DSC) were also computed on the cortical ribbon segmentation, comparing the segmentation from the seven scans to the average subject space.

Results: The cortical ribbon segmentation was reproducible across sites, as no significant difference in brain cortical volume was present either between sites (p = 0.62) or repeats (p = 0.74) (3-way ANOVA). This was also true when testing only the left cortical hemisphere volume (p = 0.81 and p = 0.51 respectively) or the right cortical hemisphere volume (p = 0.19 and p = 0.30 respectively). CoV and ICC were also mapped on an average subject for cortical thickness (Fig. 1), showing good reproducibility when comparing all data together, or only away visits or home scans. The reproducibility was good overall, with little difference between home and away data, also visible with the DICE similarity coefficient (Fig. 2).

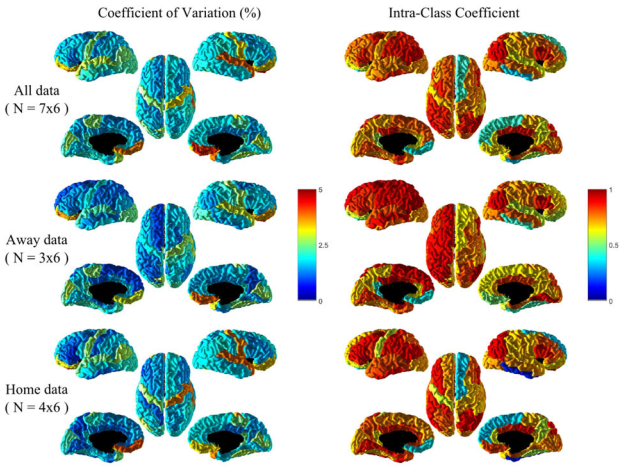

CoV (left) and ICC (right) of the cortical thickness measure of the DKT across sites and repeats. All data from all sites are gather together on the top row, away sites data on the middle row, with home sites scan only represented on the bottom row.

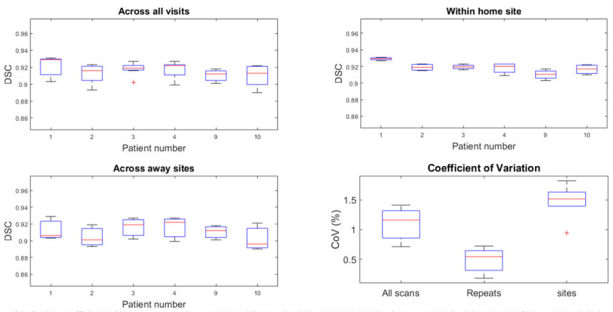

Dice Similarity coefficient of the segmentation computed for each visit compared to the base anatomical (average of the seven visits) considered as the ground truth. Note the higher CoV across sites compared to the CoV of the repeats.

Discussion/Conclusion: Future work will include processing of the full dataset, including 10 subjects scanned over the 5 UK7T sites.

References:
[1]Mougin, MRM 2016, 76: 1512–1516.
[2]Marques, PLoS One 2014, 9(6): e99676.

L07.08

Towards continuous learning for glioma segmentation with elastic weight consolidation

K. van Garderen, S. van der Voort, F. Incekara, M. Smits, S. Klein
Erasmus MC, Radiology and Nuclear Medicine, Rotterdam, The Netherlands

Purpose/Introduction: Automatic segmentation of glioma from MR imaging is a relevant problem that can be solved by convolutional neural networks (CNNs). Ideally, the model would be trained continuously with new data, especially if there is change in the source distribution, e.g. due to a new scanner. However, a neural network will suffer from catastrophic forgetting of the information from previous datasets if they are not also included in this re-training.
In this study we evaluate the use of Elastic Weight Consolidation (EWC) [1] to overcome catastrophic forgetting when training a network on new data without access to the original training set. EWC

penalizes large changes in the weights through an additional term in the loss function, which is specifically computed for each parameter based on its importance for the original dataset. The EWC loss has to be tuned by a general weight factor.

Subjects and Methods: We used two datasets: the 2018 BraTS benchmark [2] (source) and an in-house dataset containing 98 subjects with non-enhancing glioma (target). They contain four MR sequences: pre- and post-contrast T1-weighted, T2-weighted and T2-weighted FLAIR. All images were skull stripped and normalized to zero mean and unit standard deviation.

A 3D UNet (fig 1) was trained first on the source and then on the target domain. This second training was performed with an EWC weight factor of 10 and 100 and without any EWC penalty. The model was evaluated on two test sets: either containing 20% of the subjects in source or target dataset. As comparison, the performance was also evaluated after training on both datasets simultaneously.

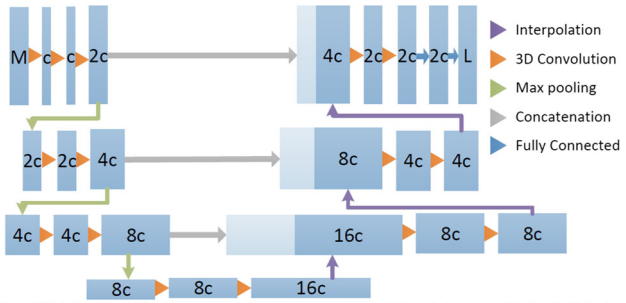

Figure 1. Illustration of the UNet architecture. The number of feature maps is indicated for each step as a multiple of c. M indicates the number of input modalities and L the number of output labels. In this study, c=32, M = 4 and L = 4.

Results: The results are presented in Table 1. The EWC penalty did improve performance on the source domain in this case, but it also limited the adaptation to the target domain. Increasing the weight from 10 to 100 decreased performance on both source and target data. Training together gives some improvement for the source domain, but for the target domain it was more effective to train specifically on that dataset.

Training	Source	Target
Target only	0.64	0.71
Source only	0.86	0.58
+ Target	0.68	0.73
+ Target EWC 10	0.78	0.72
+ Target EWC 100	0.73	0.69
Source & Target	0.87	0.67

Table 1. Performance results in mean Dice coefficient. The + operator indicates an additional training of the model pre-trained on source only.

Discussion/Conclusion: EWC is effective against catastrophic forgetting and only slightly limits the adaptation capacity for the new domain. Adapting to the new domain leads to better performance than training together or training on the target domain only. The results also show that tuning the EWC weight factor is important to achieve good results. More extensive evaluation with different models and datasets is needed to gain further insight into whether and how EWC can enable continuous learning for glioma segmentation.

References:

[1] Kirkpatrick, J. et al.: Overcoming catastrophic forgetting in neural networks. Proceedings of the national academy of sciences 114(13), 3521–3526 (2017)

[2] Menze, B.H et al.: The multimodal brain tumor image segmentation benchmark (BraTS). IEEE Transactions on Medical Imaging 34(10), 1993–2024 (2015)

L07.09

Multi-modal segmentation with missing MR sequences using pre-trained shared representation networks

K. van Garderen, M. Smits, S. Klein
Erasmus MC, Radiology and Nuclear Medicine, Rotterdam, The Netherlands

Purpose/Introduction: Tumor segmentation is a key task in brain imaging research, as it is a prerequisite for obtaining quantitative features from the tumor. Research into automatic segmentation methods for glioma has been accelerated by the recurring BraTS multi-modal segmentation challenge [2], which contains four MR modalities: a pre- and post-contrast T1-weighted image, a T2-weighted image and a T2-weighted FLAIR image. In practice, especially in a retrospective or multicenter study, the availability of these images is not always guaranteed. We therefore developed a CNN that is robust to missing MR sequences.

Subjects and Methods: As a baseline, we use the 3D UNet [1] architecture where the number of features is defined by one parameter c = 32 (see figure). Our proposed model has a separate path for each image, shaped like a UNet, and information is fused through a shared feature representation [3]. For each path, we set c to 16 to make both models of similar size. However, the multipath model requires twice as much GPU memory to train end-to-end. Through pre-training of the paths and then training only the combination layers, the demand on memory was reduced by a factor 4 while the total training time increased by factor 1.5.

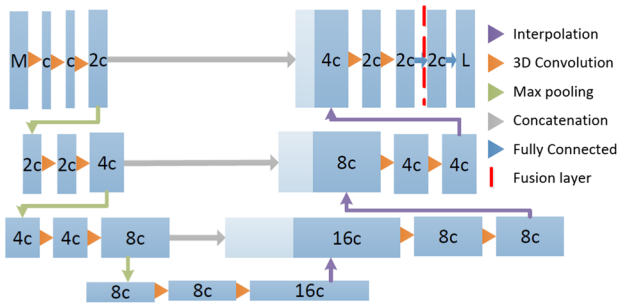

Figure 1: Illustration of the UNet architecture. In the multi-path network four UNets are fused at the indicated location. C indicates the number of feature maps per convolution, M is the number of input modalities and L the number of labels.

The UNet and multipath network, trained end-to-end and pre-trained, were evaluated in five-fold cross-validation on the BraTS training set with Dice score as performance metric. Evaluation took place on each combination of MR modalities. For comparison, a UNet model was also trained specifically for each of the combinations.

Results: Results are shown in Table 1 for three regions of interest: the whole tumor, the tumor core and the contrast-enhancing part. Our multi-path model shows significant improvement with respect to the baseline, and pre-training the paths does not harm performance and shows slight improvement on cases with lower performance in general, which is also where

the dedicated models show most improvement with respect to the generic models.

	All	All but T1W	All but T1WC	All but T2W	All but FLAIR	T2W, FLAIR	T1WC, FLAIR	T1WC, T2W	T1W, FLAIR	T1W, T2W	T1W, T1WC	FLAIR	T2W	T1WC	T1W
Whole tumor															
UNet	83	65	78	74	43	65	43	46	63	23	18	37	30	14	4
Multipath	83	82	82	79	72	81	74	71	76	71	48	72	69	36	29
Multipath + Pretraining	83	83	82	81	74	81	77	72	79	73	58	75	69	52	44
Dedicated	83	81	81	79	73	79	77	74	76	72	59	73	71	49	48
Tumor core															
UNet	71	47	43	59	46	43	26	36	35	23	26	28	27	9	2
Multipath	70	69	43	66	64	41	60	59	38	37	50	30	31	38	20
Multipath + Pretraining	67	66	42	64	63	43	59	60	37	37	53	34	29	49	23
Dedicated	71	64	46	64	63	45	61	63	42	43	56	37	43	43	25
Enhancing core															
UNet	63	40	6	55	43	2	21	36	6	4	25	7	6	6	3
Multipath	62	61	8	60	58	7	54	55	10	7	48	5	5	39	6
Multipath + Pretraining	60	60	10	58	59	12	54	57	9	8	50	9	8	48	9
Dedicated	63	60	17	63	59	18	60	58	17	14	56	10	16	45	9

Table 1: Numeric results in terms of mean Dice percentage on the three different regions of interest. Color scales are different for each region.

Discussion/Conclusion: We showed that it is possible to design and train a multi-path CNN to be robust to missing MR modalities in the context of the BraTs multi-modal segmentation challenge with four MR sequences. Pre-training the paths provides similar performance while reducing the demand on GPU memory, which is a major bottleneck for 3D segmentation networks. However, comparison with the dedicated models shows that there is room for improvement.

References:

[1] Çiçek, Ö. et al.: 3D U-Net: Learning dense volumetric segmentation from sparse annotation. MICCAI 2016. pp. 424–432. Springer International Publishing, Cham (2016)

[2] Menze, B.H et al.: The multimodal brain tumor image segmentation benchmark (BraTS). IEEE Transactions on Medical Imaging 34(10), 1993–2024 (2015)

[3] Havaei et al.: Hemis: Hetero-modal image segmentation. MICCAI 2016. pp. 469–477. Springer International Publishing, Cham (2016)

L07.10

Fast and accurate long-axis cine cardiac MRI segmentation using deep learning

C. Tiago[1], M. Veta[2], M. Breeuwer[3]

[1]*University of Lisbon, Biomedical Engineering and Biophysics, Lisbon, Portugal,* [2]*Eindhoven University of Technology, Biomedical Engineering—Medical Image Analysis, Eindhoven, The Netherlands,* [3]*Philips Healthcare, MR Clinical Science, Best, The Netherlands*

Purpose/Introduction: Long-axis cine cardiac MRI (LA CMR) is clinically used to estimate left-ventricular (LV) functional parameters stroke volume (SV), ejection fraction (EF) and cardiac output (CO). To simplify and accelerate the estimation, fast and accurate automatic segmentation of the LV endocardial contour and valve plane is needed in all acquired phases (time moments) in the cardiac cycle. We have investigated to what extent this can be achieved with convolutional neural networks (CNNs).

Subjects and Methods: We trained CNN models with the widely used U-Net architecture[1] to automatically segment the LV endocontour and detect the valve plane and apex landmarks. Our data consisted of 55 anonymized clinical LA CMR scans (5809 images) with manually created reference contours and landmarks (various Philips 1.5/3T MR scanners, routine clinical scan protocol, 70/20/10% used for CNN training/validation/testing). None of the images contained anatomical abnormalities. After data augmentation (scaling, translation, rotation, intensity variation) the dataset consisted of 102,650 images.

Before CNN training the manual reference contours were translated to either a distance map (DM, distance to reference contour) or to a closed LV area (marked by the endocontour and valve plane), which were then used as references (labels) to train 2 different models: CNN-DM and CNN-Area. Training took 24 h on 4 NVIDIA TITAN Xp GPUs, using open-source software Theano and Lasagne.

The performance of the CNN-based segmentation was evaluated using the Dice similarity coefficient (DSC) and distance to reference contour (mm). Additionally, the cardiac parameters SV, EF, CO were compared, estimated from the reference and CNN-based contours using the clinically accepted area-length approach[2].

Results:

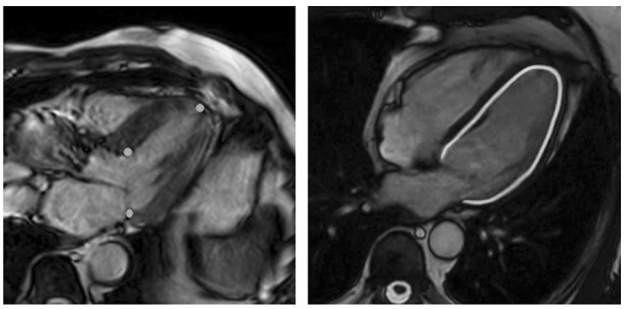

Figure 1: Example result: detected landmarks (left), segmented endocontour (right) (CNN-DM)

The mean and standard deviation of the distances between reference and contours segmented with CNN-DM (example in Fig. 1) was 1.93 ± 0.50 mm and the DSC of the areas enclosed by these contours was 0.88 ± 0.04. CNN-DM performed consistently better than CNN-Area, which produced contour distances 3.44 ± 1.08 mm (paired t test, $p < 0.001$). Segmentation took less than 1 s per dataset (NVIDIA GeForce GTX 980 m GPU). SV, EF and CO derived from the CNN-DM contours did not differ significantly from those derived from the reference contours (Wilcoxon signed-rank test, $p > 0.5$). Figures 2 and 3 show the SV scatter and Bland–Altman plots.

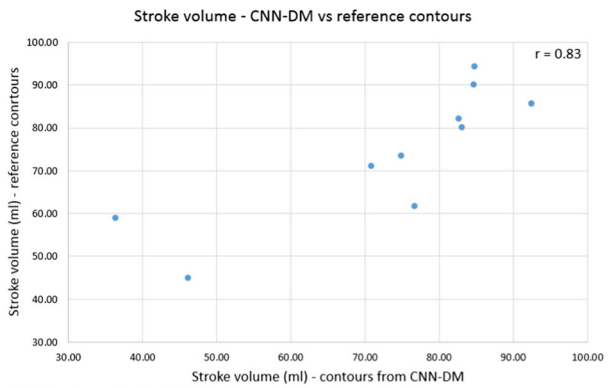

Figure 2: Stroke volume resulting from CNN-DM contours vs reference contours (scatter plot)

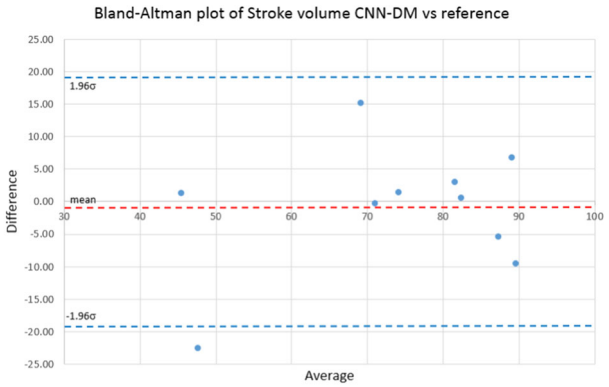

Figure 3: Stroke volume resulting from CNN-DM contours vs reference contours (Bland-Altman plot)

Discussion/Conclusion: LA CMR segmentation can be accurately performed automatically with deep learning. We found average contour distances of 1.93 mm (for CNN-DM), which is similar to the in-plane MRI acquisition resolution of 2 mm, and an average DSC of 0.88. Functional parameters SV, EF and CO can be as accurately calculated from the CNN-DM as from the reference contours.

References:

1. Ronneberger et al., MICCAI 2015, Springer, LNCS, Vol 9351:234–241.
2. Lessick et al., Can J Cardiol 2008, Vol 24 No 9:685–689.

L07.11

Landmark-guided Hip Segmentation in 3D MR Images of a Large-Scale Cohort Study

M. Fischer[1], **M. Schwartz**[1], C. Klinger[2], B. Yang[3], M. Notohamiprodjo[2], F. Schick[1]
[1]University Hospital Tübingen, Section on Experimental Radiology, Department of Radiology, Tübingen, Germany, [2]University Hospital Tübingen, Diagnostic and Interventional Radiology, Tübingen, Germany, [3]University of Stuttgart, Institute of Signal Processing and System Theory, Stuttgart, Germany

Purpose/Introduction: Studying subtle prevalent degenerative findings of the hip in high resolution 3D MRI is of great interest. To reliably analyze femoral acetabular impingment[1] and further precursors of osteoarthritis, automatic hip bone segmentation becomes a mandatory prerequisite with respect to large-scale cohort data such as the German National Cohort (NAKO)[2]. Subsequently, accurate geometrical and structural properties can be derived and quantitative evaluation can be performed. Leveraging recent Deep Learning (DL) advancements a neural network architecture named MedPatchNet[3] is extended, by providing additional anatomical landmarks for guidance. Thereby, accurate semantic hip bone segmentation is investigated.
Subjects and Methods: Data: Fat saturated PD-weighted FSE images of 20 NAKO subjects have been manually annotated obtaining 3D voxel-wise label ground truth and the center landmark positions of the femur heads (see Fig. 1). 3T MR scans have been acquired with 1.0 mm isotropic res., size 384 × 264 × 160, TE/TR = 33/1200 ms and BW = 500 Hz/px. **Concept:** The network architecture is based on concepts such as UNet[4], VNet[5], DeepLabv3 + [6] and ESPNet[7]. Distance vectors from the center of an input patch to each predefined landmark are incorporated by means of a Dynamic Filter Network (DFN)[8] providing relative positional information and thus guidance to the segmentation process. Implicit locality sensitive learning of the underlying anatomy and its textural and structural characteristics is thereby alleviated. The architecture is depicted in Fig. 2. Small isolated misclassifications present in the prediction are removed by morphological operations. **Evaluation:** Sound analysis is performed by relying on fourfold cross-validation resulting in splits of 15/5 training/test subjects. The Dice Similarity Coefficient (DSC) and Average Symmetric Surface Distance (ASSD) are employed for quantitative assessment.

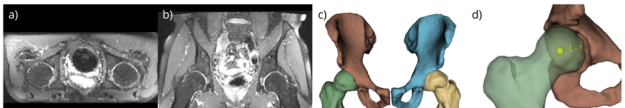

Fig.1: a-b) Axial and coronal slices of fat-sat PD-weighted MRI data from a NAKO participant. c) Corresp. manually annotated 3D ground truth, incorporating femora and pelvis. d) Anatomical landmark (L-1) placed at the center of the right femur head.

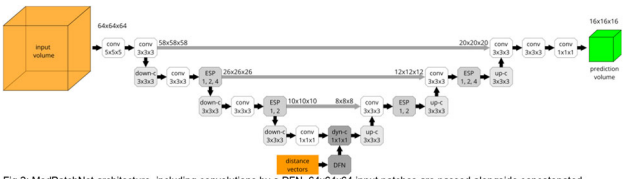

Fig.2: MedPatchNet architecture, including convolutions by a DFN. 64x64x64 input patches are passed alongside concatenated distance vectors from patch center to both anatomical landmarks. A prediction on the central 16x16x16 region is performed.

Results: Quantitative findings are shown in Fig. 3a, b). Bones are segmented with very high mean DSC values of 0.938 ± 0.028. Mean ASSD values of 0.864 ± 0.349 mm indicate that the surface of the prediction deviates only slightly from the ground truth. Both Femora and Pelvis are correctly and robustly delineated including the acetabulum region, as can be seen by the exemplary segmentation results in Fig. 3c).

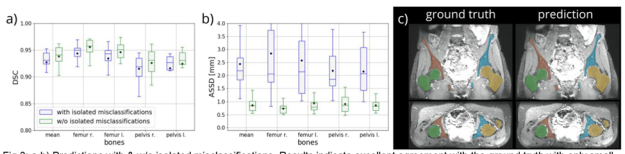

Fig.3: a-b) Predictions with & w/o isolated misclassifications. Results indicate excellent agreement with the ground truth with only small deviations between surface boundaries. c) Side-by-side comparison for a subject with a mean DSC of 0.957.

Discussion/Conclusion: A suitable segmentation approach for hip bones in intricate MR images of cohort data is established, with the proposed DL architecture relying on an efficient architecture, dynamic filters and landmark guidance. Improving upon previous approaches[9], a high resolution differentiation of bone tissues sharing common characteristics is achieved for the complex anatomy despite limited amounts of data.

References:

1: K. Hack, JBJS, 2010. 2: F. Bamberg, Radiology, 2015. 3: M. Fischer, ISMRM, 2019. 4: O. Ronneberger, MICCAI, 2015. 5: F. Milletari, 3DV, 2016. 6: LC. Chen, ECCV, 2018. 7: S. Mehta, ECCV, 2018. 8: X. Jia, NIPS, 2016. 9: CM. Deniz, Sci. Rep., 2018.

L07.12

Automated prostate multiregional segmentation in magnetic resonance using deeply supervised convolutional neural networks

R. López-González[1, 2], V. Venugopal[3], A. Jimenez-Pastor[2], M. Barnwal[4], V. Mahajan[4], Á. Alberich-Bayarri[5], L. Martí-Bonmatí[6]
[1]QUIBIM, Research and developement, Valencia, Spain, [2]QUIBIM, Research and Development, Valencia, Spain, [3]CARING, Radiology, New Delhi, India, [4]CARING, New Delhi, India, [5]QUIBIM, Management, Valencia, Spain, [6]Hospital Universitario y Politécnico La Fe, Radiology, Valencia, Spain

Purpose/Introduction: Due to the limitations of techniques such as PSA and ultrasound (US), the relevance of Magnetic Resonance to detect prostate cancer increased. In parallel, the use of Artificial Intelligence to automatically extract information from medical images is becoming more important to reduce variability and improve disease management. A step further can be achieved in the use of Magnetic Resonance for prostate cancer diagnosis by the automation of image segmentation task due to it is a time consuming and not rewarding task that hinders clinical workflow. Automatic segmentation speeds up and improve treatment planning by providing accurate region delineations in within seconds. The purpose of our work was to develop a Convolutional Neural Network based automatic prostate segmentation method, aiming to identify and differentiate central-transitional and peripheral prostate glands as well as seminal vesicles.
Subjects and Methods: A total of 131 axial T2-weighted MR prostate examinations were acquired in different 3T machines and with different acquisition protocols. The central and peripheral glands and the seminal vesicles were manually labelled in all the acquired T2-weighted series by an expert to train the models. Additionally, the clinical validation was performed on a different set of 25 T2-weighted cases from an external centre which was not part of the training set. A deeply supervised U-Net based architecture was used to train this network with the Dice score coefficient as cost function and Adam as optimization algorithm. To maximize the performance of the CNN, a Cyclic Learning Rate was used during the training stage. Also, Image Processing algorithms were used to further refine the predicted segmentation masks during inference.
Results: The segmentation results from the network in the clinical validation set were compared and corrected by an expert radiologist to match best truth. Finally, the Dice score coefficient between the model's predictions and the expert corrected masks was calculated. The scores for the central-transitional gland, peripheral gland, seminal vesicles and background were 0.92 ± 0.03, 0.90 ± 0.05, 0.91 ± 0.05, and 0.99 ± 0.00, respectively.
Discussion/Conclusion: Fully automated multiregional segmentation of the prostate gland and seminal vesicles can be addressed by deeply-supervised CNN. This step will help localizing prostatic lesions and characterizing the pattern of prostatic enlargement.
References:
[1] Ronneberger O., Fischer P., Brox T. (2015). U-Net Convolutional Networks for Biomedical Image Segmentation. arXiv:1505.04597.
[2] Smith L. (2017). Cyclical Learning Rates for Training Neural Networks. arXiv:1506.01186.
[3] Zhu Q., Turkbey B., Choyke P., et al. (2017). Deeply-Supervised CNN for Prostate Segmentation. arXiv:1703.07523.

L07.13
Glomerular quantification from undersampled data using compressed sensing reconstructions

E. Ilicak, L. R. Schad, J. Chacon-Caldera
Heidelberg University, Medical Faculty Mannheim, Computer Assisted Clinical Medicine, Mannheim, Germany

Purpose/Introduction: The quantification of glomeruli using MR imaging in rodent kidneys has recently gained attention since it offers a direct biomarker to assess the filtration capacity of the kidney. However, it is technically challenging in terms of data acquisition and post-processing. Considering the required 3D acquisitions at resolutions of up to $25 \times 25 \times 25\text{um}^3$ with low channel counts[1], compressed sensing (CS) is, theoretically, a suitable approach to reduce scan times. In this work, CS reconstruction of undersampled data is performed to investigate acceleration factors that allow reliable glomerular quantifications.

Subjects and Methods: Measurements were performed in a 9.4T system with a cryogenically cooled quadrature transceiver coil (Bruker Biospin, Ettlingen, Germany). A kidney was prepared and scanned ex vivo as previously described[1]. The dataset was retrospectively undersampled in the phase encoding dimensions to yield acceleration rates (R) between 1.3 and 2.7. The sampling masks were generated using variable density random sampling, with polynomial order of 6 to emphasize higher spatial frequency locations near the periphery of k-space. The reconstructions were obtained by solving the optimization problem in Fig 1.

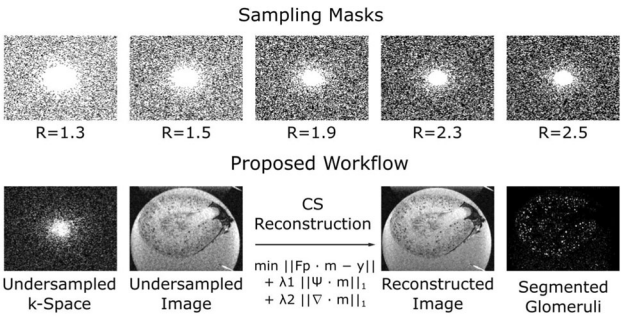

Figure 1, undersampling masks for various acceleration rates (Top), with the overview of the proposed workflow (Bottom), starting from the undersampled data to glomeruli segmentation

There, F_p is the Partial Fourier operator, m is the reconstruction, y is the acquired k-space data. Ψ and ∇ represent the wavelet and total variation transformations, with λ_1 and λ_2 representing the regularization weights. The regularizations weights were empirically selected and were fixed among all acceleration rates.
Results: CS allowed quantification with accelerations of up to a 1.7x factor within a 5% difference in glomerular number compared to the fully sampled case.

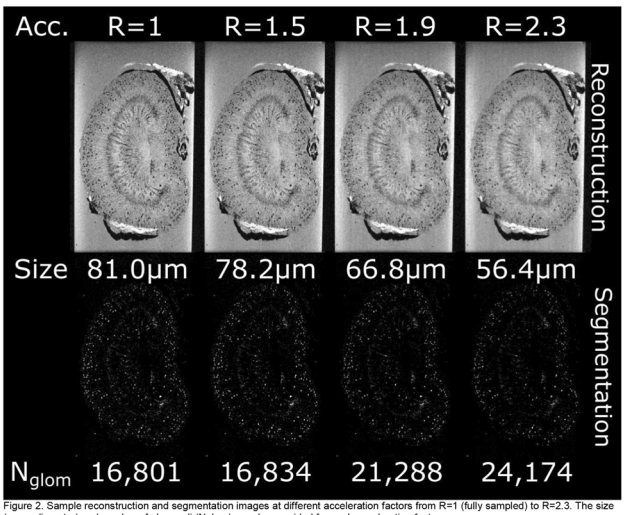

Figure 2. Sample reconstruction and segmentation images at different acceleration factors from R=1 (fully sampled) to R=2.3. The size (mean diameter) and number of glomeruli (Nglom) are also provided for each acceleration factor.

Differences of 20–50% were observed for higher acceleration factors due to the decreasing of apparent size of the glomeruli which skewed the glomerular distribution as it merged with noise (Fig. 3).

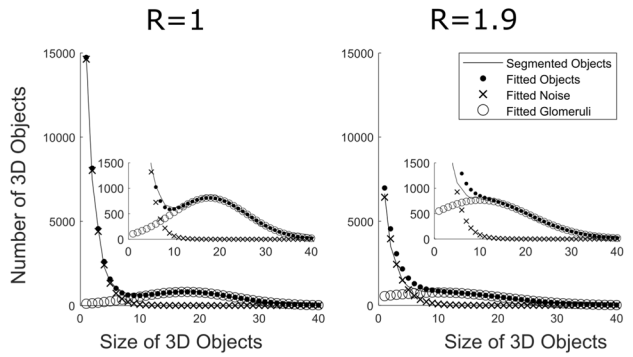

Figure 3. Histogram of the 3D objects segmented including noise and glomeruli. The glomerular distribution is found and fitted to quantify Nglom but it cannot be separated from noise at R=1.9

Discussion/Conclusion: Unlike conventional CS MRI applications, the figure-of-merit to assess the reconstruction performance is not defined by structure similarity or signal-to-noise ratio but rather by the robustness in the number and size of the glomeruli. Here, we achieved a promising initial assessment of the performance of CS for glomerular quantification for a sample mouse kidney. Optimized reconstruction and tailored quantification algorithms could increase the gains in acquisition times showed here.

References:

1. Chacon-Caldera et al. Z Med Phys 2016;26(1):54–62

L07.14
Texture analysis as a tool for liver steatosis estimation

M. Dezortova, S. Knoppova, P. Sedivy, M. Burian, M. Hajek
Institute for Clinical and Experimental Medicine, MR-Unit, Dept Diagnostic and Interventional Radiology, Prague, Czech Republic

Purpose/Introduction: Liver steatosis is usually determined from liver biopsy samples or non-invasively by ^{1}H MR spectroscopy. In this study we studied if texture analysis is sensitive enough to distinguish different degrees of steatosis in routinely obtained MR images.

Subjects and Methods: Liver examination at 3T MR system Trio using body array coil was done in 52 volunteers (38 m/14f, 21–74 years old) without healthy problems (except for obesity in 12 cases) after overnight fasting to estimate degree of liver steatosis. All subjects signed an informed consent approved by the local ethical committee.

HASTE transversal slices (TR/TE = 1800/96 ms, voxel size $2.0 \times 1.6 \times 10.0$ mm^3) were obtained in breath hold and served for the spectra localization. Localized ^{1}H MR spectroscopy was performed and hepatic fat content was calculated [1]. Based on spectroscopic results Kleiner score widely used for steatosis stage was assigned to each subject [2].

HASTE images were evaluated using 3D texture analysis in MaZda program [3]. Regions of interest were selected over whole liver with exception of visible vessels. The most important texture features were reduced from almost 300 calculated ones and selected by Fisher score, classification error combined with the correlation coefficient (POE-ACC), mutual information (MI) methods and/or their combination. Then, potential of various statistical methods (principal component analysis (PCA), linear and nonlinear discriminant analyses (LDA, NDA) was tested.

Results: MR spectroscopy assigned 10 subjects to steatosis of Kleiner score 0, 21 subjects to Kleiner-1, 12 subjects to Kleiner-2, and 9 subjects to Kleiner-3 group.

Whereas all classification methods distinguished Kleiner-0 and Kleiner-3 groups without any misclassification, Kleiner subgroups 0–1–2–3 reached about 20–30% of errors. The best results were obtained when combination of Fisher, POE-ACC and MI methods was applied for the features reduction together with LDA incorporated in MaZda program (part B11) for subjects classification (Fig. 1). In this case, the misclassification was only found in 3 cases; all of them were retrospectively found on the border line between steatotic degrees.

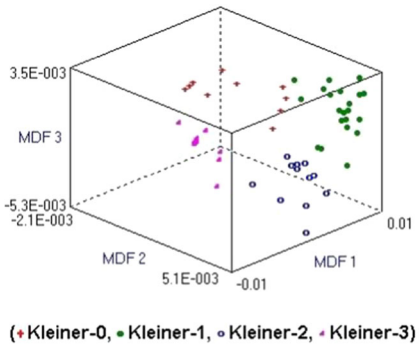

Figure 1. Graphical results of linear discriminant analysis. Subjects are assigned according to steatotic Kleiner score.

Discussion/Conclusion: Our study showed that it is possible to distinguish degree of steatosis even from the standard MR images without any special resolution. Texture analysis is an evaluation technique which enables automatic classification of image data into groups based on various input criteria. It has a potential to be useful in objective evaluation even if only standard MR images without any special resolution are available.

The study was supported by MH CR: AZV 16-28427A, 15-25906A, DRO IN 00023001IKEM, and MEYS CR: Mobility Czech-Austria 8J18AT023.

References:

[1] Hajek M, et al. MAGMA 2011;24(5):297–304.
[2] Kleiner DE, et al. Hepatology 2005;41(6):1313–1321.
[3] Hajek M, et al. Texture analysis for Magnetic Resonance Imaging. Med4publishing 2006.

L07.15
Non-uniform_Fourier-decomposition_MRI

D. Bondesson[1], M. Schneider[1], T. Gaaß[2], B. Kühn[3], G. Bauman[4], O. Dietrich[1], J. Dinkel[1]
[1]*University Hospital, LMU Munich, Department of Radiology, Munich, Germany,* [2]*Siemens Healthcare Pty Ltd, Bowen Hills, AUSTRALIA,* [3]*Siemens Healthcare GmbH, Erlangen, Germany,* [4]*University of Basel Hospital, Division of Radiological Physics, Department of Radiology, Basel, Switzerland*

Purpose/Introduction: Several studies have shown the Fourier decomposition (FD) MRI method to be a viable tool for locally assessing pulmonary ventilation and perfusion function 1. However, variations of respiratory or cardiac frequencies during free-breathing pulmonary measurements were shown2 to cause issues for the approach. The purpose of this study was to improve the robustness of FD MRI by correcting for frequency variations and replace the standard fast Fourier transform with the more general non-uniform fast Fourier transform (NUFFT), yielding non-uniform FD (NUFD).

Subjects and Methods: Dynamic coronal single-slice MRI of the thorax was acquired on 11 patients with different pulmonary

pathologies and 5 healthy volunteers with temporal resolutions between 4 and 9 images/second, using a 2D balanced SSFP sequence. The proposed method requires transforming the initially evenly sampled time points of a signal with variable frequencies into unevenly sampled signals with perceived constant frequency. Frequency-variations were tracked with synchro-squeezed wavelet transform [3], yielding the new time points. The spectral analysis of the time series was then performed using NUFD. Spectral separation was performed by observing the average time series within the lungs and selecting the ventilation and perfusion frequency peaks for their respective maps. Amplitude and time delay maps were then generated and compared to FD-maps based on their SNR. SNR was calculated pixel wise by comparing signal peak heights against noise floor in the frequency spectrums.

Results: Figure 1 exemplifies the principal of collecting perfusion and ventilation signal intensity onto a single frequency bin.

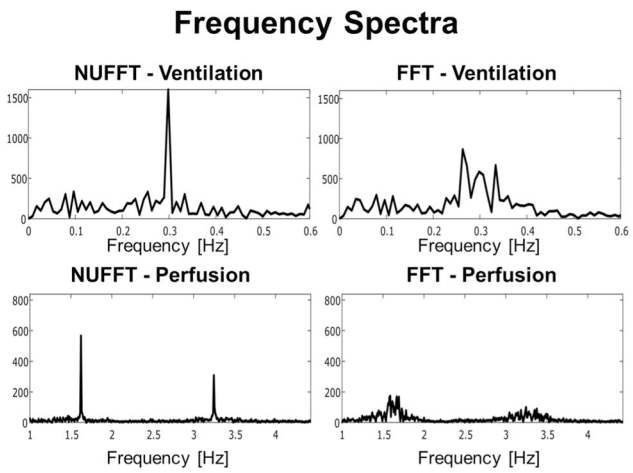

Figure 1. NUFFT and FFT evaluations of ventilation and perfusion time signals

Figure 2 displays maps of a volunteer with the calculated SNR of the perfusion and ventilation signal.

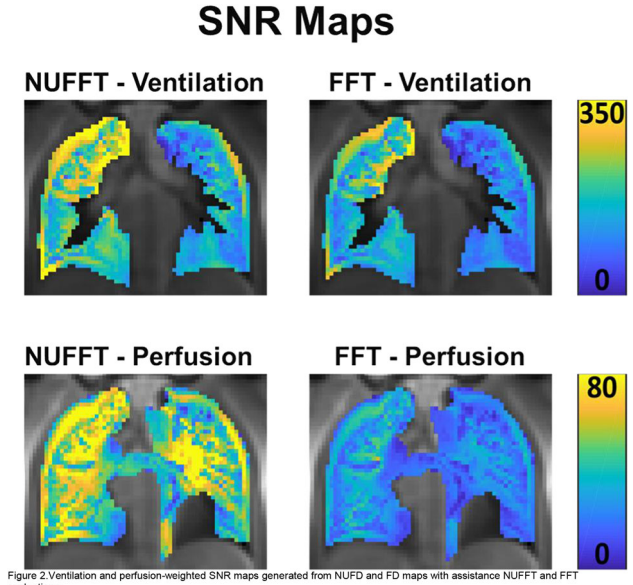

Figure 2.Ventilation and perfusion-weighted SNR maps generated from NUFD and FD maps with assistance NUFFT and FFT evaluations.

Table 1 summarizes statistical comparisons of obtained signal to noise ratios using NUFD and conventional FD. NUFD showed significant increases of SNR for patients and volunteers in both Ventilation (24.4% ± 31.9% and 43.4% ± 25.3% respectively) and perfusion (75.6% ± 62.8% and 93.0% ± 36.1% respectively) maps.

	SNR NUFD	SNR FD	SNR increase (absolute)	SNR increase (relative)	p-value
Volunteer V (n=11)	144.1+-32.6	102.7+-27.8	41.4+-17.7	43.4%+-17.7%	2 * 10^-5
Volunteer Q (n=11)	52.3+-11.6	27.8+-6.8	24.5+-8.3	93.0%+-36.1%	7 * 10^-6
Patient V (n=11)	121.8+-64.5	95.1+-41.1	26.7+-36.3	24.4%+-31.9%	3 * 10^-2
Patient Q (n=11)	18.5+-13.5	11.2+-7.5	7.3+-7.9	75.6%+-62.8%	3 * 10^-3

SNR results for ventilation and perfusion measurements from FD and NUFD method. Average and standard deviation SNR of all volunteer and patient measurements. Average increase (absolute and relative(%)) is also displayed.

Occasional changes in signal delay patterns were also observed with NUFD compared to FD and two patients showed perfusion signal in pulmonary areas that could not be imaged with FD.

Discussion/Conclusion: This study presents a modification of functional Fourier-decomposition lung imaging with frequency-adapted Fourier transform to compensate for variability in perfusion and ventilation frequency. We demonstrated that utilizing NUFFT in combination with frequency tracking can significantly increase SNR of the generated parameter maps.

References

1. Bauman G, et al. Magn Reson Med. 2009;62(3):656–664. https://doi.org/10.1002/mrm.22031

2.Voskrebenzev A, et al. Magn Reson Med. August 2017. https://doi.org/10.1002/mrm.26893

3.Daubechies I, et al. Appl Comput Harmon Anal. 2011;30(2):243–261. https://doi.org/10.1016/j.acha.2010.08.002

L07.16

Model selection in quantifying hemodynamic parameters using DCE-MRI

M. Y. Zhao, M. A. Chappell

University of Oxford, Institute of Biomedical Engineering, Oxford, UK

Purpose/Introduction: Several pharmacokinetic models have been proposed to quantify the hemodynamic parameters in DCE-MRI data[1]. The two-compartment exchange model (2CXM) serves as the most general description. It can be transformed, under certain physiological conditions, into simpler models such as the compartmental tissue update model (CTUM) or the Tofts model[2]. Model selection metrics can be used to determine the appropriate model on a voxel-wise basis and might be indicative of the underlying tissue physiology. However, model selection is also affected by CNR and choice of temporal sampling. Hence, here we sought to determine in what conditions model selection can correctly identify the true model to help understand in what conditions we might be able to interpret model selection in vivo.

Subjects and Methods: Three simulated DCE-MRI datasets were generated with different TRs. For each dataset, the simulated pharmacokinetic signal was created using, from high to low model complexity, 2CXM, CTUM, Extended Tofts Model (ETM), and Simple Tofts Model (STM)[3, 4, 5]. A population-averaged AIF was used in all data[6]. The parameters of the dataset using 2CXM and CTUM were: plasma flow Fp = 60 ml/100 g/min, extraction flow Fe = 1.4 ml/100 g/min, plasma volume Vp = 24%, EES volume Ve = 62%. The K^{trans} value was set to 0.4 min^{-1} for the data using ETM and STM while the other values were the same with the 2CXM

and CTUM. In all datasets, the other parameters were FA = 12°, T_{10} = 1.3 s, R_1 = 4.5 $s^{-1}mM^{-1}$, Hct = 42% for a total acquisition time of 7 min. The TRs were chosen to be 1, 3, and 6 s to represent high, medium, and low temporal resolutions. Noise was added to the simulated data using CNR ranging from 1 to 100 with 1000 realizations. Model-fitting was conducted using the models of the same or lower than the complexity of the simulated data, e.g. simulated data using ETM was fitted by ETM and STM. All model-fitting were performed using Variational Bayesian inference method[7]. The model selection metrics included Akaike information criterion (AIC), Bayesian information criterion (BIC), and free energy (FE). A lower AIC or BIC and a higher FE indicates a preferred model choice.

Results: Figures 1, 2, and 3 shows the model selection results for low, medium, and high temporal resolutions at different CNRs.

Discussion/Conclusion: The different model selection metrics did not all perform the same under the conditions tested here. Notably, the AIC metric consistently selected only STM. As expected, models with a lower complexity were always selected at low CNRs. Model selection was most notably affected by SNR, whereas the choice of temporal sampling was less important. For data with the same resolution, the true model can be selected for CNR higher than 50 using BIC and FE.

References:

1 Tofts et al., MRM 1991
2 Sourbron et al., NMR Biomed 2013
3 Tofts, JMRI 1997
4 Flouri et al., MRM 2016
5 Duan et al., MRM 2017
6 Parker et al., MRM 2006
7 Chappell et al., IEEE, 2009

L07.17

Comparison between the phase contrast MRI and the Lattice Boltzmann method of computational fluid dynamics for a turbulent flow in vitro using an aortic valve phantom

R. Fucik[1], P. Paus[1], P. Eichler[1], J. Klinkovsky[1], **R. Galabov**[2], J. Tintera[2], J. Rydlo[2]
[1]Czech Technical University, FNSPE, Prague, Czech Republic, [2]Institute for Clinical and Experimental Medicine, Prague, Czech Republic

Purpose/Introduction: Phase contrast magnetic resonance imaging (PC MRI) is an established method of flow assessment in cardiac patients. Its limitations (turbulent flow, implanted stents etc.) can be circumvented by its coupling with computational fluid dynamics (CFD) [1]. Common CFD models suffer from impractically long computational times. In this work, a relatively new model based on a different approach is concerned, the lattice Boltzmann method (LBM), and the results from the implemented LBM are compared to in vitro PC MRI data.

Subjects and Methods: The PC MRI data were measured in vitro using a plastic phantom comprising a rigid tube with a dummy aortic valve (one healthy and three diseased valves were used). Water was run through the phantom at constant rate and four different flow rates were investigated for each valve. The known geometry of the phantom was used to setup a 3D computational domain and the flow PC MRI data served as boundary conditions for the LBM model. The objective of the study was to determine regions of turbulent backflow behind the valve and compare the mean velocity magnitude between the PC MRI measurements and the LBM simulated data. The 3D LBM model was based on the Cumulant LBM [2–4] in order to simulate turbulent flow that occurs at high Reynolds numbers. The LBM model was implemented using an in-house C ++ and CUDA code suitable for multi-GPU computations.

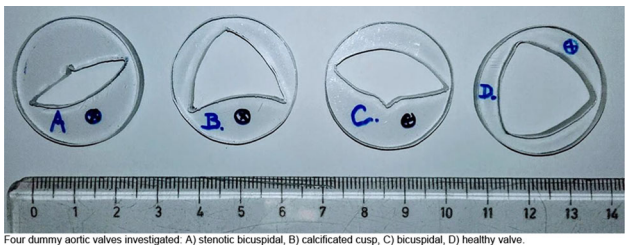

Four dummy aortic valves investigated: A) stenotic bicuspidal, B) calcificated cusp, C) bicuspidal, D) healthy valve.

Results: The LBM and PC MRI results matched relatively well in the case of the healthy valve. A turbulent flow caused by the diseased valves was underestimated by the PC MRI and complicated the comparison. In all the scenarios, however, a region of backward vortical flow following the valve was successfully detected. The LBM discriminated between different backward flow rates, where PC MRI failed due to turbulences. The localization of a backward flow by LBM showed a systematic inaccuracy caused by discretization errors of the computational domain. For low flow rates, the magnitude of the backflow behind the valve was the same for both LBM model and PC MRI measurements. For larger flow rates, however, the PC MRI data exhibit substantial underestimation of the backflow compared to the LBM model.

Discussion/Conclusion: The LBM and PC MRI results are quantitatively comparable. LBM is able to distinguish between possibly clinically significant flow regimes, unlike PC MRI. The LBM model implementation studied in this work achieved good results but improvements regarding mainly the resolution of the computational domain are still needed for a reliable quantitative flow assessment.

Supported by grant no. NV19-08-00071 of the Ministry of Health of the Czech Republic.

References:

[1] Zhong et al., Front Physiol. 2018;9:742.
[2] Geier et al., Computers & Mathematics with Applications 70.4 (2015): 507-547.
[3] Geier et al., Journal of Computational Physics 348 (2017): 862-888.
[4] Geier et al., Journal of Computational Physics 348 (2017): 889-898.

L07.18

Retrospective deep learning based motion correction from complex-valued imaging data

T. Kuestner[1], K. Mo[2], B. Yang[2], F. Schick[3], S. Gatidis[4], K. Armanious[2]
[1]King's College London, London, UK, [2]University of Stuttgart, Institute of Signal Processing and System Theory, Stuttgart, Germany, [3]University Hospital of Tübingen, Section on Experimental Radiology, Tübingen, Germany, [4]University Hospital of Tübingen, Department of Radiology, Tübingen, Germany

Purpose/Introduction: Motion is the main extrinsic source for imaging artifacts in MRI which can strongly deteriorate image quality and thus impair diagnostic accuracy. Numerous motion correction strategies have been proposed to mitigate the artifacts[1–10]. These methods have in common that they need to be applied during the actual measurement procedure with already a priori knowledge about the expected motion type and appearance. Only few methods have

been proposed for the correction of already acquired data such as auto-focusing[11].

We recently proposed a deep learning (DL) framework[12–14] (MedGAN) to perform motion correction in various body regions simultaneously without the existence of any a priori knowledge about the motion. This approach focused only on processing of magnitude images while phase information carrying significant motion information was not considered. In this work, we propose to overcome this limitation by extending our previously proposed approach to complex-valued data processing in architecture and loss function.

Subjects and Methods: The proposed complex-valued MedGAN (cMedGAN) is depicted in Fig. 1a. The generator consists of 8 cascaded UNets and receives a complex-valued motion-affected image as input. The first 2 UNets jointly correct magnitude and phase (channel concatenated). Since the phase is spatially slowly varying, correction over two stages was empirically found sufficient. In the subsequent 6 UNet stages, only the more detailed magnitude image is further corrected. This reduces the amount of trainable weights and improves convergence stability. A patch-based magnitude/phase discriminator classifies each patch as either real or fake from the magnitude/phase motion-corrected/affected and motion-free (training only) image input.

All network parts are trained end-to-end according to the loss function which consists of an adversarial L_{adv}, perceptual L_p and a style transfer L_{style} loss with the latter two being directly obtained from the trained discriminators. Training is conducted for 100 epochs via ADAM optimizer[15].

The training database consists of 18 healthy subjects imaged in head, abdomen and pelvis with a T1w and T2w FSE on a 3T MRI with parameters stated in Fig. 1b. Each acquisition was performed twice to get a motion-free and motion-affected image.

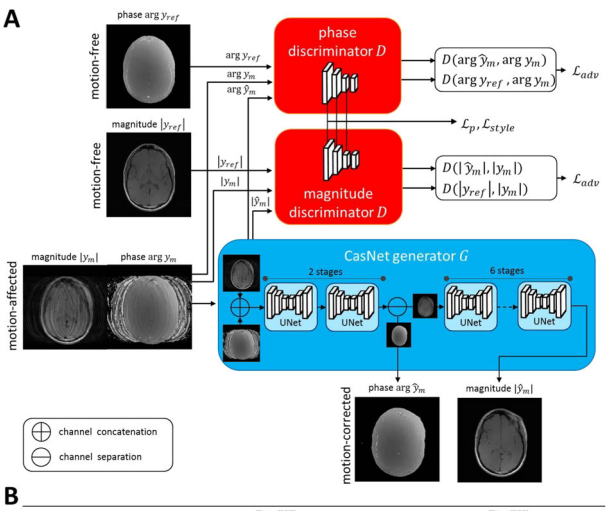

B

	T1w FSE			T2w FSE	
body region	head	abdomen	pelvis	abdomen	pelvis
matrix size	256 × 196 × 40	320 × 192-256 × 30	320 × 192-240 × 40	384 × 228-288 × 32	210 × 192-240 × 40
voxel size [mm³]	1 × 1 × 3	1.25 × 1.25 × 5	1.25 × 1.25 × 5	1.04 × 1.04 × 5	1.25 × 1.25 × 5
TE [ms]	8.4	10	11	100	86
TR [ms]	750	800	900	5800	4200
flip angle	140°	150°	160°	120°	150°
bandwidth [Hz/px]	260	190	190	195	200
averages	2	2	2	2	2
phase-encoding direction	left-right	anterior-posterior	anterior-posterior	anterior-posterior	anterior-posterior

Fig. 1: A) Proposed cMedGAN: Motion correction of complex-valued images is controlled via adversarial L_adv, perceptual L_p and style transfer L_style loss. B) MR acquisition parameters to create training database.

Results: Figure 2 shows qualitative images in head, abdomen and pelvis of the proposed cMedGAN in comparison to the magnitude-only based MedGAN. cMedGAN motion correction improves due to the phase consideration recovering more fine-grained structures.

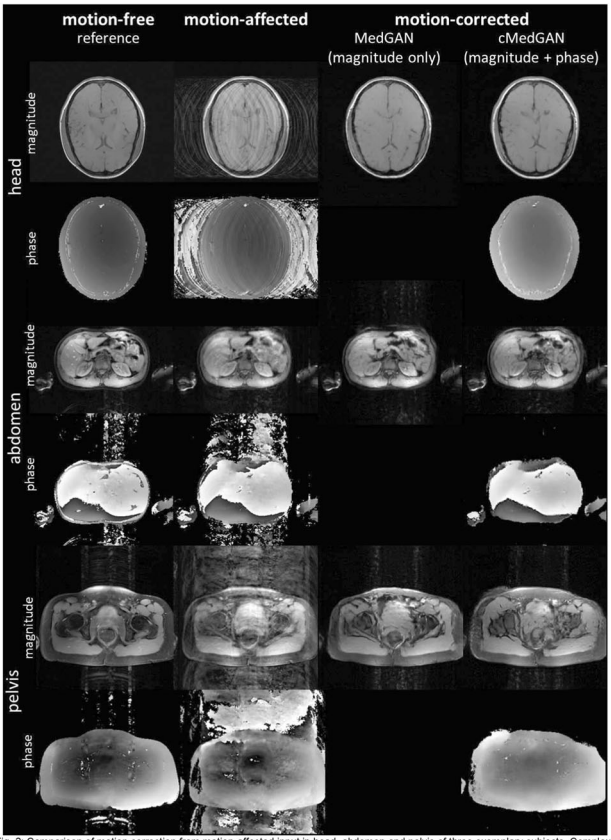

Fig. 2: Comparison of motion correction from motion-affected input in head, abdomen and pelvis of three exemplary subjects. Complex-valued processing is superior to magnitude-only processing.

Discussion/Conclusion: The current study has limitations: Only 2D MR images of a single sequence type (spin echo) were corrected, i.e. through-plane motion correction and phase correction due to field inhomogeneities is limited.

Retrospective motion correction with DL is feasible to recover motion-obstructed content. The inclusion of phase information improves the motion correction task.

References:

1. Cheng JMRI 2015;42(2).
2. Cruz MRM 2017;77(5).
3. Henningsson MRM 2012;67(2).
4. Küstner MRM 2017;78(2).
5. Maclaren MRM 2013;69(3).
6. Prieto JMRI 2015;41(3).
7. Skare MRM 2015;73(3).
8. Speck MAGMA 2006;19(2).
9. Wallace MRM 2019;81(1).
10. Zaitsev JMRI 2015;42(4).
11. Atkinson TMI 1997;16(6).
12. Küstner MRM 2019;[epub ahead of print].
13. Armanious IEEE International Symposium on Biomedical Imaging (ISBI) 2019.
14. Armanious arXiv preprint arXiv:180606397 2018.
15. Kingma arXiv preprint arXiv:14126980 2014.

L07.19
Radial MR image reconstruction through deep learning

M. Arshad, M. Qureshi, I. Khattak, H. Omer
COMSATS University Islamabad, Electrical & Computer Engineering, Islamabad, Pakistan

Purpose/Introduction: Radial under-sampling of *k*-space data is a fast MRI data acquisition method. Its major benefit is the relative insensitivity to motion artifacts [3]. However, the reconstruction of artifact-free images from the radially encoded MRI data poses a complex task [3]. We propose a novel method to reconstruct under-sampled radial data with the help of deep convolutional neural network (U-Net [1]).
Subjects and Methods: Radial under-sampling generates data points that do not fall on a grid. The acquired radial data points are first gridded using NUFFT [3]. IFFT of this gridded *k*-space produces an image with streaking artifacts which is given as an input to a trained U-Net to reconstruct the artifact free image.

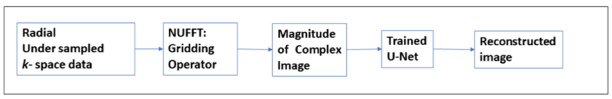

Figure 1. Block diagram of the proposed method

U-Net is trained by using a training set of 1400 T2-weighted magnitude images [4] (gridded under-sampled images of radial trajectory as part of this research) obtained from 30 patients. The ground truth for training were fully sampled MR images. For training purpose, all the weights of the convolutional layers were initialized by a zero-centered normal distribution with standard deviation 0.05 without a bias term [2]. The loss function was minimized by using the RMSPropOptimizer with learning rate of 0.001, mini-batch size 5, and 300 epochs. Training was implemented on Python 3.7.1 by Keras using TensorFlow as backend on Intel(R) core (TM) i7-4790 CPU, clock frequency 3.6 GHz, 16 GB RAM and GPU NVIDIA GeForce GTX 780. The network required approximately 12 h for training in our experiments. The proposed method was tested on 430 radially under-sampled MR images (Acceleration Factor (AF) = 10) of human brain.

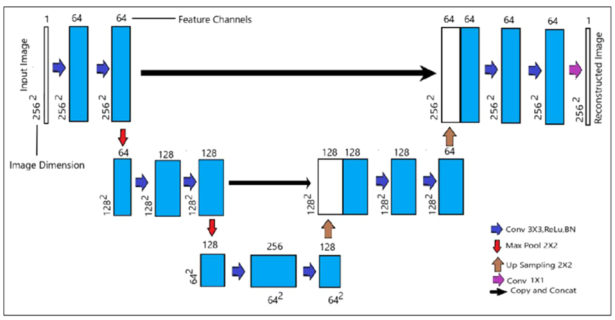

Figure 2. Block diagram of the U-Net Architecture used in our proposed method

Results: Figure 1 shows the block diagram of the proposed method. Figure 2 shows the block diagram of U-Net that we used in our experiments. Figure 3 shows the reconstruction results of our experiments. Figure 4 compares the central line profiles of the ground truth and reconstructed images. For a proof-of-concept, AF = 10 was used for both the training and testing purposes. However, the proposed method works well at other AFs as well.

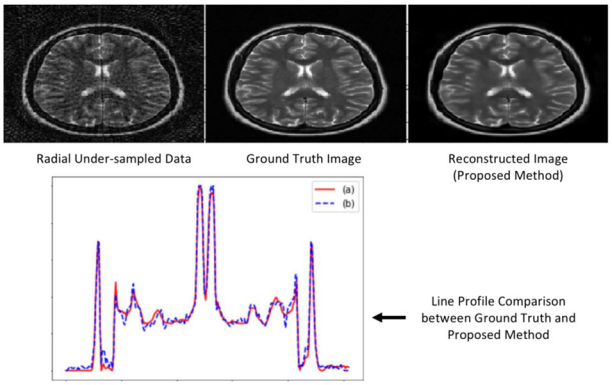

Figure 3. Reconstruction results of the proposed methods and the line profile comparison between ground truth and reconstruction images

Discussion/Conclusion: The results show that the proposed method provides accurate reconstruction results and may be a great step towards a quick reconstruction of MR images from the radial data.
References:
[1] Ronneberger et al. (2015) U-Net: biomedical image segmentation (arXiv:1505.04597)
[2] Hyun et al. (2017) Deep learning for under-sampled MRI reconstruction (arXiv:1709.02576)
[3] Fessler et al. (2003) NUFFT Using Min–Max Interpolation. *IEEE Trans. On Signal Processing, VOL. 51, NO. 2*
[4] Loizou et al. (2011) Multi-scale AM-FM texture analysis of MS in brain MRI *IEEE Trans. Inform. Tech. Biomed.*

L07.20
WITHDRAWN

L07.21
Magnetic resonance angiography image restoration by super resolution based on deep learning

S. Kitazaki[1], M. Kawakita[2], Y. Jitsumatsu[1], S. Kuhara[3], A. Hiwatashi[4], J. Takeuchi[1]
[1]Kyushu University, Graduate School of Information Science and Electrical Engineering, Fukuoka City, Japan, [2]Nagoya University, Graduate School of Informatics, Nagoya City, Japan, [3]Kyorin University, Department of Medical Radiological Technology, Tokyo, Japan, [4]Kyushu University, Faculty of Medical Science, Fukuoka City, Japan

Purpose/Introduction: The examination of MRI takes from 30 min to 40 min. Reduction of examination time is an important issue of MRI. Examination time can be reduced by under-sampling with Compressed Sensing (CS), but. CS has a problem that computing time is too long. Our approach is to apply a deep learning-based image super-resolution method [1] (we refer this method as SRCNN) to restore MR images in a short time. However, we face a problem in applying the SRCNN to MR image due to the difference of the degradation ways in super resolution and MRI; various frequency signals are lost in under sampling in MRI. We propose a new convolutional neural network (CNN) named Multi-Resolution CNN (MRCNN) for MRI. The final goal of this study's restoration accuracy is the level that radiation doctor can recognize aortic aneurysms.
Subjects and Methods: MRCNN consists of several SRCNNs. SRCNN performs super resolution process for each small regions called patches. First layer convolution performs patch decomposition and this filter size corresponds to the patch size. The degradation way

in under sampling of MRI is done in K space. It is necessary to restore not only high frequency components but low frequency components in the under-sampling method generally used. However, since SRCNN performs patch decomposition in the first layer, it can only capture high frequency components and can not restore low frequency components. Increasing the filter size to restore low frequency components make learning difficult because the number of parameters to be learned increases. Therefore, we reduce the size of the input image to relatively increase the filter size. In the proposed MRCNN, three SRCNNs are employed for restoring each frequency component and restoration is performed by integrating outputs. (Fig. 1) The square error in K space was used as the error function. As a related work based on deep-learning, ADMM net [2] is famous. We are currently doing comparison with it.

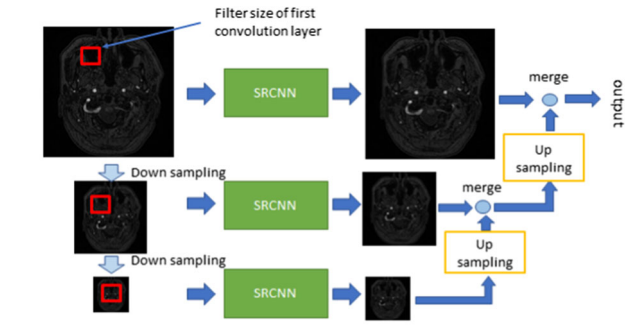

Figure.1 Structure of MRCNN.

Results: We evaluated PSNR of the reconstructed images by the three methods (Table1). We can see that MRCNN performs significantly better than Zero-filling and SRCNN. Figure 2 shows the reconstructed MRA images and the original (full sampled) images. From this, we observe that quality of the images reconstructed by MRCNN is significantly higher than those of the SRCNN and the zero-filling images. Computing time for one patient is only 2.27 s by GPU(GeForce GTX 1080 Ti). MIP(top) PSNR is 33.176(dB) despite only 10% of acquisition rate.

	Source images of MRA	MIP(top)	MIP(side)	MIP(front)
Zero-filling	35.925	29.488	25.248	25.692
SRCNN	35.950	31.069	27.683	27.796
MRCNN	37.130	33.176	29.973	30.268

Table.1 Table of PSNR(dB). Values in the table are average of data for ten people. Zero-filling is the degraded image. Three MIP images are projected from head of top, side, front.

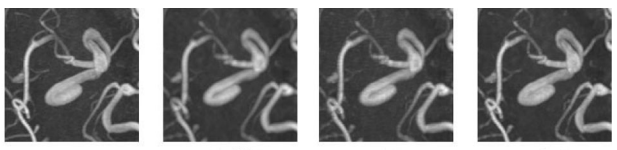

Figure.2 The reconstructed MRA images.

Discussion/Conclusion: By empirical evaluation, we confirm that MRCNN can reconstruct MRA images of nice quality, even if the acquisition rate is only 10%.

References:

[1] C. Dong, C. C. Loy, K. He and X. Tang, "Learning a Deep Convolutional Network for Image Super-Resolution," ECCV, 2014.
[2] Y. Yang, J. Sun, H. Li, Z. Xu,"Deep ADMM-Net for Compressive Sensing MRI" NIPS, 2016

L07.22
Optimized HDL architecture of SENSE reconstruction algorithm

D. Shahid, **S. Ayyaz**, M. F. Siddiqui, H. Omer
COMSATS University Islamabad, Electrical and Computer Engineering, Islamabad, Pakistan

Purpose/Introduction: SENSitivity Encoding (SENSE) is a widely used parallel MRI algorithm that reconstructs MR image from the under-sampled multi-coil data [1]. SENSE is a computationally intensive algorithm which includes the computation of inverse of the encoding matrix. To overcome the limitations of the computationally expensive algorithm, hardware solutions have emerged as an attractive alternate to the software solutions. This research presents an optimized HDL architecture of SENSE algorithm [2] which will be based on Left Inverse Method (for matrix inversion) [3]. The goal of the proposed design is to achieve the optimal performance on FPGA in terms of throughput and area.

Subjects and Methods: An HDL architectural design of SENSE is proposed for 8 channel receiver coils with an acceleration factor (AF) of 2. The proposed design is shown in Fig. 1. Optimized complex matrix multiplier, matrix inverse and matrix transpose modules are designed in this research. To optimize the area utilization of the complex matrix multiplication modules, a sequential approach is used where a single value of the output matrix is computed in each cycle. To improve the throughput of HDL design, each matrix multiplier is pipelined using three stages where each module is separated by sequential logic registers. The encoding matrix and under-sampled data is stored in the Block RAM of the FPGA. Experiments are performed on the datasets acquired from MRI scanner.

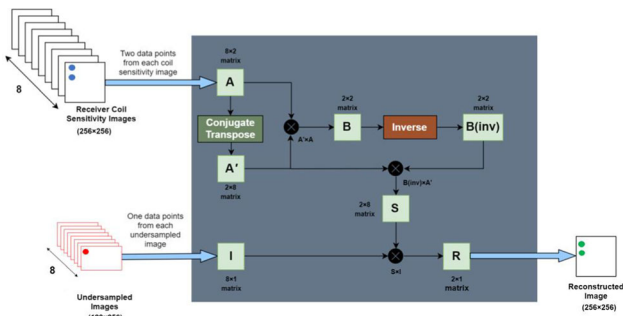

Block diagram of the proposed SENSE architecture

Results: Figure 1a illustrates the reconstructed image using the proposed design and MATLAB reconstructions. Figure 2a, b show that there are no significant differences between both the reconstructed images.

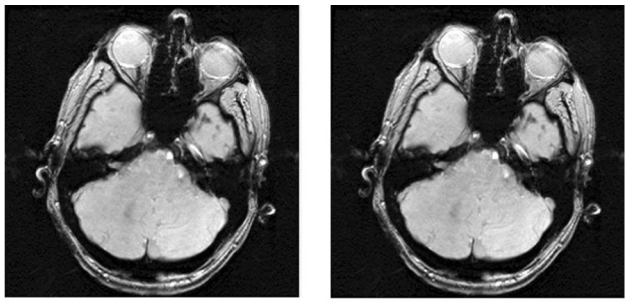

(a) Conventional SENSE reconstruction (Matlab) (b) Reconstructed image from the proposed design

The reconstruction time of the proposed architecture is much less (82.45 ms) than the coventional (2600 ms) SENSE on MATLAB. Device utilization summary for the proposed architecture is shown in Table 1. The results show that the proposed design uses a smaller number of total device resources on FPGA (Virtex-6). Therefore, multiple modules can be used to compute the output pixels in parallel on the same FPGA to improve the reconstruction time.

Logic Utilization	Used	Available	Utilization
Slice Registers	6708	301440	2%
Slice LUTs	6802	150720	4%
DSP48E1s	322	768	41%

Device Utilization Summary of the proposed HDL architecture of SENSE algorithm on FPGA (Xilinx Virtex-6)

Device Utilization Summary of the proposed HDL architecture of SENSE algorithm on FPGA (Xilinx Virtex-6).

Discussion/Conclusion: Efficient and optimized HDL architecture of SENSE reconstruction algorithm is presented in terms of throughput and resource management. The architecture provides good results for image reconstruction from under-sampled data with significantly less computation time. The proposed architecture can be easily used in portable MRI scanners for real time SENSE reconstruction.

References:

[1] Pruessmann, K.P., et al., MRM, 1999.
[2] Siddiqui MF et al., Springer, 2015.
[3] MIT OpenCourseWare, ''Left and right inverses; pseudoinverse'', Accessed March 2015

L07.23

Adaptive noise reduction in parallel magnetic resonance imaging using SVD based filtering in wavelet domain

O. Inam, **H. Jarral**, H. Omer, M. Qureshi
COMSATS University Islamabad, Electrical & Computer Engineering, Islamabad, Pakistan

Purpose/Introduction: The quality of the image reconstructed using SENSE (a parallel MRI method) may get affected by spatially varying noise originated as part of the reconstruction process. In this paper, adaptive SVD based filtering is applied in the wavelet domain to suppress the noise while preserving the fine details and sharp edges in the SENSE reconstructed MR images. The proposed method uses adaptive SVD based filtering as a shrinkage process which typically involves threshholding the small wavelet coefficients in order to reduce noise without affecting the important features in the reconstructed MR image.

Subjects and Methods: In the proposed method, discrete wavelet transform is applied on the noisy SENSE reconstructed image to obtain Z level wavelet decomposition with multiple frequency sub-bands, where each sub-band is divided into local patches [1]. In order to perform SVD based filtering, a group of non-local similar patches are chosen for each local patch and the appropriate weights are estimated using singular values of each patch group. The values of the estimated weights are used as a threshold for SVD based filtering of the patch group under consideration. The same process is repeated for each sub-band before applying inverse discrete wavelet transform on the filtered output to obtain the de-noised image (Fig. 1).

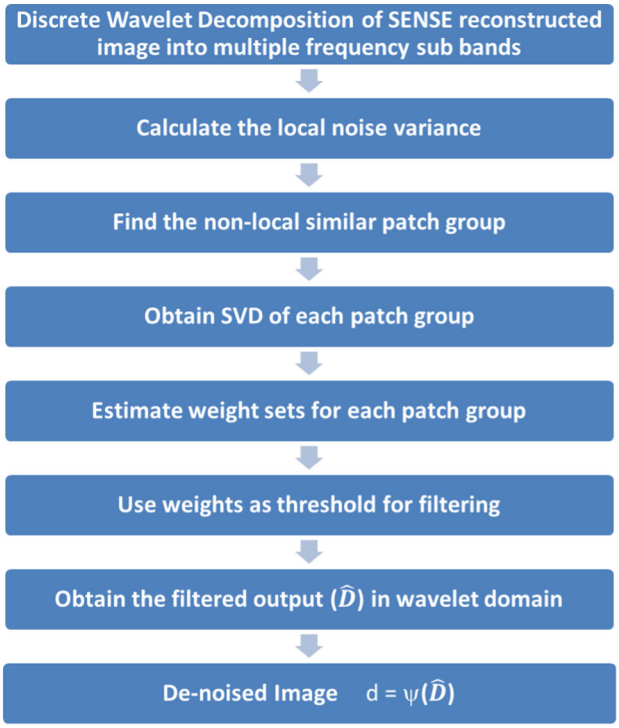

Figure1. Proposed adaptive noise reduction method using SVD based filtering in wavelet domain

To evaluate the de-noising capabilities of the proposed method, the Gaussian noise having standard deviation σ ranging between ($5 \leq \sigma \leq 30$), is added to the fully sampled 12-channel data set of human head data acquired using 3T scanner (Table 1).

Scanner	3.0T Siemens
No of receiver coils	12
Matrix Size	448 x 224
FOV	230mm^2
TR	938ms
TE	2ms
Slice thickness	5mm
Flip angle	58 degree

Table 1. Data Aquisition Details

The noisy human head data set is retrospectively under-sampled at various acceleration factors, i.e., ($2 \leq R \leq 4$) and the resultant aliased image is fed to the SENSE reconstruction algorithm. The SENSE algorithm unfolds the aliased images for each receiver coil; these images are then (pixel-wise) linearly combined to form one

composite image. Thus the final magnitude image has noise properties that can be described by Rayleigh distribution. The composite image is denoised using the proposed algorithm and other contemporary image de-noising techniques i.e. Bayes [2] and LLSURE [3].

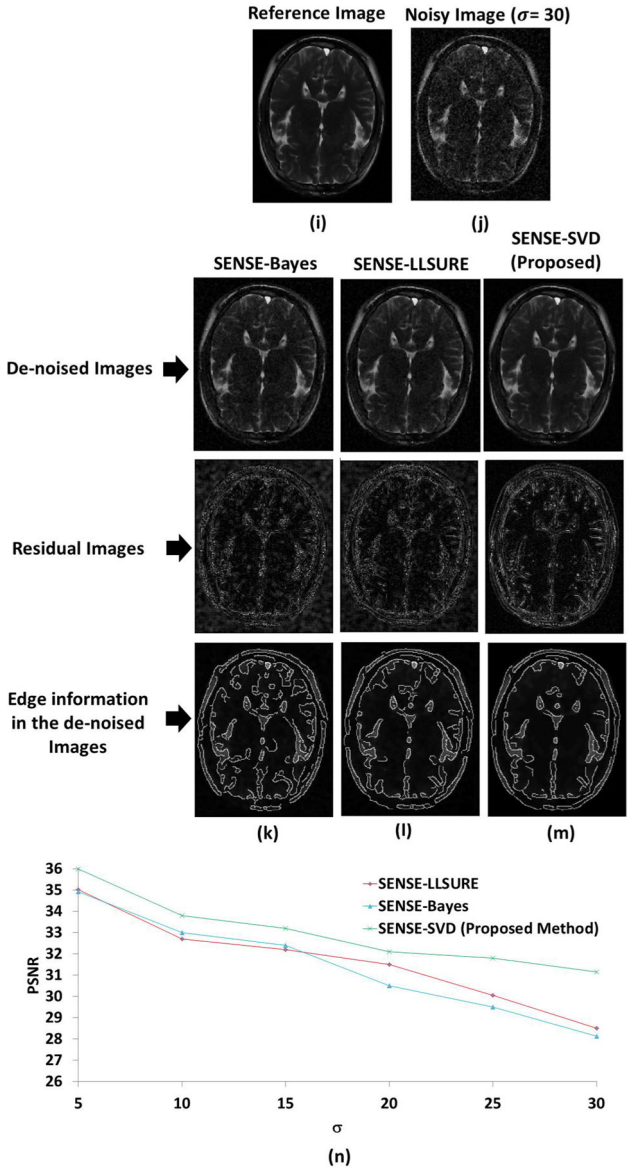

Figure 2: Reconstruction results using SENSE-SVD (Proposed method), SENSE-Bayes and SENSE-LLSURE

Results: The results (Fig. 2) show that the that the proposed method effectively reduces noise and also preserves the important features of SENSE reconstructed image i.e. edges and contours, thereby producing the de-noised image closer to the reference image as compared to the contemporary techniques.

Discussion/Conclusion: The proposed SVD based adaptive de-noising method effectively reduces noise in the SENSE reconstructed MR image recovering more information than the contemporary methods.

References:

[1] P. Jain et al., *Multimedia Tools and Applications,* vol. 76, pp. 1659–1679, 2017.

[2] H. Choi and R. G. Baraniuk, *IEEE Signal Processing Letters,* vol. 11, pp. 717–720, 2004..

[3] T. Qiu etal., *IEEE Transactions on Image Processing,* vol. 22, pp. 80–90, 2013

L07.24

Deep Learning Based MR Image Quality Assessment and Artifact Localization for Application in Clinical Practice

M. Schwartz[1, 2], Y. Wilhelm[2], Y. Liu[2], P. Martirosian[1], B. Yang[2], F. Schick[1], S. Gatidis[3], T. Küstner[1]

[1]*University Hospital of Tübingen, Section on Experimental Radiology, Tübingen, Germany,* [2]*University of Stuttgart, Institute of Signal Processing and System Theory, Stuttgart, Germany,* [3]*University Hospital Tübingen, Diagnostic and Interventional Radiology, Tübingen, Germany*

Purpose/Introduction: Magnetic resonance imaging is prone to several kinds of artifacts. However, artifact-free MR images are important for reliable diagnosis, especially in small anomalous structures. Automatic image quality assessment and assurance[1–3] during ongoing MR examination can provide an online feedback about the expected image quality. This reduces the effort of manual data inspection, avoids overlooking corrupted images and enables objectivity. The aim of the present work is an integration of a deep-learning based artifact detection and localization approach into the clinical environment in order to provide real-time feedback regarding image quality. An artifact detection pipeline based on the open-source framework Gadgetron[4, 5] in conjunction with a convolutional neural network has been developed.

Subjects and Methods: Data Acquisition: T1-weighted Fast-Spin Echo images from 18 healthy volunteers (age: 27 ± 5, 4 female) were acquired on a 3T MR with and without voluntary rigid and involuntary non-rigid (respiration, heart) motion, forming a training database. Imaging parameters are given in Fig. 1A.

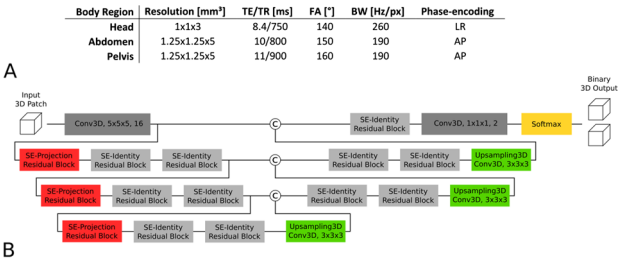

Figure 1: A: MR imaging parameters for the specific body regions used in network training. B: CNNArt: 3D patch-based network architecture for artifact detection and localization. An artifact probability map is generated as output.

Artifact Detection: Voxel-wise artifact probability prediction is based on a neural network (CNNArt)[1–3], as shown in Fig. 1B. It is composed of volumetric encoder-decoder architecture with skip-connections for dense prediction[6, 7], Squeeze-and-Excitation projection and identity residual blocks[8, 9] for channel-wise feature response calibration. The network is trained offline on pre-acquired training database. **Image Quality Feedback:** Online scanner feedback was implemented in the open-source Gadgetron AI framework by a self-defined Python Gadget as shown in Fig. 2.

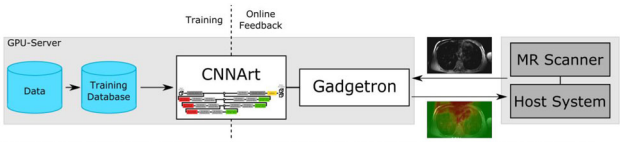

Figure 2: Online integration of the artifact detection network CNNArt into the clinical workflow. Raw data is sent to Gadgetron and processed by the pre-trained network. Probability maps are sent back to the host system as quality feedback for user.

The imaging data is sent to a GPU-server for binary artifact probability prediction by a pre-trained network, requiring a few seconds only. Probability maps together with reconstructed images are sent back to the MR system for visual inspection by the user. For ease of quality assessment, slice-wise artifact scores are determined enabling slice-wise reacquisition of motion-corrupted data. Codes are publicly available under: https://github.com/thomaskuestner/CNNArt.

Results: Exemplary transverse slices were recorded in a water phantom and in the head of two subjects (Fig. 3). Motion artifacts (LR phase-encoding) in the water phantom and in subjects as well as wrap-around artifacts were detected. Derived probability maps highlight corrupted image regions and provide feedback to the user.

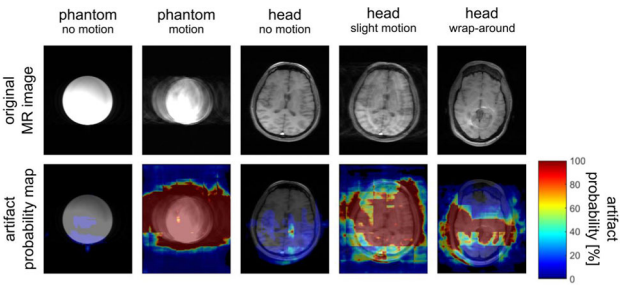

Figure 3: Exemplary MR images with artifact probability maps (probability in %). Distinct differences are visible between motion-free and motion-corrupted images. Moreover, a wrap-around artifact is visible on the MR image farthest to the right.

Discussion/Conclusion: An integration of a real-time image quality feedback into the clinical examination workflow is presented. The proposed setup can easily be extended for more generic quality feedback and to other applications such as motion correction by deep learning methods[10].

References:

1: Küstner, MAGMA, 2018.
2: Küstner, MRI, 2018.
3: Küstner, ICASSP, 2018.
4: Hansen, MRM, 2013.
5: Xue, MRM, 2015.
6: Ronneberger, MICCAI, 2015.
7: Milletari, ArXiv, 2016.
8: He, CVPR, 2016.
9: Hu, ArXiv, 2017.
10: Küstner, MRM, 2019.

L07.25

Non-local means noise filtering (NLMF) improves Hyperpolarized ^{13}C-pyruvate imaging PSNR compared to linear minimum mean square error (LLMSE)

E. S. S. Hansen, C. Laustsen
Aarhus University, MR Research Centre, Århus N, Denmark

Purpose/Introduction: Hyperpolarized ^{13}C-pyruvate imaging is a fast developing metabolic imaging modality with the property to measure metabolic conversion rates from the main tracer ^{13}C-pyruvate to downstream metabolites (^{13}C-lactate, ^{13}C-alanine, ^{13}C-bicarbonate) [1]. Although hyperpolarized MR increases the signal-to-noise-ratio significantly (SNR), the SNR is still low for most metabolic derivatives and thus denoising is essential for improving quality and reliability of the low SNR regime images [2].

The aim of this study was to improve dynamical and anatomical features by two well-known MRI noise filter methods on hyperpolarized ^{13}C-pyruvate. This project was limited to investigate the performance between filtering Rician content by estimating linear minimum mean square error (LLMSE) and Non-Local Means noise filtering (NLMF) [3, 4]. Filter performance was measured by global peak-SNR(PSNR).

Subjects and Methods: Pigs weighing 30 kg in the kidney data(N = 4) and 40 kg in the cardiac data(N = 4). The MR experiments were performed on a clinical 3T scanner.[1-^{13}C]pyruvate and its metabolic conversion was imaged used dedicated coils. LLMSE and NLMF algorithms were implemented in MATLAB.

Results: Cardiac

PSNR measurements for LLMSE and NLMF on the summed metabolic images gave the following differences: ^{13}C-lactate(PSNR mean of difference = − 8.1, SEM = 2.5, p = 0.047*), ^{13}C-alanine(PSNR mean of difference = − 5.3, SEM = 2.6, p = 0.028*), ^{13}C-bicarbonate(PSNR mean of difference = − 6.2, SEM = 1.9, p = 0.047*).

Kidney

PSNR measurements for LLMSE and NLMF on the summed metabolic images gave the following differences: ^{13}C-lactate(PSNR mean of difference = − 4.7, SEM = 0.2428, p = 0.0003*), ^{13}C-alanine(PSNR mean of difference = − 6.3, SEM = 1.6, p = 0.03*), ^{13}C-bicarbonate(PSNR mean of difference = − 7.6, SEM = 0.61, p = 0.001*).

Results from PSNR measurements on summed metabolic images are shown in Fig. 1.

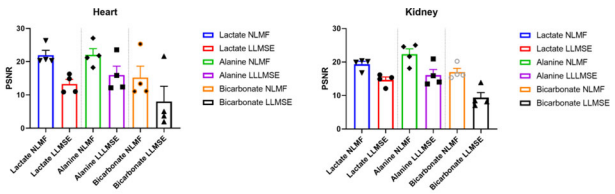

Figure 1 – heart and Kidney PSNR measures plotted with mean and SEM.

Figures 2 and 3 are examples of the summed metabolic images from the heart and kidney, respectively. For both organs, it is clearly to see how background noise is suppressed and anatomical details are preserved.

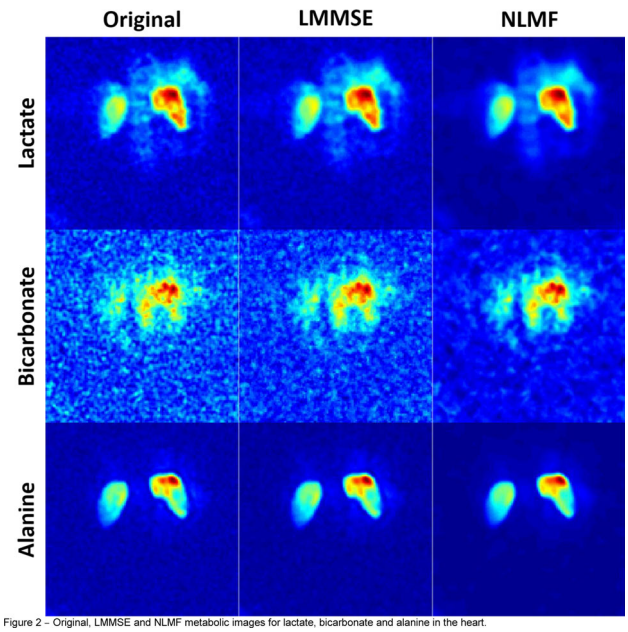

Figure 2 – Original, LMMSE and NLMF metabolic images for lactate, bicarbonate and alanine in the heart.

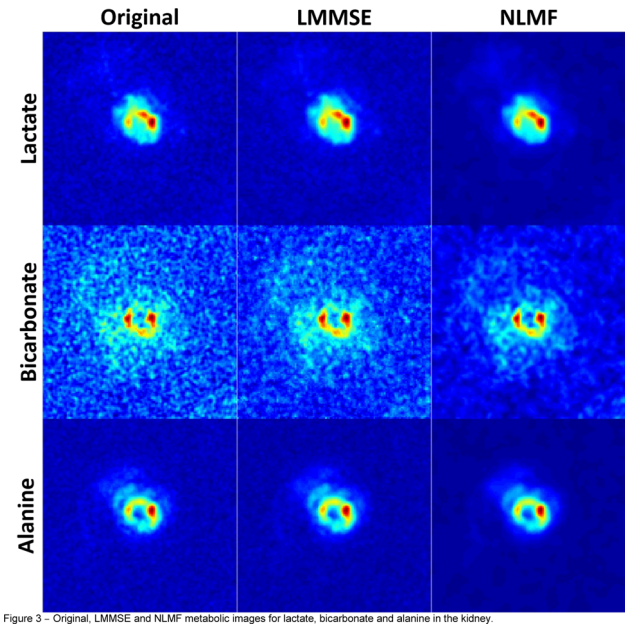

Figure 3 – Original, LMMSE and NLMF metabolic images for lactate, bicarbonate and alanine in the kidney.

Discussion/Conclusion: In this study, we found that NLMF significantly improves global PSNR for hyperpolarized ^{13}C-pyruvate metabolic images. Background noise is visually suppressed by the NLMF and anatomical details preserved.

Parameters for LLMSE and NLMF such as kernel size, background noise estimation, regulation parameters are all chosen from value found in the literature. Future investigation in an optimal, adaptive or learning parameter algorithm is aimed following this preliminary work. The NLMF method may provide further strength to the quantification of hyperpolarized ^{13}C-imaging with for example Michealis-Menten kinetics or perfusion measurement [5, 6].

References:

1. Wang, Z.J,…, 2019
2. Zhang, X.,…, 2014
3. Aja-Fernandez, S.,…., 2008
4. Buades, A.,…, 2005
5. Zierhut, M.L.,…, 2010
6. Schulte, R.F.,…, 2013

L07.26

An application of the automated brain segmentation for the evaluation of localization reliability of in vivo magnetic resonance spectroscopy: a preliminary study

C.-H. Yoo[1], H.-M. Baek[2], B.-Y. Choe[1]
[1]*The Catholic University of Korea, Seoul, South Korea,* [2]*Gachon University, Department of Health Sciences and Technology, Incheon, South Korea*

Purpose/Introduction: Recently, the heterogeneity in brain tissues can be identified by the signals of MRI, and the registration of the morphologic image to the brain atlas would potentialize the segmentation of brain tissues. In addition to the morphologic insights, metabolic insights of brain have been widely investigated with in vivo ^{1}H MRS, which can quantify over 20 major neurometabolites in the selected brain region. The aim of this preliminary study was to apply the brain segmentation involved with registration to the brain atlas, to analyze volumetric contribution of brain tissues within the localized voxel of MRS, and to evaluate the reliability of the localization of MRS.

Subjects and Methods: All the MRI/MRS scans of C57BL/6 N mouse were performed using a Bruker BioSpec® 94/20 USR MRI system. To evaluate tissue composition in the MRS voxel, high-resolution 3D T2-weighted image was acquired using TurboRARE sequence with the following parameters: TR/TE, 2000/8.5 ms; effective TE, 42.5 ms; RARE factor, 16; average, 1; FOV, 12 × 12 × 16 mm^3; matrix size, 150 × 150 × 200; spatial resolution, isotropic 80 μm. The MRS voxels were located in the prefrontal, striatal, and hippocampal region. *In vivo* ^{1}H MRS spectra were obtained using PRESS sequence. Atlas normalization toolbox using ELASTIX (ANTX) toolbox and MATLAB software was used, and high-resolution 3D T2-weigted image was used. Automated registration to the Allen mouse brain atlas, and ELASTIX-based segmentation was performed to obtain the tissue compartment masks for the prefrontal, striatal, and hippocampal region. The MRS voxels were manually drawn in the image and the volumetric contribution of each tissue compartment was evaluated, respectively.

Results:

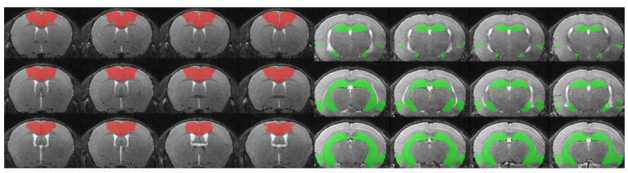
Figure 1. High-resolution 3D T2-weighted image of the mouse brain reconstructed in the axial slices mainly containing the prefrontal region. The region of interest, reconstructed for the prefrontal region, was highlighted with the red mask. The MRI scan was performed with the TurboRARE sequence with the following parameters: TR, 2,000 ms; TE, 8.5 ms; effective TE, 42.5 ms; RARE factor, 16; average, 1; FOV, 12 × 12 × 16 mm3; matrix size, 150 × 150 × 200; with six saturation slices (two slices for axial/coronal/sagittal plane).

Figure 2. High-resolution 3D T2-weighted image of the mouse brain reconstructed in the axial slices mainly containing the hippocampal region. The region of interest, reconstructed for the hippocampal region, was highlighted with the green mask. The MRI scan was performed with the TurboRARE sequence with the following parameters: TR, 2,000 ms; TE, 8.5 ms; effective TE, 42.5 ms; RARE factor, 16; average, 1; FOV, 12 × 12 × 16 mm3; matrix size, 150 × 150 × 200; with six saturation slices (two slices for axial/coronal/sagittal plane).

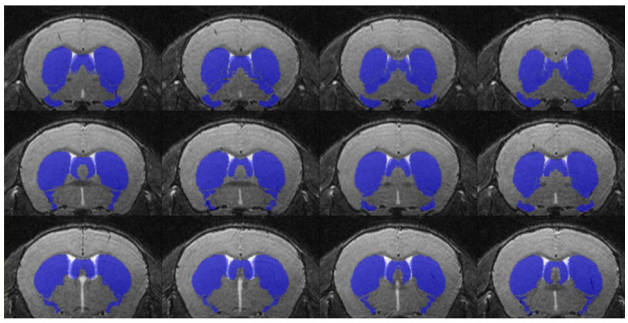

Figure 3. High-resolution 3D T2-weighted image of the mouse brain reconstructed in the axial slices mainly containing the striatal region. The region of interest, reconstructed for the striatal region, was highlighted with the blue mask. The MRI scan was performed with the TurboRARE sequence with the following parameters: TR, 2,000 ms; TE, 8.5 ms; effective TE, 42.5 ms; RARE factor, 16; average, 1; FOV, 12 × 12 × 16 mm3; matrix size, 150 × 150 × 200; with six saturation slices (two slices for axial/coronal/sagittal plane).

Figures 1, 2 and 3 illustrates high-resolution 3D T2-weighted MRI of the mouse brain, reconstructed in the axial slices mainly containing the prefrontal, striatal, and hippocampal region, respectively. The tissue compartment masks were reconstructed for each region and overlaid in each image for the visual inspection.

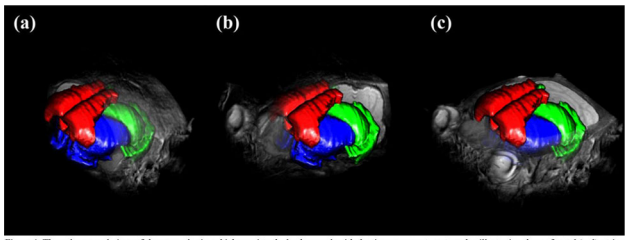

Figure 4. The volume renderings of the mouse brain, which consists the background, with the tissue compartment masks, illustrating the prefrontal (red), striatal (blue), and hippocampal (green) region. The background was reconstructed in the (a) axial, (b) sagittal, and (c) coronal projection with the masks.

Figure 4 illustrates the volume rendering of the mouse brain (background) and tissue compartment masks of the prefrontal (red), striatal (blue), and hippocampal region (green), reconstructed from high-resolution 3D T2-weighted MRI.

Discussion/Conclusion: The automated brain segmentation was applied to high-resolution 3D MRI and high-field short-TE MRS. The image quality of MRI was comparably good, and the tissue compartment masks and volume renderings of the prefrontal, striatal, and hippocampal region were well overlaid with the brain. Our results showed that the volumetric analysis for the tissue composition within the MRS voxel can be performed by the brain segmentation, and also the localization reliability can be evaluated.

References:

Koch S, et al. Atlas registration for edema-corrected MRI lesion volume in mouse stroke models. J Cereb Blood Flow Metab. 2017 Jan 1:271678X17726635.

I26 Teaching Session

15:40–16:40 *Room 1 - Willem Burger Zaal*

Machine Learning for Reconstruction

I26.01
Reconstruction with Machine Learning: Comparison to Existing Methods and Challenges

M. Uecker
University Medical Center Göttingen, Diagnostic and Interventional Radiology, Göttingen, Germany

Learning Objectives:—Differences between image reconstruction methods based on machine learning and other methods
- Advantages and disadvantages of various types of image reconstruction methods.
- Challenges when applying machine learning to image reconstruction.

Body: In recent years, machine learning methods attracted a lot attention in the scientific community because they started to outperform conventional methods for certain applications, e.g. certain image classification tasks. But machine learning techniques are very generic, and new techniques to perform image reconstruction in MRI using deep learning are currently being developed by the MRI community. In this talk, we will compare such methods to conventional reconstruction methods, discuss conceptual differences, potential advantages and disadvantages, and remaining challenges.

References:

- Hammernik K, Klatzer T, Kobler E, Recht MP, Sodickson DK, Pock T, Knoll F. Learning a variational network for reconstruction of accelerated MRI data. Magnetic Resonance in Medicine 79:3055–3071 (2018).
- Qin C, Schlemper J, Caballero J, Price AN, Hajnal JV, Rueckert D. Convolutional Recurrent Neural Networks for Dynamic MR Image Reconstruction. IEEE Transactions on Medical Imaging 38:280–290 (2019)
- Zhu B, Liu ZJ, Rosen BR, Rosen MS. Image reconstruction by domain transform manifold learning. Nature 555:487–492 (2018)

I26.02
Neural Networks for Undersampled MR Reconstruction

J. Schlemper
Imperial College London, Department of Computing, London, UK

Learning Objectives: 1. Understand the basic framework of deep learning for undersampled MR reconstruction.
2. Understand the intuition behind state-of-the-art methods.
3. Understand the current challenges of these approaches and identify what are the ongoing works.

Body: The first part of the talk will cover the basics[1, 2]:
- What motivates us to use deep learning for undersampled MR reconstruction?
- How is undersampled MR reconstruction problem formulated in deep learning framework?
- How are deep learning models evaluated?

The second part of the talk will cover the intuition behind state-of-the-art approaches.
- unrolled methods[3–8].
- generative adversarial networks[9, 10].
- k-space approaches[11–13].

The last part of the talk will discuss the unsolved questions and motivate some approaches[14, 15].
- How do I know when my method fails?
- How many subjects do I need to train my data? What if I cannot/do not want to get more subjects?
- How far away are we from using them in clinical environments?

References:

[1] Wang, Shanshan, et al. "Accelerating magnetic resonance imaging via deep learning." IEEE ISBI, 2016.
[2] Zhu, Bo, et al. "Image reconstruction by domain-transform manifold learning." *Nature,* 2018.
[3] Schlemper, Jo, et al. "A deep cascade of convolutional neural networks for dynamic MR image reconstruction." IEEE TMI, 2017.
[4] Hammernik, Kerstin, et al. "Learning a variational network for reconstruction of accelerated MRI data." MRM, 2018.
[5] Sun, Jian, et al. "Deep ADMM-Net for compressive sensing MRI." NeurIPS, 2016.
[6] Aggarwal, Hemant K., et al. "Modl: Model-based deep learning architecture for inverse problems." IEEE TMI, 2018.
[7] Qin, Chen, et al. "Convolutional recurrent neural networks for dynamic MR image reconstruction." IEEE TMI, 2018.
[8] Mardani, Morteza, et al. "Deep generative adversarial neural networks for compressive sensing MRI." IEEE TMI, 2018.
[9] Yang, Guang, et al. "DAGAN: deep de-aliasing generative adversarial networks for fast compressed sensing MRI reconstruction." IEEE TMI, 2017.
[10] Quan, Tran Minh, et al. "Compressed sensing MRI reconstruction using a generative adversarial network with a cyclic loss." IEEE TMI, 2018.
[11] Han, Yoseob, et al. "k-space deep learning for accelerated MRI." arXiv 2018.
[12] Eo, Taejoon, et al. "KIKI-net: cross-domain convolutional neural networks for reconstructing undersampled magnetic resonance images." MRM, 2018.
[13] Souza, Roberto, et al. "A Hybrid, Dual Domain, Cascade of Convolutional Neural Networks for Magnetic Resonance Image Reconstruction." MIDL, 2019.
[14] Schlemper, Jo, et al. "Bayesian Deep Learning for Accelerated MR Image Reconstruction." MLMIR, 2018.
[15] Akçakaya, Mehmet, et al. "Scan-specific Robust Artificial-neural-networks for k-space Interpolation-based (RAKI) Reconstruction: Database-free Deep Learning for Fast Imaging." ISMRM Meeting, 2018.

S22 Scientific Session

15:40–17:10 *Room 2 - Van Weelde Zaal.*

Improving Functional MRI

S22.02

Spiral fMRI using the gradient impulse response function for trajectory prediction

N. N. Graedel[1], L. Kasper[2], M. Engel[2], J. Nussbaum[2], B. J. Wilm[2], K. P. Pruessmann[2], S. J. Vannesjo[1]
[1]*University of Oxford, Wellcome Centre for Integrative Neuroimaging, FMRIB, Oxford, UK,* [2]*ETH Zurich and University of Zurich, Institute for Biomedical Engineering, Zurich, Switzerland*

Purpose/Introduction: Spiral trajectories are well suited for functional MRI[1], however their use has been limited by artifacts caused by gradient imperfections and B_0 inhomogeneity. Obtaining high quality spiral images requires accurate knowledge of the traversed k-space trajectory. With the goal of making spiral fMRI more accessible we have evaluated image reconstruction using trajectories predicted by the gradient impulse response function (GIRF), which can be determined in a one-time calibration step[2/3].

Subjects and Methods: The GIRF was measured[2] on a 7T Philips Achieva using a dynamic field camera[5]. 2D single-shot spiral data (res = 0.8 × 0.8 mm^2, R = 4, 36 slices, 0.8/0.2 mm slice thickness/gap, TR ∼ 3.3 s, T_{acq} 5 min) were acquired in 6 healthy volunteers. A multi-echo GRE scan (ΔTE = 1 ms) was used to estimate coil sensitivities/B_0 maps. Concurrent field monitoring was performed in all scans using NMR field probes mounted[5] on the 32ch head Rx coil. The visual fMRI paradigm consisted of 15 s blocks of upper-left/lower-right quarter field stimulation interleaved with upper-right/lower left stimulation, separated by 10 s of rest.

CG-SENSE image recon with multi-frequency interpolation for B_0 correction was performed using (a) delay-corrected nominal k-space trajectories (b) GIRF-predicted trajectories and (c) trajectories measured with concurrent field monitoring. For b/c the data was demodulated by the predicted/measured 0th-order field integrals. GLM-analysis was performed using FEAT/FSL using no spatial smoothing/clustering.

Results: The GIRF-predicted reconstructions show substantially improved image quality compared to the nominal spiral images, which are corrupted by blurring and geometric distortion (Fig 1). The RMSE to the monitored recon for all slices/volumes (averaged over all subjects) was 2.1/5.7 for the GIRF-predicted/nominal reconstruction (RMSE reduction of ∼ 63%).

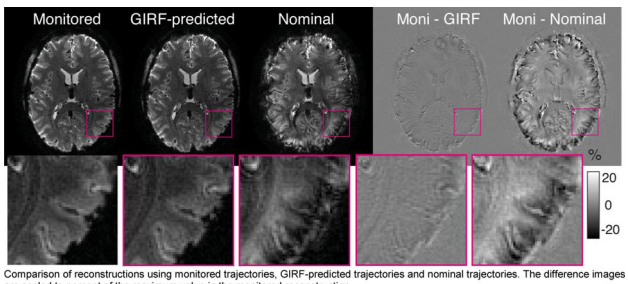

Comparison of reconstructions using monitored trajectories, GIRF-predicted trajectories and nominal trajectories. The difference images are scaled to percent of the maximum value in the monitored reconstruction.

The fMRI results show good correspondence of the activation with the gray matter architecture of visual cortex in the monitored and GIRF-pred. reconstructions, while the nominal data contain more misplaced activation.

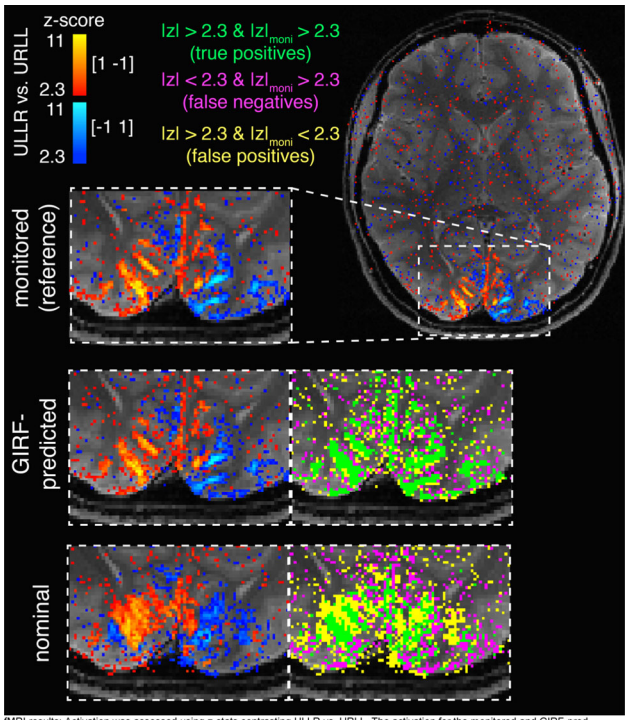

fMRI results: Activation was assessed using z-stats contrasting ULLR vs. URLL. The activation for the monitored and GIRF-pred. reconstructions match the gray matter architecture well, while nominal reconstruction results in misplaced activation.

The spatial specificity of the activation was assessed via ROC plots (Fig 3). The average area under the curve over all subjects was 5830/5669/5331 for monitored/GIRF-pred./nominal reconstructions.

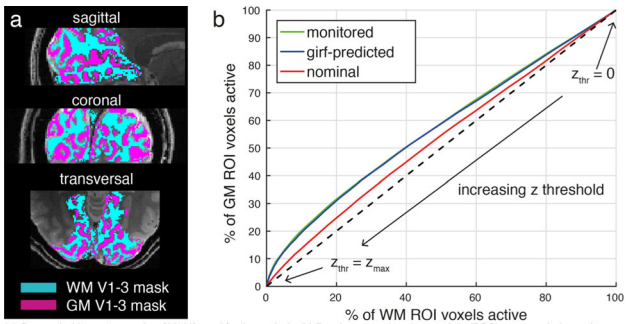

(a) Gray and white matter masks of V1-V3 used for the analysis. (b) Receiver operating characteristic (ROC) curve analysis used to assess the specificity of the different reconstructions. The area under the curves (AUC) was used as a summary metric.

Discussion/Conclusion: The GIRF-reconstruction generates image quality and fMRI results, which are comparable to using a concurrently monitored trajectory. Slight residual artifacts and loss in specificity are expected, as the GIRF-prediction cannot capture nonlinear or time-dependent effects. The GIRF prediction is based on a one-time system calibration, thus does not prolong the fMRI acquisition nor complicate the acquisition setup. The proposed method can enable high-quality spiral fMRI when concurrent field monitoring is not feasible.

References:

1. Glover GH, NeuroImage 2012
2. Vannesjo SJ, MRM 2013
3. Vannesjo SJ, MRM 2016
4. Dietrich BE, MRM 2016
5. Barmet C, MRM 2008

S22.03

The effect of slice saturation in 3D TFEPI SS-SI VASO for 7T fMRI applications

I. A. F. d. Oliveira, W. v. d. Zwaag, S. O. Dumoulin, J. C. W. Siero
Spinoza Centre for Neuroimaging, Amsterdam, The Netherlands

Purpose/Introduction: VASO provides an alternative measure to BOLD fMRI of brain function, that becomes more feasible at Ultra-High Field[1, 2, 3]. VASO is sensitive to changes in cerebral blood volume (CBV), and takes advantage of T1 differences between blood and tissue, by using an inversion recovery pulse to null the blood while maintaining part of the tissue signal. In slice-selective slab-inversion VASO (SS-SI VASO), an increase in tissue signal is realized by manipulating the longitudinal magnetization of the stationary tissue separately from the blood. A 90° RF pulse is applied in the imaging plane before the adiabatic inversion and will act as a magnetization reset module[4]. The magnetization reset module should result in increased sensitivity to task-evoked VASO signal changes. Here, we compare two different VASO schemes; we used a conventional 3D fast gradient-echo EPI readout, which employs a constant flip angle and a version where we replace the last excitation pulse by a 90° RF pulse (Fig. 1).

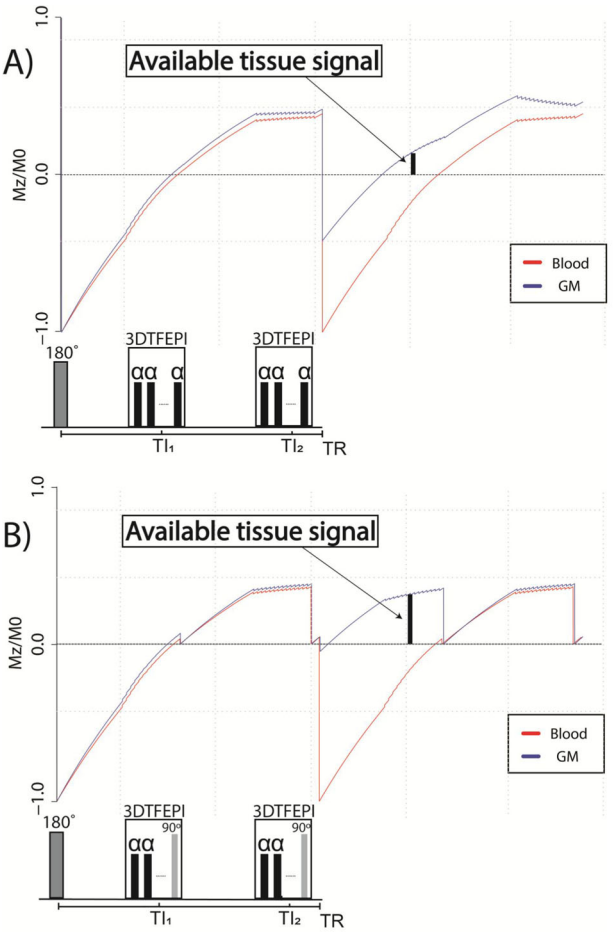

TFEPI VASO Bloch simulations showing the available tissue for both approaches: A) conventional VASO TFEPI B) VASO TFEPI with reset module.

Subjects and Methods: 2 healthy volunteers participated in the study. Imaging was performed on a 7T scanner Philips System using a 32-channel head coil for reception (Nova Medical). SS-SI VASO images were obtained using a 3D single-shot fast gradient-echo EPI (Turbo Field Echo EPI, TFEPI), sequence with the following parameters: TI1/TI2/TE/TR = 1100/2600/17/3000 ms, FA = 15°, FOV = 192 × 192 × 21 mm^3, matrix = 128 × 128 with 14 slices and 1.5 mm isotropic voxels. SENSE = 2.5. The task consisted of move both hands on a visual cue from a rest position, with 30 s on/off. Data processing consisted of motion correction for BOLD and VASO images separately, followed by a bold correction scheme to correct for extravascular BOLD signals[2]. Software used; SPM12, in-house scripts and GLM analysis using FEAT in FSL with z-threshold 3, $p < 0.05$ cluster-wise. tSNR maps were generated and evaluated across 5 different ROIs (Fig. 2).

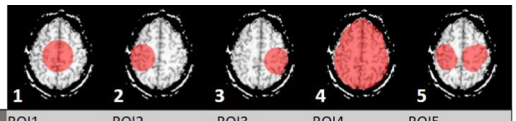

VASO schemes	ROI1	ROI2	ROI3	ROI4	ROI5
Conventional	20.44 ± 0.53	18.33 ± 0.43	20.90 ± 1.38	17.15 ± 1.36	19.86 ± 0.60
Reset module	21.31 ± 0.02	19.13 ± 0.79	21.46 ± 1.44	18.25 ± 0.67	20.72 ± 1.44

Hand-drawn ROIs per subject with tSNR values for VASO in motor cortex for both approaches. Depicted value are the mean tSNR across subjects.

Results: The Bloch simulations (Fig. 1) clearly indicate the benefit of replacing the last excitation pulse by a 90° RF pulse to the TFEPI SS-SI VASO readout scheme. Compared to the standard sequence, this yielded higher tSNR for all ROIs and subjects (Fig. 2). Significant signal changes were detected in both participants in both runs. Fig. 3 shows BOLD and VASO statistical activation maps for the conventional 3DTFEPI VASO with a constant FA = 15° and the proposed single 90° pulse.

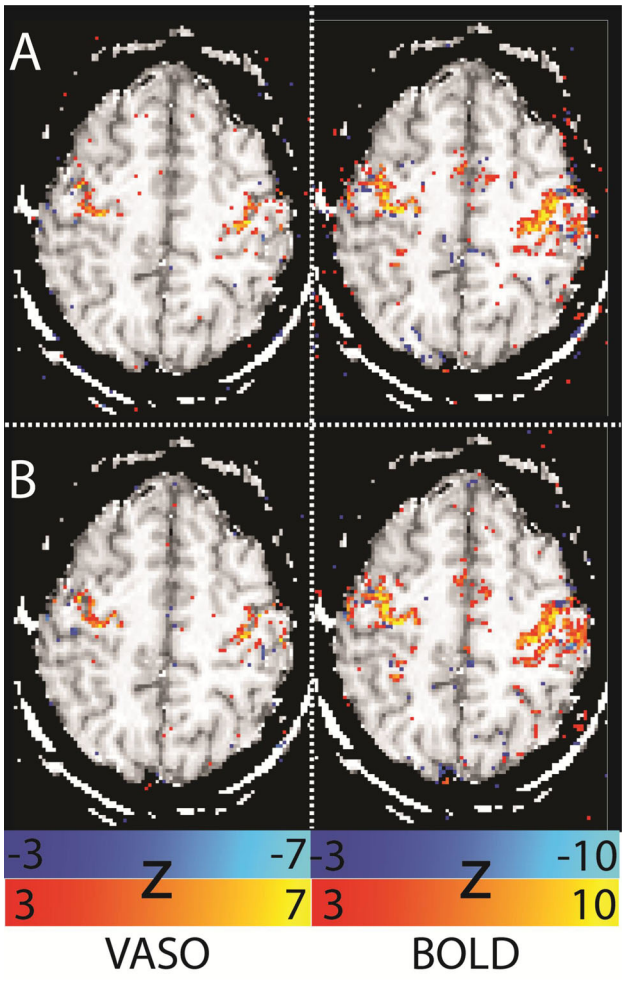

z-score of VASO and BOLD activation map from one subject; A) conventional VASO TFEPI B) VASO TFEPI with reset module.

Note the increased extent of the activation for both VASO and BOLD images for the additional 90° RF pulse approach and indicates the increased sensitivity for tissue signal changes.

Discussion/Conclusion: We compare two different VASO schemes by substituting the last 15° RF pulse with a 90° pulse that will act as magnetization reset module. We demonstrate that this modification yields a substantial increase in the tissue signal, resulting in increases in tSNR and detectability of VASO signal changes.

References:
1. Lu, 2003
2. Huber, 2014
3. Huber, 2017
4. Hua, 2013

S22.04
Improving real-time fMRI using multi-echo acquisition

R. Lamerichs[1], S. Heunis[2], M. Versteijlen[1], M. Versluis[3], B. Aldenkamp[4]
[1]Philips Research, Eindhoven, The Netherlands, [2]Eindhoven University of Technology, Eindhoven, The Netherlands, [3]Philips Healthcare, Best, The Netherlands, [4]Epilepsy Centre Kempenhaeghe, Heeze, The Netherlands

Purpose/Introduction: In recent years real-time fMRI has received increasing interest. One of the applications of real-time fMRI is neurofeedback. The functional activity of an area or areas of the brain is assessed and the activity level is displayed to the subject. In this manner, the subject can be trained to alter the activity level of the selected areas. Studies have reported relief of symptoms in several mental and neurological disorders following feedback training [1, 2]. Here we present a method to derive detailed functional information per image volume and at the same time reduce the effect of physiological confounders.

Subjects and Methods: fMRI data were recorded on a Philips Ingenia Elition 3T. Gradient echo EPI sequence with 3 echo times; TE = 10.3, 29.3, 48.3 ms; TR = 1500 ms; 2.75 mm^3; MB = 2 and Sense = 3. For Philips Achieva 3T: TE = 12, 35, 58 ms; TR = 2000 ms; 3.5 × 3.5 × 4.5 mm; Sense = 2.7.

The processing pipeline existed of realignment and smoothing with a Gaussian kernel (SPM, https://www.fil.ion.ucl.ac.uk/spm/). Relaxation curves were fitted with a mono-exponential function, using MATLAB, to determine the R_2* and S_0 maps [3].

Functional analysis was done on R_2* data obtained during a block design task paradigm. The R_2* maps acquired at rest were averaged, excluding the first 3–5 time-points in order to avoid activation from the previous task block. For each individual task dynamic, the activation was calculated as percentage-signal-change (PSC) with respect to the average of the preceding rest period.

Combined-echo data (CE) were computed according to [3]. Confounder analysis was done on S_0, R_2*, echo-2 and CE. Physiology was measured using PPU and respiratory belt. Common patterns were determined by ICA on spatially concatenated data (FSL melodic, https://fsl.fmrib.ox.ac.uk/fsl/fslwiki/). Physiology data were used to classify components related to these confounders.

fMRI data were acquired on healthy subjects, after giving consent.

Results: Spatial activation patterns determined per time point for R_2* are similar compared to the results obtained by SPM on echo-2 and ICA. R_2* measures the BOLD response while S_0 captures more physiology related signal changes. Furthermore, the per dynamic analysis shows that the functional activations can vary during the task, in particular, in cognitively demanding tasks such as silent word generation (fig. 1).

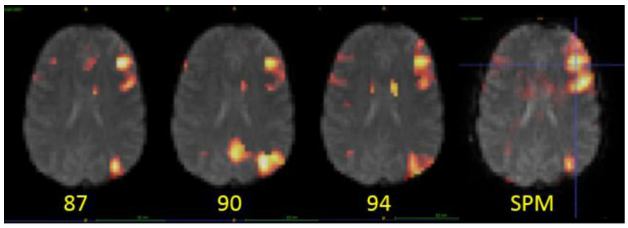

Figure 1. Example of activation per dynamic, silent word generation paradigm. Dynamic 90 shows a different pattern of activation not found by SPM. During this task block (16 dynamics) activation of the precuneus was seen in 2 consecutive dynamics.

The PSC for the R_2* data is found to be higher compared to echo-2 and CE. Analysis of confounders indicates that the R_2* maps are less prone to contamination with physiological components (fig. 2).

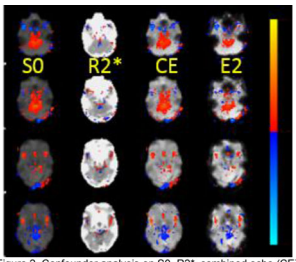

Figure 2. Confounder analysis on S0, R2*, combined echo (CE) and echo 2 (E2). Shown is the spatial distribution related to cardiac induced motion of the brain stem. The artifact is clearly shifted to the S0, leaving the R2* map virtually unaffected

Discussion/Conclusion: Multi echo acquisition increases the sensitivity in task-based rt-fMRI. Per dynamic analysis provides more detailed information on the functional activity. The contaminating effect of physiology confounders is significantly reduced.

References:

1) Young et al., PLOS ONE 9 (2014)
2) Subramanian et al., J. NeuroscI., 31 (2011)
3) Kundu et al., NeuroImage, 60 (2012)

S22.05

The influence of short breath-hold periods on Blood-Oxygen-Level-Dependent (BOLD) MRI signal

L. Zerweck, T.-K. Hauser, U. Klose
Eberhard Karls University Tübingen, Department of Neuroradiology, Tübingen, Germany

Purpose/Introduction: Keywords: BOLD MRI, Hypercapnia, Breath-hold, Cerebrovascular reserve
CO_2-triggered Blood-Oxygen-Level-Dependent (BOLD) functional MRI is a technique to investigate cerebrovascular reserve and can be used to detect cerebrovascular disease [1, 2]. Hypercapnia is known to induce cerebral vasodilation in healthy brain regions, leading to increased cerebral blood flow (CBF) and BOLD signal rise [3]. Breath-hold is a noninvasive and easily implementable method to evoke hypercapnia. While previous studies focused on breath-hold periods of longer duration, we investigated the required minimum breath-hold duration to detect a reliable BOLD signal increase.

Subjects and Methods: 14 healthy subjects underwent functional MRI at 3T in order to detect the global cerebrovascular response to hypercapnia induced by short end-expiration breath-hold periods. We investigated the breath-hold duration of 3 s, 6 s, 9 s and 12 s in separate runs. Each run included five breath-hold periods interleaved by periods of regular breathing (Fig. 1). Respiratory instructions were given verbally.

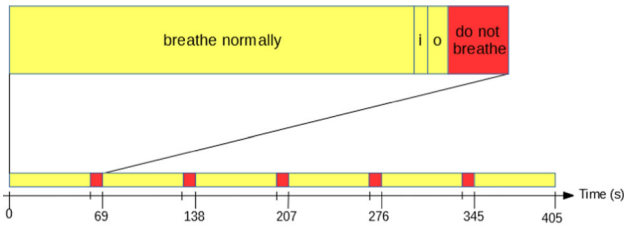

Fig.1. Paradigm: 5 repetitive cycles (69s) including breathing (yellow) and breath-hold periods (red) followed by 60s of breathing. One cycle consisted of the instructions 'breathe normally', 'breathe in' (i), 'breathe out' (o) and 'do not breathe'.

During data acquisition we measured respiratory movements using a respiratory belt to ensure that the instructions were followed correctly. We averaged the signal change of the cortex over all five periods and all subjects and calculated activation maps by integrating the signal time-course over a time period of 12 s during maximum signal change.

Results: Distinct BOLD signal increases were measured using breath-hold periods of 12 s (0.9%) and 9 s (0.8%) (Fig. 2). Breath-hold periods of 6 s led to only small signal rises (0.3%), while no comparable signal changes were observed after periods of 3 s.
Additionally we observed initial signal rises before the expected signal increases.

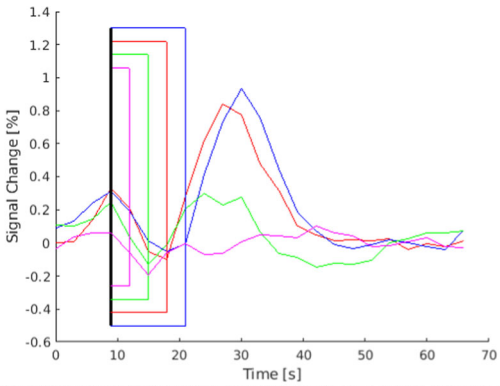

Fig.2. Mean signal changes during different breath-hold durations (blue: 12s, red: 9s, green: 6s, magenta: 3s). The colored rectangles indicate the corresponding breath-hold periods.

We observed higher BOLD signal increase in the gray than in the white matter (Fig. 3).

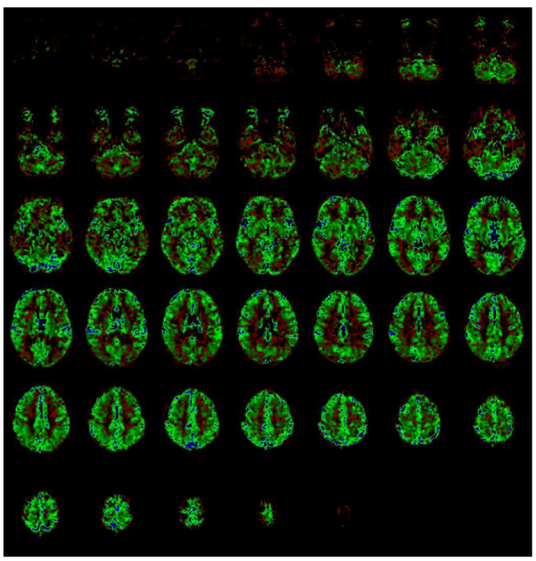

Fig.3. Activation map during 9s breath-hold task: Integral values of the signal change were averaged over all subjects after normalisation and color-scaled (blue >green>red >black).

Discussion/Conclusion: We suggest breath-hold periods of 9 s to measure the cerebrovascular reserve in routine clinical practice, as they result in reproducible BOLD responses and can be performed easily. Extending the breath-hold periods to 12 s leads to negligible additional signal increase.
We explained the initial signal rises by deep inhalation just prior to the breath-hold period.
The spatial distribution pattern of CO_2-triggered BOLD signal rise was in accordance with the findings of previous studies [1].

References:

1. Kastrup A, Li TQ, Takahashi A, Glover GH, Moseley ME. Functional magnetic resonance imaging of regional cerebral blood oxygenation changes during breath holding. Stroke. 1998;29(12):2641–5.
2. Hauser TK, Seeger A, Bender B, Klose U, Thurow J, Ernemann U, et al. Hypercapnic BOLD MRI compared to H2(15)O PET/CT for the hemodynamic evaluation of patients with Moyamoya Disease. Neuroimage Clin. 2019;22:101713.
3. Fierstra J, Sobczyk O, Battisti-Charbonney A, Mandell DM, Poublanc J, Crawley AP, et al. Measuring cerebrovascular reactivity: what stimulus to use? J Physiol. 2013;591(23):5809–21.

S22.06

Preliminary results of functional line-scanning in humans: submillimeter, subsecond resolution evoked responses

L. Raimondo[1], T. Knapen[1], I. A. F. d. Oliveira[1], X. Yu[2], W. van der Zwaag[1], J. C.W Siero[1]
[1]*Spinoza Centre for NeuroImaging, Amsterdam, The Netherlands,*
[2]*Max Plank Institute for Biological Cybernetics, Tuebingen, Germany*

Purpose/Introduction: In order to advance fundamental and clinical neuroscience it is necessary to understand the relative contributions of large vessel and microvessel signals in human cortex BOLD fMRI responses. Line-scanning fMRI[1, 2, 3] achieves extremely high resolution across both cortical depth (250 μm) and time (100 ms), by sacrificing volume coverage and resolution along the cortical surface. This unprecedented spatiotemporal resolution can allow us to identify microvessel responses and to characterize the distribution of blood flow across cortical depth. Here we present preliminary results of a human line-scanning fMRI experiment investigating hemodynamic signals in human visual cortex.

Subjects and Methods: Two volunteers were scanned at 7T (Philips) with a 32 channel receive head coil (Nova Medical). Line scans were acquired with: line resolution = 250 μm, TR/TE = 103/12 ms, 2400 timepoints, flip angle = 16°, array size = 720, line thickness = 2.5 mm, in-plane line width = 5 mm, fat suppression using SPIR. Two saturation pulses (5 ms pulse duration) were used to suppress the signal outside the line of interest. The phase-encoding in the direction perpendicular to the line was turned off[2]. The line was positioned in right/left direction, crossing the visual cortex (Fig. 1). Data was acquired during intermittent bilateral visual stimulation in 4 runs. Visual stimuli were 8 Hz flickering gratings, presented for 750 ms with an exponential ISI distribution (mean of 2 s, plus a minimum of 2 s). Reconstruction was performed offline with MatLab and Gyrotools. Multiple coil data were combined weighting the signal with the temporal signal to noise ratio (tSNR) per coil; tSNR was computed for the coil-combined data. HRF shape was estimated by deconvolution from the timeseries using 'nideconv'.

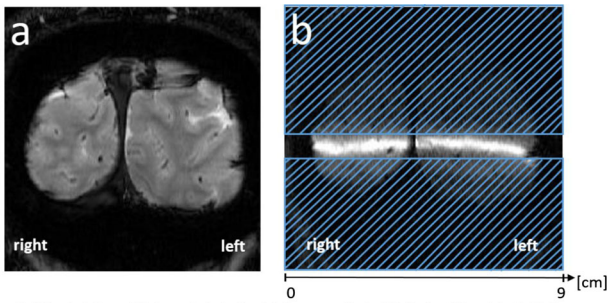

Figure1. (a) Acquired slice and (b) placement of saturation slabs to suppress signal outside the line of interest, depicted by the gap (5mm) between the saturation slabs, in right/left direction across visual cortex.

Results: Figure 2 shows line-scanning profiles along the human visual cortex. tSNR was comparable to sub-millimeter 3D-imaging and sufficient for BOLD signal detection[4]. From the results of the functional experiment (Figures 2b and 3), active points along the line due to visual stimulation are detectable in both primary visual cortex (V1) and lateral occipital cortex (LOC). The BOLD response peaks are measured at around 5 s post stimulus-onset. Positive responses are followed by an undershoot in all active regions.

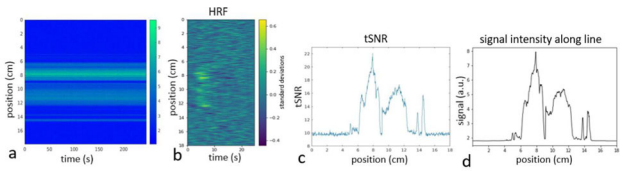

Figure2. (a) line-scanning fMRI data (run1) (b) timeseries analysis in signal standard deviations showing clear hemodynamic responses along line that crosses the two hemispheres (c) computed tSNR along the line (d) signal intensity along the line.

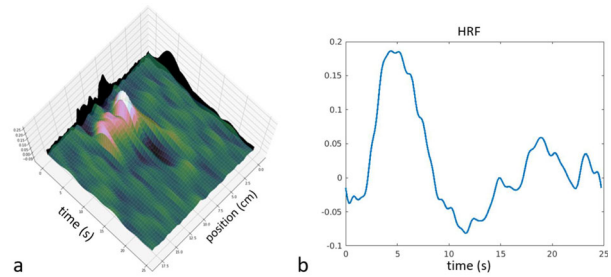

Figure 3. a) HRF response along time and space for most active voxels. b) average HRF over central 5 mm (72.5mm – 75.0mm).

Discussion/Conclusion: Our line scanning results indicate that hemodynamic response function mapping with very high spatiotemporal resolutions can be achieved in humans. Overall, the line-scanning fMRI technique seems very promising due to its potential in detailed mapping of hemodynamics in humans for clinical research on small vessel diseases but also for fundamental neuroscience at the mesoscopic scale (cortical lamina).

References:

[1] Yu X et al. Nat Methods 2014
[2] Siero J.C.W et al. ISMRM 2019, #3933
[3] Siero J.C.W. et al., BRAIN 2019, #10538
[4] van der Zwaag W et al. MRM 2012

S22.07

Differential R2′-mapping of baseline and visual stimulus states in the human brain using streamlined-qBOLD

F. Arzanforoosh[1], G. Kotek[2], A. Berman[3], J. A. Hernandez-Tamames[4], M. Smits[5], E. A. H. Warnert[5]
[1]Erasmus MC, Radiology Department, Rotterdam, The Netherlands, [2]Erasmus mc, Rotterdam, The Netherlands, [3]Harvard Medical School, Charlestown, USA, [4]Erasmus MC, Radiologyg & Nuclear Medicine, Rotterdam, The Netherlands, [5]Erasmus MC, Radiology & Nuclear Medicine, Rotterdam, The Netherlands

Purpose/Introduction: Cerebral hypoxia occurs in a plethora of brain diseases, including stroke, chronic hypertension and brain tumor [1]. This work provides a step towards a rapid, non-invasive imaging protocol for clinically feasible cerebral oxygenation mapping.
In this study we use an asymmetric spin echo (ASE)-based streamlined-qBOLD (sq-BOLD) technique [2] [3] to non-invasively monitor hemodynamic properties of the brain in two states (baseline and activation), while comparing different combinations of Echo Time/Inversion time.
Subjects and Methods: A simulation was performed to investigate the dependency of SNR on echo time according to previously described methods [2]. Four healthy volunteers (2 females and 2 males; age 30 ± 2 years) were scanned at 3 Tesla (Discovery MR750, GE, Waukesha, USA). sq-BOLD data were acquired with: FOV = 240 mm^2, 128 × 128 matrix, slice thickness 2 mm and 1 mm inter-slice gap, TR = 8 s, BW = 3906 Hz/px, ASE-sampling scheme = 0 and 16–56 ms in increments of 4 ms, total scan duration of 96 s. To compare the experimental results to the simulation study, echo times of 60 and 74 ms were tested. Note that for scans with TE = 60 ms the largest was set to 48 ms. Additionally, two TI's were investigated to establish the most effective nulling of the CSF signal (TI = 1225 versus 2000 ms). All four combinations of TE/TI were acquired during baseline and during a visual stimulus (flashing checkerboard with a frequency of 8 Hz). T_1-weighted images were acquired for each subject to segment the gray and white matter and CSF. A visual cortex ROI was selected from the "Juelich Histological Atlas" [4], and registered to the ASE-image space for each subject.
Results: The simulation showed that the highest SNR for R2′ in gray matter can be found between TE = 60–80 ms (Fig. 1). Example images at two TEs and two TIs are shown in Fig. 2. The result shows using a TI of 2 s resulted in better CSF nulling than a TI of 1.225 s; and the median value of R2′ in the visual cortex decreases in during stimulation (Fig. 3).

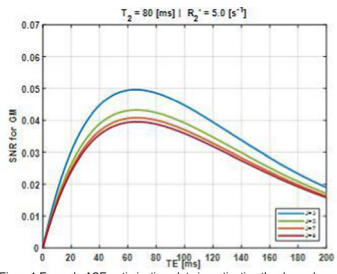

Figure1:Example ASE optimization plots investigating the dependence of SNR on tissue T2, echo time and number of τ-weighted sampling points (J).

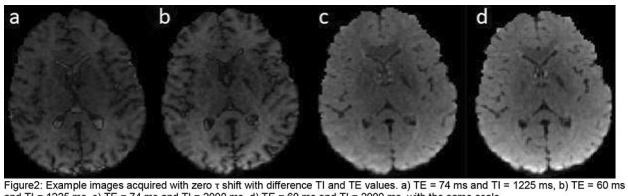

Figure2: Example images acquired with zero τ shift with difference TI and TE values. a) TE = 74 ms and TI = 1225 ms, b) TE = 60 ms and TI = 1225 ms, c) TE = 74 ms and TI = 2000 ms, d) TE = 60 ms and TI = 2000 ms, with the same scale.

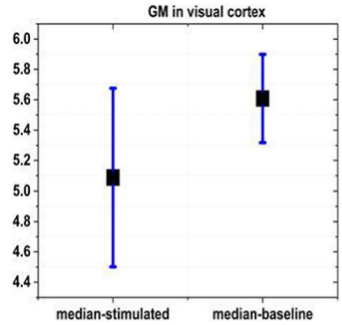

Figure3: Comparison of median value of R2′ of gray matter in 2 states of baseline and stimulated for GM located in visual cortex.

Discussion/Conclusion: This pilot study shows the feasibility of using sq-BOLD to measure R2′ changes in vivo. The current optimal combination of echo time and Inversion time is (TE/TI = 60 ms/2000 ms), as this results in gray matter R2′ estimation with minimal CSF contamination and highest SNR. The decrease in R2′ in the visual cortex upon stimulation can be explained by the increase in oxyhemoglobin due to the overshoot in cerebral blood flow when neurons are activated [5]. Future work includes further optimization of image acquisition to ultimately lead to acquisition rapid MRI protocol for assessing cerebral oxygenation.
References:
[1] F. Colliez, et al., *Front. Oncol.*, 2017.
[2] A. J. Stone, et al., *Neuroimage*, 2017.
[3] M. E. MacDonald, et al., *Neuroimage*, 2018.
[4] K. Amunts, et al., *Neuroimage*, 2000.
[5] R. B. Buxton, et al., *Front. Neuroenergetics*, 2010.

S22.08

High-frequency fluctuations in the brainstem using resting-state fMRI—a feasibility study

M. van den Kerkhof[1], J. Jansen[1], L. Canjels[1], R. van Oostenbrugge[2], B. Poser[3], W. Backes[1]
[1]Maastricht University Medical Center, School for Mental Health & Neuroscience, Radiology & Nuclear Medicine, Maastricht, The Netherlands, [2]Maastricht University Medical Center, School for Mental Health & Neuroscience, Neurology, Maastricht, The Netherlands, [3]Maastricht University, Maastricht Brain Imaging Center, Faculty of Psychology and Neuroscience, Maastricht, The Netherlands

Purpose/Introduction: Resting-state (rs-)fMRI is mostly used to detect spontaneous low-frequency fluctuations (10–100 mHz). Dynamic scanning with a high sampling rate (> 1000 mHz) enables unaliased sampling of cardiac fluctuations in the BOLD signal[1]. Therefore, the cardiac signals can be discerned from the neuronal activity fluctuations. In (cerebro)vascular disorders, these fluctuations may be affected and reflect abnormal neurovascular coupling. Here, we explored the feasibility of obtaining an extended frequency

spectrum in different brain regions, including brainstem, using high-frequency rs-fMRI.

Subjects and Methods: Data of three healthy females (21.7 ± 0.6 years) was acquired using a 7T MRI system (Magnetom, Siemens Healthineers, Erlangen, Germany) with a 32-channel phased-array head coil. An MP2RAGE (TR/TE = 5000/2.47 ms, TI1/TI2 = 900/2750 ms, $\alpha1/\alpha2 = 5°/3°$, $0.7 \times 0.7 \times 0.7$ mm^3) and SA2RAGE (TR/TE = 2400/0.78 ms, TI1/TI2 = 58/1800 ms, $\alpha1/\alpha2 = 4°/10°$, $2 \times 2 \times 2$ mm^3) for $B1^+$ correction[2], were applied to acquire a whole brain T1w anatomical reference. Rs-fMRI data was acquired using a whole brain multiband-EPI sequence (TR/TE = 383/17 ms, multiband factor 4, $2.5 \times 2.5 \times 2.5$ mm^3, 1000 dynamics, 6:32 min). Simultaneously, physiological signals were recorded using a pulse oximeter and a respiratory belt.

Bias field correction, brain extraction and distortion correction were performed on the structural and functional images. Structural images were segmented using FreeSurfer v6.0[3]. Temporal filtering and slice timing correction were performed on the functional data. Next, ROIs were defined in the frontal and temporal cortex and the brainstem, for which the power spectrum and fractional amplitude of low frequency fluctuations (fALFF) were calculated[4].

Results: The power spectra of the ROIs show a higher amplitude of the low frequencies (0–100 mHz), compared to the high-frequency fluctuations (> 100 mHz) (Fig. 1). For the frontal lobe, the power–frequency relation roughly follows a 1/f dependency and has strongly attenuated signal components for the highest frequencies. For the brainstem and temporal lobe, however, two additional peaks (near 300 and 1200 mHz) become visible, which were confirmed as the cardiac and respiratory signals by means of the physiological logs (Fig. 2). Table 1 shows that the fALFF values vary between the ROIs, matching the expected attenuated pulsation downstream the vascular tree.

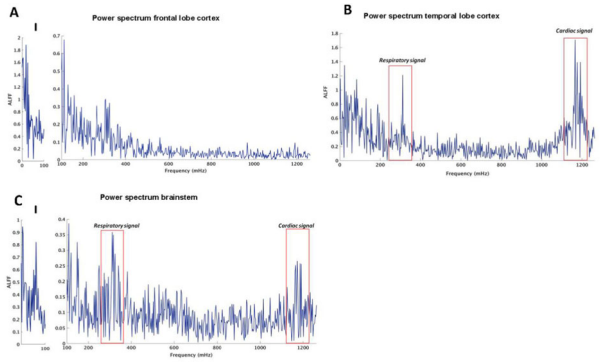

Fig.1. The power spectrum in the frontal lobe(A), temporal lobe(B) and brainstem(C) of subject 1. Panel I shows the amplitude of the low frequency fluctuations (0-100mHz). B and C show the expected respiratory and cardiac peaks near 300 and 1200mHz.

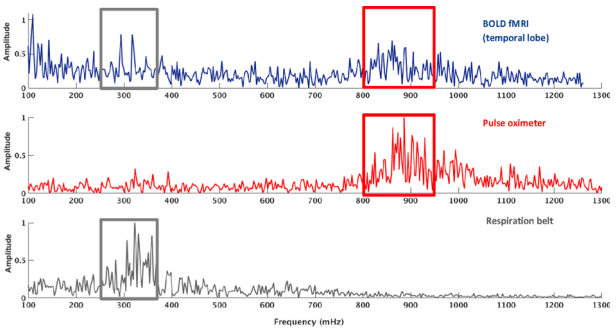

Fig.2.The frequency spectrum in the temporal lobe(blue), simultaneous recordings from the pulse oximeter(red), and respiratory belt(grey) for subject 3. The BOLD signal shows the contribution of the physiological signals at corresponding frequencies.

	Frontal cortex ($x10^{-3}$)	Temporal cortex ($x10^{-3}$)	Brainstem ($x10^{-3}$)
10-100 mHz	5.4 ± 0.2	3.2 ± 0.5	3.8 ± 0.2
200-400 mHz	2.3 ± 0.2	2.3 ± 0.1	2.2 ± 0.3
750-1000 mHz	1.5 ± 0.2	1.7 ± 0.2	1.7 ± 0.2
1000-1200 mHz	1.3 ± 0.2	2.0 ± 0.5	1.7 ± 0.2

Table 1. The fALFF values (mean ± standard deviation between the three subjects) of four frequency bands for different brain regions

Discussion/Conclusion: This study shows the feasibility to acquire extended high-frequency spectra in different brain regions, among which the brainstem, using a short-TR fMRI protocol. The respiratory and cardiac signals could be detected and were validated with physiological monitoring. Future applications will be in hypertensive patients, which may gain more insights in the cerebral regulation of blood circulation and functional abnormalities observed in hypertension.

References:

[1]Trapp, NeuroImage, 2018
[2]Marques, PLoS One, 2013
[3]Fischl, Neuron, 2002
[4]Zou, J. Neurosci. Methods, 2008

S22.09

Thermonoxious stimulation evokes BOLD responses within area 3a of human primary somatosensory cortex

R. Sanchez Panchuelo[1], S. Eldeghaidy[1], F. McGLone[2], O. Favorov[3], S. Francis[1]
[1]*University of Nottingham, Sir Peter Mansfield Imaging Centre, Nottingham, UK,* [2]*Liverpool John Moore University, Liverpool, UK,* [3]*University of North Caroline at Chapel Hill, Chapel Hill, USA*

Purpose/Introduction: Previous studies in monkeys have demonstrated that the posterior parts of area 3a is highly responsive to thermal pain stimulation [1], and further proved that monkeys who had this region surgically removed showed permanently reduced pain sensibility. In humans, the involvement of area 3a in pain sensation has not been explored. Here we use 7T fMRI to map the functional representations of noxious heat and vibrotactile stimuli in human primary somatosensory cortex.

Subjects and Methods: Four subject were scanned at 7T using a 32-channel receive coil. fMRI data were acquired using a GE-EPI acquisition (TE/TR = 25 ms/2 s, 1.5 mm isotropic resolution, 54 slices, SMS = 3) during painful thermal stimulation delivered to either the palm or digits 2 and 3 tips on the right hand using an MRI compatible Peltier thermode (Medoc pathway). The paradigm consisted of a block design of 5 s periods of stimulation at the subject's painful threshold followed by baseline (40 °C) periods of varying duration (25–30 s). Two runs (8 trials) were delivered to the palm and to the fingertips. In a separate session, a travelling wave paradigm with non-noxious vibrotactile stimulation was used to map the representation of the individual digits in contralateral primary sensory cortex (S1) [3]. Thermonoxious data were analyzed using a GLM. Fourier analysis was performed on the travelling wave data to form digit somatotopic (phase) maps. Activations maps to thermonoxious stimulations were compared against the hand digit ROI from the vibrotactile paradigm in flattened cortical space.

Results: Painful thermal stimulation elicited BOLD responses in contralateral S1 in all subject scanned (except for stimulation of the fingertips in subject 3). Activation maps for the palm and fingertip stimulation conditions are similar (Fig. 1): these maps, located in the depth of the central sulcus, lie within (and beyond) the anterior part of

the vibrotactile defined hand ROI and also extend medially (particularly for subjects 2 and 4).

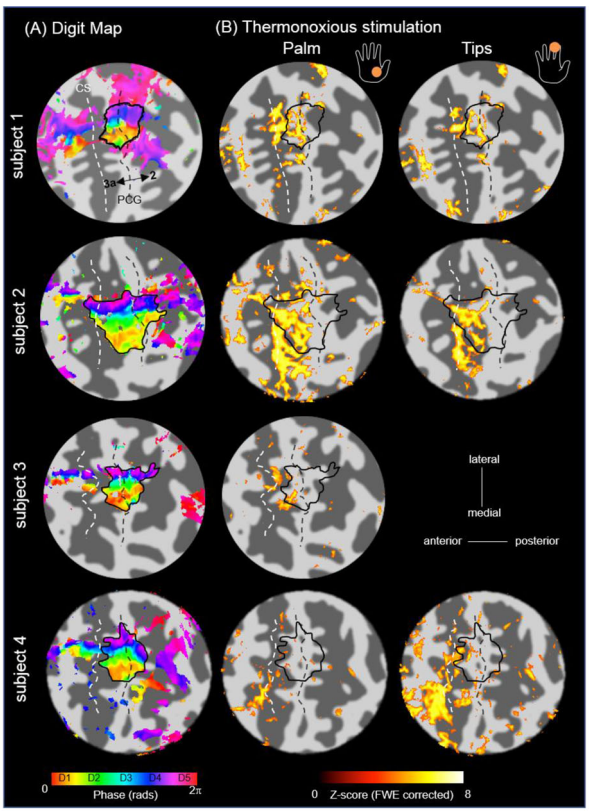

Figure 1. (A) Digit somatotopy (phase map) in response to non-noxious vibrotactile stimulation shown in a flattened representation of the contralateral (left hemisphere) central sulcus (CS) and post-central gyrus (PCG). Light grey represent sulci and dark grey corresponds to gyri. Black outline: Hand digits ROI. (B) Activation maps to thermonoxious stimulation of the palm (left) and the fingertips of digits 2 and 3. Notice that activation extends anteriorly and also laterally with respect to the hand digits ROI, consistent with the location of area 3a.

Figure 2 shows that activation maps to painful stimulation of the palm are highly reproducible across scanning sessions.

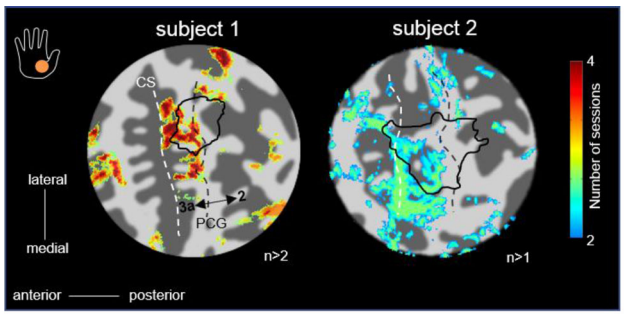

Figure 2. Overlap of active areas to painful thermal stimulation of the palm across n=4 scanning sessions for subject 1, and n=2 scanning sessions for subject 2. Conjunction map was formed based on responses with a significant threshold z>3.08 after false-discovery correction.

Discussion/Conclusion: Area 3a primarily represents deep receptors and musculature of the contralateral body. Here we demonstrate a nociresponsive region within human S1 which lies anteriorly with respect to non-noxious responses to vibrotactile stimulation of the digits, consistent with the location of area 3a. We have shown that activation maps are very robust and reproducible. This region could potentially be targeted for surgery in patients suffering from chronic pain, making it a highly attractive means of treating chronic pain [1].

References:

1. Tommerdahl et al. J Neurophysiol. 1996, 75:2662–70.
2. Favorov et al. Soc Neurosci Abstracts. 2017:486.15.
3. Sanchez Panchuelo et al. J Neurophysiol. 2010, 203:2544–56.

S23 Scientific Session

15:40–17:10 *Room 3 - Ruys & van Rijckevorsel Zaal*

Spectroscopy Applications

S23.02

Evolution of glial and axonal changes in human brain tissue after ischemic stroke investigated with diffusion-weighted magnetic resonance spectroscopy at 3 T

G. Genovese[1], B. Diaz[2], M. Marjanska[3], R. Valabregue[1], I. Ronen[4], S. Lehericy[1], C. Rosso[1], F. Branzoli[1]

[1]Institut du Cerveau et de la moelle epiniere (ICM), Centre de NeuroImagerie de Recherche (CENIR), Paris, France, [2]Hòpital Pitié-Salpétrière, Service des Urgences Cérébrovasculaires, Paris, France, [3]University of Minnesota, Center for Magnetic Resonance Research and Department of Radiology, Minneapolis, USA, [4]Leiden University Medical Center, C. J. Gorter Center for High Field MRI, Department of Radiology, Leiden, The Netherlands

Purpose/Introduction: Diffusion-weighted MR spectroscopy (DW-MRS) is a unique technique capable of disentangling different pathological mechanisms taking place in brain tissue, by providing specific markers of axonal and glial cells damage[1–2]. In particular, diffusion of *N*-acetylaspartate + *N*-acetylglutamate (tNAA) has been suggested as a marker of intra-axonal damage[3], while diffusion of choline containing compounds (tCho) provides insight into alterations of glial cells[4]. The goal of this study was to investigate with DW-MRS microstructural changes occurring at different time points after ischemic stroke (IS) in the human brain, in both infarcted and non-infarcted hemispheres.

Subjects and Methods: Eighteen ischemic stroke patients (62 ± 12 years) and 18 gender- and age-matched healthy volunteers (HVs) (57 ± 11 years) were scanned at 3T, using a DW-semi-LASER sequence[5]. Patients were scanned at three different stages of the disease: in the acute (V1, ≈ 10 days after IS), sub-acute (V2, ≈ 30 days after IS) and chronic phase (V3, ≈ 90 days after IS). HVs were scanned once. Volumes of interest (VOI) of 10 ml were positioned in the lesion area (VOI_{les} and VOI_{les}^{HV} for patients and HVs, respectively) and in the contralateral side (VOI_{cl} and VOI_{cl}^{HV}, respectively) (Fig 1A-B).

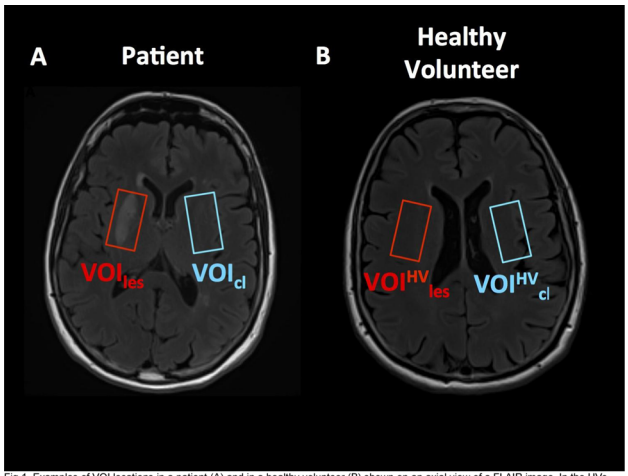

Fig 1. Examples of VOI locations in a patient (A) and in a healthy volunteer (B) shown on an axial view of a FLAIR image. In the HVs, VOIs were positioned in the same locations as for the corresponding age- and gender-matched patients.

Diffusion weighting was applied in three orthogonal directions with two *b*-values of 11 and 3550 s/mm^2 and 16 averages were acquired per condition. Post-processing corrections[5] were performed on single averages before summation. LCModel[6] was used for metabolite quantification. ADC of tNAA, tCho and tCr (creatine + phospho-creatine) were estimated from mono-exponential decays.

Results: Example of spectra acquired in patients and in HVs are shown in Fig 2A-B.

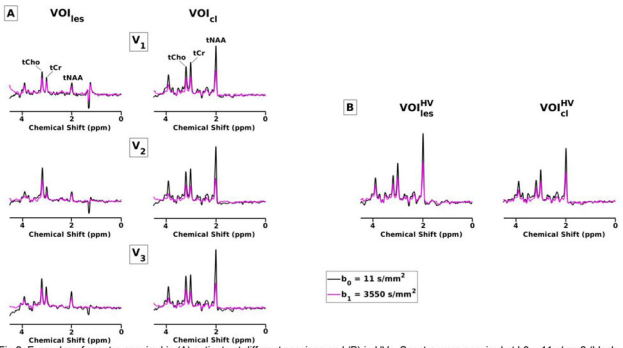

Fig 2. Examples of spectra acquired in (A) patients at different sessions and (B) in HVs. Spectra were acquired at b0 = 11 s/mm2 (black lines) and b1 = 3550 s/mm2

ADC of tCho increased at V2 in VOI_{les} in comparison with both VOI_{cl} and VOI_{les}^{HV} (Fig 3A). A significant difference was observed in the longitudinal change of the ADCs of tCho (V1 vs. V2 and V2 vs. V3) in VOI_{les} with respect to VOI_{cl} (Fig 3A). ADC of tCr increased at V2 and V3 in VOI_{les} vs. both VOI_{cl} and VOI_{les}^{HV} (Fig 3B). The longitudinal change of ADC of tCr (V1 vs. V2 and V1 vs. V3) was significantly different in VOI_{les} vs. VOI_{cl} (Fig 3B). No variations of ADC of tNAA were observed (Fig 3C).

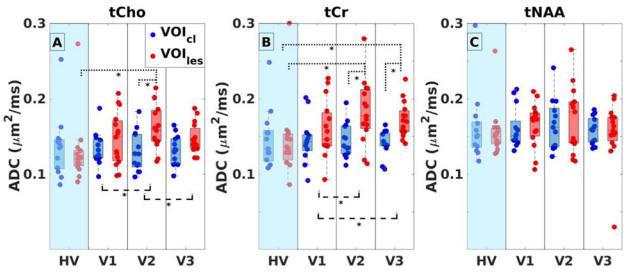

Fig 3. Box plots of the ADCs for (A) tCho (B), tCr and(C) tNAA. Comparisons in VOI_les vs. both VOI_cl and VOI_HV_les at each stage (dotted lines). Comparisons between different stages in VOI_les vs. VOI_cl (dashed lines). *p<0.05.

Discussion/Conclusion: The increase of ADC of tCho in VOI_{les} vs. both VOI_{cl} and VOI_{les}^{HV} at V2, and of tCr at V2 and V3, are consistent with glial cell activation and/or swelling induced by inflammatory processes. Interestingly, the increase of ADC of tCr in VOI_{les} at V3 suggests that the inflammation is still present in the chronic phase. This could give clues on the optimal therapeutic window for anti-inflammatory therapies.

References:

[1] Nicolay et al., NMR Biomed 14: 94–111 (2001).
[2] Palombo et al., NeuroImage 182: 97–116 (2018).
[3] Wood et al., J Neurosci 32(19): 6665–6669 (2012).
[4] Ercan et al., Brain 139(5): 1447–1457 (2016).
[5] Genovese et al., Proc ISMRM 26: 1064 (2018)
[6] Provencher, MRM 30: 672–679 (1993).

S23.03

T_1 relaxation times of macromolecular resonances for grey and white matter voxels in human brain at 9.4 T

S. Murali-Manohar[1], A. M. Wright[1], A. Henning[2]
[1]*Max Planck Institute for Biological Cybernetics, MRZ, Tuebingen, Germany,* [2]*UT Southwestern Medical Center, Advanced Imaging Research Center, Dallas, Texas, USA*

Purpose/Introduction: Determining T_1 relaxation times of macromolecular (MM) resonances aid us to understand their behavior better. Very few attempts have been made to estimate the T_1 relaxation times of MM resonances. T_1 relaxation time of MM baseline as a whole [1] or for individual MM resonance at 0.916 ppm [2] have been previously reported. T_1 relaxation times for individual MM resonances have been estimated in our previous work [3] for a grey matter rich region in the occipital lobe. This work extends to estimate the T_1 relaxation times in both GM rich and WM rich voxel as well as to report the T_1 values in pure GM and WM voxels.

Subjects and Methods: 11 inversion time (TI_1 and TI_2) combinations (Fig. 1) were determined by performing Bloch simulations for a double inversion recovery (DIR) sequence and considering those combinations for which the metabolite contributions were minimal. A metabolite-cycled semiLASER sequence was used to localize voxels in the occipital lobe and left parietal lobe preceded by a DIR technique [4] (TE/TR: 24, 8000 ms; NEX: 32). MP2RAGE images [5] were acquired to calculate the tissue volume fractions. Data were acquired from 11 and 6 healthy volunteeers in GM and WM rich regions respectively. The raw data were pre-processed and the fitted in LCModel-v6.3-1L [6] using simulated Voigt lines. Residual subtraction from the MM spectra was performed by fitting sharper Voigt lines at the observed shifts in LCModel. The LCModel concentrations were then fit to the DIR signal equation and the T_1 relaxation times were calculated. Furthermore, by using a linear relationship of T_1 time variations across tissue composition [7], a system of linear equations were simultaneously solved to estimate the T_1 relaxation times for pure GM and WM voxels.

Results:

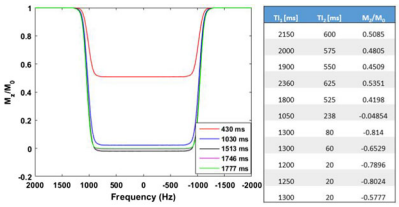

TI_1 [ms]	TI_2 [ms]	M_z/M_0
2150	600	0.5085
2000	575	0.4805
1900	550	0.4509
2360	625	0.5351
1800	525	0.4198
1050	238	-0.04854
1300	80	-0.814
1300	60	-0.6529
1200	20	-0.7896
1250	20	-0.8024
1300	20	-0.5777

Fig. 1: Bloch simulation result for TI1/TI2 = 2150/600 ms. Final chosen set of TI1/TI2 combinations and their Mz/M0 are shown in the table.

Fig. 1 shows Bloch simulation for 2150/600 ms where metabolite contribution is minimal and MM contribution is considerably higher. A similar metabolite nulling was achieved for almost all TI combinations covering a range of magnetizations for MMS except 1050/238 ms which is an MM null point.

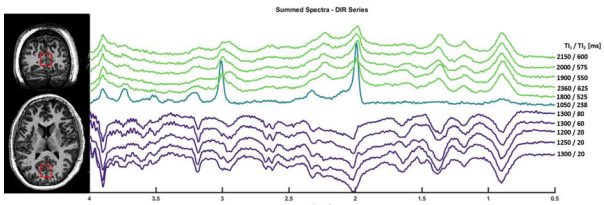

Fig. 2: DIR series for summed spectra are shown with their corresponding TI1/TI2 (right). The voxel was positioned in a gray matter rich area in the occipital lobe is shown (left).

The MM spectra DIR series is shown in Fig. 2 for GM rich voxel.

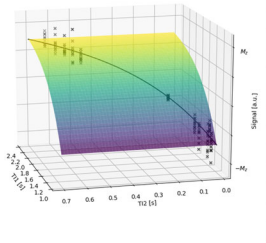

	T1 GM rich (ms)	T1 WM rich (ms)	T1 Pure GM (ms)	T1 Pure WM (ms)
MM-0.92	286.33 ± 9.51	280.27 ± 13.34	315.22 ± 8.00	270.69 ± 16.88
MM-1.21	287.26 ± 25.46	301.22 ± 35.60	303.97 ± 21.49	310.79 ± 44.97
MM-1.39	336.26 ± 19.63	283.28 ± 26.33	398.27 ± 17.25	228.13 ± 32.48
MM-1.67	237.62 ±13.84	303.49 ± 24.47	218.18 ± 8.55	363.40 ± 34.46
MM-2.04	345.82 ± 8.82	356.64 ± 17.02	369.60 ± 4.57	362.43 ± 24.75
MM-2.26	324.81 ± 8.41	310.72 ± 15.46	362.00 ± 4.83	292.94 ± 22.10
MM-2.56	262.26 ± 17.59	270.10 ± 25.88	280.52 ± 14.06	273.14 ± 33.58
MM-2.7	269.05 ± 18.89	310.77 ± 24.87	267.16 ± 16.89	347.15 ± 30.34
MM-2.99	452.18 ± 18.77	475.09 ± 17.81	477.91 ± 21.01	491.05 ± 16.64
MM-3.21	237.01 ± 22.05	211.32 ± 19.44	273.58 ± 25.59	183.60 ± 16.65
MM-3.62	772.70 ± 33.69	767.33 ± 48.99	843.93 ± 27.28	751.98 ± 63.19
MM-3.75	478.30 ± 20.02	501.39 ± 26.85	506.22 ± 17.60	517.17 ± 33.12
MM-3.86	232.13 ± 22.68	251.65 ± 20.39	240.59 ± 26.07	267.27 ± 17.90

Fig. 3: Curve fitting for MM peak at 0.916 ppm (left). T1 relaxation times of individual MM resonances for GM rich, WM rich, pure GM and pure WM voxels (right).

Fig. 3 also shows a curve fitting for the DIR signal equation for MM at 0.916 ppm. Fig. 3 tabulates the T_1 relaxation times of individual MM peaks for GM rich, WM rich, pure GM and pure WM voxels.

Discussion/Conclusion: A novel DIR technique was developed for acquiring DIR series MM spectra. The T_1 relaxation times of individual MM resonances for both GM rich and WM rich regions in the human brain at 9.4 T are reported. Further solving a system of linear equations, T_1 values for pure GM and WM voxels are reported additionally.

References:

1. Xin et. al., MRM 2013
2. Behar et. al., MRM 1994
3. Murali-Manohar et. al., ISMRM Proceedings, Montreal 2019
4. Giapitzakis et. al., MRM 2018
5. Hagberg et. al., NeuroImage 2017
6. Provencher et. al., LCModel & LCMgui user's manual 2005
7. Hetherington et. al., Ann Neurol 1995

S23.04

The concentrations of glutamate, glutamine, aspartate and GABA during continuous visual stimulation at 3 Tesla

A. Manzhurtsev[1], A. Yakovlev[2], P. Menshchikov[3], M. Ublinskiy[4], N. Semenova[1], T. Akhadov[4]
[1]*Emanuel Institute of Biochemical Physics of the Russian Academy of Sciences, Moscow, Russian Federation,* [2]*Moscow State University, Moscow, Russian Federation,* [3]*Semenov Institute of Chemical Physics of the Russian Academy of Sciences, Moscow, Russian Federation,* [4]*Clinical and Research Institute of Emergency Pediatric Surgery and Traumatology, Moscow, Russian Federation*

Purpose/Introduction: Cerebral concentrations of neurotransmitters GABA, glutamate (Glu) and glutamine (Gln) are of high interest, especially during neuronal activation. The concentrations of their metabolism participants (that are, among others, aspartate (Asp) and N-acetyl aspartate (NAA) are of interest as well. This is the first functional MRS (fMRS) of aspartate at 3 Tesla; also, TE averaging [2] was used for the fMRS of Glu and Gln for the first time. The stimulation effect on GABA was also studied.

Subjects and Methods: The study consisted of 3 parts (17 subject in each, total of 54). At first, spectroscopy was performed at rest, after that—during 8 Hz visual stimulation. For voxel location see fig. 1. Shimming and water suppression parameters were the same for resting and stimulus spectra.

Acquisition.

Figure 1. Voxel location in visual cortex (20x40x30 mm) in all three parts of the study.

GABA-: MEGA-PRESS sequence, 20 ms editing pulses (δOn = 1.9, δOff = 1.5 ppm), TE = 80 ms, TR = 2 s, NSA = 288, processed in Gannet.

Aspartate: MEGA-PRESS sequence [3], 27 ms editing pulses (δOn = 3.89, δOff = 5.21 ppm), TE = 90 ms, TR = 2 s, NSA = 288. PRESS spectra with TE = 90 ms were compiled from OFF-series (PRESS-90), processed in jMRUI.

Glu and Gln: TE averaged, TE = 35, 45, …185 ms, NSA = 16 × 16, TR = 2 s. Processed in LCModel with basis set simulated in FID-A.

GABA-/Cr, Asp/Cr, Glu/Cr, Gln/Cr and NAA/Cr, as well as their absolute concentrations were found. In order to compensate for BOLD linewidth changes, the relative effect of stimulation on Cr-normalized values was found. Statistical significance test: Mann–Whitney.

Results: Typical spectra and processing are demonstrated on fig. 2.

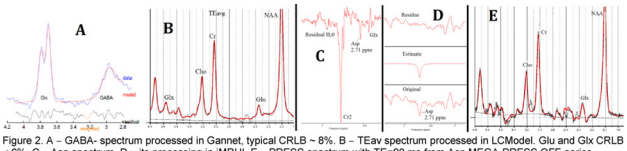

Figure 2. A – GABA- spectrum processed in Gannet, typical CRLB ~ 8%. B – TEav spectrum processed in LCModel. Glu and Glx CRLB ≤ 6%. C – Asp spectrum, D – its processing in jMRUI. E – PRESS spectrum with TE=90 ms from Asp MEGA-PRESS OFF-series

Visual stimulation caused the statistically significant decrease in GABA-/Cr (8%) and Asp/Cr (7%); increase in Glu/Cr (3%), Gln/Cr (10%); NAA/Cr remained unchanged. For absolute concentrations see fig. 3.

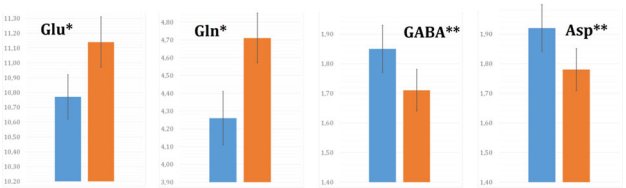

Figure 3. Absolute concentrations of the metabolites changed under continuous visual stimulation. * - p<0.01, ** - p<0.05

Discussion/Conclusion: To our knowledge, fMRS of aspartate is performed at 3T for the first time. The intensity of the Asp peak obtained in this study is enough for the confident quantitative analysis. The decrease in [Asp] as well as the [GABA] reduction in response to continuous activation is in good agreement with previous findings at 7T [4, 5]. TE averaged allowed to confidently observe the increase in [Glu] (in agreement with [4, 5]) and increase in [Gln] (previously was believed to remain unchanged, e.g. [4, 5]). The increase in [Gln] may signify the activation of Glu-Gln cycle. The reduction of [GABA] means the participation of the inhibitory neurotransmitter in the neuroactivation process. Aspartate may be lowered in order to maintain the main neuronal marker [NAA] constant. The results allow to speculate about the Glu-Gln neurotransmitter function predominance, and the metabolic nature of changes of the other parameters studied.

References:

1. Hurd et al. https://doi.org/10.1002/mrm.20007
2. Menshchikov et al. https://doi.org/10.1002/mrm.27700
3. Bednarik et al. https://doi.org/10.1038/jcbfm.2014.233
4. Chen et al. https://doi.org/10.1016/j.neuroimage.2017.05.044

S23.05

The origin of ^{31}P MR signal at 5.35 ppm in patients with critical limb ischemia

P. Sedivy[1], M. Dezortova[1], M. Drobny[1], M. Dubsky[2], M. Hajek[1]
[1]*Institute for Clinical and Experimental Medicine, MR unit, Prague, Czech Republic,* [2]*Institute for Clinical and Experimental Medicine, Diabetology Department, Prague, Czech Republic*

Purpose/Introduction: A group of diabetic patients with limb ischemia was studied by rest and dynamic ^{31}P MRS. An unknown intensive signal with the mean chemical shift of 5.3 ppm (labeled as Pi_2) was observed in calf muscle spectra in several patients (Fig 1). Recently, the signal with a similar chemical shift has been assigned to inorganic phosphate (Pi) from mitochondrial and other phosphate alkaline pools[1, 2]. Another candidate to explain the presence of the unknown signal is glucose-1-phosphate (G1P).

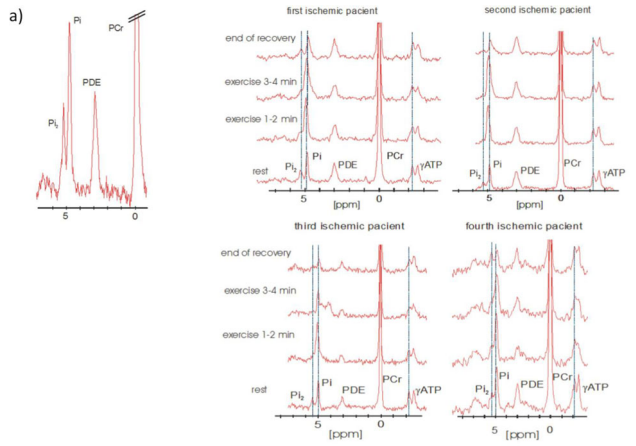

Fig 1. a) The detail of rest ^{31}P MR spectrum of ischemic patients in the range 5-5.5 ppm (PCr – phosphocreatine, PDE – phosphodiesters, Pi – inorganic phosphate, Pi $_2$ – unknown signal). b) Spectra of 4 patients measured by dynamic ^{31}P MRS.

Subjects and Methods: 68 diabetic patients (66.3 ± 8.6 yrs; BMI = 28 ± 9 kg/m^2) were examined by rest and dynamic ^{31}P MRS (3T system, ^{31}P/^{1}H coil). Phantoms with G1P and Pi were measured at pH 7.05 and 7.51.

^{31}P MR spectra were analyzed by AMARES (jMRUI 5.0). Lorentzian line shapes were applied: phosphocreatine (PCr), Pi, unknown Pi_2 signal (5.0–5.5 ppm).

All the subjects provided their informed consent in line with local Ethical Committee rules.

Results: According to the histogram (Fig 2) Pi_2 signals with the intensity > 50% of the Pi intensity (S/N > 2) were visible in 10 patients from 65 examined diabetic subjects. Intramyocellular pH based on chemical shifts of PCr and Pi was 7.05 ± 0.02, pH corresponding to the unknown Pi_2 signal was 7.54 ± 0.05. Dynamic ^{31}P MRS was performed only in 4 of 10 patients, see Fig 1.

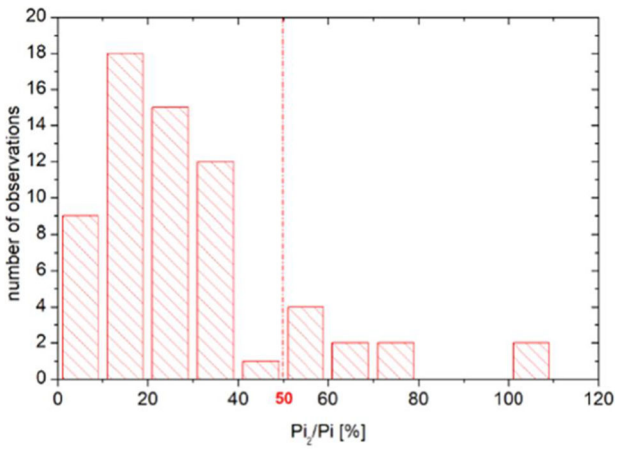

Fig 2. Histogram of number observation of ratio Pi2/Pi in ischemic diabetic patient group (n=68).

Discussion/Conclusion: Our data demonstrate that the Pi_2 signal between 5.2 and 5.4 ppm is not an artifact. We followed two hypotheses of the Pi_2 signal origin: a) phosphorus in the alkaline phosphate pool or b) phosphorus in unknown phosphomonoester. The alkaline pool could consist of a) Pi in cytoplasma of the mitochondria[3] (mitochondria pH 7.3) b) Pi in cytosol of considerably damaged muscle cells[4] or c) Pi in interstitium/blood vessels. Interstitium and blood vessels have a referred value between 7.36 and 7.44; moreover, extracellular concentration of Pi is obviously low and the volume of tissue fluid is smaller than the volume of cytosol. Mean pH calculated from Pi_2 in our patients group is 7.54 ± 0.05, it means close to but higher than pH discussed for all the theoretically mentioned hypotheses.

The other signal in the above mentioned range of chemical shifts are the signals of 2,3-diphosphoglycerate and G1P. The first one can be excluded because the signal at 6.3 ppm is missing. G1P could be a candidate as shown in Fig 3; nevertheless, phosphorus chemical shift is still below the Pi_2 signal of about 0.2 ppm.

We assume that the Pi_2 signal at 5.3 ppm is probably the Pi signal from the interstitial alkaline pool around a heavily damaged tissue. This increased Pi_2 signal in patients with the syndrome of diabetic foot could be considered as a biomarker of the heaviest muscular damage.

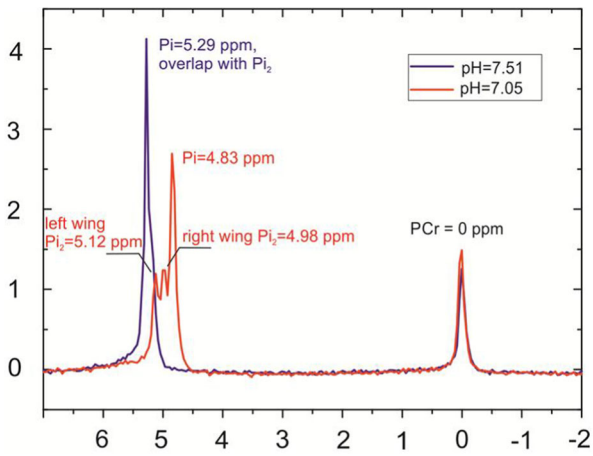

Fig 3. 31P MR spectrum of two phantoms with PCr (phosphocreatine), inorganic phosphate (Pi), glucose-1-phosphate (G1P) in pH = 7.05 and 7.51.

Supported by MH CZ—DRO ("IKEM, IN 00023001" support).

References:

[1]Valkovic L et al. Sci Rep. 2016; 6:20087
[2]Sedivy P et al. Int Angiol. 2018 Aug;37(4):293–299
[3]Kan HE et al. NMR Biomed. 2010 23(8):995–1000
[4]Wary C et al. NMR Biomed. 2012 Oct;25(10):1160–9

S23.06

A 1H-HRMAS study of the effects of a vanadium derivative on the metabolism of different animal tissues to unveil its insulin-mimetic capacity

A. M. Metelo[1], N. Arias-Ramos[2], M. Castro[1], **P. López-Larrubia**[2]
[1]University of Coimbra, Coimbra, Portugal, [2]Instituto de Investigaciones Biomédicas, CSIC/UAM, Madrid, Spain

Purpose/Introduction: The pharmacological action of $VO(dmpp)_2$ was already evaluated in vivo with obese Zucker rats treated during 4 weeks with this compound [1]. Besides the promising results concerning biological parameters indicative of insulin-mimetism, a specific biological activity in mitigating impaired lipid metabolism was observed as well. This work aims at complementing and reinforcing data previously attained and unveil the mechanism of action of this compound at the molecular level, particularly on the metabolic profile of different organs. *Ex vivo* experiments with samples of the brain, liver and skeletal muscle from treated and non-treated obese Zucker rats, using lean Zucker as control, were carried out by 1H-HRMAS.

Subjects and Methods: Lean Zucker (fa/+) and obese Zucker (fa/fa) rats (7 w-old) were used to test the insulin-mimetic properties of $VO(dmpp)_2$. During 4 weeks, lean and obese animals were daily weighted and intraperitoneally injected with $VO(dmpp)_2$ (15 mg/Kg bw) or serum (n = 6 *per* group). On the last day of the experiment, a glucose tolerance test was performed to evaluate the glycaemic profile of the rats, and then were sacrificed with a focused high-power MW. Different organs were excised (brain, liver and muscle) and stored at − 80 °C until their posterior use. 1H HR-MAS spectra of the tissues were acquired in a 11.7T system and processed with LCModel (brain spectra) or MestReNova (liver and muscle spectra).
Results: The analysis of the spectra detected lipid metabolites in brain (signals A to J in **Fig. 1**-left) in much higher concentration in obese rats than in lean groups. This indication is significantly decreased in obese treated animal, clearly observed in lipid-signal B (1.30 ppm in **Fig. 1**-right).

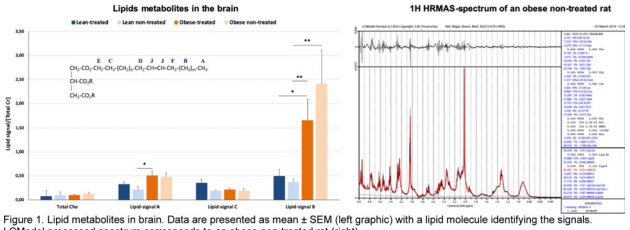

Figure 1. Lipid metabolites in brain. Data are presented as mean ± SEM (left graphic) with a lipid molecule identifying the signals. LCModel processed spectrum corresponds to an obese non-treated rat (right)

Some metabolites in liver (Lac, tCho, glc, ATP) presented significant differences between groups, recovering normal values in obese-treated rats (**Fig. 2**).

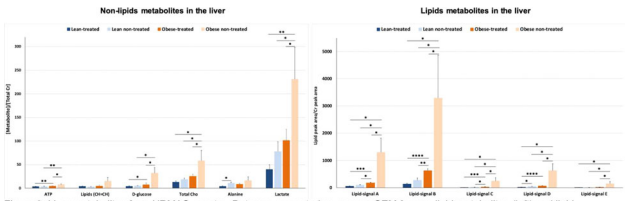

Figure 2. Liver metabolites from HRMAS spectra. Data are presented as mean ± SEM for non-lipid metabolites (left) and lipid metabolites (right).

These differences are clearly appreciated by comparing spectra from non-treated and treated obese animals (**Fig. 3**).

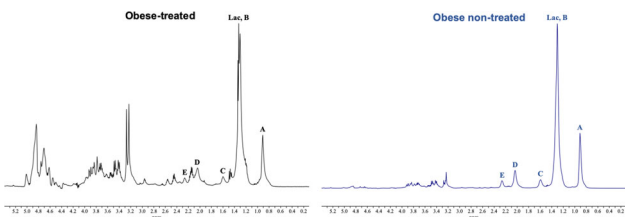

Figure 3. 1H HRMAS spectra from liver samples. An obese treated (left) and an obese non-treated rat, are presented as examples. Lipid content is clearly higher in the non-treated one.

The gain of body weight was similar in all animal groups, but in non-treated obese rats the increase of weight was significantly higher at the end of the experiment (data not shown). The glucose tolerance test showed a normal behaviour for lean-treated, lean non-treated and obese treated groups, while a typical glucose intolerant profile was observed in non-treated Zucker fa/fa (data not shown).
Discussion/Conclusion: After 4 weeks of $VO(dmpp)_2$ treatment, parameters such as gain of body weight and glucose tolerance, and some surrogate MRS indicators of insulin resistance, obesity and pre-diabetic state -measured from metabolic profile of different organs- were reverted in treated fatty Zucker rats. 1HRMAS is revealed as a powerful tool to assess the metabolic effects of this vanadium compound in different organs and thus to evaluate its efficacy as an anti-obesity drug.
References:
[1] Metelo et al. *J Inorg Biochem.* **2012**, 115:44–9

S23.07
Effect of trigger delay on human cardiac ^{31}P MR spectra at 7T

S. Wampl[1], T. Körner[1], M. Meyerspeer[1], E. Moser[1], S. Trattnig[2], A. I. Schmid[1]
[1]*Medical University of Vienna, Center for Medical Physics and Biomedical Engineering, Vienna, Austria,* [2]*Medical University of Vienna, Department of Biomedical Imaging and Image-guided Therapy, Vienna, Austria*

Purpose/Introduction: In western countries, cardiovascular diseases are among the leading causes of death. Magnetic resonance spectroscopy (MRS) is the only non-invasive tool to monitor pathological alterations of cardiac energy metabolism, in e.g. heart failure [1]. The heart is turning over ATP at a high rate, yet its metabolic activity and shape varies over the cardiac cycle. This has been shown to influence ^{31}P metabolite signals in animal studies [2, 3]. To further improve spectral quality and reproducibility, we investigate the effect of trigger delays on in vivo human cardiac ^{31}P spectra.
Subjects and Methods: 6 healthy volunteers were measured using a 7 T MR scanner (Siemens Healthineers, Germany) and a cardiac ^{31}P-^{1}H loop coil (Rapid, Germany). Acquisition-weighted ^{31}P chemical shift imaging (CSI) [7] data (8 × 16 × 8 matrix size, 220 × 220 × 200 mm^3 FoV, TR two heart beats, 12–15 min acquisition time) were acquired untriggered and five times using acoustic triggering (MRI Tools, Germany). The cardiac cycle was sampled equidistantly at 5 different time points (labelled 1–5), starting with end-systole. Heart phases were visually identified on cine short axis images reconstructed to 20 phases.

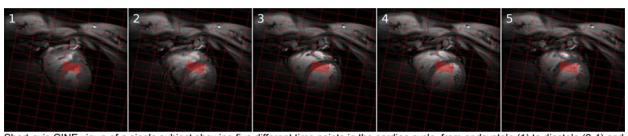

Short-axis CINE views of a single subject showing five different time points in the cardiac cycle, from endsystole (1) to diastole (2-4) and back to early systole (5). Grid of the 31P CSI acquisition and a representative voxal are drawn as overlay.

^{31}P spectra from the septum were post-processed using Matlab (Mathworks, USA) and the OXSA toolbox [8]. Peaks fitted included γ- and α-ATP, PCr and 2,3-DPG.

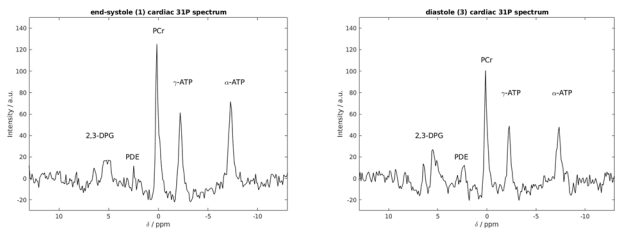

Cardiac 31P spectra from a single subject at phase 1 (end-systole, left) and phase 3 (diastole, right).

Results: Measured peak intensities of PCr and γ-ATP are highest end-systole (phase 1), with significant ($p < 0.05$) differences for all trigger delays compared to end-systole (trigger point 1), decreasing by 25% and 22% during diastole (trigger points 3–4), respectively. Consequently, PCr/γ-ATP ratios remain stable over the cardiac cycle while PCr/2,3-DPG and 2,3-DPG/gATP ratios during diastole differ significantly from phase1.

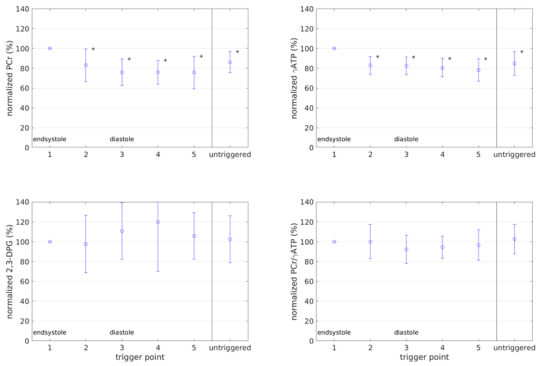

Normalized peak intensities of metabolites PCr, g-ATP and 2,3-DPG as well as PCr/γ-ATP ratio are shown with mean and standarc deviation of all voxels and subjects, and normalized to the phase 1 (end-systole). (* p<0.05)

Discussion/Conclusion: Our data show that it matters to SNR and metabolite ratios at which point in the cardiac cycle data are acquired. End-systole seems to be a favourable time since PCr is maximal and DPG minimal. This probably is due to a higher fraction of myocardium signal compared to blood within the voxel.

Our evaluations show the importance of proper localization and dedicated triggering for data quality and reproducibility. Future work will be invested to disentangle the effect of genuinely varying metabolite concentrations from partial volume effects.

This project was supported by the Austrian Science Fund (FWF) project P28867-B30.

References:

[1] Neubauer S., NEJM 2007. http://doi.org/10.1056/NEJMra063052

[2] Fossel E. T., et al., PNAS 1980. http://doi.org/10.1073/pnas.77.6.3654

[3] Illing B., et al., MRM 2007. http://doi.org/10.1002/mrm.1910400513

[4] Robson M. D., et al., MRM 2005. http://doi.wiley.com/10.1002/mrm.20344

[5] Purvis L. A. B. et al., PLOS ONE 2017. http://doi.org/10.1371/journal.pone.0185356

S23.08

Water and lipid T_2 are associated with hepatic lipid content

P. Veeraiah[1], K. H. M. Roumans[2], M. C. G. J. Brouwers[3], M. K. C. Hesselink[2], J. E. Wildberger[4], P. Schrauwen[2], L. Lindeboom[1], V. B. Schrauwen-Hinderling[1]

[1]*Departments of Radiology and Nuclear Medicine, Nutrition and Movement Sciences, NUTRIM School for Nutrition and Translational Research in Metabolism, Maastricht University Medical Center, Maastricht, The Netherlands,* [2]*Nutrition and Movement Sciences, NUTRIM School for Nutrition and Translational Research in Metabolism, Maastricht University Medical Center, Maastricht, The Netherlands,* [3]*Internal medicine, NUTRIM School for Nutrition and Translational Research in Metabolism, Maastricht University Medical Center, Maastricht, The Netherlands,* [4]*Department of Radiology and Nuclear Medicine, NUTRIM School for Nutrition and Translational Research in Metabolism, Maastricht University Medical Center, Maastricht, The Netherlands*

Purpose/Introduction: ^{1}H-MRS is extensively used to measure hepatic lipid content by using relative signal intensities of lipid and water[1, 2]. Usually, a fatty liver is defined as > 5.56% lipid content as measured by ^{1}H-MRS[2]. The absolute estimation of hepatic lipid content requires accurate T_2 correction for both water and lipid signals. Conventionally, we assume constant T_2 decay for both water and lipid among individuals; therefore fixed T_2 relaxation times are used. However, T_2 values reported in literature for 3T vary widely[3, 4], which might be due to small number of subjects involved and/or other methodological discrepancies (e.g. fed vs fasted). Therefore, we here aimed to determine the T_2 relaxation times of water and lipid in the fasted state at 3T in a group of subjects with a wide range of hepatic lipid content and to evaluate whether there is a dependence of the T_2 relaxation times and hepatic lipid content.

Subjects and Methods: A total of 60 subjects (30 male), age between 19 and 72 years and BMI between 20 and 38 kg/m^2, were included. Hepatic ^{1}H-MR spectra were acquired in overnight fasted condition on a 3T MR system(Philips Achieva 3T-X) using a 32-channel sense cardiac coil with a series of 6 TEs (32.5, 45, 50, 60, 70 and 80 ms) without water suppression using PRESS (TR = 4000 ms, NSA = 16, Voxel = 8 cm^3). All spectra were post-processed and fitted with a home-written MATLAB script (Fig 1). The T_2 of water and lipid-CH_2 resonance was determined by assuming a mono-exponential decay. The hepatic lipid content was calculated from the uncorrected peak areas of CH_2 and water from the post-processed spectra acquired at TE = 32.5 ms.

Results:

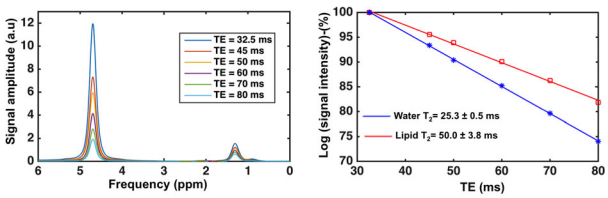

Figure 1: In vivo hepatic lipid spectra acquired with 6 different TEs (left); logarithmic plot of signal intensity over different TEs with calculated T2 decay for water and lipid peak (right).

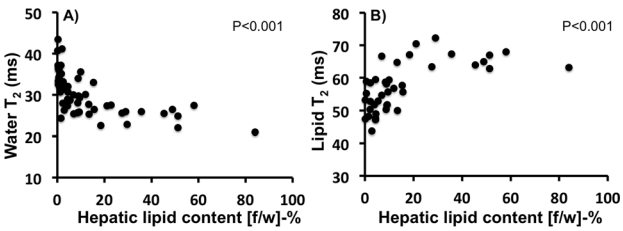

Figure 2: Scatter plot showing the uncorrected hepatic lipid (%) and its relationship with measured water-T2 relaxation times (A, n=60) and with lipid-CH2 T2 relaxation times (B, n=40).

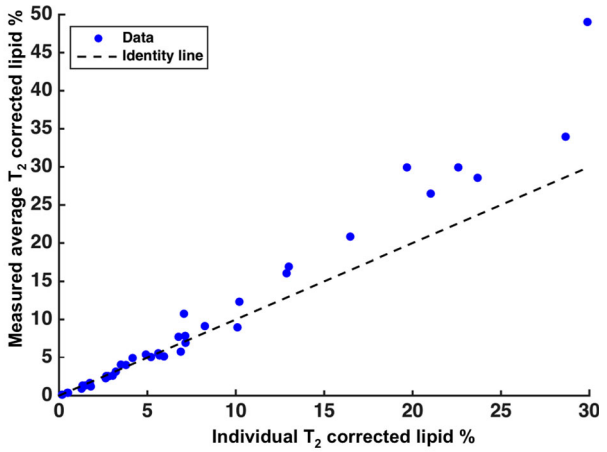

Figure 3: Scatter plot showing the hepatic lipid (%) calculated with individual T2 correction versus fixed value (measured average) T2 correction (n=40).

The average T_2 of water and lipid-CH_2 was found to be 31 ± 5 ms and 57 ± 7 ms respectively. There was a significant negative correlation ($P < 0.001$; Pearson correlation = − 0.63) between water T_2 and hepatic lipid content and a positive correlation between lipid-CH_2 T_2 ($P < 0.001$; Pearson correlation = 0.63) and hepatic lipid content (Fig 2). Our data suggest that for absolute quantification of hepatic lipid content, correction with a fixed T_2 relaxation time for all subjects leads to a small error (average CV = 13 ± 9%); an underestimation in low lipid content and a (marked) overestimation in subject with high lipid content (Fig 3).

Discussion/Conclusion: Thus, water and lipid-CH_2 T_2 vary among individuals. The individual variability in T_2 relaxation times is associated with hepatic lipid content. Therefore, individual T_2 measurements would be the best choice for accurate quantification of fatty liver or alternatively, different T_2 correction factors should be applied in different groups (i.e. depending on steatosis level).

References:

1. Thomsen C et al. *(1994); 2. Szczepaniak L.S* et al. *(2005); 3. Gambarota G* et al. *(2011); 4. Guiu B* et al. *(2009)*

S23.09

Non-invasive measurement of lactate concentration in whole human breast tumours using advanced magnetic resonance spectroscopy (MRS)

S. M. Cheung[1], E. Husain[2], Y. Masannat[3], I. D. Miller[2], K. Wahle[4], S. D. Heys[3], J. He[1]

[1]University of Aberdeen, Aberdeen, UK, [2]Aberdeen Royal Infirmary, Pathology Department, Aberdeen, UK, [3]Aberdeen Royal Infirmary, Breast Unit, Aberdeen, UK, [4]University of Strathclyde, Strathclyde Institute of Pharmacy and Biological Sciences, Glasgow, UK

Purpose/Introduction: Breast cancer is the most common female malignancy in the UK, with 1 in 8 women diagnosed in their lifetime (1). The inadequacy in early markers for treatment response is a barrier to further improving patient care. Aerobic glycolysis (AG) is the central metabolic feature of tumour leading to elevated lactate production (2). Although lactate production can be assessed through lactate dehydrogenase A (LDH-A) in immunostaining (3), the method has to be performed on excised tissue or biopsy samples. To avoid partial sampling errors of biopsy measurement in heterogeneous tumours, a non-invasive method sensitive to the lactate concentration of the whole breast tumour is a desirable clinical tool for assessing AG. Double quantum filtered (DQF) magnetic resonance spectroscopy (MRS) (4), a specialist method recently translated into clinical research, allows measurements specific to lactate. We hypothesised that lactate concentration from DQF MRS can be a prognostic marker for breast tumours.

Subjects and Methods: Thirty female patients (age 39–78 years, 15 grade II and 15 grade III) with invasive ductal carcinoma undergoing wide local excision or mastectomy were enrolled in the study (Table 1). Freshly excised whole breast tumours were scanned on a 3T whole body clinical MRI scanner (Achieva TX, Philips Healthcare, Best, The Netherlands) using body coil for uniform transmission and a 32-channel coil for high sensitivity detection. Lactate spectrum was acquired from a single voxel snug-fit to the tumour using single voxel DQF PRESS sequence (4), with TR/TE of 1.25 s/144 ms, spectral editing frequency at 4.1 ppm and 512 averages. All spectra were quantified using AMARES algorithm (5) in the jMRUI software (v5.0, TRANSACT, Leuven, Belgium) (6). Nottingham Prognostic Index (NPI), LDH-A and Ki-67 were assessed histologically.

Parameters	All (n=30)	Grade II (n=15)	Grade III (n=15)	*p*-value
Age	61.1 ± 11.5	61.0 ± 12.0	61.2 ± 11.3	0.9628
Body Mass Index (BMI)	30.4 ± 6.4	30.4 ± 6.6	30.3 ± 6.6	0.9771
Tumour Size (cm)	2.5 ± 0.8	2.4 ± 0.9	2.5 ± 0.7	0.7650
Nottingham Prognostic Index (NPI)	4.41 (3.62 – 4.56)	3.62 (3.46 – 4.29)	4.50 (4.44 – 5.44)	<0.0001*
Tumour Type				
Invasive Ductal Carcinoma, No Special Type (IDC, NST)	30	15	15	-
Oestrogen Receptor (ER+)	22	13	9	-
Human Epidermal growth factor Receptor 2 (HER2+)	6	2	4	-
Triple-Negative Breast Cancer (TNBC)	7	1	6	-

Table 1. Patient demography – Tumour grade study. Patient demography and routine clinical histopathological findings of excised breast tumours are shown for each group and the entire cohort. Significant findings are marked by '*'.

Results: There was a significantly higher lactate concentration ($p = 0.0349$) in grade III (7.7 ± 2.9 mM) than in grade II (5.5 ± 2.4 mM) (Fig 1). There was a significant difference in LDH-A ($p = 0.0231$) and Ki-67 ($p = 0.0002$) expression between grade II and grade III. Lactate concentration was correlated with NPI ($rho = 0.3618$, $p = 0.0495$), but not with LDH-A, Ki-67 or tumour size (Fig 2).

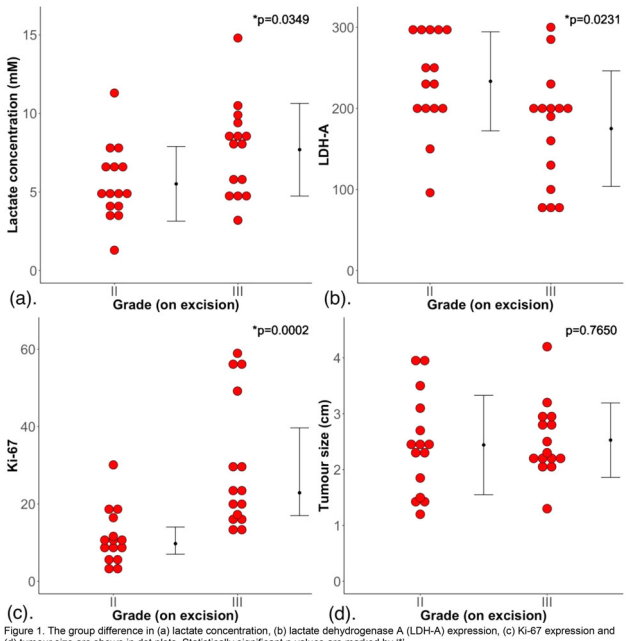

Figure 1. The group difference in (a) lactate concentration, (b) lactate dehydrogenase A (LDH-A) expression, (c) Ki-67 expression and (d) tumour size are shown in dot plots. Statistically significant p values are marked by '*'.

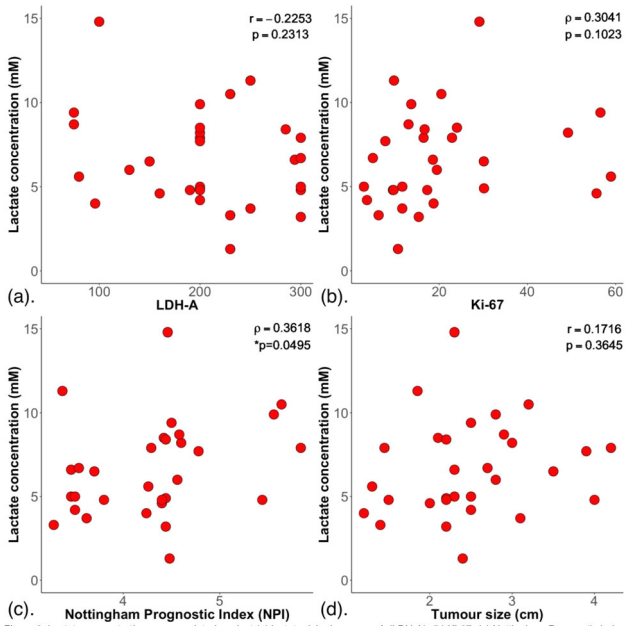

Figure 2. Lactate concentration was correlated against (a) lactate dehydrogenase A (LDH-A), (b) Ki-67, (c) Nottingham Prognostic Index (NPI) and (d) tumour size within the entire cohort. Statistically significant p values are marked by '*'.

Discussion/Conclusion: Our results showed that lactate concentration from DQF MRS is increased in high grade breast tumours and is associated with prognostic markers, in turn holds a prominent role in disease progression and providing the foundation for a clinical prognostic tool sensitive to AG.

References:

1. Cancer Research UK. *Breast cancer statistics*. London; 2019.
2. Vander Heiden MG, et al. *Science*, 2009 May 22;324(5930): 1029–33.
3. Semenza GL, et al. *J Biol Chem*, 1996 Dec 20;271(51): 32529–37.
4. He QH, et al. *JMR Series B*, 1995;106(3): 203–11.
5. Vanhamme L, et al. *JMR*, 1997;129(1): 35–43.
6. Naressi A, et al. *Comput Biol Med*, 2001;31(4): 269–86.

S24 Scientific Session

15:40–17:10 *Room 4 - Plate & Van der Vorm Zaal*

Perfusion Imaging: Contrast Agent Methods

S24.02

An extracorporeal circulation mouse model for simultaneous measurements of arterial input functions for dynamic contrast-enhanced MRI and PET

P. Backhaus[1], F. Büther[1], L. Wachsmuth[2], L. Frohwein[3], K. Schäfers[3], S. Hermann[3], M. Schäfers[1], C. Faber[2]
[1]University Clinic Münster, Department of Nuclear Medicine, Münster, Germany, [2]University of Münster, Translational Research Imaging Center—TRIC, Münster, Germany, [3]University of Münster, European Institute for Molecular imaging—EIMI, Münster, Germany

Purpose/Introduction: Quantification of the arterial input function (AIF) in small animals is challenging in both dynamic contrast-enhanced (DCE)-MRI and in radiotracer studies. Only few examples of direct AIF-measurements of MR contrast agent (CA) in mice are published in the literature[1–3]. Its precise measurement however is crucial for quantitative kinetic modeling and consequently for MRI quantification of blood flow, blood volume and permeability as well as PET quantification of radiotracer binding potentials. We developed a novel extracorporeal circulation mouse model for DCE-MRI and PET radiotracer measurements of the AIF in mice.

Subjects and Methods: Mice received an extracorporeal shunt from the femoral artery to the tail vein. A MRI-compatible measuring chamber for a β-Microprobe (biospace lab) was included in the circulation. The extracorporeal line featured two reservoirs (R1 & R2) which resided in the MRI field of view.

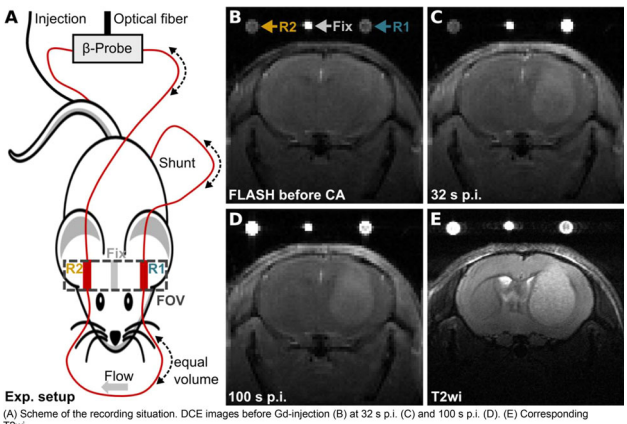

(A) Scheme of the recording situation. DCE images before Gd-injection (B) at 32 s p.i. (C) and 100 s p.i. (D). (E) Corresponding T2wi.

MRI scanning was conducted using a 9.4 T MRI (Bruker BioSpec) and a cryo-cooled surface coil. DCE of the head was performed for 15 min using a 3D FLASH with a matrix 80 × 80 × 8, spatial resolution 0.175 × 0.175 × 1 mm and a temporal resolution of 4.015 s.

Results: The calculated AIFs of 11 consecutively recorded, representative mice show typical AIF curve shapes.

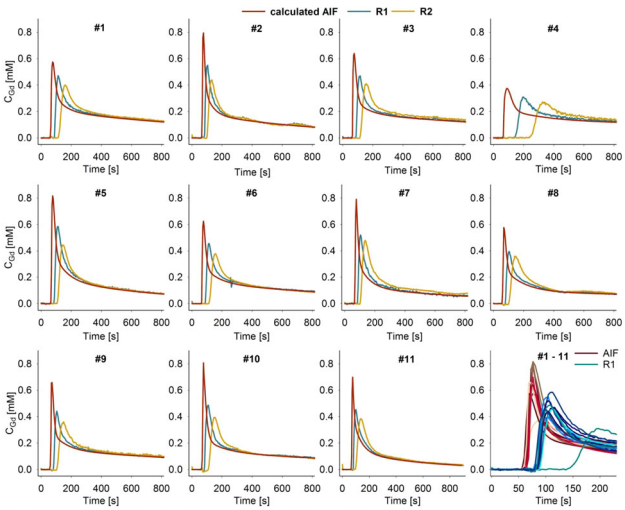

Dynamic CA blood concentrations from 11 consecutively recorded, representative animals. AIFs were calculated by monoexponential deconvolution of reservoir 1 (R1) based on the recorded distinct dispersion effect between the two reservoirs.

10 of 11 mice show a close range of peak concentrations (mean 0.7, range 0.58–0.82 mM) and shunt flow velocities (mean 46.7, range 35–61 µl/min). PET radiotracer input functions could be recorded simultaneously. Mass spectrometry analysis of mouse blood withdrawn right after DCE and calibration measurements with circulated (human) blood at defined C_{Gd} and flow velocities demonstrated quantitative robustness of the method. Yet influence on quantification of shunt flow velocity and chosen approach of signal-to-concentration conversion was noted.

Discussion/Conclusion: We provide a novel method with high potential for quantitative robust recordings of DCE-MRI AIFs in mice. Moreover, we present (to our knowledge) the first simultaneous recordings of AIFs of MRI CA and a PET radiotracer in mice. This supports evaluation approaches to deduce the CA/PET tracer AIF from one another. Further, it might provide the basis for simultaneous and integrated modeling of PET tracer and CA kinetics in mice, which is of high interest in integrated, simultaneous small animal PET/MRI.

References:

[1]Loveless et al. A quantitative comparison of the influence of individual versus population-derived vascular input functions on dynamic contrast enhanced-MRI in small animals. Magn Reson Med. 2012;67:226–236.
[2]Moroz et al. Rapid measurement of arterial input function in mouse tail from projection phases. Magn Reson Med. 2014;71:238–245.
[3]Zhang et al. Rapid dynamic contrast-enhanced MRI for small animals at 7T using 3D ultra-short echo time and golden-angle radial sparse parallel MRI. Magn. Reson. Med. 2018:140–152

S24.03

Advanced pharmacokinetic modeling in small-animal compressed-sensing DCE-MRI

R. Jiřík[1], M. Mangová[2], P. Rajmic[2], O. Macíček[1], K. Souček[3], Z. Starčuk, jr.[1]
[1]Institute of Scientific Instruments, Czech Academy of Sciences, Brno, Czech Republic, [2]Brno University of Technology, Department of Telecomunications, Brno, Czech Republic, [3]Institute of Biophysics of the Czech Academy of Sciences, Department of Cytokinetics, Brno, Czech Republic

Purpose/Introduction: To overcome the physical limits of the achievable spatial and temporal resolution in Dynamic Contrast-Enhanced (DCE) MRI, compressed-sensing (CS) techniques have been proposed [1]. So far, CS has been combined only with simpler pharmacokinetic (PK) models (e.g. generalized kinetic model [2]), which do not provide estimates of blood flow, Fb, and permeability-surface area product, PS. To the authors' knowledge, no CS DCE has been shown for advanced PK models, i.e. models providing also estimates of Fb and PS. This is probably because the requirements of these models on temporal resolution and the signal-to-noise ratio (SNR) are much higher than for simple PK models.

We use an advanced PK model (adiabatic approximation of the tissue homogeneity model—ATH) in combination with CS, based on a 3D radial golden-angle (GA) stack-of-stars (SOS) acquisition [3] and the L + S reconstruction [4].

Subjects and Methods: The MiaPaCa-2 pancreatic tumor cells were subcutaneously implanted in the right flank of 7 SHO mice (approved by the National Animal Research Authority). The MRI protocol (9.4T Bruker) included 2 DCE reference scans using 2D GA spoiled gradient echo, one with GadoSpin P (Miltenyi Biotec, Germany) and one with Magnevist (Bayer HealthCare Pharmaceuticals, Germany), TR/TE = 15/1.5 ms, FA = 20°. Then, the 3D GA SOS DCE scan [4] (TR/TE = 5.5/1.4 ms, FA = 15°, 25 slices) with Magnevist was acquired. The delay between the contrat-agent administrations was 45 min.

The 2D data were reconstructed using plain nonuniform fast Fourier transform (NUFFT). The 3D data were reconstructed using NUFFT and also using a decomposition model where the signal is assumed to be a sum of a low-rank component and a component with a constrained magnitude of differences in time [5]. The reconstructed image sequences were fitted with the ATH model.

Results: Image reconstruction of the 3D DCE data using CS led to clearly better spatial consistence than NUFFT (Fig. 1, row 1), giving tissue curves with suppressed noise (Fig. 1, row 2) and PK parameters clearly more consistent with the reference 2D DCE (Fig. 1. rows 3–6, Fig. 2, Table 1).

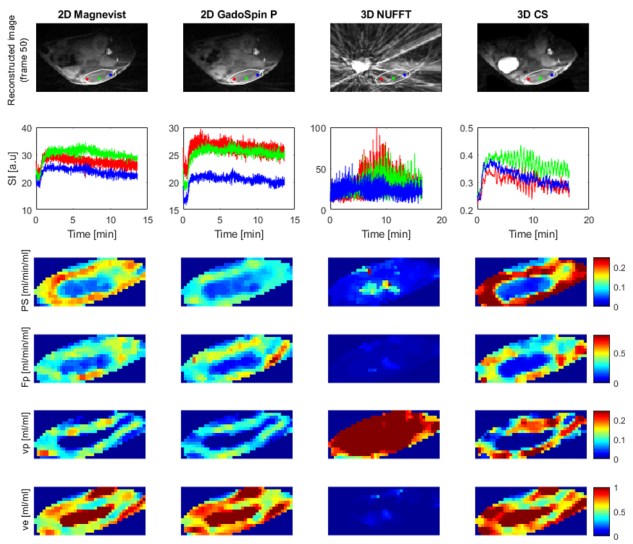

Fig.1. Results for mouse 7, reference 2D DCE with Magnevist and GadoSpin P (columns 1, 2) and the corresponding slice of 3D NUFFT and 3D CS (columns 3, 4). Reconstructed image sequences (row 1), example perfusion curves (row 2), and perfusion maps.

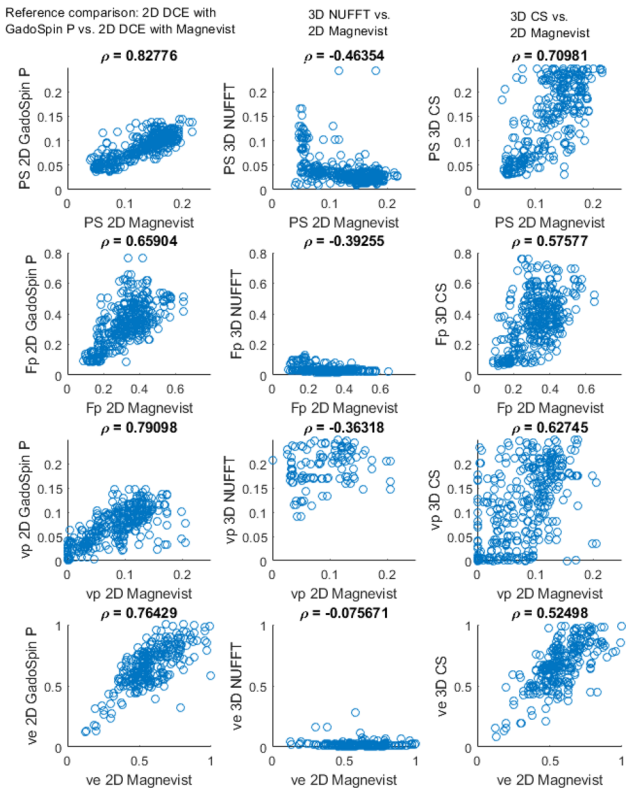

Fig.2. Example scatter plots, mouse 7. 3D NUFFT reconstruction leads to PK parameters inconsistent with the reference 2D DCE, while 3D CS reconstruction from the same 3D DCE data leads to a good match with the 2D reference.

PK parameter	PS	PS	PS	Fp	Fp	Fp	vp	vp	vp
DCE dataset	2D GadoSpin P	3D NUFFT	3D CS	2D GadoSpin P	3D NUFFT	3D CS	2D GadoSpin P	3D NUFFT	3D CS
mouse 1	0.83	0.22	0.66	0.60	0.18	0.57	0.55	0.27	0.49
mouse 2	0.88	0.41	0.78	0.34	0.16	0.26	0.89	0.56	0.58
mouse 3	0.79	-0.20	0.68	0.01	-0.14	0.28	0.79	0.32	0.75
mouse 4	0.78	0.16	0.54	0.74	-0.05	0.61	0.37	0.07	0.50
mouse 5	0.76	0.66	0.69	0.53	0.27	0.49	0.88	0.79	0.81
mouse 6	0.84	0.56	0.74	0.33	0.08	0.44	0.85	0.53	0.76
mouse 7	0.83	-0.46	0.71	0.66	-0.39	0.58	0.79	-0.36	0.63

Tab.1. Correlation coefficients of voxel-based PK parameters in the tumor region. Reference 2D Magnevist DCE versus 2D GadoSpin P DCE (shows achievable corr. coeffs. in the fully sampled 2D case), 3D NUFFT and 3D CS (in the same slice as the 2D DCE).

Discussion/Conclusion: Our results show that advanced PK modeling using 3D CS is feasible. The corr. coeffs. of 3D CS vs. 2D NUFFT are only slightly lower than the reference comparison of the 2D NUFFT methods using two different contrast agents. Hence, advanced PK modeling in DCE can be used also in a full 3D setup, providing full coverage of the tumor and estimates of Fb and PS.

Acknowledgement: Supported by GACR (GA16-13830S), AZV (16-30299A) MEYS (CZ.02.1.01/0.0/0.0/16 013/0001775, LO1401), SIX Center, NVIDIA Corp. (donation of GPU).

References:

[1] LUSTIG, M. et al. IEEE SIGNAL PROC MAG, 2008, 25(2), 72–82
[2] WINKEL, D. et al. RADIOLOGY, 2019, 290(3), 702–8
[3] FENG, L. et al. MRM, 2014, 72(3), 707–717

[4] OTAZO, R. et al. MRM, 2015, 73(3), 1125–1136
[5] MANGOVÁ, M. Brno Univ. of Technology, 2018, PhD Thesis

S24.04

Comparison of fitting approaches in dynamic contrast-enhanced magnetic resonance imaging: direct estimation from raw k-space signals vs. conventional approach from concentration–time curves

M. Bartoš[1], O. Maier[2], R. Stollberger[2], R. Jiřík[3]
[1]*Institute of Information Theory and Automation of the Czech Academy of Science, Prague, Czech Republic,* [2]*Institute of Medical Engineering, Technical University Graz, Graz, Austria,* [3]*Institute of Scientific Instruments of the Czech Academy of Science, Brno, Czech Republic*

Purpose/Introduction: DCE-MRI provides information about tissue perfusion and capillary permeability. It is based on T1-weighted image acquisition before, during, and after an intravenous administration of a contrast agent [1].
Conventionally, image sequences are first reconstructed from the k-space data, followed by conversion to contrast-agent concentration [1]. The quantitative perfusion-parameter maps are then obtained by fitting a pharmacokinetic (PK) model to the measured data, which relates the PK parameters to concentration–time curves. Recently, a direct estimation scheme has been presented employing a full compound model including the preprocessing [2]. Alternatively, an intermediate model working with the reconstructed images can be formed. We have extended the approaches using a more realistic PK model and a state-of-the-art spatial regularization and compared them.
Subjects and Methods: Estimation of PK parameters is a least-mean-squares minimization problem: $\mathbf{p} = \arg\min_{\mathbf{p}} \|f(\mathbf{p})-\mathbf{y}\|^2 + R(\mathbf{p})$, where $\mathbf{p}$ are the PK parameter maps, $\mathbf{y}$ is the measured data, $f(\mathbf{p})$ is the model and $R(\mathbf{p})$ is a spatial regularizer. We solve this non-linear non-differentiable problem using the recently proposed Gauss–Newton approach with the primal–dual algorithm [3]. Table 1 defines the data and gives an overview of the three fitting approaches we used in this work.

Approach	Conventional	T1w	Direct
Data to fit, y	Concentration images	T1-weighted images	K-space samples
Model, f(p)	PK model	PK model + SPGR model	PK model + SPGR model + Coil sensitivities + K-space sampling
Additional preprocessing steps	Image reconstruction Conversion to concentration	Image reconstruction	Estimation of coil profiles
Noise in data	Non-Gaussian with spatial-dependent variance	Rician (close to Gaussian) with constant variance	Gaussian with constant variance
Pros	Voxel-wise computation The simplest model The fastest computation Estimation in ROI	Voxel-wise computation Noise characteristic Estimation in ROI	Complete information Noise characteristic No image reconstruction
Cons	Image reconstruction needed Conversion needed Noise characteristic Strongly nonlinear Potentially accumulated errors	Image reconstruction needed	Computationally demanding No arterial voxel available for AIF Coil profiles needed

Table 1: Overview of the fitting approaches

The comparison was performed on a numerical rat phantom (41 tissue regions with experiment- and literature-based PK parameters) simulating DCE-MRI using the PK tissue homogeneity model [4] combined with an SPGR sequence under realistic noise conditions. The T1-weighted images were reconstructed from the 4 channels using the sum-of-squared reconstruction. Coil profile, SNR and sequence parameters are given in Fig. 1.

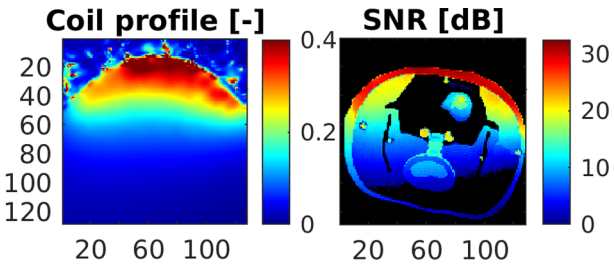

Figure 1: Coil profile of 4-channel rat head surface coil used with simulated SPGR sequence and SNR of the phantom. Simulation parameters: 1mm slice, TR/TE 8/2.1 ms, FA 17°, acquisition matrix 128×128, temporal resolution 0.8 s, scan time ~13 min.

Results: The approaches are compared in Fig. 2 together with their spatial-regularized variants. The regularization always improved the readability of the estimated maps. The conventional approach led to the worst result. The T1w and direct approaches appeared to be equal, however the non-regularized direct approach had values closer to the ground truth.

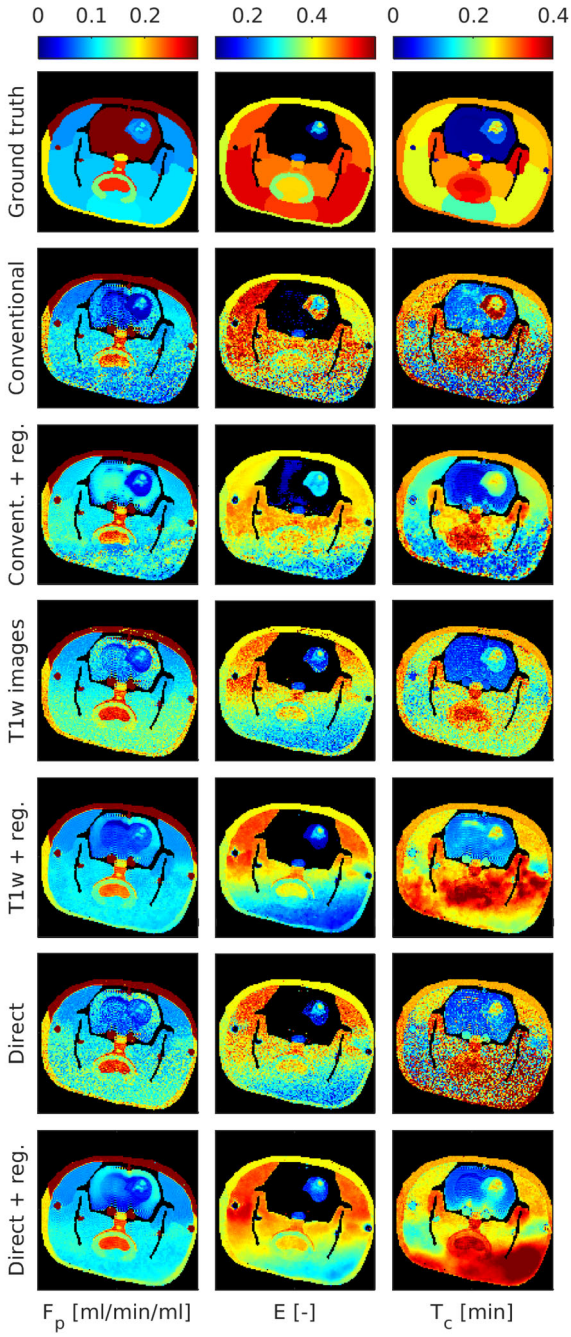

Figure 2: Comparison of the DCE-MRI fitting approaches (defined in Table 1) with and without spatial regularization. Only three out of five perfusion-parameter maps are shown.

Discussion/Conclusion: Based on the pros and cons listed in Table 1 and the comparison experiment (Fig. 2), the best approach, in our configuration, is to fit T1-weighted images. This yields results close to ground truth with tractable complexity. The conventional approach had convergence issues, even in case of regularization. The state-of-the art approach of the direct fitting is tractable, but in case of a full Cartesian sampling, it seems excessive.

References:

[1] Jackson A, et al. (2005) DCE-MRI in Oncology. Springer
[2] Guo Y (2017). Magn Reson Med 78:1566–1578
[3] Maier O (2019). Magn Reson Med 81:2072–2089
[4] Garpebring A (2009). IEEE Trans Med Imaging 28:1375–83

S24.05

Rapid cardiac MR myocardial perfusion quantification using machine learning trained with synthetically generated sample data

T. Hoh, J. von Spiczak, T. Joyce, R. Lingwood, H. Dillinger, S. Kozerke
University and ETH Zurich, Institute for Biomedical Engineering, Zurich, Switzerland

Purpose/Introduction: While myocardial hypoperfusion is routinely diagnosed by visual assessment of dynamic contrast-enhanced (DCE) cardiac MRI, exact quantification of perfusion parameters (MBF = myocardial blood flow, PS = permeability surface area product, Vp = plasma volume, Ve = extracellular volume) is desirable. The blood tissue exchange model (BTEX)[1] applied in recent studies[2] offers detailed modelling, but its complexity increases computational costs and vulnerability to noise when applying conventional fitting. Our study sought to predict perfusion parameters fast and accurately using a convolutional neural network (CNN) trained with synthetically generated sample data.

Subjects and Methods: Perfusion standard parameters[3] (**Fig. 1a**) and an arterial input function (AIF) averaged from 6 healthy volunteers were used as input for the pharmacokinetic BTEX model (**1b**) extending the cardiac MRXCAT[4] phantom framework (**1c**). Resulting DCE images (**1d**) mimicked spoiled saturation recovery GE acquisition in breath-hold with a Gd dose of 0.05 mmol/kg bodyweight.

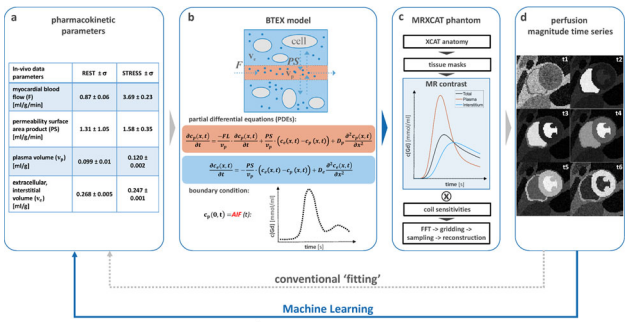

Figure 1: End-to-end perfusion mapping. a) Parameters[3] inserted into blood tissue exchange model (BTEX). b) Arterial Input Function (AIF) is required. c) Total change of concentrations defines contrast in the phantom. d) Image time series.

5000 datasets at random myocardial positions were simulated and Gaussian noise was added to model contrast-to-noise, then tested on levels (CNR = 10/15/30/100, **Fig. 2a**). Simulation data was split in test, validation, and training sets (**2b**). A 1D CNN consisting of 8 convolutional, 4 pooling, and 2 densely connected layers (**2c**) was implemented and trained using training and validation data (activation = Relu, loss function metric = MAE, optimizer = first-oder gradient based Adam, epochs = 1000, batch size = 32). For comparison, conventional least squares fitting (FIT) of the BTEX model was implemented—being dependent on simulated AIFs for finding the best-matching perfusion parameter estimates (**2d**). A pre-computed lookup-table and later refinement via L2 norm grid search were applied for computational efficiency. CNN and FIT were compared to the known ground truth as absolute difference.

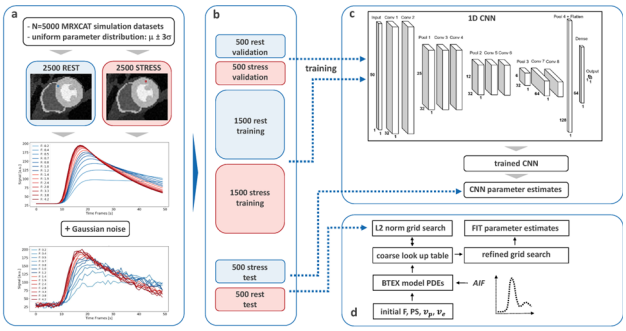

Figure 2: Data generation and evaluation. a) Initialization of MRXCAT perfusion simulations and data pre-processing. b) Choice of datasets. c) Architecture of 1D CNN. d) Iterative L2 norm fitting procedure with a coarse/fine grid search approach.

Results: Estimated perfusion parameters under rest and stress conditions are plotted in Fig. 3. Average relative error of CNN versus FIT was under rest: 0.1 vs 0.6%, 0.2 vs 0.4%, 11.1 vs 31.6%, and 7.0 vs 22.4% (for MBF, PS, Vp, and Ve, respectively) and under stress: 0.1 vs 0.4%, 0.1 vs 0.2%, 8.8 vs 18.3%, and 6.7 vs 16.0% (ditto). CNN was computationally faster than FIT by two orders of magnitude.

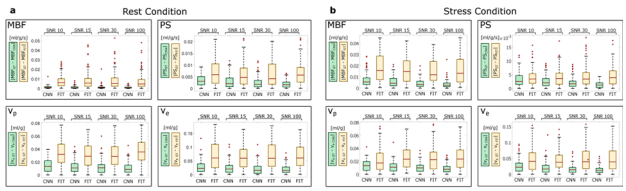

Figure 3: Estimated perfusion parameters under rest (a) and stress conditions (b). Abbreviations: MBF = myocardial blood flow, PS = permeability surface area product, Vp = plasma volume, Ve = extracellular volume.

Discussion/Conclusion: CNN based estimation of quantitative perfusion parameters proved more efficient and robust than conventional least squares fitting. The need for large numbers of training data could be solved by using numerically simulated myocardial perfusion data. Moreover, CNN based perfusion quantification rendered additional AIF acquisition unnecessary.

References:

[1]Bassingthwaighte, Circ Res, 1989 Oct;65(4):997–1020
[2]Kellman, J Cardiov Magn Reson, 2017 Apr 7;19(1):43
[3]Xue, SCMR workshop, 2018 ("Other parameters in perfusion modelling")
[4]Wissmann, J Cardiov Magn Reson, 2014 Aug 20;16:63

S24.06

Comparison of perfusion markers in the ex vivo perfused porcine kidney: hyperpolarized [1-^{13}C]pyruvate versus gold standard ^{1}H DCE MRI

C. Mariager[1], E. Hansen[1], S. Beck[1], A. Munk[2], M. Lyhne[2], K. Søberg[3], P. Nielsen[3], S. Ringgaard[1], C. Laustsen[1]
[1]*Aarhus University, Department of Clinical Medicine, The MR Research Centre, Aarhus, Denmark,* [2]*Aarhus University, Department of Clinical Medicine, Aarhus, Denmark,* [3]*Aarhus University, Department of Anesthesia and Intensive Care, Aarhus, Denmark*

Purpose/Introduction: Normothermic machine-perfusion is an emerging method for donor organ care and therapy [1]. Hyperpolarized ^{13}C-pyruvate MRI is an emerging non-invasive means of probing the metabolic state of these organs [2]. Here we investigate the possibility to extract perfusion estimates from dynamic hyperpolarized ^{13}C-pyruvate data, in addition to metabolic information. This is done by comparing ^{13}C-pyruvate perfusion to gold standard ^{1}H DCE perfusion using gadolinium, in the ex vivo kidney.

Subjects and Methods: Five kidneys (131 ± 4 g) from female pigs were connected to a perfusion system, see Fig. 1. Perfusion was performed using oxygenated blood at 37 °C, using a flow of 170 mL/min. Glucose, amino acids and insulin was infused to keep blood gas parameters in the physiological range [3]. The MRI protocol was performed using a 3.0 T Signa HDx MRI scanner. Intra-renal anatomy was assessed using ^{1}H T_1 weighted FLAIR. ^{13}C imaging was performed following a 9 mL injection of hyperpolarized [1-^{13}C]pyruvate, using a SPSP imaging sequence with 1 s temporal resolution. ^{1}H DCE was acquired following an injection of 0.3 mL Dotarem, using a 3D fast gradient echo sequence with 1.87 s temporal resolution. Perfusion analysis was performed with a model-free deconvolution approach, using a ROI covering the renal cortex. ^{13}C derived perfusion estimates were corrected for T_1 decay, using T_1 = 42 s.

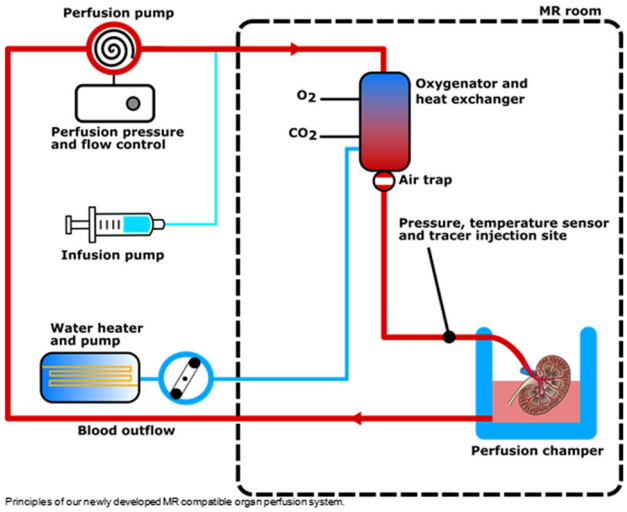

Principles of our newly developed MR compatible organ perfusion system.

Principles of our newly developed MR compatible organ perfusion system.

Results: Ex-vivo renal perfusion with accurate control of physiological parameters was achieved and verified with ^{1}H MRI and [1-^{13}C]pyruvate MRI, see Fig. 2. Results show a linear correlation (slope = 0.77, R^2 = 0.97, p = 0.0025) between DCE and ^{13}C-pyruvate derived cortical perfusion (mean of 554 ± 238 and 376 ± 187 mL/100 mL/min, respectively), see Fig. 3.

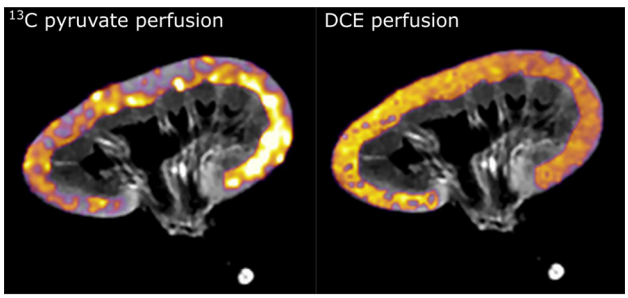

Calculated cortical perfusion maps in the renal cortex for 13C-pyruvate and DCE MRI, overlaid on a T1 weighted anatomical image.

Calculated cortical perfusion maps in the renal cortex for 13C-pyruvate and DCE MRI, overlaid on a T1 weighted anatomical image.

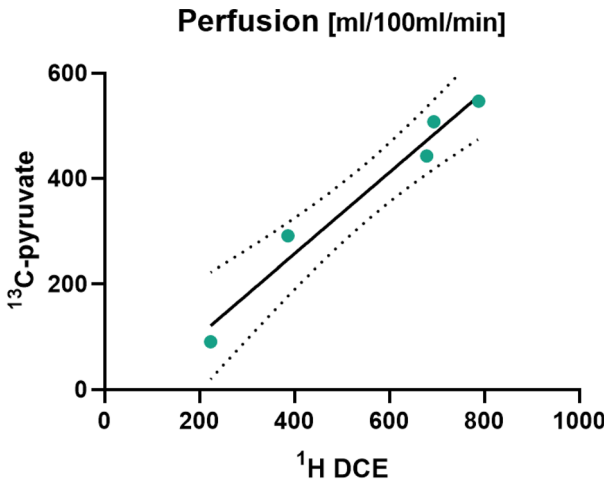

Mean 13C-pyruvate perfusion values versus 1H DCE perfusion values extracted from five ex-vivo perfused porcine kidneys.

Discussion/Conclusion: This study displays a clear linear correlation between ^{13}C-pyruvate perfusion and gold standard ^{1}H DCE perfusion, with a consistently lower perfusion value estimated for ^{13}C-pyruvate. Accureta perfusion measures are important to hyperpolarized metabolic imaging in order to correct for variations in tracer delivery to different tissues. Hence, the ability to extract both metabolic and perfusion information from the same experiment is very useful. However, ^{13}C-pyruvate perfusion is somewhat limited by the metabolic turnover of the tracer. This can be alleviated by accounting for the metabolic turnover rate or by utilizing co-polarized ^{13}C-urea for the perfusion estimation, since urea is not metabolized.

References:

[1] S. Hosgood et al., "*Successful Transplantation of Human Kidneys Deemed Untransplantable but Resuscitated by Ex Vivo Normothermic Machine Perfusion,"* Am J Transplant 2016.

[2] M. Lauritzen et al., "*Imaging Regional Metabolic Changes in the Ischemic Rat Heart In Vivo Using Hyperpolarized [1–13 C]Pyruvate*," Tomography 2017.

[3] J. M. Kaths et al., "Normothermic Ex Vivo Kidney Perfusion for the Preservation of Kidney Grafts prior to Transplantation," JoVE *20*15.

S24.07

Quantitative and spatial agreement of simultaneously acquired quantitative MRI DCE blood volume measurements and 18F-FET PET/MRI in patients with suspected recurrent high-grade gliomas

O. Henriksen[1], A. Muhic[2], M. Lundemann[2], H. Larsson[3], A. Hansen[3], V. Larsen[4], H. Poulsen[2], I. Law[3]

[1]Rigshospitalet, Dept. of Clini. Physiology, Nuclear Medicine and PET, Copenhagen, Denmark, [2]Rigshospitalet, Dept. of Oncology, Copenhagen, Denmark, [3]Rigshospitalet, Dept. of Clin. Physiology, Nuclear Medicine and PET, Copenhagen, Denmark, [4]Rigshospitalet, Dept. of Radiology, Copenhagen, Denmark

Purpose/Introduction: MRI blood volume (BV) measurements may be of value in differentiation of progressive disease from treatment related changes in patients with suspected recurrent high-grade gliomas [1]. The commonly used dynamic susceptibility contrast approach, however, has shown at best modest agreement with aminoacid positron emission tomography (PET), possibly due to insufficient leakage correction and compromised tumor coverage due to susceptibility artefacts [2]. The DCE (dynamic contrast enhanced) based approach is less prone to artefacts and allows also for more elaborate kinetic modelling and thus potentially more correct separation of blood volume from contrast leakage [3]. We investigated the quantitative and spatial agreement of DCE MRI with simultaneous ^{18}F-fluoro-ethyl-tyrosine (FET) PET in high-grade glioma patients after standard therapy.

Subjects and Methods: Forty-two consecutive hybrid FET PET/MRI scans with DCE MRI from 41 adult patients with WHO III astrocytoma (n = 5) or WHO IV glioblastoma (n = 37) were included. A total of 72 (61 contrast enhancing) lesions were analyzed. For each lesion both the contrast enhancing (CE), FET positive ($> 1.6 \times$ cortical uptake) and blood volume positive (qualitatively) volumes were delineated, and respective maximal lesion BV (log-BV), and relative maximal BV and FET to background ratios (log-TBR-BV and TBR-FET) were calculated. Spatial overlap between CE, BV and FET positive volumes were investigated by paired DICE coefficients. Level of visual agreement was rated on a 5 step scale (0 no agreement to 4 full agreement) both lesion and patient wise. A score of < 2 was considered discordant and > 2 concordant.

Results:

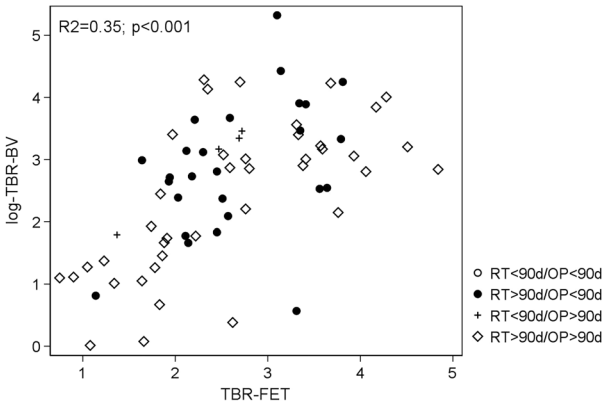

Fig 1. Relative maximum blood volume vs maximal FET uptake: influence of recent surgery (OP) and radiotherapy (RT)

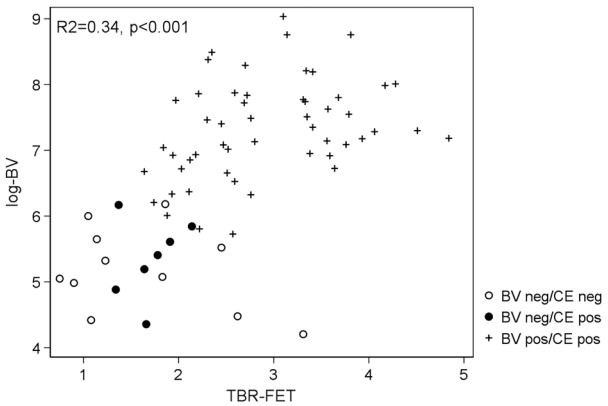

Fig 2 Maximum blood volume vs relative maximal FET uptake: influence of contrast enhancement

Overall both log-TBR-BV and log-BV were highly correlated with TBR-FET (Figs 1 and 2) with no apparent effect of recent surgery or radiotherapy on this correlation. Of 11 non-enhancing lesions all were BV negative and 5 were FET positive. Small CE lesions (< 1 ml) had lower values of TBR-FET and log-BV, and also lower DICE coefficients compared to larger CE lesions. Visual agreement was fair in

CE lesions with 40/61 (66%) being mostly concordant and only 6/61 (10%) being mostly discordant, whereas in non-CE lesions 5/11(46%) were discordant. On patient-wise analysis 67% of scans were concordant and 7% discordant.

	Non-enhancing (n=11)			Enhancing < 1ml (n=20)			Enhancing≥1 ml (n=41)		
	median	range		median	range		median	range	
VOL-FET (ml)	0	0-47.9	ǂ	0.7	0.0-4.9		12.4	0-121	†
VOL-CE (ml)	-	-		0.2	0.1-0.8		4.4	1.00-63.1	†
VOL-BV (ml)	-	-		0.3	0.00-2.2		5.2	0-56.4	†
DICE FET-BV	-	-		0.19	0.00-0.67		0.47	0-0.72	†
DICE FET-CE	-	-		0.20	0.00-0.70		0.50	0-0.60	†
DICE CE-BV	-	-		0.32	0.00-1.00		0.44	0-0.75	†
TBR-FET	1.23	0.75-3.31	ǂ	1.98	1.34-3.33		3.14	1.64-4.84	†
Log-BV	5.08	4.20-6.18	†ǂ	6.27	4.36-7.86		7.46	5.41-9.04	†
Log-TBR-BV	1.10	0.01-1.83	†ǂ	2.24	0.08-3.64		3.17	1.26-5.32	†
Lesion agreement score	4/1/0/0/6		†ǂ	0/2/4/9/5			1/3/11/20/6		

†<0.01 vs CE<1ml; ǂ p<0.01 vs CE>1ml

Table 1. Summary statistics

Discussion/Conclusion: DCE BV measurements shows good quantitative agreement in patients with FET PET in patients with suspected progressive high-grade glioma after standard therapy, whereas spatial and visual agreement depends on the presence and volume of contrast enhancement, limiting the ability of DCE BV to identify infiltrative tumor tissue.

References:

[1] S. Bisdas et al., *AJNR Am. J. Neuroradiol.* 2009
[2] O.M. Henriksen et al., *Eur. J. Nucl. Med. Mol. Imaging* 2016
[3] H.B. Larsson et al., *Magn Reson. Med* 2009

S24.08

Multi-modal evaluation of haemodynamic impairments within individual watershed areas reveals increased sensitivity in unilateral carotid artery stenosis

S. Kaczmarz[1], J. Göttler[1], J. Petr[2], M. B. Hansen[3], J. Kufer[1], C. Zimmer[1], K. Mouridsen[3], F. Hyder[4], C. Preibisch[1]
[1]*Technical University of Munich (TUM), School of Medicine, Department of Neuroradiology, Munich, Germany,* [2]*Helmholtz-Zentrum Dresden-Rossendorf, PET center, Institute of Radiopharmaceutical Cancer Research, Dresden, Germany,* [3]*Aarhus University, Institute of Clinical Medicine, Aarhus, Denmark,* [4]*Yale University, MRRC, New Haven, USA*

Purpose/Introduction: Internal carotid-artery stenosis (ICAS) is a major public health issue and causes complex haemodynamic impairments.[1–3] However, influences of microvascular effects remain poorly understood. Furthermore, increased sensitivity for regional pathophysiological changes is required to detect early disease stages. The aim of our study was therefore to establish a multi-modal MRI protocol allowing deeper insights into the pathology. Furthermore, we hypothesize to be most sensitive to ICAS-impairments within individual watershed areas (iWSAs), which were proposed to be most vulnerable to haemodynamic compromise.[4]

Subjects and Methods: Fifty-nine participants (29 unilateral ICAS-patients, age = 70.1 ± 4.8y and 30 age-matched healthy controls [HC]) underwent MRI on a Philips 3T Ingenia. The imaging protocol yielded oxygenation, perfusion and microvascular biomarkers which are summarized in Fig. 1. Additionally, iWSA's were defined for each participant.[4] Mean haemodynamic parameter values were compared within each hemisphere of ICAS-patients vs. HC and inside vs. outside iWSAs (Fig. 2A, B) in GM and WM.

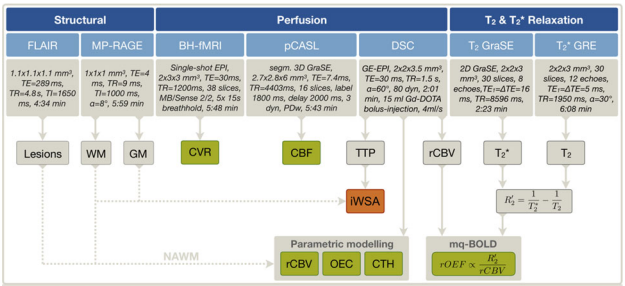

Figure 1: Overview of MRI protocol and derived parameters. Cerebrovascular reactivity (CVR) was measured by breathhold-fMRI (BH-fMRI)[5] and cerebral blood flow (CBF) by pseudo-continuous arterial spin labelling (pCASL). Relative cerebral blood volume (rCBV), oxygen extraction capacity (OEC) and capillary transit-time heterogeneity (CTH) maps were calculated by parametric DSC modelling.[6] Relative oxygen extraction fraction (rOEF) was calculated by mq-BOLD based modelling of rCBV, T_2^* and T_2.[7] Individual watershed areas (iWSA, orange) were derived by TTP-maps, GM/WM masked and applied to haemodynamic parameters (green).[4]

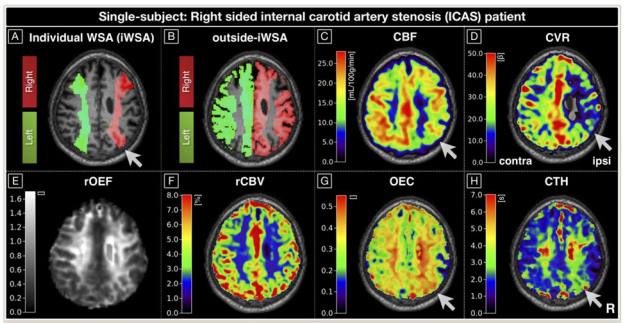

Figure 2: Exemplary parameter maps of a right-sided ICAS-patient. iWSA was semi-automatically segmented for each participant (A).[4] Haemodynamic impairments ipsilateral to the stenosis coincide with iWSA locations (arrows). For group analyses, each hemisphere's subject specific iWSA (A) and non-iWSA masks (B) with additional GM/WM-masks were applied to parameter-maps (C-H) and mean values per hemisphere calculated.

Results: Exemplary data of an ICAS-patient is shown in Fig. 2. On group-level, significant lateralisation of CBF, CVR, rCBV, CTH and OEC were found in ICAS, while rOEF was not lateralized (Fig. 3). Lateralisation was significantly enhanced inside iWSAs compared to outside of iWSAs for CBF and CVR, with a strong trend for rCBV—and strongest in WM of iWSAs (t test, $p < 0.05$). OEC and CTH were indeed lateralized, but not different inside vs. outside iWSAs (Fig. 3). All HC parameters were symmetrical (data not shown).

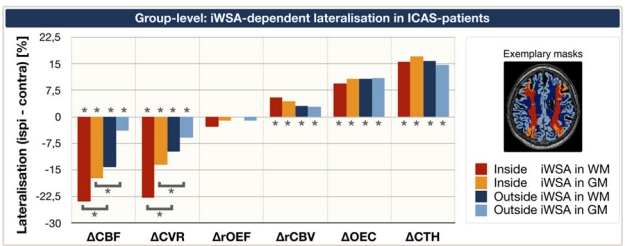

Figure 3: Haemodynamic lateralisation on group-level of ICAS-patients within iWSAs. Lateralisation between ipsilateral and contralateral hemispheres was compared in four VOI's (see inlay). Asterisks indicate statistically significant differences (t-test, p<0.05). CBF and CVR were ipsilaterally decreased, rOEF was unaffected and ipsilateral increases measured for rCBV, OEC and CTH. While ΔCBF, ΔCVR and ΔrCBV were significantly enhanced within iWSA, ΔOEC and ΔCTH effects were comparable inside and outside of iWSA.

Discussion/Conclusion: We successfully applied the proposed multimodal MRI-protocol and demonstrated its sensitivity to haemodynamic impairments in ICAS. Specificity was affirmed by symmetrical HC results. Individual parameter lateralisation in ICAS excellently agrees with the literature. Decreased CVR along with increased rCBV indicates chronic vasodilation.[1] Pronounced effects in WM-iWSA fit with the different blood supply in GM/WM. Ipsilaterally decreased CBF, symmetrical rOEF[2] and increased CTH also coincide with recent studies[3]. The ΔCBF vs. ΔrOEF mismatch could

relate to variable oxygen diffusivity[8]—potentially moderated by CTH[3, 9]. Interestingly, CTH and OEC lateralisation were iWSA-location independent, which matches previous findings.[10] These complimentary information of TTP and CTH about macrovascular effects, respectively microvascular flow[3] are highly promising to gain deeper insights into the pathology. And as initially hypothesized, evaluation within iWSA significantly increased the sensitivity to CBF, CVR and rCBV impairments and allows to detect even subtle changes.

References:

1: Vagal, AJNR, 2009.
2: Bouvier, HBM, 2015.
3: Mundiyanapurath, PLoSOne, 2016.
4: Kaczmarz, Neurorad, 2018.
5: Vondrácková, ISMRM, 2016.
6: Jespersen, JCBFM, 2012.
7: Hirsch, NMRBiomed, 2014.
8: Hyder, JApplPhysiol, 1998.
9: Rasmussen, JCBFM, 2015.
10: Calamante, Stroke, 2010.

S24.09

Effective oxygen diffusivity is ipsilaterally decreased in asymptomatic unilateral internal carotid artery stenosis

J. Kufer[1], J. Goettler[1], C. Zimmer[1], F. Hyder[2], C. Preibisch[1], S. Kaczmarz[1]

[1]*Technical University of Munich, School of Medicine, Klinikum rechts der Isar, Department of Neuroradiology, Munich, Germany,*[2]*Yale University, MRRC, New Haven, CT, USA*

Purpose/Introduction: Internal carotid artery stenosis (ICAS) is a major public health issue, accounting for 10% of all strokes.[1] Even asymptomatic patients without stroke signs showed impaired cognition, [2] perfusion and oxygenation.[3, 4, 5] Nevertheless, the microvasculature's role in ICAS is still poorly understood and imaging of the effective oxygen diffusivity of the capillary bed[6, 7] could provide significant insights. Thus, oxygen diffusivity is a high potential biomarker of microvascular health, but clinical applicability of existing diffusivity mapping methods based on complicated gas challenges[7] is limited. Therefore, we aim to derive diffusivity maps more easily by applying the Hyder-model[6] to MR-based relative oxygen extraction fraction (rOEF) and cerebral blood flow (CBF) maps. Furthermore, we hypothesize to be sensitive to oxygen diffusivity impairments in ICAS.

Subjects and Methods: Fifty-nine participants (29 asymptomatic, unilateral ICAS-patients, age = 70.1 ± 4.8y, and 30 age-matched healthy controls [HC], age = 70.3 ± 7.3y) underwent MRI on a Philips 3T Ingenia. Quantitative T_2, T_2* and rCBV imaging yielded normalized maps of mqBOLD-based rOEF, [8] while CBF was obtained by pseudo-continuous arterial spin labelling (pCASL)[9] (Fig. 1). Maps of relative oxygen diffusivity (D) were calculated voxel-wisely following the Hyder-model[6] with $D = -CBF \times \ln(1-rOEF)$. Lateralization of rOEF, CBF and D between both hemispheres was investigated in grey matter (GM) within the carotid arteries' perfusion territories[10] in ICAS and HC.

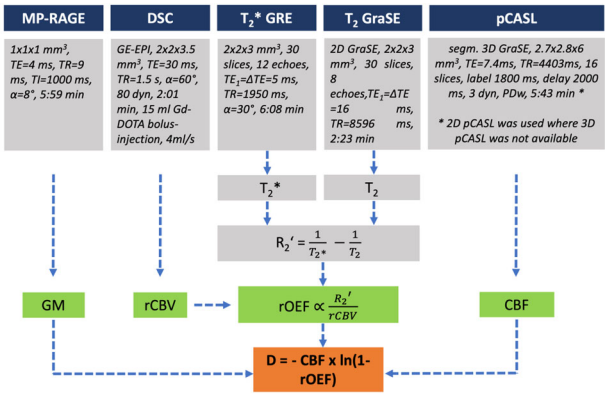

Fig.1: MRI protocol. MP-RAGE was applied for grey matter(GM) masks. rOEF was calculated from R2' and rCBV. Pseudo-continuous arterial spin labelling(pCASL) yielded cerebral blood flow(CBF). rOEF and CBF were combined to derive oxygen diffusivity(D).

Results: Figure 2 shows exemplary parameter maps of an ICAS-patient. While rOEF was not significantly lateralized in the ICAS-group (t test, $p = 0.81$), both CBF and diffusivity were significantly decreased ipsilateral to the stenosis ($p < 0.01$, Fig. 3a). For HC, all parameters were symmetrical (Fig. 3b).

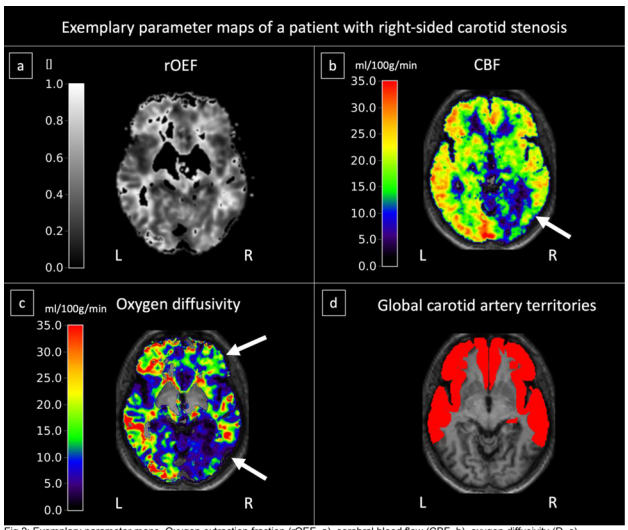

Fig.2: Exemplary parameter maps. Oxygen extraction fraction (rOEF, a), cerebral blood flow (CBF, b), oxygen diffusivity (D, c) and carotid artery territories used for group-level analysis (d). CBF and diffusivity are ipsilaterally decreased (arrows).

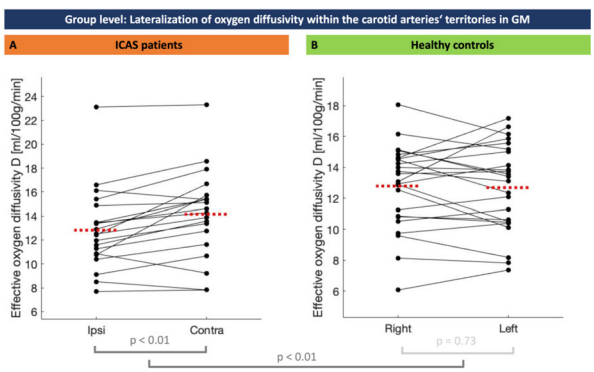

Fig.3: Paired scatterplot of oxygen diffusivity lateralization. Diffusivity is ipsilaterally decreased in ICAS(t-test,p<0.01) and symmetrical in HC(p=0.73). Lateralization is also significantly different between ICAS and HC(two-sample t-test,p<0.01).

Discussion/Conclusion: We successfully obtained oxygen diffusivity maps based on mqBOLD and pCASL. Significantly decreased oxygen diffusivity and CBF were found in ICAS-patients. Notably, diffusivity decreases were distributed more diffusely than hemodynamic reductions. This apparent diffusivity-perfusion mismatch points to oxygen permeability disturbances at the microvasculature level, which are not identical to hemodynamic impairments, and may be related to increased capillary transit time heterogeneity (CTH), [3, 11] a potential modulator of diffusivity.[7] In contrast to more sophisticated gas inhalation-based methods, [7] our proposed approach is readily applicable in clinical settings. To conclude, our approach is highly promising to facilitate deeper insights into ICAS pathophysiology arising from mismatched disturbances of oxygen permeability and blood circulation.

References:

1: Petty, Stroke (1999).
2: Göttler, JCBFM (2018b).
3: Kaczmarz, ISMRM (2019).
4: Göttler, JCBFM (2018a).
5: Bouvier, HBM (2015).
6: Hyder, JApplPhysiol (1998).
7: Germuska, Neuroimage (2019).
8: Hirsch, NMR Biomed (2014).
9: Kaczmarz, ESMRMB (2016).
10: Tatu, Neurology (1998).
11: Jespersen, JCBFM (2012).

L08 Lightning Talks

15:40–16:30 *The Stage*

Neuroimaging

L08.01
Maturation effects of tract-specific myelin content

G. Drenthen[1], W. Backes[1], E. Fonseca Wald[2], A. Aldenkamp[3], J. Jansen[1]
[1]*Maastricht University Medical Center, Department of Radiology and Nuclear Medicine, Maastricht, The Netherlands,* [2]*Maastricht University Medical Center, Department of Neurology, Maastricht, The Netherlands,* [3]*Epilepsy Center Kempenheaghe, Department of Behavioral Sciences, Heeze, The Netherlands*

Purpose/Introduction: The structural brain network is most commonly characterized using diffusion weighted imaging (DWI). While DWI provides useful information on the integrity of white matter tracts, it cannot provide specific information on the most characteristic component of white matter, myelin. Myelin is wrapped around the axons and acts as an electrical insulator material. It is essential for fast propagation of electrical signals in the central nervous system, and thus effects the efficiency of the brain network. The process of myelination is most active during the first 2 years of life, but continues through adulthood. In this study we set out to characterize the maturation of axonal myelin-content.

Subjects and Methods: Thirteen children (6–12y) and 5 adults (25–32y) were scanned on a 3T unit (Philips Achieva) with a 32-ch head coil. T1-weighted 3D turbo field echo images, multi-echo 2D Gradient-Spin Echo (GRASE) images, and diffusion weighted images (DWI) were acquired.

For structural networks, nodes were based on Freesurfer T1-w segmentation of 68 cortical and 16 sub-cortical regions, and edges were defined using whole brain tractography on DWI using ExploreDTI. Whole brain myelin-water fraction (MWF) maps were calculated from T2-relaxometry of the GRASE images as described previously [1], and registered to the diffusion data.

The effect of age on the tract-specific MWF was determined by linear regression, correcting for effects of sex and tract density (#streamlines/tract volume). Furthermore, we explored whether the MWF and maturation effect differ for edges connecting hubs (i.e. rich-club) compared to edges to hubs (i.e. feeder) and other edges (i.e. local) [2].

Results: Figure 1a shows an example of an early myelinated tract (relative small age effect), while Figure 1b shows a late myelinated tract (relative large age effect).

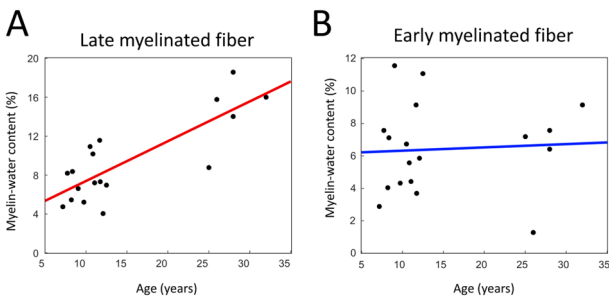

Figure 1: A) shows an example of an early myelinated tract (i.e. relative small effect of age), B) shows a late myelinated tract (i.e. relative large effect of age).

The whole brain maturation pattern is shown in Fig. 2.

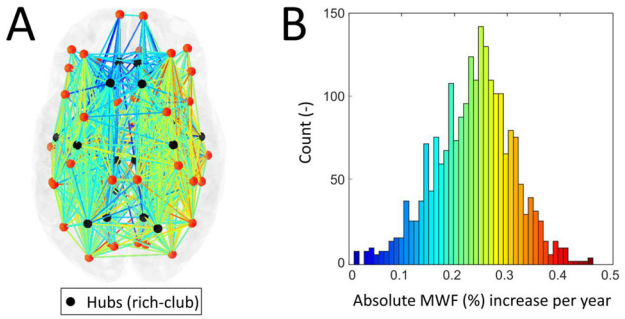

Figure 2: A) Whole brain maturation patterns of myelin-specific tracts. Please note that hubs are indicated as black nodes. B) corresponding histogram of absolute increase of the tract-specific myelin-water fraction per year.

Figure 3 shows the myelin-content for the rich-club, feeder and local edges for both age groups.

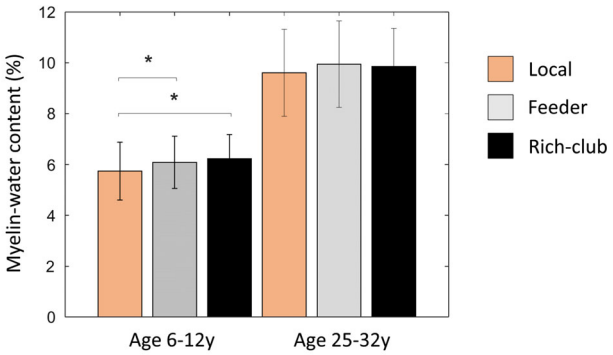

Figure 3: Myelin-water content of the local, feeder and rich-club edges for both age groups. (* $p < 0.05$)

Non-parametric sign tests reveal significantly lower myelin content of the local edges in the children. Furthermore, the maturation effect (i.e. absolute increase of myelin-water content per year) of local ($0.24 \pm 0.08\%$) and feeders ($0.24 \pm 0.07\%$) edges is significantly higher compared to the rich-club ($0.22 \pm 0.07\%$).

Discussion/Conclusion: We showed that the maturation effects differ for specific tracts. For example, edges between hubs seem to be myelinated in an earlier stage compared to the other edges. Indicating that fast and efficient communication between hubs (i.e. rich-club) is an important aspect of healthy neuronal development.

References:

[1] Drenthen et al. Applicability and reproducibility of 2D multi-slice GRASE Myelin Water Fraction with varying acquisition acceleration. *NeuroImage,* 2019

[2] Mancini et al. Introducing axonal myelination in connectomics: A preliminary analysis of g-ratio distribution in healthy subjects. *NeuroImage,* 2018

L08.02

Accuracy of neurophysiological and functional MRI data in chronic disorders of consciousness differentiation

D. Sinitsyn[1], **E. Kremneva**[2], L. Legostaeva[1], E. Yazeva[1], D. Sergeev[1], A. Poidasheva[1], A. Sergeeva[1], N. Suponeva[1], M. Piradov[1]
[1]*Research center of neurology, Moscow, Russian Federation,* [2]*Research center of neurology, Neuroradiology, Moscow, Russian Federation*

Purpose/Introduction: Diagnostic accuracy of different chronic disorders of consciousness (DOC) can be affected by the false negative errors in up to 40% cases and might lead to important care-taking and ethical ramifications. We aimed to investigate the accuracy of patient differentiation between VS (vegetative state) and MCS (minimally conscious state) based on TMS-EEG and resting fMRI data.

Subjects and Methods: 35 patients were enrolled into the study (21 VS, 14 MCS), all patients underwent 3 T resting-state FMRI and then TMS-EEG. The analysis of functional connectivity according to TMS-EEG obtained the values of perturbation complexity index (PCI). Resting-state functional connectivity was computed in a ROI-to-ROI analysis with an atlas of 278 areas (Shen X et al., 2013). The Fisher-transformed correlation coefficients of the average BOLD signals in every ROI comprise a symmetric matrix, its upper triangle forms a connectivity vector. An *index of connectome intactness (ICI)* was computed as the correlation coefficient of an individual connectivity vector and the mean vector of the reference group. A variant of the index (*index of thresholded connectome intactness, ITCI)* was evaluated by the same procedure after thresholding connectivity vectors at a given level. Hub disruption index (HDI) was calculated as index measuring the disruption of the nodal degrees in the connectom graph.

Results: PCI index provides a more accurate VS and MCS group separation (area under the ROC curve: AUC = 0.86) than ITCI (AUC = 0.69) and HDI (AUC = 0.72) indices. Comparison of the results of clinical evaluation, as well as the data obtained by the TMS-EEG and rs-fMRI methods, showed that PCI index has a significant correlation with the average strength CRS-R scale (Spearman test, $\rho = 0.59$, $p = 0.0002$). The correlation between ITCI and HDI indices with the CRS-R scale does not reach statistical significance ($\rho = 0.28$, $p = 0.08$ and $\rho = 0.31$, $p = 0.06$, respectively). The values of the PCI index do not have a significant correlation with ITCI and HDI indices ($\rho = 0.18$, $p = 0.3$ and $\rho = 0.23$, $p = 0.2$, respectively). At the same time, the indices based on rs-fMRI have a strong correlation between each other ($\rho = 0.78$, $p < 0.0001$).

Discussion/Conclusion: TMS-EEG showed prevalence in DOC differentiation and higher correlation with clinical scale than resting-state FMRI. But FMRI makes it possible to visualize resting-state netorks and their connections that are most severely disturbed in VS patients compared to MCS, which means, presumably, to maintain the process of consciousness. So both methods are feasible in consciousness and its disorders research.

Study was supported by RSCF grant 16-15-00274

References:

Shen X. et al.//Neuroimage 2013. 0: 403–415.
Biswal, B. et al.//PNAS. 2010. V. 107, pp. 4734–4739.

L08.03

Comparison of MTsat and MTR as biomarkers of white matter tissue integrity: correlation with clinical features and conventional MRI-visible lesions load

E. York[1], M. Thrippleton[1], R. Meijboom[1], S. Chandran[2], P. Connick[3], A. Coles[4], A. Waldman[1]
[1]*University of Edinburgh, Centre for Clinical Brain Sciences, Edinburgh Imaging, Edinburgh, UK,* [2]*University of Edinburgh, Centre for Clinical Brain Sciences, Euan MacDonald Centre for Motor Neurone Disease Research, Anne Rowling Regenerative Neurology Clinic, Edinburgh, UK,* [3]*University of Edinburgh, Anne Rowling Regenerative Neurology Clinic, Edinburgh, UK, Edinburgh, UK,* [4]*University of Cambridge, Department of Clinical Neurosciences, Cambridge, UK*

Purpose/Introduction: Magnetization transfer (MT) imaging allows quantitative imaging of 'bound' protons, and indirect measurement of myelin integrity in vivo. MT ratio (MTR) has been used to detect white matter (WM) damage in multiple sclerosis (MS), but is not a reliable indicator of clinical disability. MTsat, which corrects for variance in MT signal due to B_1 inhomogeneity and T_1 relaxation, has been proposed as a more accurate measure of myelin content[1], and may better correlate with clinical disability in MS than MTR[2]. Here we aim to determine whether MTR and MTsat signal in grey matter (GM), normal-appearing WM (NAWM), sub-cortical regions (SC) and WM lesions (WML) correspond with clinical data in MS in the context of a phase 2a clinical trial.

Subjects and Methods: Patients with relapsing–remitting MS (n = 18; 12 F; mean age 39 yrs) were recruited in a randomised, placebo-controlled and double-blinded trial of a putative remyelinating agent plus standard disease modifying therapy. The authors remain blinded to treatment arm.

Expanded disability status score (EDSS), blood markers and general health data (e.g. blood pressure) were collected at baseline only.

Images, acquired on a 3T MRI system (Prisma, Siemens Erlangen, DE), included 3D T1w, post-contrast T2 FLAIR and MT imaging (3D FLASH dual-echo: 1 mm^3 resolution + on/off MT RF pulse; T1w) at baseline and 6 months.

Sequences were registered for each time-point (FSL 5.0.1). Median and standard deviation (SD) values were extracted from MTR and MTsat maps (Fig 1) for GM, NAWM, SC and WML and averaged over time-points (MATLAB2018b). Pearsons's correlations were performed for MTSat and MTR in GM, NAWM, SC and WML, and for clinical markers including EDSS ($\alpha = 0.05$; RStudio).

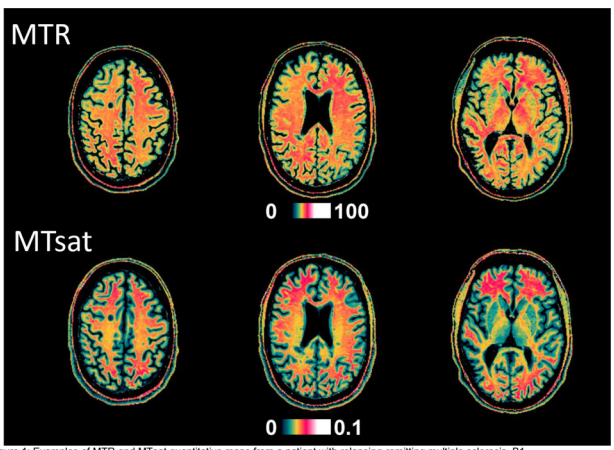

Figure 1: Examples of MTR and MTsat quantitative maps from a patient with relapsing-remitting multiple sclerosis. B1 inhomogeneities are visible to a greater extent for MTR than MTsat.

Results: Significant correlation coefficients are shown in Fig 2, uncorrected for multiple comparisons. Median MTsat in NAWM and WB correlated with triglycerides; in NAWM, WB and WML, with alkaline phosphatase (AP); in GM, with alcohol consumption and Free T4 and, in SC, with TSH. Median MTR did not correlate with clinical data.

MTsat (but not MTR) SD in WML correlated with EDSS and disease duration. Correlations for MTR SD and MTsat SD were seen with blood pressure, AT, AP and age, plus MTsat SD with TSH and MTR SD with Free T4.

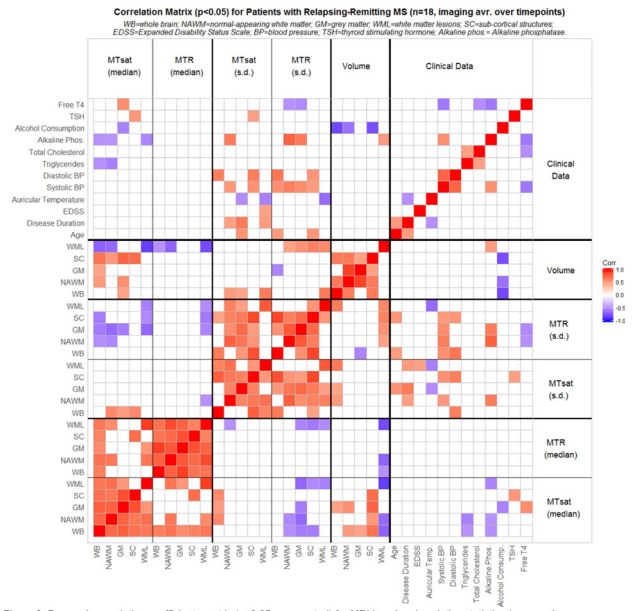

Figure 2: Pearson's correlation coefficients matrix (p<0.05 uncorrected) for MRI imaging descriptive statistics (averaged between baseline and 6 month follow-up) and baseline clinical data for people with relapsing-remitting multiple sclerosis.

Discussion/Conclusion: Stronger clinical correlations for median MTsat compared to median MTR indicate MTsat may be a superior disease biomarker in MS, likely due to reduced B_1 and T_1 effects which add variability in MTR data. Only MTsat correlated with EDSS, suggesting it is better linked to disability and demyelination than MTR. Following unblinding, we will assess MTsat as a biomarker of remyelinating therapy effectiveness.

References:

1. Helms et al. High-res. maps of MT with inherent correction for RF inhomogeneity and T1 relaxation obtained from 3D FLASH MRI. Magn Reson Med 2008.

2. Lema et al. A Comparison of MT Methods to Assess Brain and Cervical Cord Microstructure in MS. J Neuroim 2017.

L08.04

Regional brain white matter hyperintensities and neuropsychological function in late-life depression

L. Emsell[1], J. Blommaert[2], K. Vansteelandt[3], W. Pille[3], F.-L. De Winter[3], S. Deprez[1], S. Sunaert[1], F. Bouckaert[3], M. Vandenbulcke[3]

[1]*KU Leuven, Translational MRI, Leuven, Belgium,* [2]*KU Leuven, Department of Oncology, Leuven, Belgium,* [3]*UPC KU Leuven, Old Age Psychiatry, Leuven, Belgium*

Purpose/Introduction: Late-life depression (LLD) is common in old age, and may be in part mediated by increasing vascular pathology[1]. Age-related T2-FLAIR white matter hyperintensities (WMH) are present in both healthy and depressed populations, therefore differences in regional, rather than global WMH burden may underlie the mood and cognitive symptoms of LLD by disrupting specific WM fibre bundles[2]. Here we characterise the distribution of WMH in severe LLD, and use structural and diffusion MRI atlas-based regions of interest to investigate the association of cognitive and affective symptoms with regional WMH burden.

Subjects and Methods: 3D T1 (TFE) anatomical and 3D T2 FLAIR data (3T Philips) were analysed from n = 37 currently depressed hospital in-patients with severe LLD (73.7 years, sd 7.5, 27 females). WMH volumes were derived automatically from 3D FLAIR segmentations using icobrain[3], and localised using the JHU ICBM-DTI-81 atlas and a regional WMH atlas including periventricular (PV), deep and juxtacortical regions[4]. Linear mixed models, controlling for age, were applied to investigate associations between both total and regional WMH volume, neuropsychological assessments of cognition and mood, and age of depression onset (before or after 55 years), where lesion burden was expressed as a percentage of the ROI.

Results: WMH most commonly occurred in the periventricular region (Fig 1) and lesion burden increased with older age ($r = 0.674$, $p < 0.0001$). Total lesion volume and lesions in the superior ($t = 6.13$, $p < 0.0001$), and posterior ($t = 3.79$, $p = 0.0002$) corona radiata, and the tapetum ($t = 5.48$, $p < 0.0001$) were associated with slower processing speed (trail-making test A, fig 2). There were no other significant associations between WMH and cognitive test scores or affective symptoms (Geriatric Depression Scale), nor any association with age of onset of depression ($p > 0.05$).

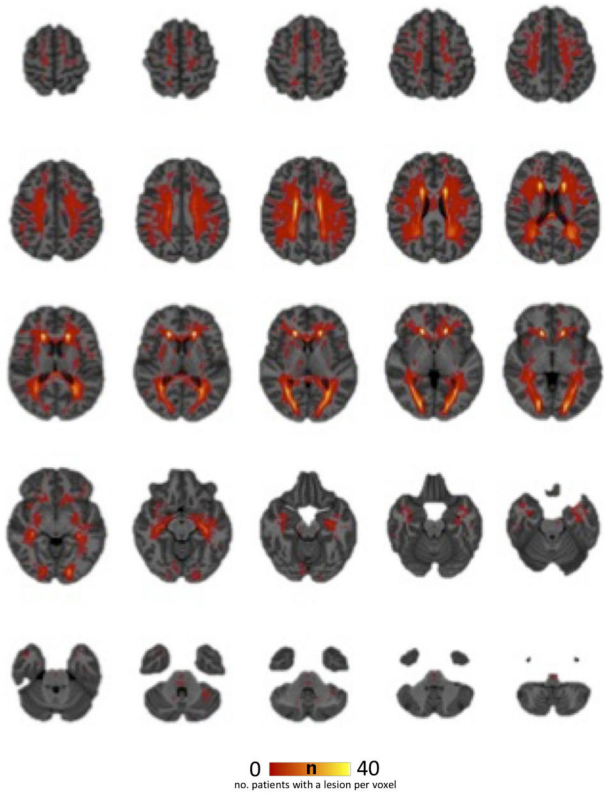

Fig 1. Distribution of WMH in late-life depression

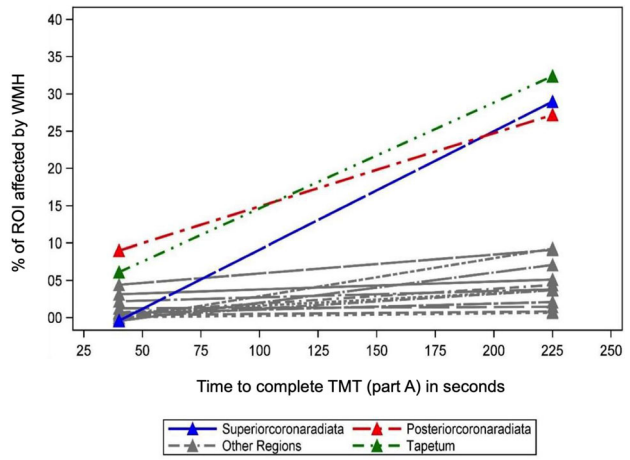

Fig 2. Association between regional WMH burden and processing speed

Discussion/Conclusion: Our findings align with previous studies with regard to the distribution and trajectory of WMH in older populations. We detected only a modest role for both total and regional WMH on cognitive performance in LLD, specifically on processing speed. As relatively few patients had deep and juxtacortical lesions, the sample may have been under-powered to detect associations in these regions. There was no association between WMH burden and depression severity arguing against vascular causes for mood symptoms in patients with a typical WMH distribution, characterised primarily by PV lesions.

References:

1. Aizenstein HJ et al. BMC Med. 2016;14(1):1–16. **2**. Biesbroek JM et al. PLoS One. 2016, 8;11(11) **3**. Jain S et al. Neuroimage Clin. 2015 May 16;8:367–75, **4.** Jackson, Michael R.; Valdés Hernández, Maria del C. Regional brain atlas for assessment of white matter hyperintensities, 2007–2016 [dataset]. 2016 https://doi.org/10.7488/ds/1580.

L08.05

NAAG reduction after single concussion. ^{1}H MRS 3T study

P. Menshchikov[1, 2], A. Ivantsova[3], A. Manzhurtsev[4], M. Ublinskiy[1], T. Akhadov[1], N. Semenova[2]

[1]*Clinical and Research Institute of Emergency Pediatric Surgery and Traumatology, Radiology, Moscow, Russian Federation,* [2]*Semenov Institute of Chemical Physics of RAS, Biophysics, Moscow, Russian Federation,* [3]*National Research Nuclear University "MEPhI", Moscow, Russian Federation,* [4]*Emanuel Institute of Biochemical Physics of RAS, Moscow, Russian Federation*

Purpose/Introduction: Majority of the MRS studies report reduced total NAA and NAAG (tNAA) white matter (WM) concentrations in the acute phase of mild Traumatic brain injury (mTBI) [1]. In about 25–30% of WM tNAA signal is determined by NAAG contamination. Therefore, reduced WM tNAA signal intensity might be associated with both NAA and NAAG changes. Currently the most promising method for the NAAG and NAA separation is a J-editing with the MEGA-PRESS [2]. Main aim of this study was to determine WM NAA and NAAG concentrations in acute mTBI.

Subjects and Methods: Two groups of participants were included in the study: patients (n = 12, mean age–15.3 ± 0.8 years) with acute mTBI (time between trauma and examination 41 ± 16 h; Coma Glasgow score—15); 15 healthy children (mean age − 15.7 ± 1.6 years) without history of any TBIs.

All investigations were performed on the 3.0T MRI scanner. The research protocol contained following spectra: NAA_MEGA-PRESS (TE/TR = 140/2000 ms, 35 ms editing pulses − 4.84 ppm and 4.38 ppm), NAAG_MEGA-PRESS (TE/TR = 35/2000 ms, 35 ms editing pulses 4.61 ppm and 4.15 ppm), PRESS (TE/TR = 35/2000 ms) and Unsuppressed water spectra (TE/TR = 35/10000 ms). All voxels in size of 50 × 19 × 27 mm were located in the left centrum semiovale (Fig. 1. WM-dominant region).

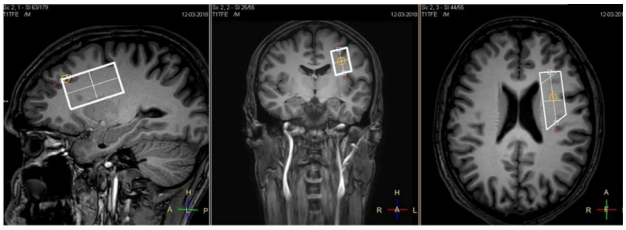

Fig.1. Typical VOI location in WM-rich region of left centrum semiovale

NAAG/tCr and NAA/tCr were quantified from MEGA-PRESS spectra using jMRUi routine. [tCr], [tCho], [tNAA], [Ins] and [GLX] concentrations were quantified with LCmodel with normalization on tissue contamination, T_2 and T_1 relaxation.

Results: The significant effect on the NAAG was found, with the patients having lower NAAG/Cr (Fig. 2) and [NAAG] (Fig. 3) as compared to the control group (19%). [tNAA], [tCho], [tCr], [GLX], [Ins] (Fig. 3) and NAA/Cr (Fig. 2) were unchanged. Mean GM-fraction in the normal and patient group were 0.26 ± 0.4 and 0.24 ± 0.5.

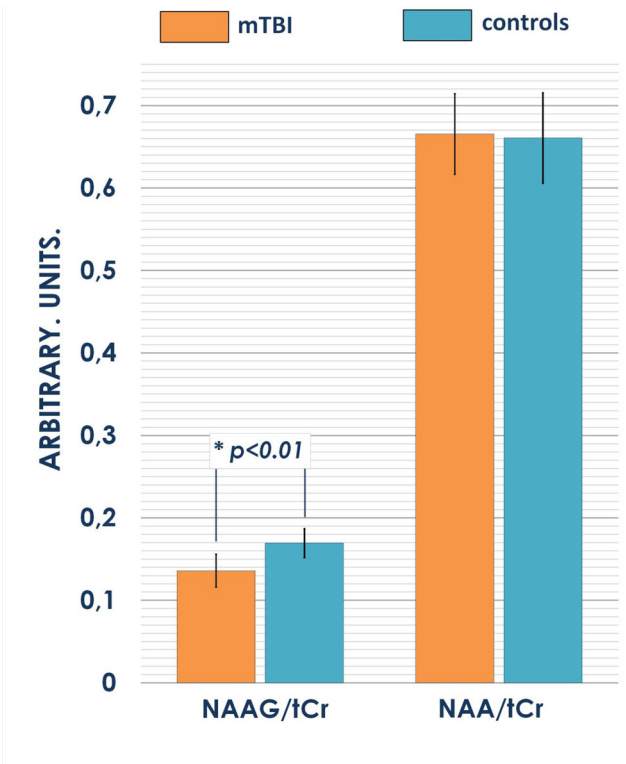

Fig.2. Comparison of NAA/tCr and NAAG/tCr ratios

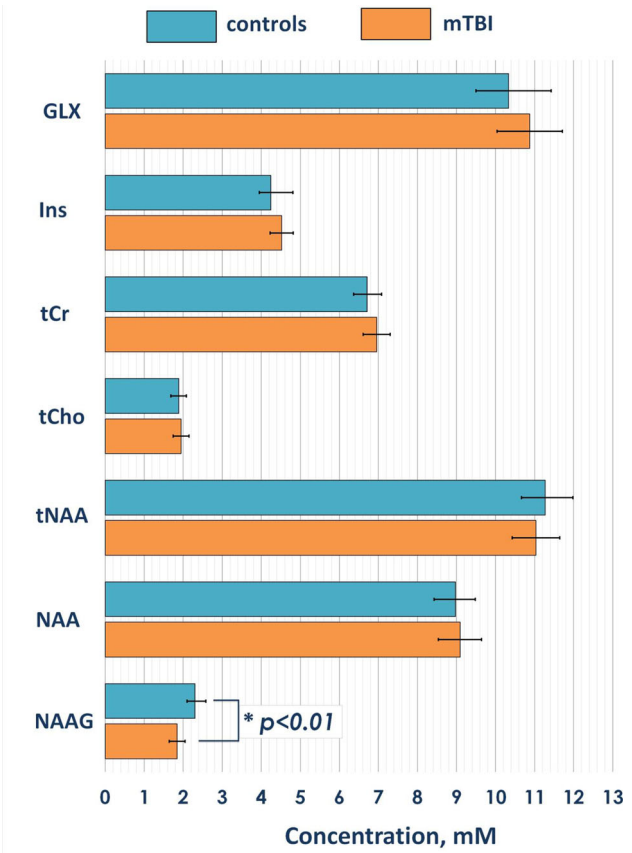

Fig.3. Absolute metabolite concentrations in left centrum semiovale in mTBI patients and controls

Discussion/Conclusion: This study for the first time revealed decreased cerebral WM [NAAG] without NAA changes in the pediatric acute mTBI. Previous findings of [tNAA] reduction in WM might not be associated with a decrease in [NAA] but just with a decrease in [NAAG], which certainly changes current vision on the following problem and highlights importance of NAAG separation from NAA. [tNAA] reduction absence in our study may be associated with GM contamination in the VOI because of its large size. Since NAAG via the action of its peptidase was suggested as an important mediary of neuronal–glial communication [3], it might be that NAAG is spent on protection and repair of nervous tissue after damage. Finally, the extensive modulatory role for NAAG on both glutamatergic and GABAergic systems implicates NAAG in the regulation of the balance between excitatory and inhibitory neurotransmission that has been shown to be shifted in acute mTBI [4]. To answer this question it is necessary to quantify [Asp] [Gln], [Glu] in this and neighboring localizations.

References:

[1] *Narayana 2017.*
[2] *Edden 2007.*
[3] *Baslow, 2000.*
[4] *Menshchikov, 2017.*

L08.06

A novel imaging biomarker for cancer from multicomponent T1 relaxometry

A.-M. Oros-Peusquens, A. Weglage, N. J. Shah
Research Centre Juelich, INM-4, Juelich, Germany

Purpose/Introduction: Most brain tumours cause brain oedema, which is a significant cause of patient morbidity and mortality. There is qualitative knowledge regarding higher water content (by definition) and longer relaxation times in oedema than in healthy tissue. However, these properties are seldom characterised in the clinic. Furthermore, multicomponent T1 relaxometry was never performed in brain tumours. We report here the novel identification of a tumour and oedema-specific T1 component.

Subjects and Methods: Fourty seven patients (30 female, 46.5 ± 0.8 years old) with a variety of malignant brain tumours underwent MRI and dynamic FET PET in a hybrid 3T MR-PET scanner. In addition, 10 healthy volunteers (5 female, 32.4 ± 0.3 years old) were measured in the same setup. Quantitative MRI was performed using a Look-Locker sequence, TAPIR[1]. The inversion-recovery curve was sampled in steps of 17 ms with 460 time-points within a single-slice TA of $\sim$ 4 min. Denoising of magnitude and phase data was performed using a PCA decomposition of the data and keeping only 3–5 components out of 460. NNLS analysis using 300 linearly spaced T1 values between 50 ms and 6 s and Tikhonov regularisation was performed. Masks for different tissue types were defined.

Results: The low SNR of the original data was dramatically increased by performing PCA-based denoising of the complex data. Subsequent NNLS analysis revealed the existence of several tissue specific components. The analysis of voxels within tissue apparently unaffected by the presence of tumour revealed the existence of a short T1 component in healthy white and grey matter, of components reflecting the characteristic WM and GM T1 values, and of components with very long relaxation times (similar to CSF). Figures 1–3 illustrate similarities and differences between healthy tissue and brain tumour. The maps corresponding to different T1 components, shown in Fig. 1 (volunteer) and 2 (patient), were obtained by splitting the T1 interval 50 ms–6 s into several bins, labeled 'Myelin', 'WM', 'GM', 'high GM' and 'CSF'.

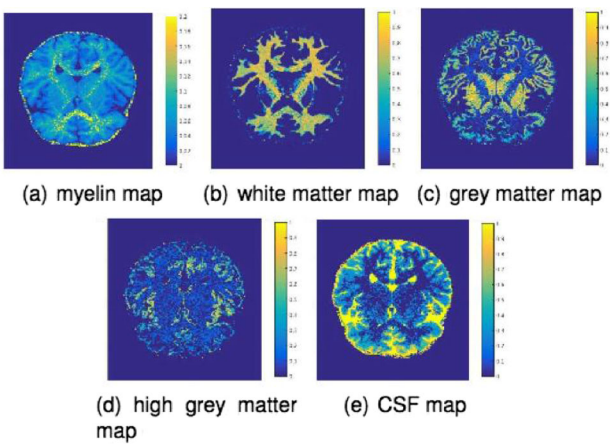

Maps corresponding to different T1 tissue components for a healthy volunteer. Here, the nomenclature (WM, CSF...) corresponds to selected T1 intervals, not to masks.

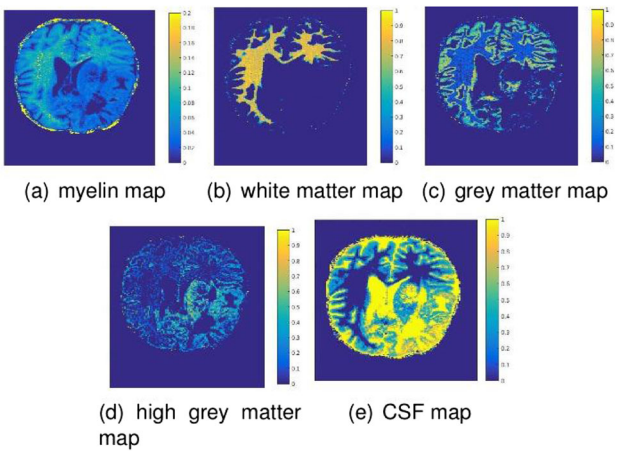

Maps corresponding to different T1 tissue components for a glioblastoma patient. Same T1 intervals and labels are used as in Fig. 1.

The number of peaks in the T1 relaxogram identified in the 'high gray matter' region, which is stronger represented in the tumour area, is compared in Fig. 3.

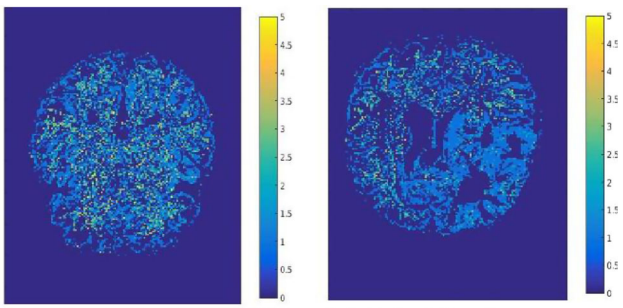

Comparison of the number of T1 peaks identified in the 'high grey matter' region in healthy vs brain tumour tissue.

The water fraction of this 'high grey matter' structure in tumour area (identified by PET) was 9.5(6.3) and in oedema (identified by FLAIR) was 9.0(5.8), vs healthy tissue 7.0(3.3).

Discussion/Conclusion: Multicomponent T1 distributions in tumour/oedema and healthy tissue are investigated for the first time. A unique single-peak component associated with tumour and oedema is identified, which is different from the multi-peak structure of healthy tissue. The properties of the healthy tissue-specific components are modified in tumours. This opens the possibility of better classification of the tumour environment and likely of better characterisation of the region of tumour infiltration.

References:

[1] Shah NJ et al. Neuroimage. 14 (2001).

L08.07

Positive effects of physical workout on working memory in healthy ageing

P. Naumczyk[1], A. Sabisz[2], B. Brzeska[2], A. Sawicka[3], K. Jodzio[1], P. Winklewski[2], E. Szurowska[2], A. Szarmach[2], R. Olek[3]

[1]*University of Gdansk, Gdańsk, Poland,* [2]*Gdansk Medical University, Gdańsk, Poland,* [3]*Gdansk University of Physical Education and Sport, Gdańsk, Poland*

Purpose/Introduction: The functioning of the elderly population has recently drawn more and more attention in psychological, sociological and medical research due to the ageing of the population in the Western societies. The study aimed at assessing the effect of regular workout on brain mechanisms of working memory.

Subjects and Methods: 16 healthy elderly women (age: M = 66, 8yo, SD = 3, 1y) with no signs of dementia were scanned twice on Philips Acheva TX 3.0T: before and after the completion of the training program involving up to total of 48 h of workout (hours of training: M = 41, 8 h, SD = 6.2 h) on the course of 6 months. Each scanning session included a high-resolution T1 sequence as well as an EPI BOLD sequence. During the fMRI exam, participants performed an n-back task in a block design with three blocks (0-back, 1-back and 2-back). The data was processed in Freesurfer's FS-FAST surface stream (version 6.0) with paired differences (after vs before) comparisons of three contrasts of interest (1-back vs 0-back, 2-back vs 0-back, 2-back vs 1-back). The data was inspected for movement and artifacts with artifact detection toolbox. The first level GLM model included additional regressors of participant's movement, and outlier timepoints. The second level analyses included variables of interest: subjects' age, between-scan's interval's length and the number of hours of training. The variables were demeaned before entering them into the model.

Results:

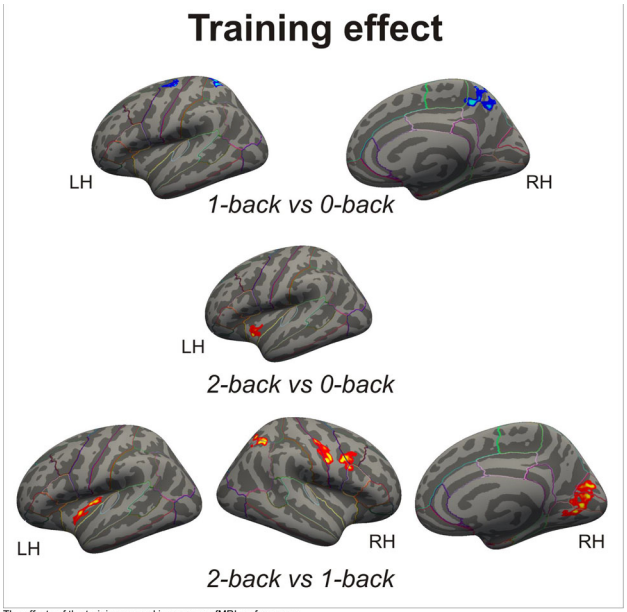

The effects of the training on working memory fMRI performance

One subject was removed from the analyses due to excessive movement (over 15% of outliers detected). All presented results are significant at $p < 0.05$ after accounting for multiple comparisons (Monte-Carlo cluster-wise sim.).

There was no main effect of the scan timepoint (after training vs before training), all the variance in the signal came from the variables of interest. Higher number of hours of training was associated with decreased involvement of the parietal regions of both hemispheres in low-demand processing (1-back vs 0-back contrast), and increased involvement of the left insula in high-demand processing (2-back vs 0-back). Also, higher number of workout hours was associated with higher involvement of the right frontoparietal network, as well as right primary visual cortex and left posterior insula in working memory processing (2-back vs 1-back). The results are presented on Fig. 1.

Discussion/Conclusion: The analyses support previous findings on beneficial role of physical workout on cognitive functioning of the

elderly. It seems that regular training alters brain mechanisms of working memory processing, suggesting some form of functional reorganization.

References:

Freesurfer: www.surfer.nmr.mgh.harvard.edu/FsFast/
ART: http://www.nitrc.org/projects/artifact_detect

L08.08

An *explainable* algorithm for automatic segmentation of glioblastoma

G. Belmonte[1], D. Latella[2], M. Massink[2], M. Biondi[1], G. De Otto[1], E. Vanzi[1], G. Rubino[3], P. Tini[3], V. Ciancia[2]
[1]*Azienda Ospedaliera Universitaria Senese, Medical Physics, Siena, Italy,* [2]*Consiglio Nazionale delle Ricerche, Istituto di Scienza e Tecnologie dell'Informazione 'A. Faedo', Pisa, Italy,* [3]*Azienda Ospedaliera Universitaria Senese, Radiotherapy, Siena, Italy*

Purpose/Introduction: Glioblastoma (GBM) is an intracranial tumor composed of infiltrating necrotic masses. Automatic contouring of GBM is an open challenging topic, since GBM is an intrinsically heterogeneous (in appearance, shape, and histology) brain tumor [1, 2]. Since 2012 a yearly challenge is organized by the MICCAI Conference, namely the Brain Tumor Image Segmentation Benchmark (BraTS). Although the actual trend is the use of machine learning to solve this problem, legal aspects about the accountability and the explainability of decisions may arise, especially in radiotherapy (RT). We present a logic-based approach using VoxLogica [3], a tool for *declarative image analysis* that provides powerful building blocks to develop concise, human-readable imaging algorithms.

Subjects and Methods: One of our algorithms [3] has been validated using the 2017 BraTS dataset containing multi-institutional pre-operative MRI scans of 210 patients affected by high grade gliomas. All the imaging data sets provided by BraTS 2017 have been segmented manually and approved by experienced neuro-radiologists. A priori, 17 cases have been excluded as the current procedure is not suitable (multi-focal tumors or artifacts in the acquisition). The executable specification of the procedure consists of a text file about 30 lines long, performing the following steps:

1) initial identification of the hyperintense regions in FLAIR (areas with intensity > 0.95 centile grown up to areas > 0.86 centile) (SEED).
2) search for voxels with a surrounding histogram similar (cross-correlation > 0.6) to SEED (SIM).
3) identification of Gross Tumor Volume (GTV) by growing SEED up to SIM area.

GTV is then enlarged by 2.5 cm to simulate the Clinical Target Volume (CTV) in RT.

Results: Segmentation results (see Fig. 1) were compared to manual ones using the DICE coefficient, Sensitivity and Specificity for GTV and CTV (Table 1). The images have size $240 \times 240 \times 155$ and the evaluation of each study takes about 10 s on a desktop computer with an Intel Core I7 7700 processor and 16 GB of RAM.

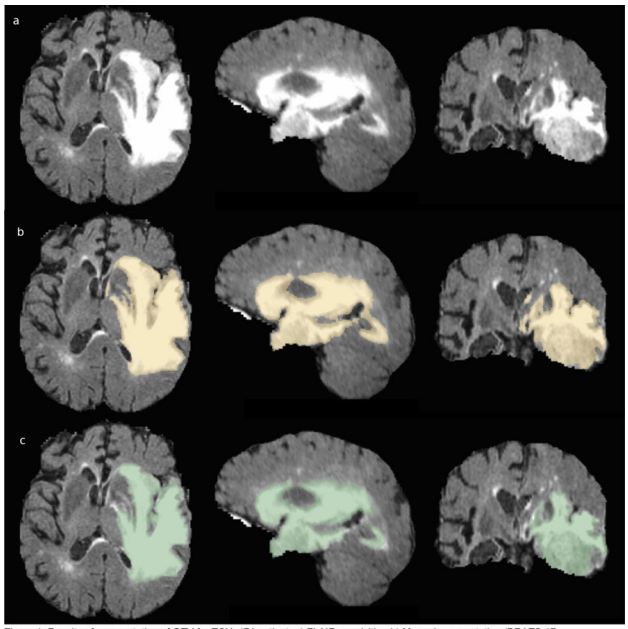

Figure 1. Results of segmentation of GTV for TCIA 471 patient: a) FLAIR acquisition b) Manual segmentation (BRATS 17 dataset) c) Segmention result of our algorithm

	DICE Coefficient			Sensitivity			Specificity		
	Mean(Std Dev)	Median	Range	Mean(Std Dev)	Median	Range	Mean(Std Dev)	Median	Range
GTV	0.85(0.10)	0.88	0.51-0.97	0.88(0.11)	0.92	0.47-1.00	1.00(0.00)	1.00	0.99-1.00
CTV	0.90(0.09)	0.93	0.52-0.99	0.95(0.07)	0.97	0.60-1.00	0.99(0.01)	1.00	0.93-1.00

Table 1. Score of comparison with manual segmentation (193 cases) [3]

Discussion/Conclusion: The presented results are in line with the state of the art [4]. Contouring GBM is a time consuming task, preliminary to planning therapy or surgery (for an expert radiotherapist it takes 30–60 min.). The obtained results (in terms of accuracy and time) make it feasible to include this method in the radiotherapy workflow. Further advantages of our approach are the huge flexibility and the use of a human readable algorithm, coded using few lines, thus transferable to a wider community to be further modified and improved.

References:

[1] Menze et al. IEEE Transactions on Medical Imaging 34(10) 2015
[2] Dupont, Betrouni, Reyns, Vermandel. IRBM 37(3) 2016
[3] Belmonte, Ciancia, Latella, Massink. Lecture Notes in Computer Science (LNCS) vol. 11427, 2019
https://github.com/vincenzoml/VoxLogicA
[4] Bakas et al. ArXiv:1811.02629 (to be published in LNCS)

L08.09

Dark Rim Lesions: novel double inversion recovery enhanced the prognostic accuracy in Multiple Sclerosis

F. B. Pizzini[1], F. Crescenzo[2], A. Giaretta[3], R. Magliozzi[2], A. Brillo[2], D. Marastoni[2], A. Tamanti[2], A. Pisani[2], M. Calabrese[2]
[1]*University Hospital Verona- Azienda Ospedaliera Universitaria Verona, Department of Diagnostics and Pathology, Verona, Italy,* [2]*University of Verona, Dept. of Neurosciences, Biomedicine and*

Movement, Verona, Italy, [3]University of Verona, Department of Diagnostics and Pathology, Verona, Italy

Purpose/Introduction: Chronic active lesions in Multiple Sclerosis (MS) characterized by a rim of iron-enriched, activated microglia and macrophages have been clearly identified in neuropathological studies.
In current study, we assessed the sensitivity of novel Double Inversion Recovery (DIR-WM) sequence in detecting lesion-rim and evaluating its role in clinical worsening of Multiple Sclerosis.
Subjects and Methods: One hundred and seven MS patients (18 RRMS and 89 PPMS) who underwent a 1.5T MRI baseline scan including a DIR-WM in 2004 and 15 years clinical and radiological follow up, were included in this longitudinal retrospective study. The presence of white matter lesions with and without a dark rim was evaluated at study entry and correlated with clinical and radiological disease course.
Results: White matter lesions surrounded by a dark rim (DRL) were found in 63 (58.9%) patients among the 107 included in the study. DRL were on average 30.1 ± 21.1% of total lesions.
DRL were more frequent in PPMS patients (13/18, 72.2%) than in RRMS (50/89, 56.1%) but this result was not significant (p = 0.207).
During follow up 28 patients out of 89 RRMS converted to the Secondary Progressive MS (SPMS). Two of them belonged to the group without DRL (2/39;5%) while 26 showed DRL at basal MRI (26/50; 52%; p value < 0.001)
The EDSS change over the 15 years follow up was greater both in RRMS (2.8 ± 2.6; p < 0.001) and PPMS (0.7 ± 1.2, p = 0.013) with DRL compared to patients without DRL (PPMS: 0.7 ± 1.2; RRMS: 0.3 ± 1.3).
The multivariate analysis (including also age, gender, age at onset, type of onset, disease duration, EDSS, CLs and spinal cord lesions) revealed that the volume of WM lesions and the volume of DRL were independent predictors of the EDSS change after 15 years.
Unusual hyperintense lesions were found in eight patients.
Discussion/Conclusion: Several WM lesions surrounded by a dark rim were identified by DIR-WM, even at 1.5T MRI. Further studies are needed to confirm that such dark rim, which we saw on DIR-WM corresponds to iron-rich microglial rim found on CA lesions; nevertheless, these lesions correlated with the disease evolution over the following 15 years. Finally the availability of such sequence at 1.5T MRI might allow its widespread application even in clinical practice.
References:
- Tillema JM et al.. Dark Rims: Novel Sequence Enhances Diagnostic Specificity in Multiple Sclerosis. AJNR Am J Neuroradiol. 2018 Jun; 39(6):1052–1058
- Absinta M, et al. Identificationof Chronic Active Multiple Sclerosis Lesions on 3T MRI. AJNR Am J Neuroradiol. 2018 Jul; 39(7):1233–1238
- Kaunzner UW et al. Quantitative susceptibility mapping identifies inflammation in a subset of chronic multiple sclerosis lesions. Brain. 2019 Jan 1; 142(1):133–145

L08.10
Assessing functional and structural connectivity in mTBI patients

N. Simard[1], M. D. Noseworhy[2]
[1]*McMaster University, Electrical and Computer Engineering, Hamilton, Canada,* [2]*McMaster University, School of Biomedical Engineering, Hamilton, Canada*

Purpose/Introduction: There are upwards of 1.7 million people each year affected by a mild traumatic brain injury (mTBI), or concussion[1]. Victims are left with poor diagnosis and a robust technique is required to identify presence, severity, and brain regions affected by a concussive injury. The goal of this research was to investigate individuals who have suffered an mTBI using diffusion tensor imaging (DTI) and resting state MRI (rsMRI). DTI is used to assess microstructural integrity whereas rsMRI is used to identify functional abnormalities through complexity analysis.
Subjects and Methods: mTBI patients (M/F age 35 to 55) having experienced an mTBI within 2 years were recruited. Healthy control subjects were sourced from data repositories (ICBM, PPMI, etc.). A GE MR750 Discovery 3T MRI scanner and 32-channel RF receiver coil were used for scanning mTBI patients. Axial DTI was acquired using a dual echo EPI sequence (TE/TR = 87/8800 ms, 122 × 122 matrix, 2 mm thickness, FOV = 244 mm). Tract-Based Spatial Statistics (TBSS) was used for analysis and parameters Fractional anisotropy (FA), Mean Diffusivity (MD), Radial Diffusivity (RD), and Axial Diffusivity (AD) were examined. Resting state data was also acquired using an EPI sequence (TE/TR = 35/2000 ms, 64 × 64 matrix, 3 mm thickness, FOV = 22 cm). A MATLAB processing pipeline was used for functional complexity analysis[2]. Voxel wise statistics were performed and commonly registered ROIs were segmented using the JHI Atlas. Group statistics were not performed as a Z-transform approach was used to identify subject-specific abnormalities[3]. The healthy control database included at least n = 25 for each age and sex.
Results:

Brain Region	FA Z-Score	MD Z-Score	AD Z-Score	RD Z-Score
WM Acoustic radiation Left	-1.340226	1.082508	0.472132	1.215568
WM Acoustic radiation Right	-1.701944	1.675214	1.15493	1.788096
WM Callosal body	-1.197766	1.223476	0.951374	1.238298
WM Cingulum Left	-0.141216	1.225352	0.95814	0.744898
WM Cingulum Right	-0.424446	1.555556	0.904348	1.125628
WM Corticospinal tract Left	-0.646458	0.313044	0.066666	0.352
WM Corticospinal tract Right	-0.811044	0.670184	0.463918	0.67647
WM Fornix	-1.44603	1.949494	1.646322	1.976744
WM Inferior occipito-frontal fascicle Left	-0.666014	0.943396	0.45	0.774648
WM Inferior occipito-frontal fascicle Right	-1.002252	0.82716	0.43	0.944444
WM Optic radiation Left	-0.687332	0.33945	-0.01444	0.470588
WM Optic radiation Right	-1.166148	0.606636	-0.065694	0.87826
WM Superior longitudinal fascicle Left	-1.226608	1.580646	-0.115384	1.5
WM Superior longitudinal fascicle Right	-1.242822	2.390244	1.267974	1.693694
WM Superior occipito-frontal fascicle Left	-1.48556	2.352202	1.436464	2.222222
WM Superior occipito-frontal fascicle Right	-1.147942	2.19024	1.147728	2.021164
WM Uncinate fascicle Left	-0.471482	0.140846	-0.44	0.385964
WM Uncinate fascicle Right	-0.920254	0.556962	-0.151658	0.726368

Figure 1. DTI TBSS Z score results shown with mildly injured areas in orange (1.65<Zscore<2), severely injured areas in red (2<Zscore< 3) and extremely injured areas in maroon (Zscore >4).

Brain Region	FD Z-Score
GM Amygdala centromedial group Left	-1.783973
GM Amygdala centromedial group Right	-2.241955
GM Amygdala laterobasal group Left	-1.814279
GM Amygdala laterobasal group Right	-2.127023
GM Amygdala superficial group Left	-1.731538
GM Amygdala superficial group Right	-2.28871
GM Anterior intra-parietal sulcus hIP1 Left	-3.051084
GM Anterior intra-parietal sulcus hIP1 Right	-2.74604
GM Anterior intra-parietal sulcus hIP2 Left	-2.744676
GM Anterior intra-parietal sulcus hIP2 Right	-2.422258
GM Anterior intra-parietal sulcus hIP3 Left	-2.139609
GM Anterior intra-parietal sulcus hIP3 Right	-1.565178
GM Broca's area BA44 Left	-0.851212
GM Broca's area BA44 Right	-1.535705
GM Broca's area BA45 Left	-0.627478
GM Broca's area BA45 Right	-1.244673
GM Hippocampus cornu ammonis Left	-1.922316
GM Hippocampus cornu ammonis Right	-1.755156
GM Hippocampus dentate gyrus Left	-1.689964
GM Hippocampus dentate gyrus Right	-1.477932
GM Hippocampus entorhinal cortex Left	-1.536378
GM Hippocampus entorhinal cortex Right	-1.404339
GM Hippocampus subiculum Left	-1.75754
GM Hippocampus subiculum Right	-1.576932
GM Inferior parietal lobule PF Left	-1.412263
GM Inferior parietal lobule PF Right	-1.121539
GM Inferior parietal lobule PFm Left	-1.768919
GM Inferior parietal lobule PFm Right	-1.572604
GM Inferior parietal lobule PFt Left	-1.43645
GM Inferior parietal lobule PFt Right	-1.289305
GM Inferior parietal lobule PGp Left	-2.072251
GM Inferior parietal lobule PGp Right	-1.296159
GM Inferior parietal lobule Pga Left	-2.062442
GM Inferior parietal lobule Pga Right	-1.328053
GM Insula Id1 Left	-1.471698
GM Insula Id1 Right	-2.445129
GM Insula Ig1 Left	-2.611503
GM Insula Ig1 Right	-4.390521
GM Insula Ig2 Left	-1.94997
GM Insula Ig2 Right	-3.193552
GM Leftateral geniculate body Left	-2.657108
GM Leftateral geniculate body Right	-1.791889
GM Mamillary body	-1.65281
GM Medial geniculate body Left	-2.815867
GM Medial geniculate body Right	-2.071372
GM Premotor cortex BA6 Left	-1.111038
GM Premotor cortex BA6 Right	-1.310035

Figure 2. rsMRI fractal dimension and/or complexity Z score results shown with mildly injured areas in orange (1.65<Zscore<2) severely injured areas in red (2<Zscore< 3) and extremely injured areas in maroon (Zscore >4).

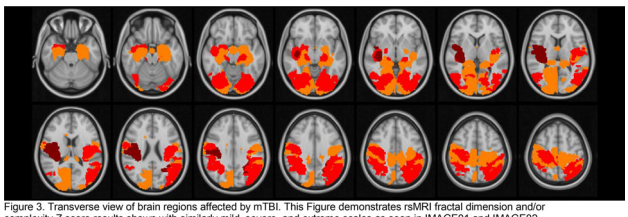

Figure 3. Transverse view of brain regions affected by mTBI. This Figure demonstrates rsMRI fractal dimension and/or complexity Z score results shown with similarly mild, severe, and extreme scales as seen in IMAGE01 and IMAGE02.

In all DTI and rsMRI parameters, control data Z scores were below 1.65($p < 0.05$). Structurally, injured individuals yielded at least 4 brain regions with Z scores above 1.65 ($p < 0.05$) in at least one DTI parameter. Functionally, injured individuals yielded at least 6 brain regions with Z scores above 1.65 ($p < 0.05$). In some cases, reduced functional connectivity was observed in the right or left brain which could infer that some injuries can induce functional changes in localized areas.

Discussion/Conclusion: Deficits in both structural and functional connectivity were clearly noted within individuals who have recently suffered an mTBI. Case by case analysis reinforces that group statistics should not be employed for this type of injury as all patients had a different clinical presentation due to heterogeneity of the cause of injury. More information on the nature of the injury should be collected to identify whether type of injury correlates with specific regional deficits.

References:

1. Faul M. (2010). Traumatic Brain Injury in the United States. Centers for Disease Control.

2. Mandelbrot. "Self-affine fractals and fractal dimension." *Physica scripta*.

3. Mayer AR. (2018). An evaluation of Z-transform algorithms for identifying subject-specific abnormalities in neuroimaging data.

L08.11

Tissue-type plasminogen activator and MRI features of cerebral sporadic small vessel disease

M. Zabitova[1], A. Shabalina[2], L. Dobrynina[1], M. Kostyreva[2], B. Akhmetzyanov[3], Z. Gadzhieva[1], **E. Kremneva**[4], M. Krotenkova[4]

[1]*Research center of neurology, Neurology, Moscow, Russian Federation,* [2]*Research center of neurology, Moscow, Russian Federation,* [3]*Medical and Rehabilitation center, Radiology, Moscow, Russian Federation,* [4]*Research Center of Neurology, Neuroradiology, Moscow, Russian Federation*

Purpose/Introduction: Cerebral sporadic small vessel disease (sSVD) is a one of the leading causes of cognitive decline, ischemic and hemorrhagic strokes worldwide. It is diagnosed with the MRI criteria elaborated by international society (STRIVE, 2013). The development of sSVD is closely related with endothelial dysfunction. Of special importance are studies of factors produced by endothelium and participating in the pathogenesis of SVD. In our study we aimed to clarify the relationships of tissue-type plasminogen activator (t-PA) and plasminogen activator inhibitor (PAI-1) with MRI features of sSVD.

Subjects and Methods: 71 patients (23 males and 48 females, mean age 60.5 yo) with sSVD diagnosed according to the STRIVE criteria were examined. Arterial hypertension of grade I was revealed in 12 patients, grade II in 7, and grade III in 37 patients. White matter hyperintensities (WMH), according to Fazekas (F) scale, were graded stage F1 in 17 patients, F2 in 23, and F3 in 30 patients. Control group comprised 21 age- and sex-matched individuals with normal brain MRI. Brain MRI (3 T) was performed in all patients, with the assessment of the following SVD features: WMH, lacunes, microbleeds, and enlarged perivascular spaces. Blood levels of t-PA and PAI-1 were measured by enzyme immunoassay. An ANOVA variance analysis was used ($p < 0.05$).

Results: High t-PA level was associated with more severe WMHs assessed with Fazekas stages ($p = 0.000$) and with larger volume of WMH ($p = 0.019$), as well as with the size of subcortical and semioval perivascular spaces ($p = 0.001$). This dependence was not related with the presence arterial hypertension or its characteristics ($p > 0.05$). PAI-1 levels were not associated ($p > 0.05$) with t-PA levels or MRI features of sSVD.

Discussion/Conclusion: The determined effect of t-PA level on the severity of WMH and perivascular spaces enlargement confirms the role of endothelial dysfunction in the development of sSVD and the involvement of t-PA in the mechanisms of brain injury.

The study was supported by Russian Foundation for Basic Research grant no 18-32-00852.

References:

1. Wardlow J.M., Smith E.E., Biessels G.J. et al. Neuroimaging standards for research into small vessel disease and its contribution to ageing and neurodegeneration. Lancet Neurol 2013; 12: 822–838. https://doi.org/10.1016/s1474-4422(13)70124-8.

2. Adibhatla R.M., Hatcher J.F. Tissue plasminogen activator (tPA) and matrix metalloproteinases in the pathogenesis of stroke: therapeutic strategies. CNS Neurol Disord Drug Targets 2008; 7: 243–253. PMID: 18673209.

3. Fredriksson L., Lawrence D.A., Medcalf R.L. tPA modulation of the bloodbrain barrier: a unifying explanation for the pleiotropic effects of tPA in the CNS. Semin Thromb Hemost. 2017; 43: 154–168. https://doi.org/10.1055/s-0036-1586229. PMID: 27677179.

L08.12

Assessing Blood–brain barrier permeability at 7T: proof of principle in a cortical ischemic stroke patient

L. Canjels[1], W. Backes[1], R. Rouhl[2], B. Poser[3], K. Bekelaar[2], R. van Oostenbrugge[2], A. Aldenkamp[4], J. Jansen[1]
[1]*Maastricht University Medical Center, School for Mental Health and Neuroscience, Radiology and Nuclear Medicine, Maastricht, The Netherlands,* [2]*Maastricht University Medical Center, School for Mental Health and Neuroscience, Neurology, Maastricht, The Netherlands,* [3]*Maastricht University, Faculty of Psychology and Neuroscience, Maastricht, The Netherlands,* [4]*Epilepsy Center Kempenhaeghe, Heeze, The Netherlands*

Purpose/Introduction: The blood–brain barrier (BBB) is a structural barrier that separates the blood from the parenchyma and regulates the exchange of biomolecules. BBB breakdown occurs in various diseases, including stroke[1]. Dynamic contrast-enhanced (DCE) MRI at 3T and kinetic modelling are often used to assess BBB leakage. This leakage can be subtle and the magnitude and rate of signal changes due to leakage are low and noisy. Using 7T, it is possible to obtain images with higher spatial and temporal resolutions and better SNR compared to 3T, enabling more subtle leakage assessment. Here, the feasibility of assessing BBB leakage at 7T was studied.

Subjects and Methods: A cortical ischemic stroke patient (male, 74 years, 5 month old lesion) and a control (female, 33 years) were scanned with a 7T MR system (Siemens Healthineers, Erlangen, Germany) and a 32-channel phased-array head coil.

T1 MP2RAGE (TR/TE: 5000/2.47 ms; TI_1/TI_2: 900/2750 ms; α_1/α_2: $5^o/3^o$; $0.7 \times 0.7 \times 0.7$ mm^3; 8 min) and Sa2RAGE (TR/TE: 2400/0.78 ms; TI_1/TI_2: 58/1800 ms; α_1/α_2: $4^o/10^o$; $2 \times 2 \times 2$ mm^3) sequences were used to obtain B_1^+ inhomogeneity-corrected T10 maps[2].

The DCE-MRI protocol consisted of a dual-time resolution with two nested volumetric interpolated brain examination sequences (TR/TE: 3.7/1.3 ms; α: 6.5^o). It included a fast sequence, to measure signal changes during early circulation, and a slow sequence, for sampling of the subtle extravasation into tissue. First, pre-contrast images were acquired. Subsequently, the fast sequence ($2 \times 2 \times 2$ mm^3; time interval: 1.7 s; 90 volumes; 3 min) was scanned during Gadobutrol injection (1.0 mmol/mL, 3 mL, flow rate: 0.3 mL/sec to avoid $T2^*$ artifacts). Next, the slow sequence ($1.5 \times 1.5 \times 1.5$ mm^3; time interval: 34 s; 36 volumes; 21 min) was applied.

The contrast agent concentration was estimated using the relative signal change and T10 map. A vascular input function was manually derived from the superior sagittal sinus and voxel-wise pharmacokinetic modeling was performed using the Patlak and a histogram approach to estimate the leakage rate (K_i) and fractional leakage volume (v_L)[3].

Results: Examples of the concentration–time curves and K_i maps are shown in Figs. 1 and 2. A higher K_i and v_L was found in the stroke lesion compared to those in other regions (Table 1). Higher K_i and v_L values of the non-lesional tissues were found in the patient compared to the control.

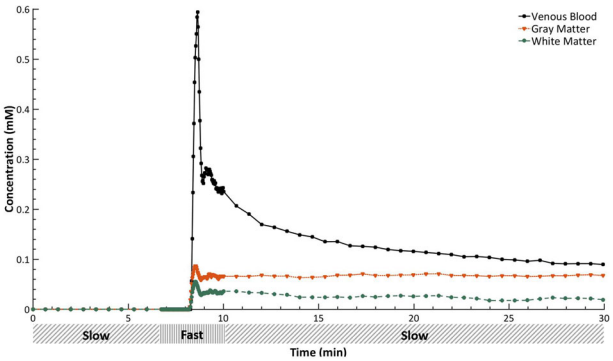

Figure 1: Example curves of the contrast agent concentration in the superior sagittal sinus and normal appearing tissues of the stroke patient. Below the time axis, there are bars to depict the fast and slow sequences.

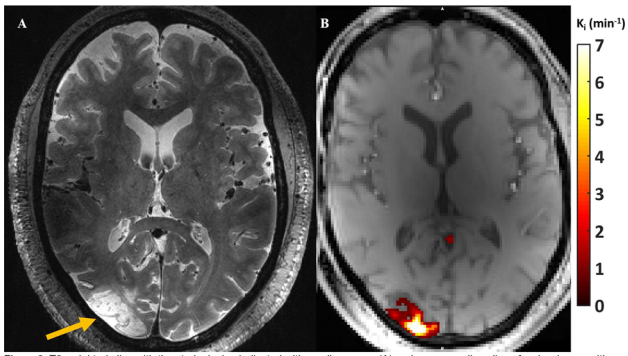

Figure 2: T2-weighted slice with the stroke lesion indicated with a yellow arrow (A) and corresponding slice of a slow image with an overlay of the Ki map (leakage in the arteries is removed) (B). Elevated leakage can be noted in the stroke lesion.

Tissue region	K_i (x 10^{-4} min^{-1}), mean ± SD			V_L (%), mean ± SD		
	Patient	Control	Literature[4]	Patient	Control	Literature[4]
White matter	3.78 ± 0.44	3.17 ± 1.10	2.96	0.44 ± 0.013	0.29 ± 0.037	0.58
Gray matter	5.32 ± 0.21	3.31 ± 0.65	3.91	1.8 ± 0.41	1.4 ± 0.22	1.20
Stroke lesion	115 ± 11	N/A	5.77	4.34 ± 0.91	N/A	0.80

Table 1: Values of the leakage rate and fractional leakage volume in different tissue regions in the stroke patient and healthy control.

Discussion/Conclusion: The feasibility of assessing BBB leakage at 7T is shown. Higher K_i and v_L values were found in non-lesional tissues in the patient compared to the control, which can be explained by the age difference and/or impaired cerebrovascular condition. The proposed method enables detection of large variations in K_i. The K_i and v_L values found were in the same order as those from literature. We are currently including more subjects to clarify the differences.

References:

[1]Kassner, Stroke, 2015.
[2]Marques, NeuroImage, 2010.
[3]van de Haar, Radiology, 2016.
[4]Heye, NeuroImage, 2016.

L08.13

fMRI as an objective tool for the assessment of olfactory function in anosmic patients

M. Gil-Correa[1], E. Sanz-Morales[1], H. Melero[1], S. Borromeo[1], C. Gomez-Calero[2], A. Toledano[3], J. A. Hernández-Tamames[4], N. Malpica[1]
[1]*Universidad Rey Juan Carlos, Medical Image Analysis and Biometrics Laboratory (LAIMBIO), Móstoles, Spain,* [2]*Universidad*

Rey Juan Carlos, Alcorcón, Spain, [3]*Hospital Universitario Fundación Alcorcón, Departamento de Otorrinolaringología, Alcorcón, Spain,* [4]*Erasmus MC, Radiology and Nuclear Medicine, Rotterdam, The Netherlands*

Purpose/Introduction: An early loss of olfactory function is considered a sign of neurodegenerative diseases (1). Nonetheless, objective quantification of anosmia still constitutes a challenge, which may be overcome using neuroimaging techniques. In order to achieve this purpose, fMRI was used to explore the neurophysiological changes (pre-post) induced by five sessions of olfactory training in a group of anosmic patients.

Subjects and Methods: Anatomical and functional images were acquired from 9 anosmic patients (age 55 ± 9; 3 male). A non-sniffing stimulation paradigm with 12 randomly-sorted odors (mint and vanilla) was applied through an fMRI-compatible olfactometer (2). The stimuli were synchronized with patients' respiration, ensuring exposure. Images were fieldmap corrected and analyzed with SPM12. PhysIO toolbox (3) was used to detect pulse and respiration artifacts and variance from WM-CSF signal. Due to the sample size, fixed factors analysis was used. For all subjects and sessions, results of RETROICOR and aCompcor were used as covariates. Statistical analysis was performed using a 2 × 2 ANOVA (factor odor: vanilla-mint; factor session: pre-post) and post hoc paired t tests (pre vs post). The ALE meta-analysis mask of olfactory areas (4) was used in order to explore differential activity in olfactory areas.

Results: Differential activity was observed in the right angular gyrus (whole brain; post hoc paired t test; Post > Pre; x = 48; y = − 70; z = 28; t = 4.51; pFWE < 0.05, cluster level) in response to vanilla (Fig. 1). Small volume correction showed differential activity in the left putamen (SVC = ALE meta-analysis mask; x = − 24; y = 2; z = − 8; t = 3.96; pFWE < 0.05, cluster level) (Fig. 2). No other effects were found.

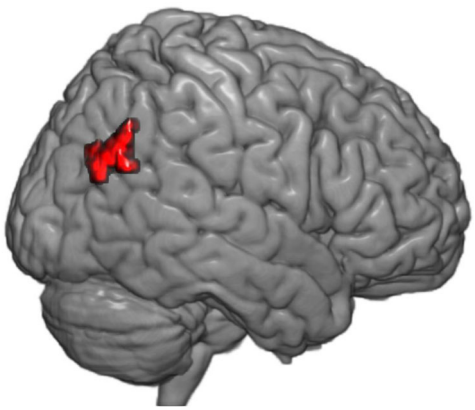

Figure 1: Vanilla; whole brain; post-hoc paired t-test; Post>Pre; pFWE<0.05, cluster level

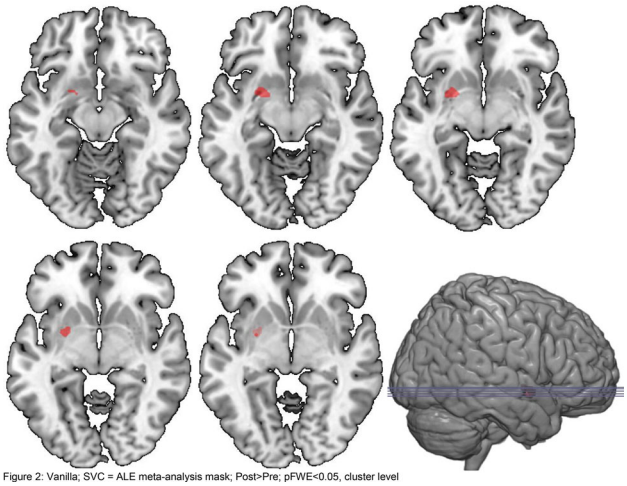

Figure 2: Vanilla; SVC = ALE meta-analysis mask; Post>Pre; pFWE<0.05, cluster level

Discussion/Conclusion: The results observed in the putamen and the angular gyrus suggest the activation response to odors of these anosmic patients changed. The fMRI methodological approach applied (non-sniffing, respiration-synchronization, fieldmap correction, physiological noise correction) increased the probability of detecting subtle functional variations, despite the high inter-subject variability of the olfactory function. In conclusion, the present study suggests that fMRI is a promising tool for the assessment of functional changes in olfaction.

References:

(1) Hummel, T., et al., (2010). Olfactory fMRI in patients with Parkinson's disease. Frontiers in Integrative Neuroscience, 4, 125.

(2) Borromeo, S., et al., (2010). Objective assessment of olfactory function using functional magnetic resonance imaging (fMRI). IEEE Transactions on Instrumentation and Measurement, 59(10), 2602–2608.

(3) Kasper, L., et al., (2017). The PhysIO toolbox for modeling physiological noise in fMRI data. Journal of neuroscience methods, 276, 56–72.

(4) Seubert, J., et al., (2013). Statistical Localization of Human Olfactory Cortex. NeuroImage, 66, 333–342.

L08.14

Magnetic resonance image compilation (MAGiC): utility in Epilepsy Imaging

R. Vadapalli[1], R. b. Annamraju[2], a. s. Vadapalli[3]
[1]*Vijaya Diagnostics, Radiology, Hyderabad, India,* [2]*GE Healthcare, Digital innovations in affordable care, Bangalore, India,* [3]*Medway Maritime Hospital Windmill Road Gillingham Kent, Orthopaedic surgery, Hyderabad 500020, India*

Purpose/Introduction: To evaluate the clinical utility of MAGIC sequence in Epilepsy Imaging in comparison with conventional epilepsy protocol.

Subjects and Methods: This is a Prospective observational comparative study of 50 patients with the history of refractory seizures in the age group of 12–54 years (Mean age 33 + _ with M: F ratio of 3:2 performed on a 3T Pioneer scanner (GE health care, Milwaukee) using conventional epilepsy protocol in addition to MAGIC sequence. DWI, Oblique T1 coronal for hippocampi, 3D T1 Bravo, 2D FLAIR axial, SWAN axial with T2 relaxometry 6 echo sequence lasting for 25 min in addition to MAGIC sequence is a one scan yielding 6 contrasts(T1, T1 FLAIR, FLAIR, STIR DIR, PSIR, quantitative T1

and T2 maps an additional 4 min. This study was done with the informed consent of the patient and ERB approval. The images were randomized and independently assessed for diagnostic quality, morphologic legibility, diagnostic radiologic findings indicative of gliosis, cortical dysplasia, Heterotopia, calcific granulomas and neoplasms and artefacts by two Independent neuro radiologists compared to the conventional Epilepsy protocol. Each case included conventional epilepsy protocol data set and MAGIC T1- and T2-weighted, T1 and T2 FLAIR, and STIR and/or proton density and synthetic reconstructions from multiple-dynamic multiple-echo imaging. The interobserver variability was recorded using Kappa statistics.

Results:

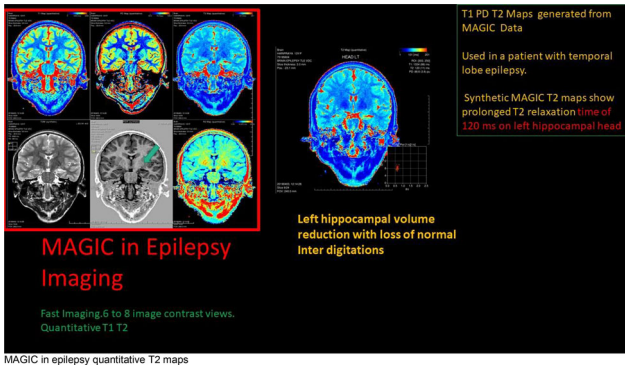

MAGIC in epilepsy quantitative T2 maps

Overall diagnostic quality of synthetic MR images was noninferior to conventional MR imaging for epilepsy on a 5-level Likert scale ($P < 0.001$; mean synthetic-conventional, -0.344 ± 0.312; $\Delta = 0.5$; lower limit of the 95% CI, -0.398). Legibility of synthetic and conventional morphology agreed in $> 95\%$, except in the basi frontal cortex and insulo opercular region in T1, T1 FLAIR (all, $> 80\%$). Synthetic T2 FLAIR had more obvious artefacts, including $+ 19.4\%$ of cases with flow artefacts and $+ 12.5\%$ cases with white noise artefacts. Interobserver variability was in acceptable limits (Cohen's kappa 0.9). T2 synthetic maps contributed to the measurement of T2 relaxation times of hippocampi which showed concordance with Multi-echo T2 relaxometry sequences.

Discussion/Conclusion: DIRMAGIC imaging with multiple contrast views significantly augmented speed and the lesion conspicuity and T2 relaxation measurement of Hippocampi in epilepsy imaging. Magnetic Resonance Image Compilation (MAGiC): Synthetic MR imaging enables reconstruction of various image contrasts from 1 scan, reducing scan times providing novel information with multiple contrasts and aids in the detection of epileptogenic substrate.

DIR and PSIR contrast views of MAGIC showed high sensitivity to FCD.

References:

Synthetic MRI for Clinical Neuroimaging: Results of the Magnetic Resonance Image Compilation (MAGiC) Prospective, Multicenter, Multireader Trial.

L.N. Tanenbaum, et al.; American Journal of Neuroradiology Apr 2017, https://doi.org/10.3174/ajnr.a5227.

L08.15

Low-level neural mechanisms support working memory performance in healthy ageing

P. Naumczyk[1], K. Jodzio[1], K. Finc[2]

[1]*University of Gdansk, Gdańsk, Poland,* [2]*Centre for Modern Interdisciplinary Technologies, Torun, Poland*

Purpose/Introduction: The functioning of the elderly population has recently drawn more and more attention in psychological, sociological and medical research due to the ageing of the population in the Western societies. The study aimed at exploring the neural mechanisms underlying good cognitive performance in the elderly.

Subjects and Methods: 27 healthy elderly participants (age: M = 70.35yo, SD = 5y; 16 women, 9 men) took part in the study. The study protocol included thorough neuropsychological assessment (fluid intelligence, crystalized intelligence, inhibition control, auditory working memory, visual working memory), as well as MRI examination on a 3.0T GE Discovery 750 scanner. The exam included T1-weighted sequence for anatomical reference as well as EPI BOLD sequence during preforming the PASAT. The fMRI was a blocked sparse design to allow for 1 s-length gap for subjects' response. The paradigm is presented on Fig. 1. The structural and the fMRI data was processed in Freesurfer's surface stream (version 6.0). The cortical thickness maps were created for each of the participants, as well as the parametrical maps with "Adding vs Repeating" as the contrast of interest. The fMRI data was inspected for movement and artifacts with artifact detection toolbox.

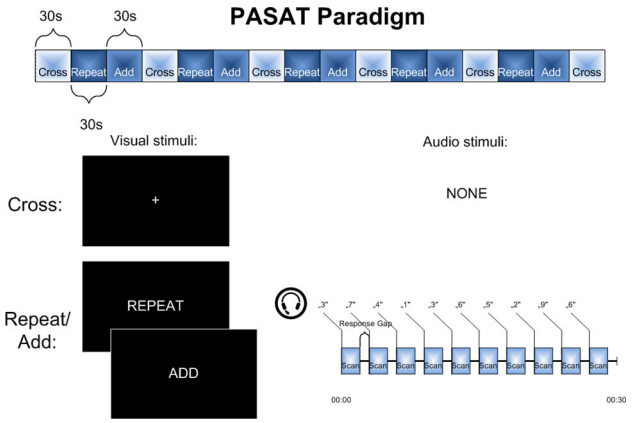

nThe first level fMRI GLM model included additional regressors of participant's movement, and outlier timepoints. The second level analyses (both for structural and functional data) included the neuropsychological variables of interest.

Results: The results are accounted for multiple comparisons (cluster-wise Monte Carlo simulation at $p < 0.01$). The main effect of the "adding-vs-repeating" contrast proved good criterion validity with multiple working memory regions significantly involved in processing (presented on panel A of Fig. 2).

Out of tested covariate models only one passed the multiple comparisons correction for cortical thickness maps—the PASAT performance one. The significant cluster was localized in the inferior temporal gyrus of the left hemisphere and is shown on panel B of Fig. 2.

For fMRI parametric maps, a significant covariate effect was found for PASAT performance and for BVRT performance, both with a positive effect (meaning the better was one's auditory/visual working memory, the bigger involvement of given areas in the fMRI adding-vs-repeating contrast). The former comprised one cluster localized in frontal lobes (namely the pars triangularis of the left hemisphere), the latter—four clusters in medial and lateral occipital lobes of both hemispheres. The results are presented on panels C and D of Fig. 2.

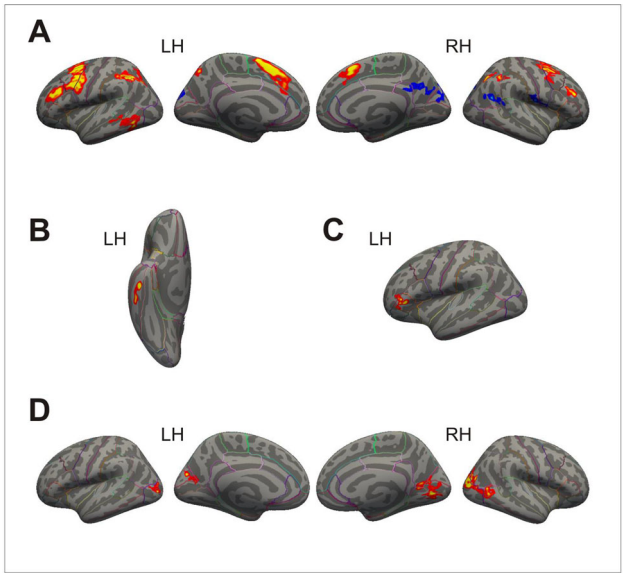

Discussion/Conclusion: The results highlight the importance of low-level processing in supporting good cognitive functioning of the elderly.

References:

Freesurfer: https://surfer.nmr.mgh.harvard.edu/
ART: http://www.nitrc.org/projects/artifact_detect

L08.16

Variation in white matter properties predicts the abilities of face recognition: a normal adult Cohort study

P.-Y. CHEN[1], C.-L. Chen[2], Y.-C. Hsu[3], C. CAN[4], M.-J. Chiu[5], W.-Y. I. Tseng[1]

[1]*Molecular Imaging Center, National Taiwan University, Taipei, Taiwan,* [2]*Institute of Medical Device and Imaging, National Taiwan University College of Medicine, Taipei, Taiwan,* [3]*AcroViz Technology Inc., Taipei, Taiwan,* [4]*Cambridge Center for Ageing and Neuroscience (Cam-CAN), University of Cambridge and MRC Cognition and Brain Sciences Unit, Cambridge CB2 3 EB, UK,* [5]*National Taiwan University, Department of Neurology, National Taiwan University Hospital, College of Medicine, Taipei, Taiwan*

Purpose/Introduction: Previous MRI and lesion studies [1, 2] have suggested the specific white matter association tracts with face recognition processing. However, the age-related patterns of the proposed white matter architecture and their association with face recognition remain to be well characterized. The present study hypothesized that variation of microstructural properties of these white matter tracts could predict the performance of face recognition.

Subjects and Methods: We performed MAP-MRI analysis [3, 4] and template-based analytical analysis [5] for diffusion images to estimate diffusion indexes FA and MD of segmented white matter tracts in a large (N = 459) sample from Cam-CAN data including normal adults ages 18–88. Table 1 displays the demographics and the accuracy of the face tests.

Age (years)							
Range	18-30	31-40	41-50	51-60	61-70	71-80	81-90
Subject number	51	62	77	73	84	84	30
Gender							
M/F	23/28	34/28	37/40	41/32	47/37	44/40	17/13
MMSE (Mini-Mental State Examination)							
range	25-30	25-30	26-30	26-30	25-30	25-30	25-30
mean (±SD)	29.25(±1.29)	29.19(±1.23)	29.09(±1.14)	29.14(±1.04)	28.53(±1.46)	28.20(±1.49)	27.83(±1.56)
HADS (hospital anxiety and depression scores) Range (Normal ≤ 7)							
anxiety	1-6	0-7	0-7	0-7	0-7	0-7	0-7
depression	0-4	0-6	0-7	0-7	0-7	0-7	0-6
Benton Face Test Accuracy (%) Total scores 27							
range	70-100	70-100	70-100	66-100	62-100	62-93	51-93
Mean (±SD)	88.60 (±7.90)	89.37(±6.76)	87.94(±6.10)	86.47(±7.79)	83.01(±9.02)	79.49(±7.73)	77.90(±8.78)
Famous Face Test Accuracy (%) Total scores 30							
range	56-100	66-100	70-100	73-100	46-100	73-100	43-100
Mean (±SD)	92.22(±10.85)	97.90 (±5.40)	97.52(±5.75)	97.18(±5.39)	93.73(±9.52)	92.20(±7.56)	82.22(±17.56)

Demographics and behavioral face tests of the 459 healthy adults in the Cam-CAN cohort.

We related performance on two behavioral face tests to white matter measures [2] including IFOF, ILF and UF. The two behavioral face tests were Benton Test of Facial Recognition [6] and face recognition test of famous faces assessing recognition of public figures.

Results: Table 2 displays more white matter tracts were involved in Benton face test which requires the ability to match the newly-seen face with variation in head orientation and lighting than those in simpler famous face test.

Dependent variable		Benton Face Test (Accuracy)					Famous Face Test (Accuracy)				
Predictor variable		$\beta_{(tract)}$	$\beta_{(age)}$	$\beta_{(gender)}$	R^2	SE	$\beta_{(tract)}$	$\beta_{(age)}$	$\beta_{(gender)}$	R^2	SE
IFOF_L	FA	0.112 p=0.027	**-0.399 p=0.000***	-0.018 p=0.663	0.218	7.804	**0.200 p=0.000***	-0.117 p=0.032	0.052 p=0.252	0.076	9.004
	MD	**-0.174 p=0.001***	**-0.361 p=0.000***	-0.026 p=0.0524	0.230	7.746	-0.046 p=0.409	**-0.204 p=0.000***	0.046 p=0.309	0.051	9.128
IFOF_R	FA	0.073 p=0.136	**-0.425 p=0.000***	-0.019 p=0.650	0.214	7.827	0.134 p=0.012	**-0.161 p=0.003***	0.050 p=0.269	0.062	9.072
	MD	**-0.159 p=0.002***	**-0.366 p=0.000***	-0.022 p=0.591	0.226	7.767	-0.131 p=0.023	-0.150 p=0.009	0.046 p=0.308	0.060	9.083
ILF_L	FA	0.013 p=0.763	**-0.460 p=0.000***	-0.020 p=0.632	0.210	7.845	**0.135 p=0.004***	**-0.200 p=0.000***	0.049 p=0.278	0.066	9.052
	MD	-0.115 p=0.011	**-0.416 p=0.000***	-0.023 p=0.573	0.221	7.791	-0.020 p=0.689	**-0.223 p=0.000***	0.047 p=0.296	0.049	9.134
ILF_R	FA	0.053 p=0.219	**-0.449 p=0.000***	-0.021 p=0.605	0.212	7.833	0.093 p=0.050	**-0.207 p=0.000***	0.045 p=0.318	0.057	9.097
	MD	**-0.135 p=0.004***	**-0.398 p=0.000***	-0.020 p=0.0629	0.224	7.776	-0.089 p=0.085	**-0.188 p=0.000***	0.048 p=0.290	0.055	9.101
UF_L	FA	0.074 p=0.085	**-0.445 p=0.000***	-0.019 p=0.655	0.215	7.821	0.115 p=0.014	-0.203 p=0.032	0.050 p=0.267	0.062	9.075
	MD	**-0.132 p=0.005***	**-0.412 p=0.000***	-0.028 p=0.495	0.225	7.772	0.094 p=0.056	**-0.268 p=0.000***	0.054 p=0.237	0.057	9.099
UF_R	FA	0.085 p=0.049	**-0.438 p=0.000***	-0.017 p=0.689	0.217	7.813	**0.133 p=0.005***	**-0.192 p=0.000***	0.053 p=0.239	0.065	9.123
	MD	**-0.154 p=0.001***	**-0.396 p=0.000***	-0.024 p=0.556	0.229	7.749	0.112 p=0.026	**-0.280 p=0.000***	0.051 p=0.260	0.059	9.086

Note: Standardised Bs (p values), adjusted R2 and standard error of the estimate of regression model reported. SE = standard error of the estimate; FA = fractional anisotropy; MD = mean diffusivity; IFOF = inferior fronto-occipital fasciculus; ILF = inferior longitudinal fasciculus; UF = uncinate fasciculus; L = left hemisphere; R = right hemisphere.
* = Significant difference after Bonferroni correction, p < 0.008.

Multiple regression models of face tests accuracy with confounding factors of age and gender.

Figure 1 shows different diffusion indexes (i.e. MD and FA) are sensitive to different face tests (i.e. Benton face test and famous face test, respectively).

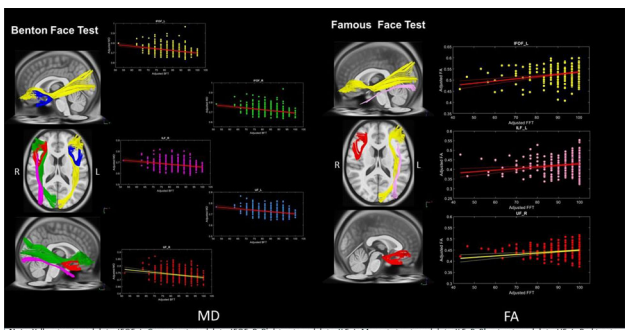

Note: Yellow tracts and dots: IFOF_L; Green tracts and dots: IFOF_R; Pink tracts and dots: ILF_L; Magenta tracts and dots: ILF_R; Blue tracts and dots: UF_L; Red tracts and dots: UF_R. (FA = fractional anisotropy; MD = mean diffusivity; IFOF = inferior fronto-occipital fasciculus; ILF = inferior longitudinal fasciculus; UF = uncinate fasciculus; L = left hemisphere; R = right hemisphere.

Significant linear relationship between the white matter tracts (y-axis) and the behavioral face tests (x axis). Individual variations in white matter substrates (MD or FA values of white matter tracts presented in colors) predicted Benton face test.

Discussion/Conclusion: Our finding suggests different cognitive loadings in face recognition processing are related to white matter integrity of the responsible tracts. Our finding also implies the measures of the directional coherence (FA) and measures of magnitude of water molecule diffusion (MD) may be sensitive to the specific cognitive attributes underlying face recognition processing and predict the performance of different face tests.

References:

1. Philippi, C.L., et al., *Damage to association fiber tracts impairs recognition of the facial expression of emotion.* J Neurosci, 2009. **29**(48): p. 15089–99.
2. Unger, A., et al., *Variation in White Matter Connectivity Predicts the Ability to Remember Faces and Discriminate Their Emotions.* J Int Neuropsychol Soc, 2016. **22**(2): p. 180–90.
3. Avram, A.V., et al., *Clinical feasibility of using mean apparent propagator (MAP) MRI to characterize brain tissue microstructure.* Neuroimage, 2016. **127**: p. 422–34.
4. Hsu, Y.C. and W.I. Tseng. *An efficient regularization method for diffusion MAP-MRI estimation.* in *Joint Annual Meeting ISMRM-ESMRM*. 2018. Paris, France.
5. Chen, Y.J., et al., *Automatic whole brain tract-based analysis using predefined tracts in a diffusion spectrum imaging template and an accurate registration strategy.* Hum Brain Mapp, 2015. **36**(9): p. 3441–58.
6. Levin, H.S., K. Hamsher, and A.L. Benton, *A short form of the test of facial recognition for clinical use.* J. Psychol, 1975. **91**(2): p. 223–228.

L08.17

The role low perfusion compartments in GBM patient survival using combing analysis of perfusion and diffusion MRI

G. Karami[1], M. Giussepe Orlando[2], M. Caulo[3], C. Del Gratta[4]
[1]*PhD student, Department Neuroscience, Imaging, and Clinical Science, Gabriele D'Annuzio University, Chieti-Pescara,, Chieti, Italy,* [2]*MD, Department Neuroscience, Imaging, and Clinical Science, Gabriele D'Annuzio University, Chieti-Pescara,, Chieti, Italy,* [3]*MD, Neuroradiologist, Department Neuroscience, Imaging, and Clinical Science, Gabriele D'Annuzio University, Chieti-Pescara, Chieti, Italy,* [4]*PhD, Physicist, Department Neuroscience, Imaging, and Clinical Science, Gabriele D'Annuzio University, Chieti-Pescara, Chieti, Italy*

Purpose/Introduction: Glioblastoma classified as Grade IV glial tumour carries the worst prognosis. Although the overall survival of patients remains low at 14.5 months, that is different among patients. Tumours exhibit intratumoral heterogeneity in diffusion and perfusion MRI, which might have prognostic significance and influence therapy response. Our purpose was to evaluate MD and CBV maps based on patients' survival to investigate their effects on survival. They may assist to planning treatment strategies.

Subjects and Methods: 12 GBM patients with known survival were selected from a database from 2011.

All patients underwent MRI examination with a 3T Philips Achieve Scanner, and pre-operative tumour protocols consists of T1 with GD, DTI with b value of 800 and DSC.

All images were co-registered on DTI-B0 images. The contour of tumour was manually drawn by a neuroradiologist. The MD and rCBV were calculated from diffusion and perfusion imaging, respectively. By clustering algorithm, low and high diffusion and low perfusion clusters were separated from the rest of tumour. Regions of lowest rCBV with the lowest MD and highest MD were identified to evaluate their effects on survival. We extracted the mean values and standard deviation of each maps and T1-Gd images. Patients were considered in 3 survival groups.

Results: First using a SVM trained model, patients survival using all data were classified with 98.96% accuracy (permutation test, $P < 0.001$). The sensitivity and specificity for each SVM classifier were 98.12, 100, 100 and 100, 99.24, 100 respectively.

The differences between MD and CBV histogram parameters and survival were assessed using pearson correlation coefficient and linear regression ($P < 0.01$) as well. Among these factors, 4 were independently associated with predicting the survival. Low perfusion values in restricted diffusion region values had higher correlation coefficient, then MD values in high diffusion. Low perfusion values in high diffusion region were smaller than in low diffusion.

Discussion/Conclusion: In this study we combined perfusion and diffusion MRI to identify two low perfusion compartments that may be responsible for treatment resistance. The method was able to predict survival significantly.

The decreased MD values are correlated with shorter survival. Low perfusion in the restricted diffusivity compartment suggests this compartment may contain other microstructures such as hypoxic which will be responsible for treatment resistant.

The negative correlation between low diffusion tumour volume and survival could indicate tumour grows. Tumours with larger low perfusion area had shorter survival which might be to prone treatment resistant due to hypoxia.

References:

1. Li C, Yan J-L, Torheim T, McLean MA, Boonzaier NR, Huang Y, et al. Low Perfusion Compartments in Glioblastoma Quantified by Advanced Magnetic Resonance Imaging and Correlated with Patient Survival. bioRxiv. 2018:180521.

L08.18

Segmentation of the arcuate fasciculus using probabilistic tractography in comparison with language fMRI

M. Jung-Botho, M. Batra, U. Klose
University Hospital Tübingen, Department of Diagnostic and Interventional Neuroradiology, Tübingen, Germany

Purpose/Introduction: Localization of functional language areas using clinical fMRI measurements is a part of pre-neurosurgical diagnostics. This procedure needs full cooperation of the patient. Tractography of the arcuate fasciculus (AF) might be an alternative since it does not require the patient to perform a specific task, being on diffusion weighted image acquisition. This study examines whether probabilistic tractography of the AF can be used as an alternative method of localizing language areas. We compare language lateralization with AF asymmetry as there have been conflicting findings regarding a possible correlation between the two. [1, 2].

Subjects and Methods: DTI sequences and fMRI data were acquired from 48 patients (29 with brain tumors, 19 with epilepsy) as part of routine preoperative imaging. The data was not normalized or preprocessed in any way that would warp or contort the original image.

Blinded from the fMRI results, we performed tractography of the AF by developing a method of manual ROI-selection based on anatomical landmarks.

Volume, fractional anisotropy and mean diffusivity of the AF were determined from its respective connectivity map. The number of

streamlines in the horizontal segment that passed through a selected slice in the coronal plane was also evaluated. For each patient, asymmetry indices (AI) for all of these values were calculated, comparing the AFs of both hemispheres to another.
fMRI data was analyzed by identifying the areas of Broca and Wernicke and quantifying the scope of cortical activation, again calculating an AI for each patient. These AIs were compared to the AIs from the tractography results.
Results: Tractography was successful in reconstructing a fiber bundle that conformed to the typical trajectory of the AF in all of the cases. Further, when comparing these results to the fMRI data, the morphology of the fiber tracts corresponded to the location of cortical activity in all of the cases as well, building a strong case for our method successfully and reliably displaying the AF.

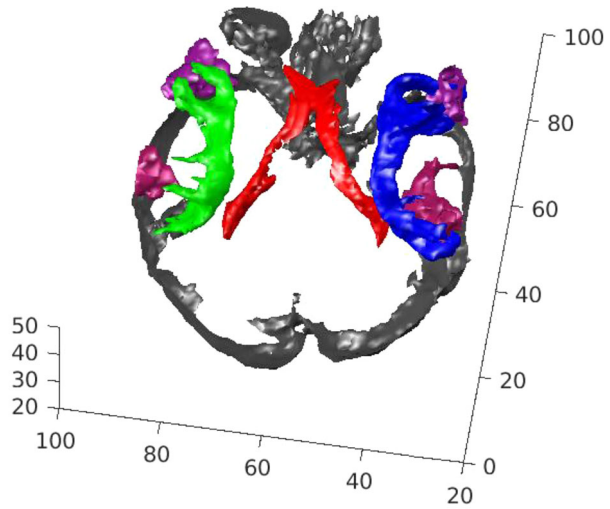

View from posterior, lateral ventricles (red) displayed for orientation. The trajectories of the left (green) and right (blue) AF correspond to the localization of language areas (purple) from the fMRI.

View from posterior, lateral ventricles (red) displayed for orientation. The trajectories of the left (green) and right (blue) AF correspond to the localization of language areas (purple) from the fMRI.
A majority of the patients showed language activation being lateralized to the left hemisphere. Leftward asymmetry of the AF in terms of volume and number of streamlines was also the most common constellation.
However, these metrics varied over a wide range and no significant correlation was found between the actual extent of lateralization of functional language areas and fiber tract asymmetry for any of the measured parameters.

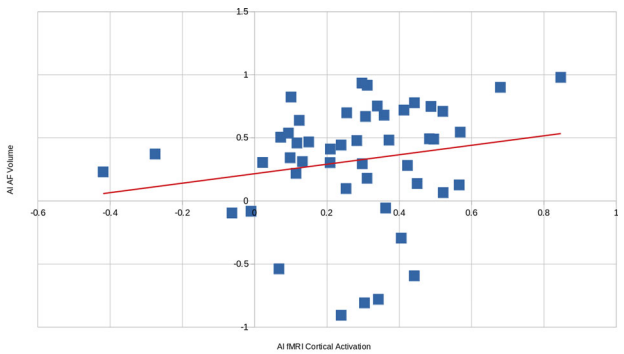

Scatterplot of AIs for fMRI cortical activation and AF volume. With a correlation coefficient of 0.185, this was the strongest correlation between fMRI and any of the measured AF parameters.

Discussion/Conclusion: We believe the employed method to be promising in terms of displaying the AF as part of pre-neurosurgical evaluation of the language areas even in the absence of fMRI data. The findings of this study may contribute to the ongoing discussion about the relationship between AF asymmetry and hemispheric language dominance.
References:
[1] Vernooij, M.W., et al., Neuroimage, 2007. **35**: p. 1064–76.
[2] Silva, G. and A. Citterio, Neuroradiol J, 2017. **30**: p. 470–476.

L08.19
Malrotation of the Coronal plane confounds callosal angle measurement in normal pressure hydrocephalus

W. Lee[1], A. Lee[1], R. Chen[1], N. Keong[2], L. L. Chan[1]
[1]*Singapore General Hospital, Department of Diagnostic Radiology, Singapore General Hospital, Singapore, Singapore, Singapore,*
[2]*Singapore General Hospital, Department of Neurosurgery, National Neuroscience Institute, Singapore, Singapore, Singapore*

Purpose/Introduction: Normal pressure hydrocephalus (NPH) represents a form of reversible dementia and can be alleviated through neurosurgical interventions such as ventriculo-peritoneal shunts. The callosal angle (CA) is a useful diagnostic tool in NPH, and a CA narrower than the cut-off value of 63° has been found to predict responders to shunt surgery amongst NPH patients[1]. While CA can be an important imaging marker, we hypothesis that slight malrotations of coronal plane can result in variable CA readings.
Subjects and Methods: CA measurements were performed on ten NPH patients recruited at a tertiary referral center. CA was measured on a coronal plane centered at the posterior commissure (PC) and perpendicular to the antero-posterior bicommissural line (AC-PC) identified on the mid-sagittal section (Fig. 1). This careful setup will hereby be referred to as coronal axis. On the coronal plane, lines were drawn tangential to the lateral ventricular roof and CA is given by the degree of intersection of both lines (Fig. 1).
Further coronal planes were created, with acute and obtuse antero-posterior angular offset of ± 5° and ± 10°, as well as right-left angular offset of ± 5° and ± 10°, with reference to the coronal axis (Fig 2). CA were measured on these malrotated coronal planes.

Figure 1.

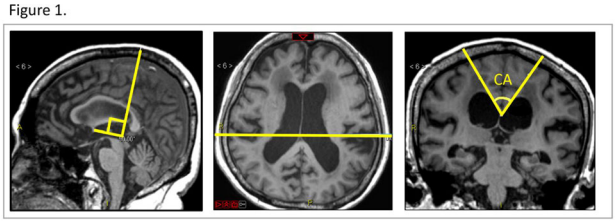

deal setup for CA measurement (coronal axis). Coronal plane at PC first identified on the mid-sagittal line, perpendicular to both AC-PC and mid-sagittal planes. CA - angle at intersection of lines drawn tangential to ventricular roof.

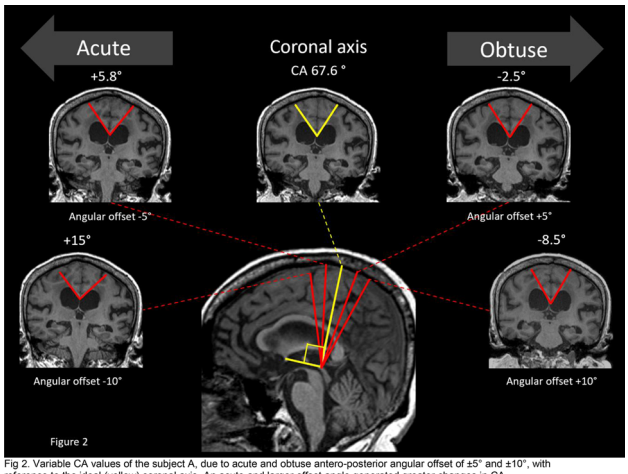

Fig 2. Variable CA values of the subject A, due to acute and obtuse antero-posterior angular offset of ±5° and ±10°, with reference to the ideal (yellow) coronal axis. An acute and larger offset angle generated greater changes in CA.

Results: Malrotated coronal planes with acute anterior angular offset of − 5° and − 10°, consistently demonstrated a wider CA, with − 10° resulting in larger change than − 5°. In contrast, malrotated coronal planes with obtuse posterior angular offset of + 5° and + 10°, consistently demonstrated a narrower CA, with + 10° generally resulting in larger change than + 5°.

Malrotated coronal planes with right-left angular offset of ± 5° and ± 10°, resulted in variable CA measurements. There was, however, a less predictable pattern inter-subjects, with no specific rotation or angular offset resulting in a greater angular change. Whilst mean change in CA is not large, it is very random and inconsistent as reflected by the range of CA change.

Table 1.

		Angular offset			
		-10°	-5°	+5°	+10°
Change in CA (°) with antero-posterior angular offset	(mean ± SD)	14.89 ± 4.57	7.29 ± 3.95	-3.11 ± 2.02	-7.08 ± 4.63
	(range)	(9.55,22.38)	(0.75,13.12)	(-5.88,-0.46)	(-16.14,-2.08)
Change in CA (°) with right-left angular offset	(mean ± SD)	3.45 ± 4.77	2.45 ± 5.27	2.80 ± 5.16	3.32 ± 4.28
	(range)	(-4.75,11.52)	(-4.46,12.29)	(-3.16,13.6)	(-2.32,12.87)

Table 1. Angular offsets of -10° to +10°, resulting in varying angular CA changes. A positive sign is a result of wider CA, and negative sign a result of narrower CA than actual angular value measured on coronal axis.

Discussion/Conclusion: CA measurements when done accurately, can be used to provide valuable prognostic information for shunt responsiveness and impact patient selection[1]. Although malrotations of the coronal plane may seem insignificant, our findings showed that these can result in variable CA measurements. Notably, a greater antero-posterior angular offset from the coronal axis, resulted in a greater angular change in CA. This is of clinical concern, when using cut-off values in selection of shunt candidates, as slight malrotation can result in impact treatment plan. A standardised setup in reformatting the coronal axis for CA measurement is therefore important to ensure consistent and reproducible CA measurements (Fig 1).

References:

1. Virhammar, Johan, et al. "The callosal angle measured on MRI as a predictor of outcome in idiopathic normal-pressure hydrocephalus." *Journal of neurosurgery* 120.1 (2014): 178–184.

L08.20

QSM as an indicator for the IDH mutational status in cerebral gliomas

J. Lindemeyer[1], **W. A. Worthoff**[1], A. Shymanskaya[2], K.-J. Langen[1], N. J. Shah[1]

[1]*Forschungszentrum Jülich, INM-4, Jülich, Germany,*
[2]*Forschungszentrum Jülich, INM-11, Jülich, Germany*

Purpose/Introduction: In this work, tumorous tissue is investigated using QSM [1] with a focus on changes in mean tissue susceptibility and heterogeneity, observed in patients with untreated cerebral gliomas and differing IDH mutational status. Data were acquired as part of a multimodal protocol [2] including [^{18}F]-FET-PET [3–5] and MRI.

Subjects and Methods: Measurements: In a host study[2], patients were measured on a 4T scanner using a multi-echo gradient echo sequence at 1 mm isotropic, FA = 11°, TR = 18 ms, and echoes at 2.5 ms(BW = 500 Hz/Px) and 12.0 ms(BW = 160 Hz/Px). All subjects gave informed consent.

The IDH mutational status was determined neuropathologically following biopsy or resection. Five IDH positive (IDHpos) and five IDH negative (IDHneg) subjects were evaluated.

Analysis: A brain mask was determined using bet2[6] and reconstruction was performed using an iterative framework[7]. Field maps were estimated via spatial unwrapping[8] and linear regression.

Harmonic and dipole fitting[9] removed background distortions and recovered phase data in the rim regions.

Susceptibility was reconstructed using a Tikhonov- and gradient-based approach[10] without spatial priors.

Segmentation of tumour (TUM) and healthy (HEA) tissue located in the contralateral hemisphere was obtained in [2]. The QSM results were coregistered to the segmentation basis. For each subject, we calculated:

·Mean difference: $\Delta\chi$ = mean(χ(TUM))-mean(χ(HEA)).

·Standard deviation within tumour/healthy tissue: σ_{TUM} = std(χ(TUM)) and σ_{HEA} = std(χ(HEA)).

·Standard deviation difference: $\Delta\sigma = \sigma_{TUM}$-$\sigma_{HEA}$.

The standard deviation serves as a measure of heterogeneity.

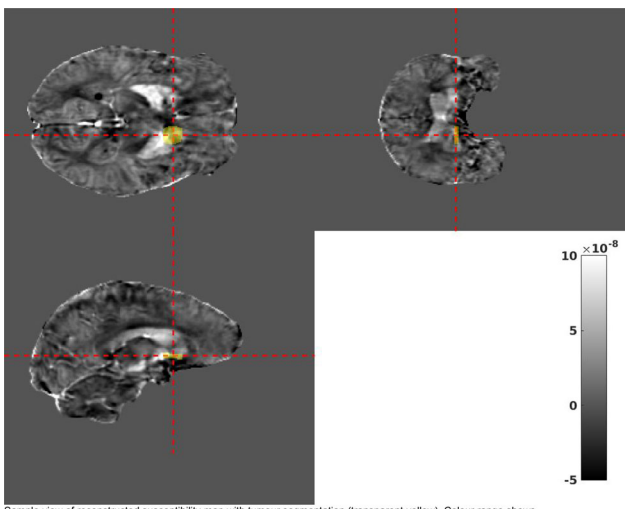

Sample view of reconstructed susceptibility map with tumour segmentation (transparent yellow). Colour range shows susceptibility in greyscale.

Results: The $\Delta\chi$ comparison shows positive and negative differences, indicating a change in tumour tissue composition. No significant difference can be observed between both patient groups. Hence, tissue changes related to the IDH status appear to have no influence on macroscopic susceptibility.

While σ_{HEA} shows no significant correlation with IDH status, σ_{TUM} exhibits higher values for IDHneg, which is further supported by an evident increase in $\Delta\sigma$. This indicates a higher tumour tissue heterogeneity in the IDHneg patients.

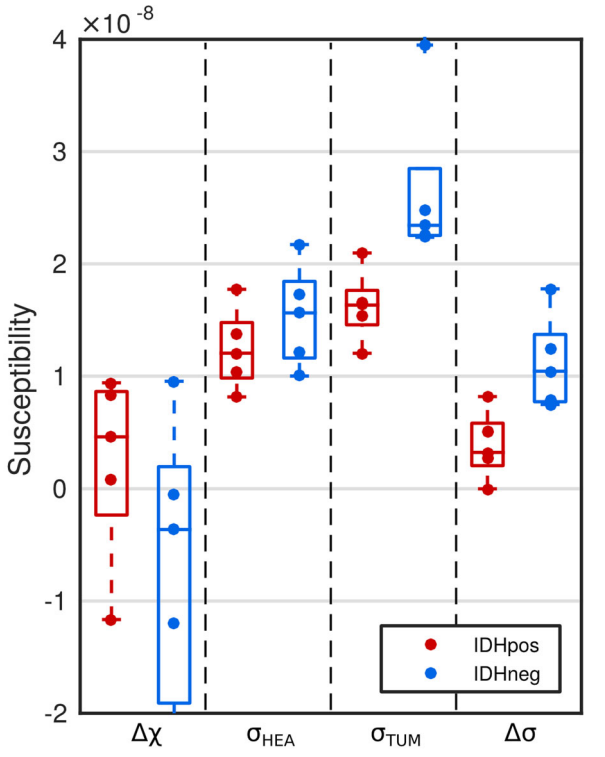

From left to right, the plots illustrate the numeric results of Δχ, σHEA, σTUM and Δσ, comparing IDHpos (red) and IDHneg (blue) patients.

Discussion/Conclusion: Tissue heterogeneity can indicate the IDH mutational status of gliomas. It would seem that tumour tissue is spatially reorganised on a microscopic scale in IDHneg patients, while the macroscopic composition evolves similarly in both groups. This information complements traditional imaging such as [^{18}F]-FET-PET and promotes understanding of tumour tissue structure.

References:

1. Wang, Magnet Reson Med, 2015, 73(1).
2. Shymanskaya&Worthoff, Mol Imaging Biol, in press.
3. Kunz, Neuro-oncology, 2018, 21(6).
4. Suchorska, Neuro-oncology. 2018; 20:279–88
5. Verger, Eur. J. Nucl Med Mol Imaging, 2018; 45:443–51
6. Smith, Hum Brain Mapp, 2002, 17(3)
7. Lindemeyer, Magn Reson Mater Phy (2017), 30(Suppl 1):1.103–104
8. Abdul-Rahman, Appl Opt, 2007, 46(26).
9. Lindemeyer, PLOS ONE, 2015, 10(9), p. e0138325.
10. de Rochefort, Magnet Reson Med., 2010, 63(1).